REPORT DOCUMENTATION PAGE

Public reporting burden for this collection of information is estimated to average 1 hour per response, including the time for reviewing instructions, searching existing data sources, gathering and maintaining the data needed, and completing and reviewing the collection of information. Send comments regarding this burden estimate or any other aspect of this collection of information, including suggestions for reducing this burden, to Washington Headquarters Services, Directorate for Information Operations and Reports, 1215 Jefferson Davis Highway, Suite 1204, Arlington, VA 22202-4302, and to the Office of Management and Budget, Paperwork Reduction Project (0704-0188), Washington, DC 20503.

1. AGENCY USE ONLY *(Leave blank)*	2. REPORT DATE	3. REPORT TYPE AND DATES COVERED
	9 Jan 97	

4. TITLE AND SUBTITLE
A Climatology Of Tropical Synopical Scale Behavior From Tovs-Estimated Precipitable Water

5. FUNDING NUMBERS

6. AUTHOR(S)
Morgan Douglas Mackey

7. PERFORMING ORGANIZATION NAME(S) AND ADDRESS(ES)
Texas A&M University

8. PERFORMING ORGANIZATION REPORT NUMBER

96-147

9. SPONSORING/MONITORING AGENCY NAME(S) AND ADDRESS(ES)
DEPARTMENT OF THE AIR FORCE
AFIT/CIA
2950 P STREET
WPAFB OH 45433-7765

10. SPONSORING/MONITORING AGENCY REPORT NUMBER

11. SUPPLEMENTARY NOTES

12a. DISTRIBUTION AVAILABILITY STATEMENT
Unlimited

12b. DISTRIBUTION CODE

13. ABSTRACT *(Maximum 200 words)*

19970117 142

14. SUBJECT TERMS			15. NUMBER OF PAGES
			276
			16. PRICE CODE

17. SECURITY CLASSIFICATION OF REPORT	18. SECURITY CLASSIFICATION OF THIS PAGE	19. SECURITY CLASSIFICATION OF ABSTRACT	20. LIMITATION OF ABSTRACT

DISCLAIMER NOTICE

THIS DOCUMENT IS BEST
QUALITY AVAILABLE. THE
COPY FURNISHED TO DTIC
CONTAINED A SIGNIFICANT
NUMBER OF PAGES WHICH DO
NOT REPRODUCE LEGIBLY.

A CLIMATOLOGY OF TROPICAL SYNOPTIC SCALE BEHAVIOR
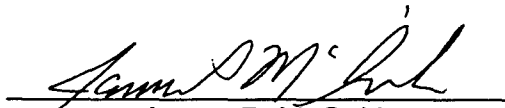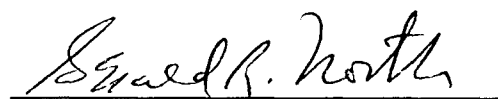# FROM TOVS-ESTIMATED PRECIPITABLE WATER

A Thesis

by

MORGAN DOUGLAS MACKEY

Submitted to the Office of Graduate Studies of
Texas A&M University
in partial fulfillment of the requirements for the degree of

MASTER OF SCIENCE

December 1996

Major Subject: Meteorology

A CLIMATOLOGY OF TROPICAL SYNOPTIC SCALE BEHAVIOR

FROM TOVS-ESTIMATED PRECIPITABLE WATER

A Thesis

by

MORGAN DOUGLAS MACKEY

Submitted to the Office of Graduate Studies of
Texas A&M University
in partial fulfillment of the requirements for the degree of

MASTER OF SCIENCE

Approved as to style and content by:

_____
James P. McGuirk
(Chair of Committee)

_____
John W. Nielsen-Gammon
(Member)

_____
Benjamin S. Giese
(Member)

_____
Gerald R. North
(Head of Department)

December 1996

Major Subject: Meteorology

ABSTRACT

A Climatology of Tropical Synoptic Scale Behavior from TOVS-Estimated

Precipitable Water. (December 1996)

Morgan Douglas Mackey, B.S., United States Air Force Academy

Chair of Advisory Committee: Dr. James P. McGuirk

Tropical synoptic scale behavior is examined using 3 to 8 day filtered precipitable water (PW) estimated from TOVS operational satellite observations for 24 three-month seasons. Zonally-oriented tropical convergence zones and regions of enhanced synoptic variance are quantified and found to be poorly correlated with each other.

Time-longitude plots (Hovmoller format) identify spatially coherent PW anomalies that can often be tracked around the globe. The strongest and most consistent signal is of eastward propagation across northern hemisphere Africa. Other regions demonstrate both eastward or westward propagation according to season and location. A general shift from eastward to westward propagation occurs between 20° and 30° latitude in each hemisphere. Hovmoller composites suggest an additional eastward propagating mode between 5°N and 12.5°N during SON across the entire Pacific Ocean.

Seven tropical regions are chosen to perform climatological studies of synoptic scale behavior. Hovmoller composites reveal 10 m/s westward propagation across the North Atlantic (zonal wavelength is 6,000 km) and 7 m/s eastward propagation of over Sahel Africa (zonal wavelength is 2,500-3,000 km). Composites over the southern Indian Ocean suggest westward motion, while propagation in the ITCZ, SPCZ, west Pacific warm pool, and Amazon basin shows little preference of zonal direction.

Interaction between the synoptic and the intraseasonal and interannual time scales is studied. The intraseasonal oscillation does not affect synoptic PW anomalies, even within the monsoon regions. Lag correlation plots reveal a directional reversal of zonal propagation of synoptic PW anomalies between warm and cold ENSO phases in the Pacific and Indian Ocean regions.

Hovmoller plots of synoptically filtered OLR and PW data show large regions void of OLR anomalies, while PW anomalies remain coherent throughout the tropics. A seasonally averaged daily point-to-point correlation between PW and OLR data over the tropical domain shows weak negative correlation, with almost zero correlation along convergence zones and in the west Pacific warm pool region, implying the PW is both a more sensitive and a more reliable signal.

DEDICATION

I dedicate this thesis to my wife, Chandra, for all the strength, help, and support she has given to me. She has set aside her own ambitions for the past several months to be actively involved in helping me focus on completing this work. She has spent many nights alone with our children, Vikash and Jayant, to take care of them while I was working at school. Above all, she has been the best friend to me that a person could have.

ACKNOWLEDGMENTS

TABLE OF CONTENTS

LIST OF FIGURES

FIGURE   Page

FIGURE   Page

LIST OF TABLES

CHAPTER I

INTRODUCTION

Tropical synoptic scale behavior includes atmospheric variations with temporal scales between those of mesoscale convective systems and large planetary circulations and intraseasonal variations. Although variations span a continuous spectrum of time scales from daily to near monthly, this research arbitrarily focuses on periods of three to eight days. Synoptic scale activity embodies many separate phenomena, including easterly waves, large cyclones and super cloud clusters, tropical plumes, cold air surges, westerly wind bursts, mid latitude intrusions, tropical upper tropospheric troughs, interhemispheric interactions, etc. (Lau and Chang, 1987).

Studies of tropical behavior have depended upon four major data sources. *In situ* observations (station and ship observations, raobs), remotely sensed data (OLR, tropospheric mean temperature, precipitation, precipitable water (PW)), operational analyses (ECMWF and NMC products), and intense observational programs (GATE, FGGE, TOGA COARE) have all assisted the study of tropical phenomena. The investigative programs supply excellent regional data coverage; thus, they offer insight on smaller scale activity. However, the study of larger scale features on a global scale is not feasible with such spatially constrained data. In order to study synoptic scale phenomena throughout the global tropics, data must be continuous through a large spatial domain. Data sources that meet this criterion include operational analyses and remotely sensed data. However, pitfalls in some of these data sources render

---

The style is that of the *Journal of the Atmospheric Sciences*

them less preferable for the study of synoptic activity. Operational analyses commonly underrepresent synoptic activity, as they greatly rely upon the first guess field for estimations of variables in data sparse regions. Microwave data offer excellent spatial coverage over the ocean, but are unusable over land regions. OLR data are useful to identify phenomena associated with convective activity, but do not distinguish between convection and persistent cirrus and fail to sense synoptic behavior not immediately associated with convection.

This study examines tropical synoptic scale activity within a gridded database of precipitable water derived by linear regression from TIROS Operational Vertical Sounder (TOVS) individual channel radiances. The TOVS-generated PW dataset is spatially continuous over land and water for the region from 30°N to 30°S and has a grid point resolution of 2.5°. This type of dataset makes it possible to study synoptic scale activity. Since the dataset is based upon contiguous remotely sensed observations of the atmosphere, no first guess fields are needed to fill in data sparse regions. Previous work by Chung (1993) and Yin (1994) has shown the usefulness of this type of dataset and Hatfield (1994) applied these data in a pilot study of atmospheric variations over the tropical Pacific.

The TOVS-generated PW data are used to identify differing synoptic scale characteristics occurring within various predetermined tropical regions. Additionally, interactions between synoptic and longer time scales are identified within the various tropical regions of study. Finally, these data are compared with OLR data to identify fundamental differences in the capabilities of each type of synoptic scale signal.

CHAPTER II

BACKGROUND

The earliest studies of synoptic scale activity relied upon direct observations. Dunn (1940) documented the easterly wave in the Caribbean. Further study of this phenomenon pinpointed its origin near Africa and revealed a westward propagation direction (Riehl, 1945). Riehl (1948) continued to document variations in tropical behavior by studying the development of typhoons in the Pacific Ocean. He concluded that the equatorial front does not extend across the entire Pacific and that typhoons develop in areas of upper level divergence in unstable regions of the northern hemisphere's trade winds. But without the existence of other data sources at that time, many phenomena went unnoticed or misunderstood.

With the help of meteorological models, Matsuno (1966) described linear quasi-horizontal wave motions in the tropics. He identified and described an eastward-moving Kelvin component, a westward-moving Rossby component, and an inertio-gravity component at different latitudes and wavenumbers. Such results initiated a paradigm shift that elevated scientific explanation of tropical phenomena, and most research thereafter has documented tropical behavior in terms of these barotropic normal mode responses. Other research concentrated on propagation of tropical behavior into the midlatitudes. Webster (1973) identified preferred geographical locations for the development and maintenance of seasonally varying transient disturbances. Webster and Holton (1982) determined that areas of westerly winds in the tropics represent regions of interhemispheric propagation. Branstator (1983) studied the propagation of wave energy in terms of critical lines, reflecting regions, and atmospheric wave

guides. Webster and Chang (1988) proposed a possible connection between equatorial flow perturbations and regions of negative stretch in the upper tropospheric westerlies where wave energy accumulates. Such regions were also proposed to be preferred locations of tropical-midlatitude interactions. Li and Nathan (1994) observed that low frequency westward-moving Rossby waves can propagate through tropical easterlies into the extratropics, in contrast to stationary Rossby waves. They concluded that these forced waves have the ability to maintain their strength well into the midlatitudes. Takayabu (1994a, b) used IR equivalent blackbody temperature signals to identify and document large scale cloud disturbances and associated them with Matsuno's (1966) predicted normal mode behavior, including gravity modes, over the Indian and western Pacific Oceans.

Other studies of tropical behavior concentrated on a wide spectrum of phenomena. Sadler (1967) examined the origin of tropical vortices and linked their initiation to tropical upper tropospheric troughs (TUTT). He determined that tropical vortices form in the directional shear zones of these troughs rather than in easterly flow. Also, he identified geographical regions of favorable vortex origin. Gruber (1972) studied ITCZ behavior and fluctuations in the Atlantic and Pacific Oceans and concluded that the ITCZ remains north of the equator in both oceans, regardless of season. For his day, he determined that the best tools to study this phenomenon were observational analyses and remotely sensed observations. Thepenier and Cruette (1981) described an interaction between the American subtropical jet stream and midlatitude synoptic scale disturbances reaching Europe. Their study described the evolution of large cloud bands originating in the eastern subtropical Pacific. McGuirk et al. (1987) defined this phenomenon as a moisture burst. In their

study, they hypothesized that moisture bursts represent transient intensification of the mean meridional circulation when the zonal Hadley circulation is weak.

Madden and Julian (1972) documented a 40-50 day oscillation in station pressure and upper air data throughout the Indian and Pacific Oceans. They determined that this eastward-propagating phenomenon was out of phase between the lower and upper troposphere. Using remotely sensed data and observational analyses, various authors have verified the existence of this phenomenon, known as the intraseasonal oscillation (ISO) (Lau and Chan, 1985; Murakami and Nakazawa, 1985; Nakazawa, 1986; Lau and Peng, 1987; Weickmann and Khalsa, 1990; Salby and Hendon, 1994). Studies have placed interest upon scale interaction between synoptic, intraseasonal, and interannual activity through various mechanisms, such as super cloud clusters (SCC) and monsoonal variations. Wang and Murakami (1988) demonstrated enhanced ISOs during ENSO cold phases, and depressed ISOs during mid-ENSO. Lau (1993) revealed coupling between synoptic scale and ISOs in the Asian monsoon regions. Also, Murakami et al. (1986) concluded that ISOs are enhanced through mutual interaction with transient disturbances, particularly over the monsoon regions. In addition, they noted that transient disturbances tend to be more active during the convective phase of the ISO. Nakazawa (1988) proposed the existence of the super cloud cluster (SCC). He observed this large-scale convective feature over the equator with eastward propagation, and in association with atmospheric disturbances having a Kelvin wave structure. A subsequent study of SCCs confirmed these observations (Hayashi and Nakazawa, 1989). Chao and Lin (1994) showed that SCCs are somewhat responsible for the ISO. In addition, they remarked on the importance that the convective parameterization scheme has on SCC model results. Such a conclusion indicates a relationship between the mesoscale and larger scale

activity as well. Lau and Wu (1994) included the effect of East Asian cold surges on SCC development during northern hemisphere winter. They proposed that SCCs in the equatorial region are much less organized during northern summer because of an absence of cold air outbreaks during this time of year. Chen et al. (1996) discussed the manner in which cloud clusters over the TOGA COARE region were organized on various time and space scales. They demonstrated that these clusters were much more active during the active phase of the ISO than during the suppressed phase (ten times more frequent). They also documented an apparent westward and eastward propagation of observed cloud clusters and offered explanations for both phenomena.

Tropical and midlatitude interactions have been the focus of several studies. Hsu et al. (1990) documented a possible chain of events starting with a Rossby wave train organizing convection over the Indian Ocean and ending with an area of Indonesian convection giving rise to a North Pacific wave pattern and increased upper tropospheric equatorial westerlies in the eastern Pacific. Kiladis and Weickmann (1992a, b) demonstrated an association between high frequency convective activity in the eastern Pacific, eastern South America, and the central South Pacific, and the intrusion of troughs from midlatitudes in regions of westerly winds.

Studies have also focused directly on synoptic scale activity in the tropics. Hayes (1988) identified active modes of the ITCZ, concentrating on their associated synoptic scale variations. Liebmann and Hendon (1990) noticed a spectral peak at 4 days in the ECMWF wind analyses and OLR data in the tropical central Pacific, marking a westward-propagating phenomenon. They identified meridional propagation into the midlatitudes in the far western Pacific along the equator, and at nearly every longitude north of the equator. The strongest disturbances along the equator are confined to the lowest half of

the atmosphere, although at many longitudes there is evidence of a weak baroclinic structure; north of the equator, disturbances are primarily barotropic. Lau and Lau (1990) identified preferred regions of synoptic scale activity in the western Pacific, eastern Pacific, Bay of Bengal/northern India, and eastern Atlantic/western Africa areas. All such activity propagates west-northwestward. Winton (1991) focused on convective variability over the eastern Pacific and identified a spectral peak at five days.

A possible link between tropical variations and SST has also been explored (Steiner and Khalsa, 1987; Chen and Yen, 1994; Li and Wang, 1994). Such research has indicated that a change in the Pacific SST results in variations in the Indian monsoon system and barotropic normal mode responses. Steiner and Khalsa concluded that changes in SST are not always associated with enhanced local convection; rather, increases in the amount of highly reflective clouds in the eastern Pacific are generally preceded by one or more months of elevated low-level PW and SST.

The use of time filtering has offered additional insights in the interpretation of tropical phenomena. Murakami (1980) demonstrated the value of this technique by time filtering an OLR dataset to identify 15-30 day variations in the Indian/western Pacific Ocean region and to quantify their propagation and intensity. Many subsequent studies have used this technique to extract information concerning tropical phenomena (Nakazawa, 1986; Hsu, et al., 1990; Kiladis and Weickmann, 1992a, b; Salby and Hendon, 1994).

Ever since Smith et al. (1979) discussed the ability of the TIROS-N series of polar-orbiting satellites to observe total column moisture content of the troposphere, variables related to this feature have been used in several studies of the tropical atmosphere. Precipitable water (PW), defined as the amount of water that would precipitate from a column of the atmosphere if all moisture

were condensed out, has been the moisture content variable of choice in some of these studies (Cadet, 1983; Cadet and Greco, 1987; Khalsa and Steiner, 1988; Hatfield, 1994). Conclusions from these studies reveal that the PW signal is useful to detect variations on the interannual time scale and may have applications on the intraseasonal scale. Also, PW maxima on the shorter time scales was found generally coincident to 250 mb velocity potential minima (Khalsa and Steiner, 1988). A relationship between PW and SST has been observed by Steiner and Khalsa (1987) and by Stephens (1990), who described a quantitative relationship between these two variables at monthly time scales. Stephens discussed how local departures from SST-predicted PW can be used as tracers of large scale circulation.

Research has also concentrated on validating the use of PW data in field programs. Lin and Mock (1986) concluded that synoptic scale events away from the equator correlate well with the PW field, especially upper-level phenomena. However, they found that correlation with synoptic scale analyses within about 10° of the equator is deficient. Nevertheless, McGuirk et al. (1989) found that satellite moisture channel data can be used to study synoptic scale features. Such a conclusion has prompted research into improving algorithms to calculate PW using satellite brightness temperature channels (Chung, 1993; Yin, 1994). Yin explained that models which use TOVS brightness temperatures (BT) to estimate PW explain about 75% of the variance of PW values observed from raobs. In agreement with Wittmeyer and Vonder Haar (1994), she determined that such models tend to overestimate PW in subtropical dry zones and underestimate PW in convergence zones. Notwithstanding, TOVS-generated PW data have proven useful for identifying tropical synoptic scale behavior. Using such a dataset, Hatfield (1994) compared PW patterns with those obtained from SSM/I and found a greater

than 90% agreement on major synoptic scale features identifiable on daily PW maps between 80E and 80W from 30S to 30N (considered to be the standard over oceans). He concluded that this dataset is sufficiently accurate to study synoptic and larger scale events.

Previous research of tropical synoptic scale behavior has been either regionally or behaviorally limited in its scope. Such studies have identified specific phenomena or events, or have been limited to a small part of the tropics, but none have attempted to document specific regional differences in synoptic behavior. A globally coherent signal in time and space is needed to complete this task. This research accomplishes this using PW data, which demonstrates both spatially and temporally coherent synoptic scale behavior throughout all regions in the world. The PW dataset is not limited to just ocean regions or convectively active behavior, but instead identifies a coherent signal of synoptic scale activity across all tropical meridians. Such a characteristic of these data allows for the identification of regionally varying synoptic scale tropical behavior over all regions of the tropics. In addition, the PW dataset contains information from other time scales, which is used in this research to identify interactions between synoptic and longer time scales within different tropical regions. Instead of supplying details limited to a specific phenomenon or region, the results provide information about specific regional differences in synoptic scale behavior as well as the interaction between synoptic and longer time scale features throughout the global tropics.

CHAPTER III

APPROACH

A. OBJECTIVES

Previous work has concluded that TOVS-generated PW data can identify tropical synoptic scale behavior. The first objective of this study is to document and discuss regionally contrasting tropical synoptic scale structure and variation through time and space. This involves identifying the regions for study, defining time periods, and employing data to reveal climatological patterns of synoptic scale behavior. Regional and temporal behavioral differences are described and placed in context with other research results. Second, the study explores relationships between synoptic and larger scale events (intraseasonal, annual, and interannual). It documents interaction between the synoptic scale and other longer time scale features and describes how this interaction varies throughout the tropics. Annual variations in synoptic scale activity are discussed throughout the body of chapters IV and V by documenting the seasonal differences in behavior for each of the study regions. Interactions between the synoptic and the intraseasonal and interannual time scales are discussed in chapter VI. A brief third objective is to compare results obtained from the PW dataset and those from OLR data to note similarities and differences (Chapter VII).

B. DATA

PW data for this study were produced using a combination of TOVS brightness temperature channels and regression established by Yin (1994). Although these channels are temperature dependent, the algorithm was established and verified against collocated raobs during 1982-84 and 1987-90, primarily over the tropical and subtropical Pacific Ocean. From this algorithm, Schroeder and McGuirk (1996) produced a 2.5° by 2.5° gridded PW dataset around the world between 30°N and 30°S from TOVS for the period from 1979-1992. Problems with daily analyses occur in cloud covered areas and regions with missing observations. Within 800 km of a grid point, observations were spatially weighted to calculate a value for the grid point. Grid points located more than 800 km from the nearest observations received interpolated values using weighted values from neighboring grid points and from grid point observations the day before and after if available. Of the 4,749 days included in the data period, fewer than 6% (263 days) required interpolation for 100 or more grid points, while only 2% (106 days) needed this procedure for 500 or more of the total 3600 grid points. 549 days (11.6%) in the data period are completely missing. Most of these data voids consist of gaps of one week or less. However, gaps of 112 and 47 days exist (Julian days 188-299 in 1980; 103-149 in 1986), as well as several ten-day to four-week gaps (Julian days 281-310 in 1984; 37-55 in 1985; 153-162, 178-187, and 237-246 in 1986; 235-250 in 1987; 8-17 in 1989; 106-125 in 1990; 63-76 in 1991). For these data gaps, the missing PW values were linearly interpolated through time to perform the temporal filtering; however, interpretations of data within these gaps will not yield useful information. Overall, more than 80% of the dataset days contain usable PW data.

Another difficulty exists with daily discontinuities in the time series of domain averaged PW, which is an index of overall data quality. Although small day-to-day changes are expected to exist, several large jumps result from instrumental changes with new satellites or with missing data. Although instruments are designed to be identical for each NOAA satellite, small variations in individual channels and different satellite orbits are apparent in the dataset. Sudden large jumps from one plateau to another occur in the middle of 1984, at the beginning of 1985 and 1987, and during the middle of 1990. In addition, several sudden daily jumps in PW average are found during 1992. They can be removed with recalibration of the PW retrieval algorithm to account for satellite platform; however, this research limits periods of study to time segments that are relatively free of such discontinuities. The three time periods that are used in this research are the longest periods free of discontinuities; namely, from late 1980 to mid 1984, between early 1985 and late 1986, and from early 1987 through late 1990.

The three time periods are divided into subsets of three-month time intervals representing seasons (SON, DJF, MAM, JJA). Any individual season missing more than nine days is excluded from this study. A total of five SON, seven DJF,. and six MAM and JJA seasons of valid data exist in the research dataset; all other periods are not analyzed. Notwithstanding all aforementioned dataset difficulties, enough information exists to constitute a robust research dataset -- effectively 6 years or 24 total seasons.

Figure 1 summarizes the aspects of the overall 12 year PW dataset used in this research using four unique time lines. Each subfigure can be followed in successive order to understand the process by which the climatology database is produced. Figure 1a is a time series plot of the grid average PW in mm between 30°N and 30°S from 1980 through 1992. Clear temporal

Time Series for Grid Average PW, Filter Periods, PW Dataset, and Final Research Dataset
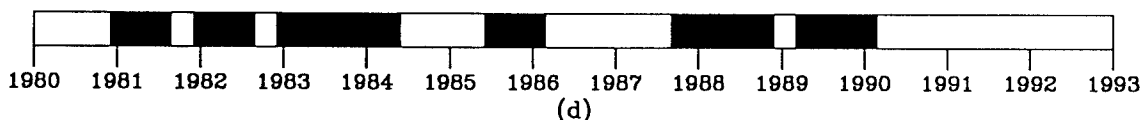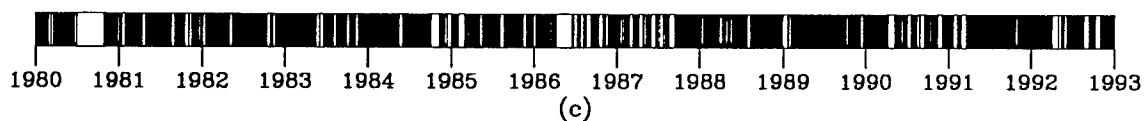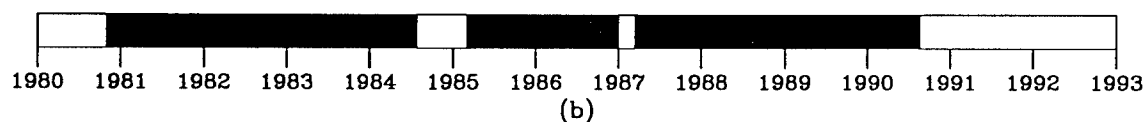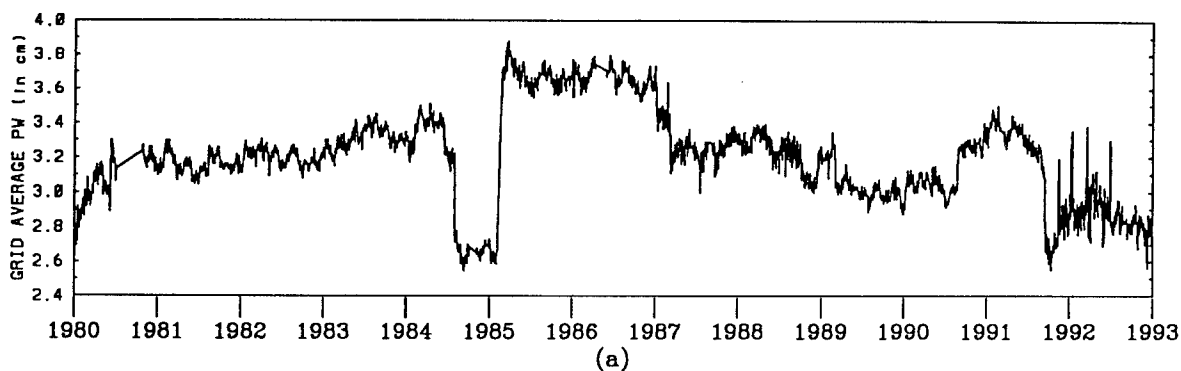

FIG. 1. (a) Time series of daily domain averaged PW between 30°N and 30°S for 1980-92 (in mm), (b) periods of continuous data without secular behavior designated for synoptic scale time filter (shaded), (c) days with sufficient data to generate a global tropical analysis (shaded), and (d) time periods used in this research (shaded).

discontinuities are visible throughout the 13-year period. Figure 1b identifies three time periods relatively absent from large temporal grid-average PW discontinuities with shading. Next, Fig. 1c identifies the data days present and missing from 1980 through 1992. It is useful to visualize the amount of data missing from the original dataset as well as the length of the data gaps. Shaded regions indicate useful analyses available in the dataset, while white regions indicate temporal gaps in the data time line. Figure 1d presents the final dataset in a timeline form from 1980 through 1992, with shaded regions representing the climatological database used in the research.

Two important facts must be remembered when interpreting this dataset. First, moisture is logarithmically distributed in the vertical through the troposphere, with the majority remaining in the bottom half (nearest the surface). Thus, the signals detected will normally correlate best with features in the lower half of the atmosphere. Second, since no information about the vertical structure of PW distribution is available from these data, it is not possible to determine precisely the depth of the features identified using this dataset. These two factors restrict interpretations of results and emphasize a barotropic view of the lower troposphere.

Although IR sources have trouble distinguishing between surface and boundary layer emission, Yin (1994) has shown that TOVS can identify significant PW variations. The analysis procedure used by this research uses spatial coherence to maximize this signal.

C. ANALYSIS STRATEGY

The first step is to identify and define regions of enhanced synoptic scale activity; namely, the normal tropical convergence zones. Since midlatitude

behavior is not the focus of the regional study, analysis of regional behavior is restricted to between 20°N and 20°S. The key indicator used for identifying the regions of study is the frequency of location of PW relative maxima. Particularly strong signals in this annual average plot determine longitudes of possible further investigation. To reduce repetition of results, each regional center is at least 5,000 km from any other, unless the two regions are over different surface types (land versus ocean) or in different hemispheres. Furthermore, the seasonal location of each regional center is assumed to vary only latitudinally: a specific longitude is assigned to each of the study regions. On the basis of these criteria, focal study points include the North Pacific ITCZ (ITCZ) at 145°W, the SPCZ at 170°W, the North Atlantic Convergence Zone (NACZ) at 30°W, the Sahel region of Africa at 5°E, the west Pacific warm pool (WPWP) at 145°E, the South Indian Ocean Convergence Zone (SICZ) at 65°E, and the Amazon Basin region at 60°W.

To determine the method for studying the selected regions, four factors are considered: migration of convergence zones, location of maximum anomalous activity, size of the regional domains, and prior knowledge of regional characteristics. Each region is centered upon a "focal point," or center point of analysis for regional behavior. Latitudes for each regional focal point are determined seasonally using the plots of preferred location of PW relative maxima for each season. Because the axis of maximum variability is shown in this study to exist on the poleward side of the frequency maximum axis, seasonal central latitudes for each region are located 5° degrees poleward of the frequency maximum at the respective longitude over oceans and 10° over land. Table 1 identifies the seven regions selected for detailed study and comparison for all seasons.

TABLE 1. Latitudinal position of focal point by region (longitude) and season.

Region	(Long.)	SON	DJF	MAM	JJA
Pacific ITCZ	(145°W)	15.0°N	10.0°N	10.0°N	12.5°N
SPCZ	(170°W)	15.0°S	17.5°S	12.5°S	15.0°S
North Atlantic ITCZ	(30°W)	12.5°N	7.5°N	7.5°N	12.5°N
Sahel Region	(5°E)	12.5°N	7.5°N	12.5°N	15.0°N
Pacific warm pool	(145°E)	2.5°N	2.5°S	2.5°S	2.5°N
South Indian ITCZ	(65°E)	7.5°S	12.5°S	10.0°S	7.5°S
Amazon Region	(60°W)	12.5°S	10.0°S	12.5°S	12.5°S

A clear signal of these convergence zones and other convectively active regions emerges from a plot of the frequency of occurrence of PW relative maxima along meridians. However, to study synoptic behavior within PW, it is necessary to find other methods of extracting the synoptic scale signals. Individual PW estimates capture only about 40% of the synoptic variance with respect to collocated raobs. Taking advantage of TOVS temporal and spatial coherence yields a more robust and meaningful signal. Time filtering and spatial compositing prove useful for isolating synoptic scale activity. Murakami (1980), Strager (1989), and Winton (1991) all applied time filtering to OLR data to extract information about the synoptic scale. A filter relates behavior of one day with that occurring both before and afterward.

The time filter used in this research, which is described in Murakami (1980), is non-linear and operates on the time series of PW at each grid point separately. It passes twice through the dataset -- once forward, and once backward -- computing a moving running mean. For this filter to function, no temporal gaps in the dataset may be present. Therefore, all temporal gaps in

the TOVS-generated PW dataset were linearly interpolated through time for all missing data.

The filter enhances the signal of behavior occurring on time scales within the predefined bandpass frequencies and diminishes the signal on time scales outside of the bandpass frequencies. Since this study focuses on synoptic scale events, the first filtering performed by this mechanism uses half-power frequencies of three and eight days, extracting the greatest signal of behavior occurring near 4.9 day periodicity. These predefined frequencies are consistent with time scales of dominant spectral peaks in several tropical sectors as noted by Lau and Lau (1990). Although some signal of behavior from shorter and longer frequencies "leaks" into the filtered data, the spectrum between three and eight days is nearly isolated.

Another important capability of the filter is that it does not introduce anomalous peaks or phase shifts into the filtered data. Although it fails to capture completely all power within the 3 to 8 day range, it does not introduce significant signals from shorter or longer frequencies. Thus, the signal produced from these filtered data is real.

The biggest disadvantage with the filtering method is that studies are bound to scales defined in the filtering process. The "synoptic scale" in this research is bounded by 3 and 8 day period PW anomalies. Likewise, the "intraseasonal scale" is bounded by the 30 and 60 day periodicity of PW anomalies. Although these bounds correspond to documented peaks in the time power spectrum, concrete definitions of synoptic and intraseasonal scales allow for the identification of scale interactions only within these narrow period ranges. Schroeder and McGuirk (1996) show that such scale interactions are not fixed at these defined time scale intervals. However, for this research, scale interaction outside the defined time scales cannot be determined.

Another disadvantage of the filter method is the temporal loss of data. A few days of data observations on each end of a time series are lost through the filtering process. Four days of data are lost to calculate the filtered values: the first two dataset days in the forward pass and the last two dataset days in the backward pass. Additionally, a few days at the beginning and end of the filtered dataset have anomalous values due to the non-linear nature of this filter. The period of time in which the filtered dataset values fail to represent the actual dataset generally corresponds to about the period of the central peak of the filter, or in the synoptically filtered dataset, approximately five days. The combination of these data days lost and misrepresented include a total of 14 dataset days that are lost during the synoptic scale filtering process, or about 2% of the data used in this research. Such a small loss is more than made up by the information gained from interpreting the filtered dataset.

Using the time-filtered data, several indicators of synoptic behavior can be identified and studied. Regions of high variance of the filtered data identify locations of enhanced synoptic activity. These regions are typically associated with either large scale rising motion or convection. Time-longitude plots of the filtered data (Hovmöller diagrams) offer a view of the temporal and spatial coherence, zonal propagation direction and speed, and preferred regions of origin and dissipation of synoptic systems during different seasons. Seasonal Hovmöller composites of anomaly patterns provide information of regional differences in synoptic scale behavior. Lag correlation plots of the filtered data offer a view of the spatial evolution of these synoptic anomalies as well as their relationship with other features in the environment.

Additional study includes scale interaction between synoptic scale and larger scale processes, such as the intraseasonal, annual, and interannual variations. To compare synoptic activity with the ISO, the time-filter is again

used with half-power frequencies of 30 and 60 days (peak power about 42 days). The filtering process using these frequency constraints costs about 90 days from each of the three original dataset periods. Still, enough intraseasonally filtered data exist to perform an objective study between this and the synoptic time scales. Time-longitude plots of the intraseasonally filtered dataset identify anomalous wet and dry variations at this time scale.

The proposed procedure to study a relationship on the interannual time scale is to composite years of ENSO warm and cold phases to identify differences in synoptic activity during opposite phases of interannual variation. The stratification by seasons emphasizes annual cycle components.

Finally, a brief comparison of the results gained from this study with those found using OLR data in previous work is performed, and similarities and differences in results are discussed. This comparison is performed for two reasons. First, a wealth of previous OLR studies has documented tropical synoptic scale behavior. It is easy to compare the results obtained from this research with previous studies using OLR data to find consistencies and any noticeable differences in behavior. Second, OLR tends to extract information about features associated with convective activity, while PW focuses on anomalies whether or not associated with convection. A comparison between these two dataset results will indicate how well PW anomalies associate with convective activity.

CHAPTER IV

GLOBAL VARIATIONS OF TROPICAL SYNOPTIC SCALE BEHAVIOR

The gradient of mean PW is greatest in the meridional direction, with the highest values near the equator on an annual average. Figure 2 displays the spatial distribution of PW for all meridians between 30°N and 30°S as averaged over the 24 season climatology. The figure (and many subsequent figures) is divided into two plots: The top extends from 110°E eastward to 70°W and the bottom covers the other half of the tropics. Most obvious from this figure is the zonally oriented maximum over the oceans along and near the equator. A hint of the locations of the convergence zones appears in the west Pacific, where maximum axes exist in both hemispheres. However, the spatial plot of PW does little to identify the convergence zones and correlates poorly with areas of enhanced synoptic activity over many parts of the tropics (especially over land).

To identify regions of enhanced synoptic scale behavior, it is necessary to define signals indicating such behavior. Two products generated for this purpose include mean maps of frequency of occurrence of local PW relative maxima and synoptic scale standard deviation of PW. The frequency of occurrence of PW relative maxima correlates well with the expected position of regional convergence zones, while the synoptic scale standard deviation of PW provides information about the strength of the synoptic signal of the PW dataset and the geographical location of the strongest synoptic scale anomalies. A comparison between these two forms of data shows that they are not spatially collocated; they do, however, appear somewhat associated with each other.

Distribution of Precipitable Water (cm)
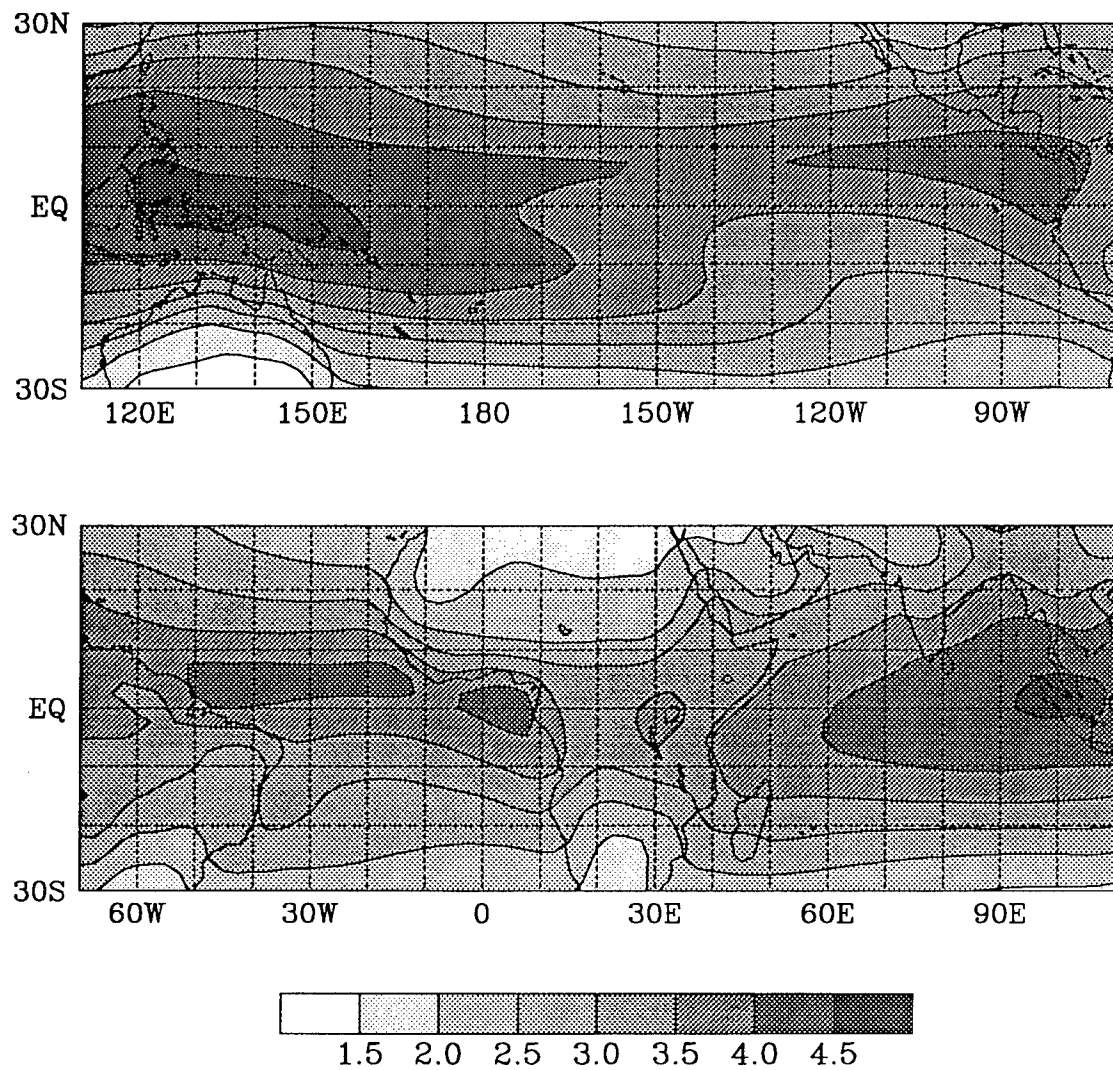## Average for 24 Seasonal Periods

FIG. 2. Average distribution of PW (in cm) for the global tropics from 30°N to 30°S for the 24 season climatology. Contour interval is 0.5 cm.

A. DISTRIBUTION OF PRECIPITABLE WATER RELATIVE MAXIMA

The distribution of average latitudinal frequency of occurrence of relative maxima indicates the existence of several large-scale features, such as convergence zones and regions of subsidence. Figure 3 displays the frequency of occurrence of PW relative maxima along meridians, where a maximum is defined locally such that, on a given day, grid points north and south have lower values than the identified local maximum. Note that, at each longitude, several maxima can exist on a given day. The values represent the percentage of time over the 24 identified seasons in which a daily local maximum occurs at a given grid point from 27.5°N to 27.5°S. In Fig. 3 the tropical band is split in half with the upper panel displaying the Pacific sector from 110°E through 70°W and the lower panel centered on the Atlantic and Indian Oceans and Africa. Zonally elongated axes of heavy shading indicate axes of high frequency of local daily maxima. These axes are clear indicators of the associated convergence zones, which follow the ITCZ and SPCZ in the upper panel and the Atlantic and Indian Ocean convergence zones in the lower panel. The most prominent of these convergence zones is the ITCZ, extending from near the dateline eastward to 120°W and continuing across the equatorial North Atlantic to the west coast of central Africa. A second prominent axis (associated with the SPCZ) extends from the east of New Guinea east-southeastward into the south central Pacific. Other regions of preferred PW relative maxima exist in the South Atlantic Convergence Zone (SACZ) east of the South American coast, from the east coast of central Africa eastward into the central Indian Ocean, and in the North Pacific near 22.5°N between 140°E and the dateline. Over land, regions with substantially elevated frequencies of PW relative maxima are found over South America and Africa. Regions of

Percent Occurrence of PW Relative Maxima
Each 2.5 degree Longitude, 27.5N to 27.5S
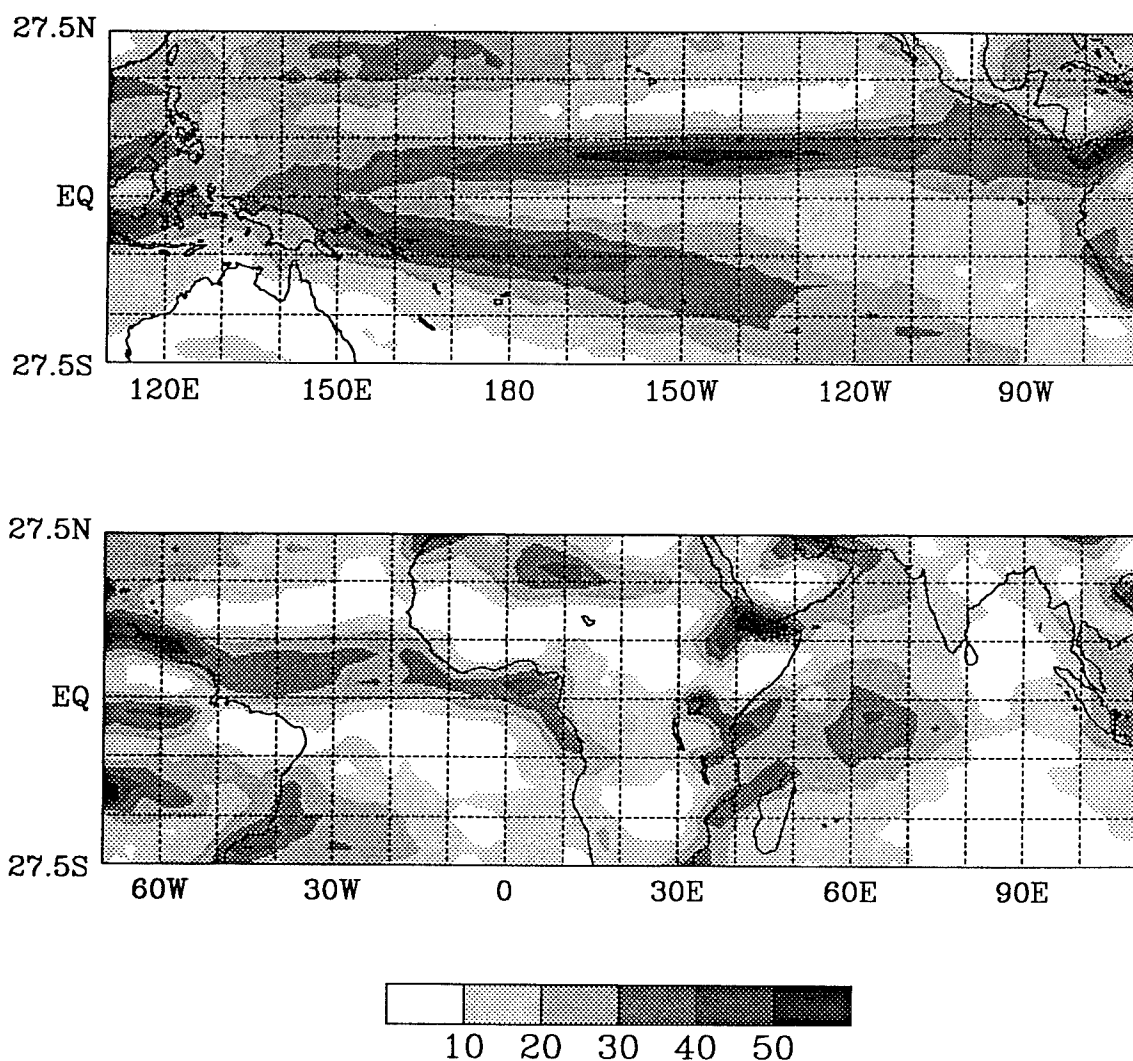## Average for 24 Seasonal Periods

FIG. 3. Percentage occurrence relative PW daily maxima along meridians to nearest 2.5° latitude from 27.5°N to 27.5°S. Average is for 24 seasonal periods (including SON 1983, 1985, 1987, 1988, 1989, DJF 1980/1981, 1981/1982, 1982/1983, 1983/1984, 1985/1986, 1987/1988, 1989/1990, MAM 1981, 1982, 1983, 1984, 1988, 1989, JJA 1981, 1982, 1983, 1985, 1988, and 1989).

subsidence appear to be associated with areas having the fewest occurrences of PW relative maxima. The largest of these regions flank the ITCZ in the Pacific along the equator from the dateline eastward into the southeast Pacific on the south, and from 150°E eastward to west of the southern tip of Baja California on the north. In the Southern Hemisphere, lowest frequencies occur across the South Atlantic from just south of the equator to near 20°S, over the Indian Ocean from the Bay of Bengal southward for over 5000 km, across Australia and south of the SPCZ, and from the central North Atlantic near 15°N through Sahel Africa. Interestingly, daily relative maxima are frequent at all latitudes throughout the Indian Ocean/Bay of Bengal region (70°E to 105°E).

These moister and drier features, which fluctuate in location and frequency of occurrence seasonally, remain coherent in some regions throughout the year. Figures 4 through 7 are similar to Fig. 3, except they plot the mean seasonal values for SON, DJF, MAM, and JJA, respectively. A comparison between these seasonal plots offers a view of seasonal differences in the position and intensity of the convergence zones. The axis of higher frequency associated with the ITCZ in the Pacific shifts northward from spring to fall, reaching its northernmost position near 10°N during SON from its southernmost position near 5°N during DJF and MAM. Occurrence of PW relative maxima exceeds 60% along the axis in the central Pacific during all seasons (greatest during DJF) except during MAM, when maximum values remain close to 50%.

The axis associated with the SPCZ attains its highest values during DJF, where frequency of occurrence exceeds 60% at 12.5°S, 160°W. In boreal spring, this axis shifts northward and splits into a configuration of two axes from 160°W to 130°W over the South Pacific, one near 5°S and the other near 15°S. Frequency is less than 40% for most of this axis during JJA, and the double

Percent Occurrence of PW Relative Maxima
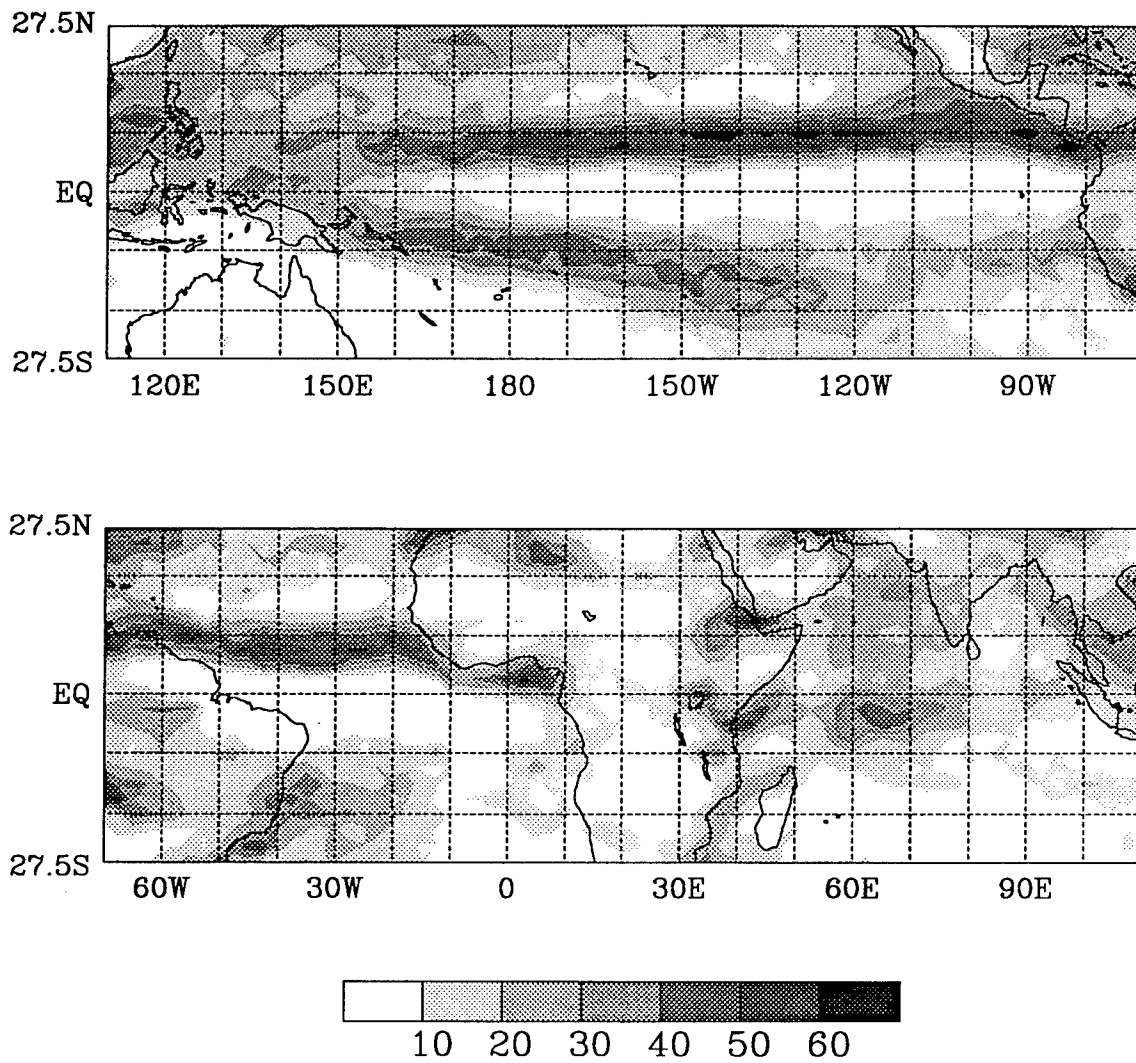## Each 2.5 degree Longitude, 27.5N to 27.5S
Average SON

FIG. 4. As in Fig. 3, except average for 5 SON seasons. Contour shading has been adjusted.

Percent Occurrence of PW Relative Maxima
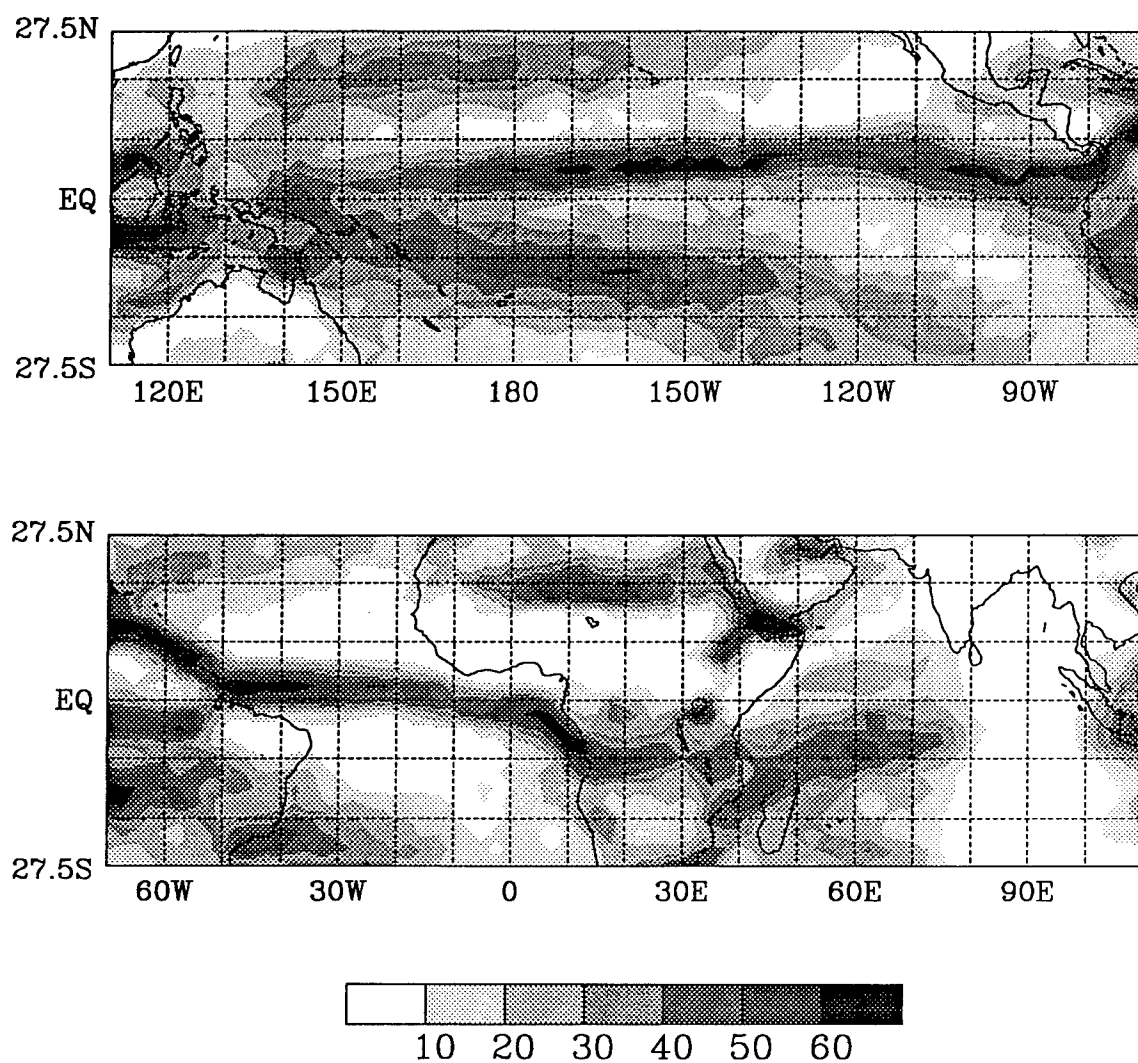## Each 2.5 degree Longitude, 27.5N to 27.5S
Average DJF

FIG. 5. As in Fig. 4, except average for 7 DJF seasons.

Percent Occurrence of PW Relative Maxima
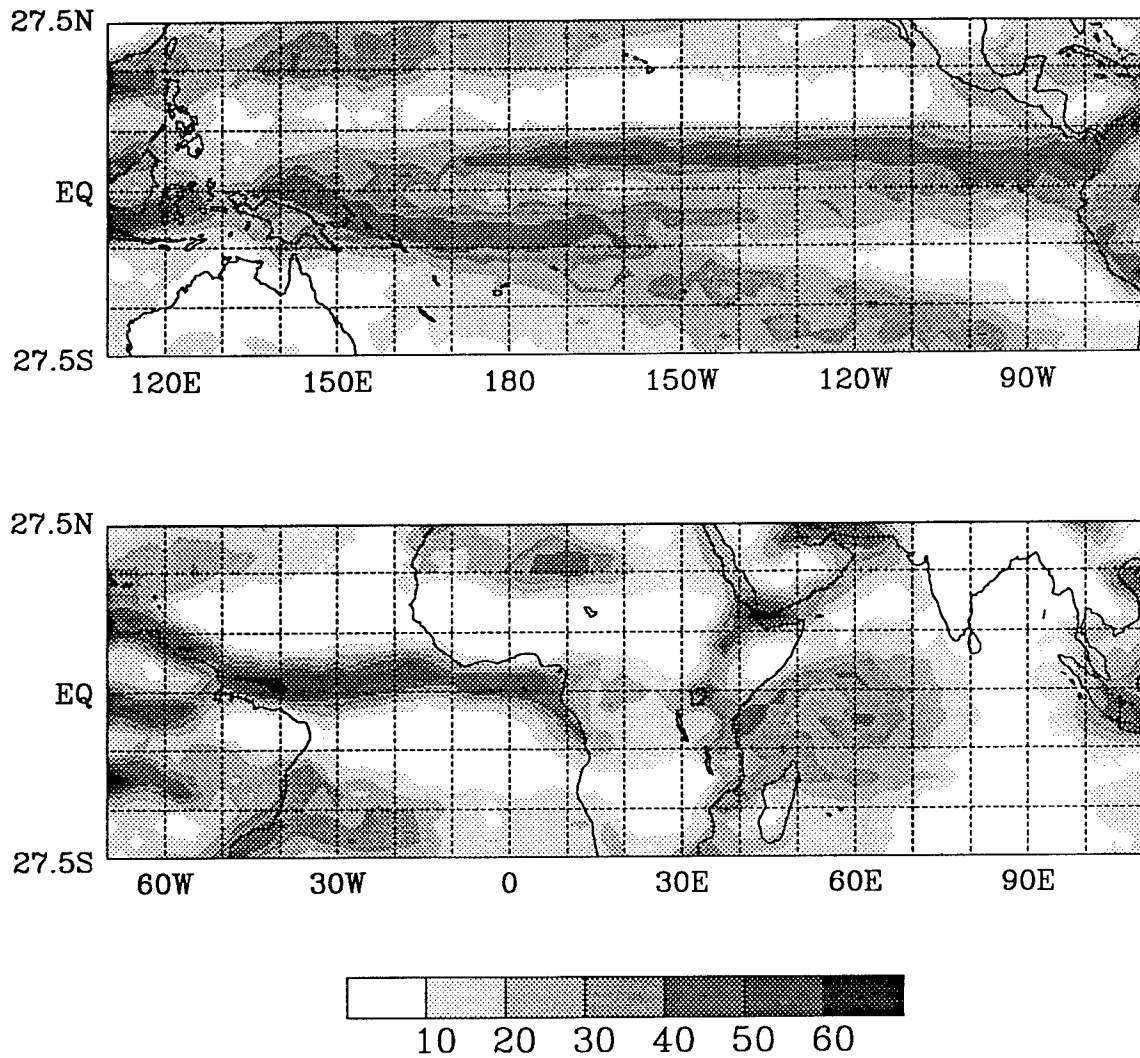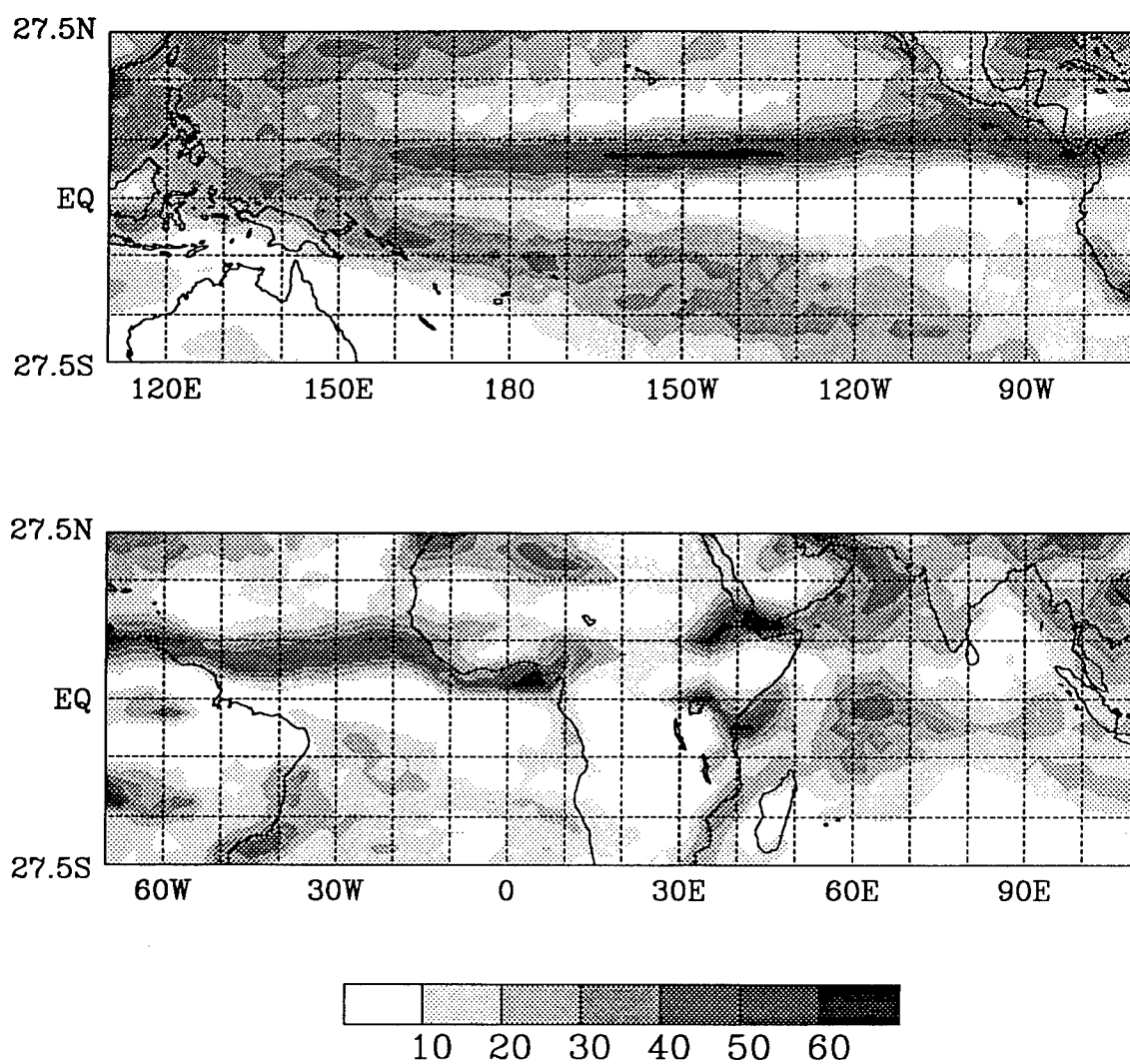## Each 2.5 degree Longitude, 27.5N to 27.5S
Average MAM

FIG. 6. As in Fig. 4, except average for 6 MAM seasons.

Percent Occurrence of PW Relative Maxima
Each 2.5 degree Longitude, 27.5N to 27.5S
Average JJA

FIG. 7. As in Fig. 4, except average for 6 JJA seasons.

convergence zone about the equator disappears. Also, axis location retreats poleward west of the dateline to near 10°S during this season. In SON, values along the SPCZ axis increase to 40-50% as it advances equatorward to near 7.5°S.

Over the Atlantic Ocean, the axis of high frequency has two preferred locations that follow an annual cycle: the northern South American/central African coastal mode, and the Atlantic/Gulf of Guinea mode. The first mode occurs during DJF/MAM, when the axis remains just north of the equator from 10°W westward to the northern coast of South America, where it stays on the ocean side of the coastline. East of 10°W, this feature crosses the equator and is displaced 7°S of the west coast of central Africa, until it crosses over land near 10°S. Occurrence of maxima exceed 60% off the coastlines of both Africa and South America along this axis during DJF. In MAM, the axis east of 10°W shifts to the northern side of the equator, except along the immediate central African coastline. Otherwise, it remains fairly consistent with the axis location of DJF with slightly lower percentages, except for a northward-bowing section near 15°W. During JJA, the major northward shift occurs to its position in the second mode, with the axis moving away from the northern coast of South America and the western coast of central Africa. Over the eastern Atlantic, it now favors the ocean side of the southern coast of west Africa in the Gulf of Guinea. The axis attains its northernmost position during this season, reaching almost to 10°N at 20°W. Although a slight equatorward shift occurs in SON, the axis remains coincident to the southern coast of west Africa on the eastern half and away from the South American coast on the west.

More diffuse features exist over the East Africa/Indian Ocean region. Frequency of PW maxima remains higher here than in surrounding areas, with values exceeding 40% at some place during every season. The most

organized structure occurs during DJF, when a continuous band extends from the Mozambique Channel east of the southern African coast east-northeastward into the central Indian Ocean. This feature is also furthest poleward during DJF, with its eastern edge located near 7.5°S and the western tail crossing 20°S. During MAM, frequency maxima occur on both sides of the equator in a disorganized fashion, with the strongest signal on the east coast of central Africa near 5°S. This feature appears to split during JJA and SON, with the eastern maxima located near 2.5°S over the central Indian Ocean, and the western maxima still positioned near 5°S on the east coast of Africa.

Locations of elevated percentages of PW relative maxima over land are found over northern Africa, between the Southern Arabian Peninsula/Horn of Africa region, and over South America (near 5°S and 15°S). A final noteworthy area of elevated percentages straddles the equator around the island of Borneo in Indonesia. This region of higher frequency is seasonal in nature, peaking during DJF and continuing into MAM; during JJA and SON, it is virtually nonexistent. One interesting region relating depressed percentages of PW relative maxima exists over the Bay of Bengal/Indian Ocean. This region lacks any occurrence of PW relative maxima except for near 5°S during JJA, where percentages exceed 20%, and during SON at 2.5°S, where percentages fail to reach 20%.

All of these plots show it is possible to locate climatological convergence zones and regions of subsidence spatially using the frequency of occurrence of PW relative maximum along meridians. Higher frequencies correspond well with the locations of the ITCZ and SPCZ and well-documented regions of subsidence are clearly identifiable by areas of lower frequencies. This manner of presenting the PW data is useful to identify regions worthy of further investigation in this research.

Two observations are particularly salient. First, for almost every regional feature or behavior, its delineation is quite sharp in seasonal mean frequency, whereas the feature is often blurred in the climate mean because of movement associated with the annual cycle. Second, almost every feature appears at a single fixed latitude for zonal swathes of many thousands of kilometers.

On the basis of the general description and upon these two geometric generalizations, seven regions are selected for further investigation. These regions are selected for their coherent frequency structure displayed in Figs. 2-6, and because they seem to span the range of large-scale convective organization throughout the global tropics. The study regions include (with central longitude and approximate latitude in parentheses): 1) the eastern Pacific ITCZ (12.5°N, 145.0°W), 2) the South Pacific Convergence Zone (15.0°S, 170.0°W), 3) the North Atlantic Convergence Zone over the ocean (10.0°N, 30.0°W), 4) the North Atlantic Convergence Zone near the African Coast (12.5°N, 5.0°E), 5) the west Pacific warm pool (0.0°, 145.0°E), 6) the South Indian Ocean (10.0°S, 65.0°E), and 7) the Amazon region (12.5°S, 60.0°W). Each of these regions become focal points for further investigation concerning synoptic scale behavior and scale interaction on a seasonal basis.

B. SYNOPTIC SCALE STANDARD DEVIATION OF PW

Spatial variation of synoptic scale standard deviation is not large; however, regions of enhanced and diminished variability become evident from spatial plots of this variable. Although these regions are shown to be only weakly collocated with the higher frequency regions of the PW maxima, an overall pattern emerges that is consistent with that of the seasonal global circulation, as with the frequency plots of PW relative maxima. Figure 8 shows

synoptic scale standard deviation of PW (associated with the variance in the 3 to 8 day bandwidth) for each grid point within the 30°N to 30°S domain for the twenty-four identified seasons. Heavy shading indicates regions of enhanced synoptic scale variability. Areas of diminished standard deviation appear to be associated with regions of broad-scale high sea level pressure and subsidence, while areas of enhanced variability seem associated with regions of surface convergence and convection. Enhanced variability is typically associated with standard deviations in the range of 1.5 - 2.2 mm (to be compared with a time and spatial mean of about 1.4 mm).

Over ocean regions, a weak axis of higher synoptic scale variability associated with the ITCZ persists north of the equator from the western Pacific near 7.5°N to the eastern Pacific around 12.5°N, somewhat farther north than where the ITCZ is normally assumed to be and where the frequency maximum of high PW is found (Fig. 3). Another weak maximum extends west-southwestward over the Atlantic Ocean from the west coast of north Africa (20°N) toward the north coast of South America (10°N). A third region of increased variability exists in the Indian Ocean around 15°S, 90°E, with a hint of an axis extending westward to 60°E. Regions with standard deviations less than 0.1 cm cover broad areas in the southeastern Pacific and the South Atlantic Oceans, associated with the subtropical highs of the southern ocean. A near-equatorial relative minimum in variation exists at almost all longitudes. Toward the poleward edges of the study domain, variability increases markedly, in association with midlatitude disturbances.

Variability is higher over land than over ocean. The Sahel region of Africa demonstrates this characteristic, with standard deviations exceeding 0.2 cm between 15°W and 30°E; however, this is not a region of common PW maxima (Fig. 3). Areas of relatively higher variations extend from the southern

Synoptic Scale Standard Deviation
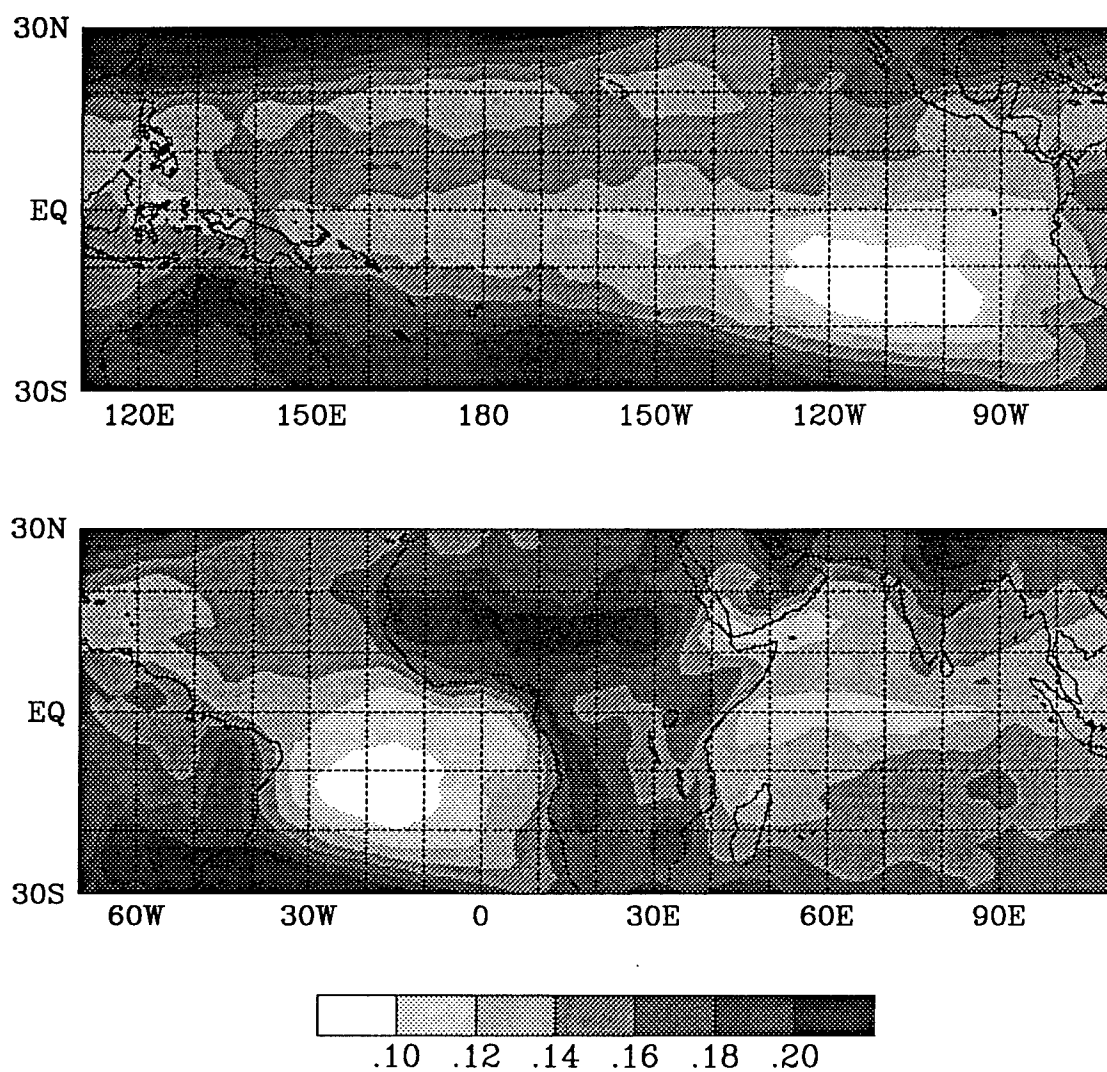## of Precipitable Water (cm)
Average for 24 Seasonal Periods

FIG. 8. Synoptic scale standard deviation of PW (within the 3 to 8 day spectral band) over 3-month seasons (in cm). Standard deviations computed for each sample season are averaged over 24 seasons.

edge of this region along the west coast of central and southern Africa, over northern India, the Persian Gulf, the northern and eastern coastline regions of Australia, along the Gulf Coast region of the United States, and over southern Brazil in South America.

Some variability features persist through the entire year, while others exist only on a seasonal basis (Figs. 9 through 12). The variance axis associated with the ITCZ is evident throughout the annual cycle, attaining its northernmost location during SON, when it reaches 12.5°N across the entire Pacific Ocean. The weakest signal of this feature occurs during MAM, when standard deviation fails to exceed 0.16 cm except in the far western Pacific. The JJA signal is relatively weaker than the SON and DJF signals, and it appears to have a double axis in the central Pacific (2.5°N and 10°N). The SON and DJF have broad regions exceeding 0.16 cm standard deviation. On the poleward edges of the study domain, the regions of persistently high variability (exceeding 0.2 cm standard deviation) increase in magnitude and advance equatorward during each hemisphere's respective winter season, probably in association with midlatitude variations.

Three seasonal axes exist only during their respective preferred times of the year: one from the west coast of northern Africa westward to the central Atlantic Ocean, a second over the southern Indian Ocean at about 10°S and 10°N, and a third over the central and eastern Pacific just south of the equator. The Atlantic maximum axis almost disappears in DJF, with only a hint of it present near 10°N. The eastern edge of the MAM axis begins to develop at 20°N near the west coast of north Africa. In JJA, a clear variability maximum axis exists and attains its most poleward position, extending from 22.5°N at the west coast of north Africa west-southwestward toward the northern coast of South America. The SON pattern remains coherent, but is shifted equatorward

Synoptic Scale Standard Deviation
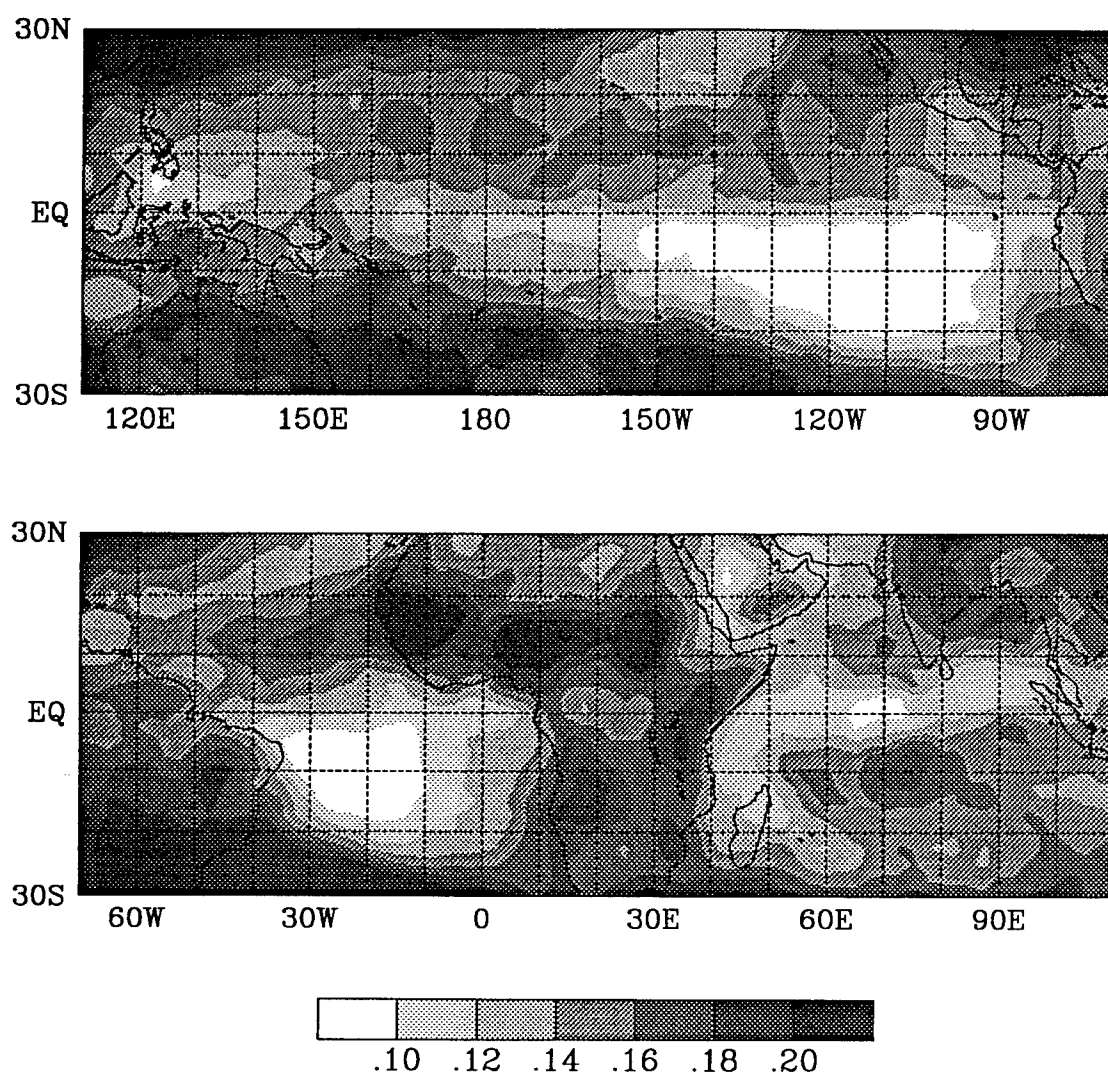of Precipitable Water (cm)
Average SON

FIG. 9. As in Fig. 8, except average for 5 SON seasons.

Synoptic Scale Standard Deviation
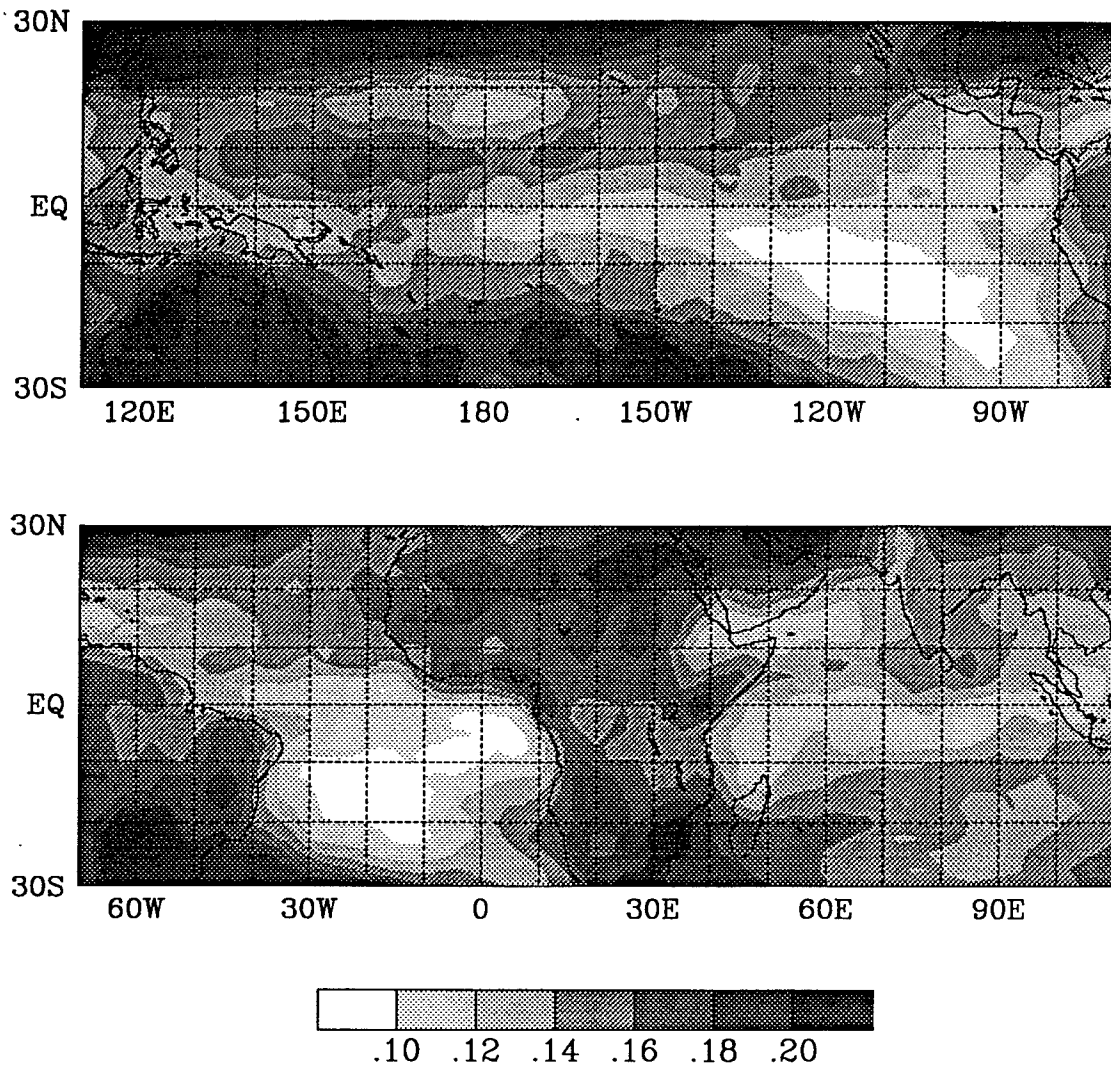## of Precipitable Water (cm)
Average DJF

FIG. 10. As in Fig. 8, except average for 7 DJF seasons.

Synoptic Scale Standard Deviation
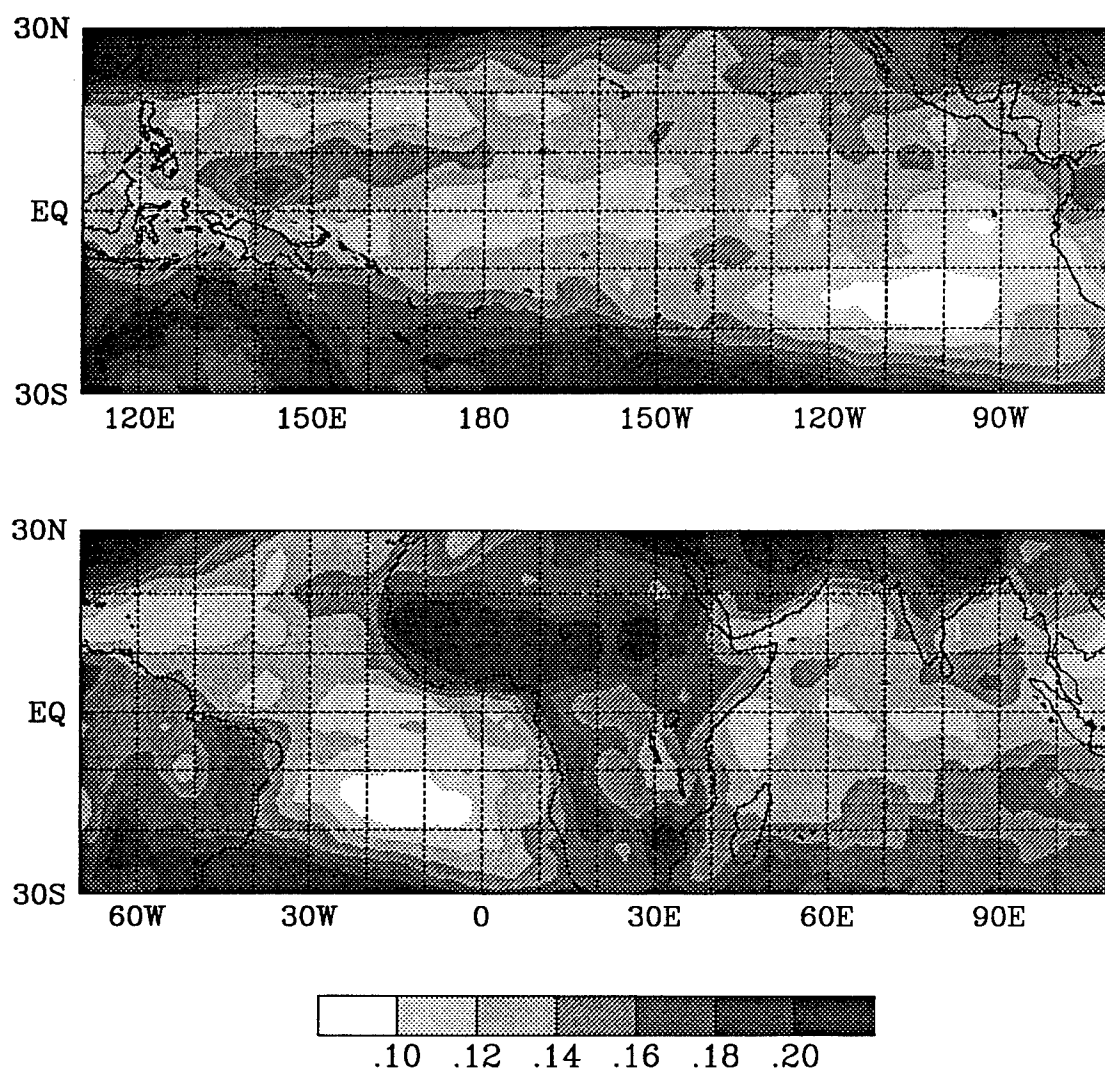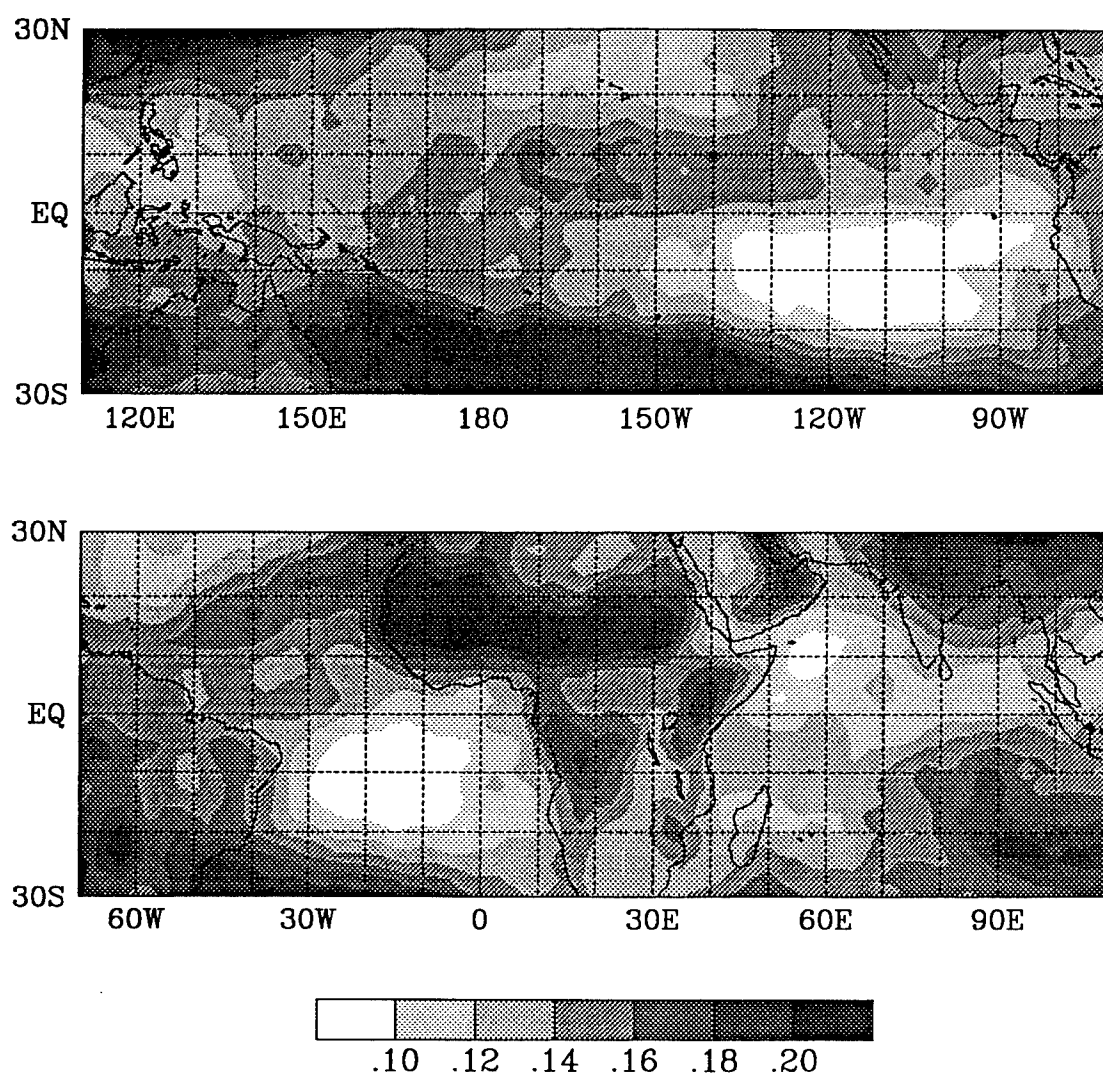of Precipitable Water (cm)
Average MAM

FIG. 11. As in Fig. 8, except average for 6 MAM seasons.

Synoptic Scale Standard Deviation
of Precipitable Water (cm)
Average JJA

FIG. 12. As in Fig. 8, except average for 6 JJA seasons.

from its summertime position by about 5°. Maximum standard deviation values exceed 0.18 cm during these two seasons.

The maximum axis over the southern Indian Ocean also follows a seasonal cycle, but different from the one in the Atlantic. This axis appears clearly in SON, extending from north of Madagascar eastward into the southern central Indian ocean. Maximum standard deviation values with this axis approach 0.2 cm during this season. The signal persists through DJF, but farther poleward and with weaker magnitude (0.14 cm) than its springtime signal. The signal weakens and signs of this axis are not evident during MAM (Fig. 11). Close by, a wintertime axis begins to form further east of this region, from 15°S, 90°E to the west coast of Australia. This axis strengthens during JJA near 22.5°S with magnitudes exceeding 0.2 cm, probably in association with wintertime midlatitude activity.

The third seasonal feature mentioned occurs in the central and eastern Pacific only during springtime. The MAM plot shows an axis of higher variability near 7.5°S, in association with the seasonal development of a third convergence zone in this region during this season. Standard deviation values associated with this feature exceed 0.14 cm between 5°S and 10°S from 142.5°W to 135°W.

Away from the equator, variability over land decreases notably during the respective winter season. The variability maximum over the Sahel region (barely evident north of the Gulf of Guinea in DJF) advances poleward during MAM, reaching its greatest magnitude (exceeding 0.2 cm standard deviation in the whole region) and northernmost position in JJA (near 15°N). High variability across northern Africa in DJF appears unrelated to the Sahel variability maximum when average monthly standard deviation data are viewed through an annual cycle (not included). The seasonal summertime maximum

along the north and east coast of Australia follows a similar seasonal pattern and signal magnitude. Also noteworthy is a summertime maximum evident over northern India, which appears to be coherent poleward of the northern boundary of the plot through all seasons.

When comparing frequency of maximum PW occurrence with average standard deviation of PW, it becomes obvious that the maximum axes of the two signals do not coincide. In most cases, axes of maximum variability are located a few degrees poleward of the preferred locations of the PW maxima. Along the Pacific ITCZ, the largest synoptic scale variation occurs north of the preferred location of the PW maximum, except during JJA when regions of higher variability straddle the PW maximum. The variability maximum over the Sahel region of Africa appears to be associated with the preferred location of the eastern Atlantic PW maximum. In the southern hemisphere, the preferred PW maximum axis associated with the SPCZ appears to be related to the enhanced synoptic scale variability on its poleward side, such that the variability from this well-documented tropical feature is difficult to distinguish from mid-latitude synoptic variability. This region of enhanced variability also appears to follow a seasonal cycle, with greatest magnitudes occurring during JJA and smallest during DJF, antisymmetric to the seasonal cycle of the PW relative maximum occurrence signal. Another region of slightly enhanced variability appears on the poleward flank of the area of higher frequency of occurrence of PW maxima signal in the southern Indian Ocean.

It is difficult to determine from these plots alone if variation in PW is related to tropical or midlatitude processes, especially near the poleward edges of active regions. However, the axes of maximum synoptic scale variability near the equator clearly do not directly coincide with the highest frequency of occurrence of the PW relative maxima. Additionally, these data suggest that

maximum synoptic scale variability does not occur where the highest PW values are located; rather, maximum variability is found on the poleward edges of the axes of maximum PW. More difficult to determine is to what extent the elevated values of variability poleward of the SPCZ are due to SPCZ tropical events and which are caused by midlatitude processes further poleward.

To conduct a regional comparison of synoptic behavior, it is useful to evaluate places with regionally specific atmospheric qualities in terms of PW, frequency occurrence of PW, and variability. Each of the seven regions selected for study possess unique characteristics with respect these variables. The ITCZ region collocates zonally to the south of the maximum standard deviation axis and just north of the maximum frequency axis in the Pacific. The ITCZ region has the highest frequency values of any in the world. The SPCZ, which is evident in the frequency plots, lacks such a unique signal in the standard deviation plots. The North Atlantic region reveals a weak maximum in standard deviation, but low frequency values, even though PW is relatively high in the area. The Sahel is a region of low PW but high standard deviation north of the percentage occurrence of PW maximum, which has a strong annual cycle. In the Pacific warm pool, the highest PW values in the world are found, but the standard deviation is relatively low (especially during the convective season along the equator). This region, known for its convective activity, reveals a weak but complicated frequency structure. In the southern Indian Ocean, a relative minimum in standard deviation is found while a bullseye of a relative frequency maximum appears. The Amazon region, noted to be convectively active on an annual cycle, reveals a complex multiple-band pattern of maxima in the frequency maximum field accompanied by higher standard deviation values, especially toward the mid-latitudes.

C. SEASONALLY AVERAGED SYNOPTIC SCALE STANDARD DEVIATION

Although the percentage occurrence of relative PW maxima find tropical convergence zones, it fails to determine the location of maximum variation of synoptic scale activity. It is important to understand how these two variables relate with respect to each other to understand processes responsible for synoptic scale activity. It becomes necessary to identify regions of enhanced synoptic scale anomalous activity for specific latitudes and longitudes. A useful tool for this purpose is the seasonally averaged synoptic scale standard deviation plotted with respect to longitude for fixed latitudes. Other valuable behaviors can be obtained by viewing 3 to 8 day filtered data through both space and time. Using time-longitude plots, it is possible to identify preferred latitudes of origin as well as propagation direction of PW anomalies (eastward versus westward). Additionally, certain longitudes which experience unique or enhanced characteristics and patterns of motion during different seasons can be identified. This section describes such characteristic behavior and relative intensity of these systems during each of the four seasons (SON, DJF, MAM, JJA).

Figure 13 plots the standard deviation of the 3 to 8 day filtered PW data at each 10° increment of latitude from 30°N to 30°S. It consists of individual columns of seven plots each representing specific seasons: SON (a) and DJF (b), MAM (c) and JJA (d). The data contained in Fig. 13 is the same data plotted in Figs. 9-12, but it emphasizes the longitudinal variation in standard deviation values at fixed latitudes.

These figures reveal two types of signals that appear from peaks in the fields of seasonally averaged synoptic scale standard deviation plotted through all longitudes: one associated with regions of enhanced midlatitude synoptic
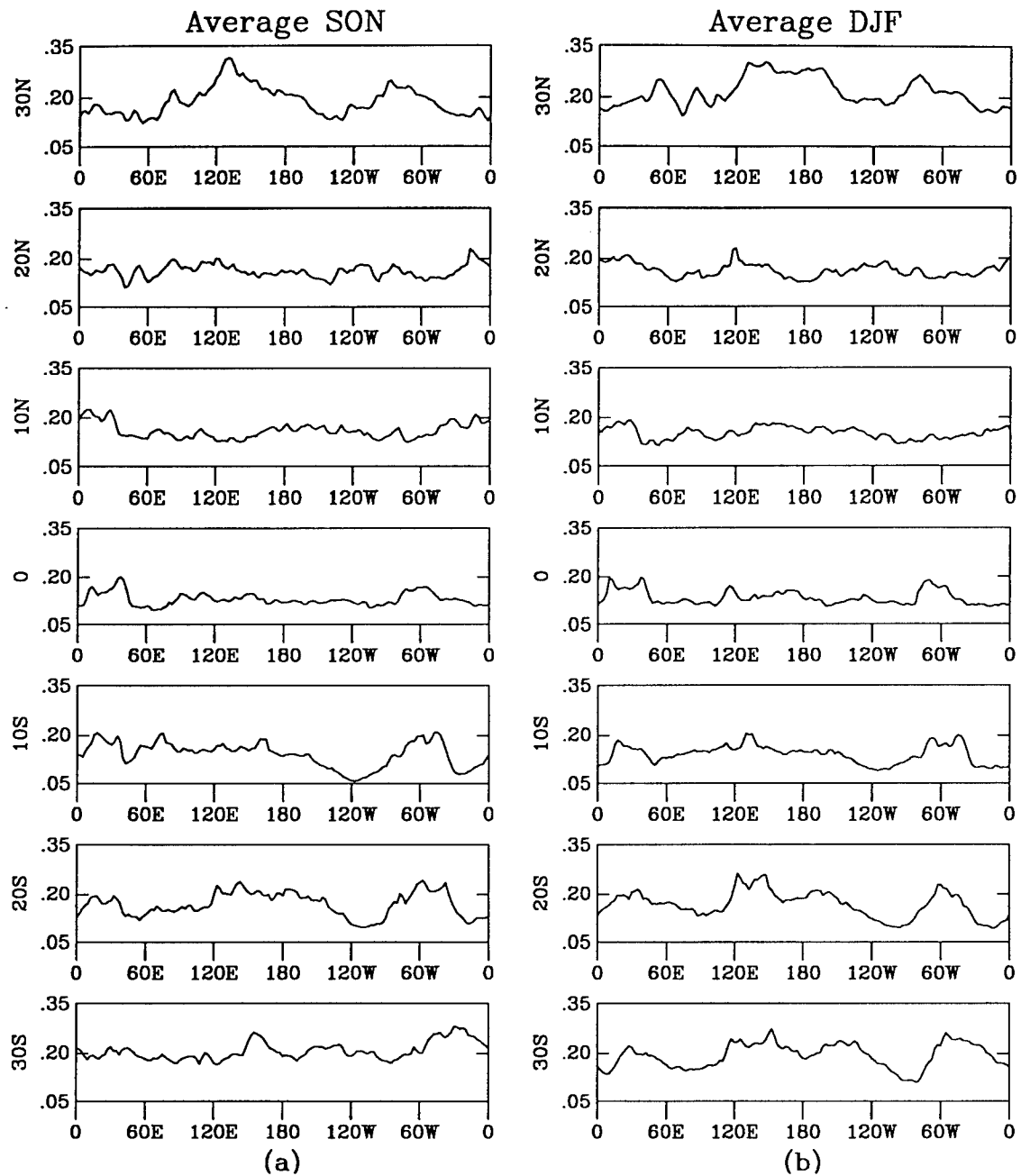
FIG. 13. Synoptic scale standard deviation (within the 3 to 8 day spectral band) in increments of 10° latitude from 30°N to 30°S: (a) 5 SON seasons, (b) 7 DJF seasons, (c) 6 MAM seasons, and (d) 6 JJA seasons (units are in cm).

Average MAM

Average JJA

(c)

(d)
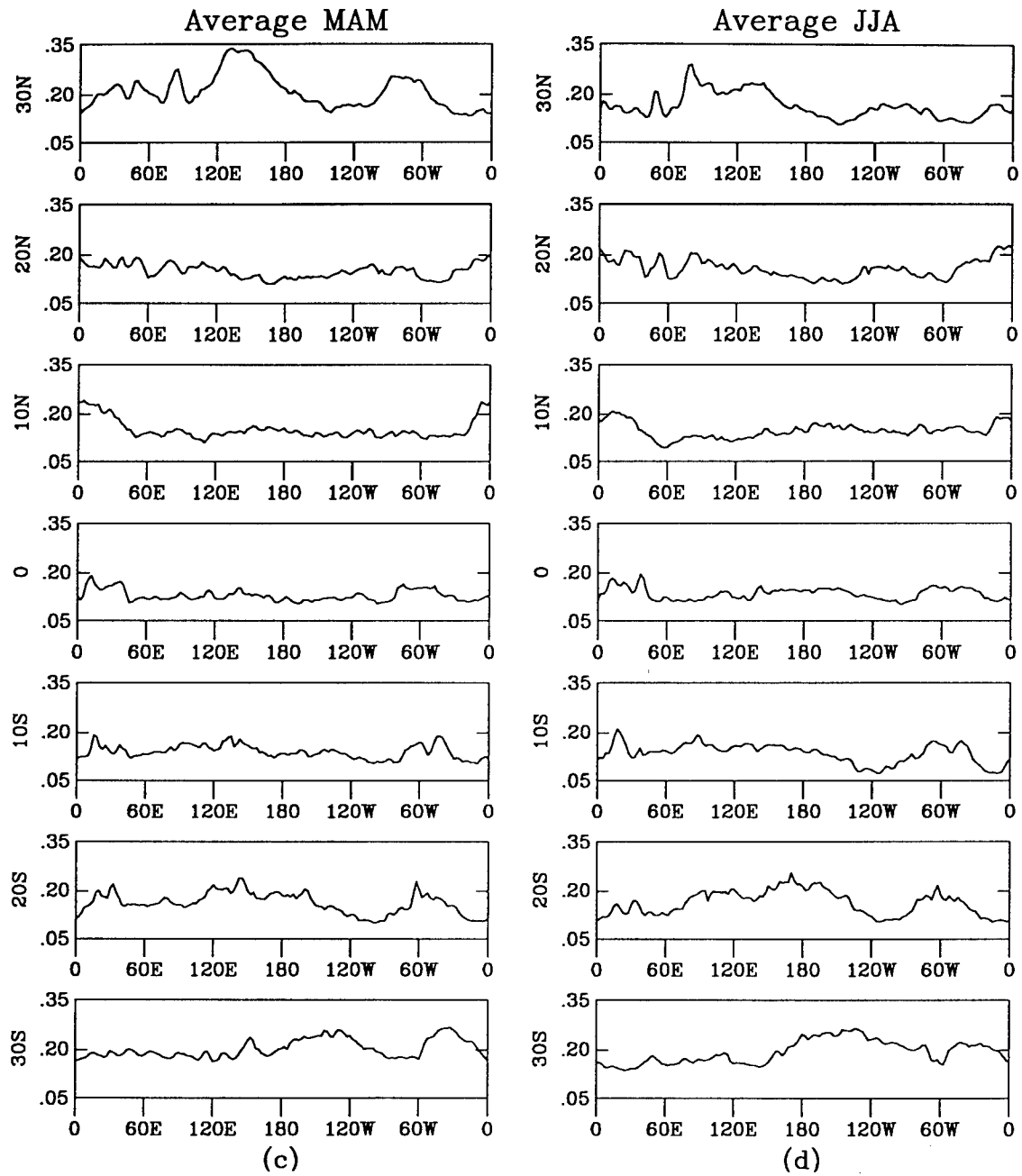
FIG. 13. Cont.

scale activity and the other with land masses. At the poleward boundaries of the study domain, peaks in these plots reveal areas of enhanced midlatitude synoptic scale activity. These regions generally exist over the ocean-induced baroclinic zones near the east coasts of China (130°E) and the United States (80°E) in the northern hemisphere, and over the southern Pacific storm track (120°E to 120°W) and near the ocean baroclinic zone east of South America (40°W) in the southern hemisphere. The northern hemisphere signal is seasonally enhanced, with the greatest magnitude and longitudinal span attained during boreal winter. The southern hemisphere signal appears to have two modes through an annual cycle, with eastern and western storm track modes. During austral fall and winter, the storm track prefers the eastern side of the South Pacific and it shifts to the western side during austral spring and summer. The enhanced region east of South America has its weakest activity during austral winter.

Nearer the equator, peaks in variability are attributable to the presence of land masses alone. A broad peak on the equator exists for all seasons between 10°E and 40°E, which almost exactly corresponds to the equatorial land region of the African continent. Another region of elevated standard deviation values is present between about 80°W and 50°W, which is close to the equatorial locations of the South American coastlines. At 10°S, a similar pattern emerges, with a stronger signal over South America than at the equator. At 10°N, the South American signal vanishes (as the South American continent does not extend to 10°N), while the African peak extends further westward to near 15°W in response to the presence of the western coast of north Africa. Peaks are found over the Arabian Peninsula and India at 20°N, while the signal at 20°S appears to indicate an increase in midlatitude activity. A seasonal cycle of activity over land masses between 10°N and 10°S is not clear; specifically,

an annual cycle over the Asian and west Pacific monsoon regions is not apparent in the variability.

A third feature becomes evident by viewing minima in the synoptic scale PW variability: Regions of subtropical subsidence associated with cool ocean surface temperatures. The largest of these regions is found west of South America between the equator and 30°S. This broad minimum covers about 50° of longitude, with the lowest values near 110°W at 10°S and close to 100°W at 20°S. This signal varies seasonally, with lowest values dipping to near 0.05 cm during austral spring at 10°N in association with the seasonal appearance of the southeast Pacific ITCZ. The signal minimum appears furthest west to near 120°W during austral winter and spring, and shifts eastward to near 100°W by fall. Farther south at 20°S, lowest values dip close to 0.1 cm during all seasons, and intensify westward to near 110°W during austral winter and spring from their summer and fall position near 95°W.

Using longitudinal plots of standard deviation of PW for several tropical latitudes, it is possible to identify several features. First, near the poleward edges of the study domain, increased values are associated with enhanced midlatitude activity. Second, more equatorward locales have higher values over land regions. Third, decreased values near 10° latitude (especially southern hemisphere) represent regions of subsidence.

D. REGIONS OF COHERENT BEHAVIOR OF SYNOPTIC SIGNALS

In addition to identifying convergence zones and regions of enhanced or diminished synoptic activity, it is important to describe the behavior of synoptic activity within different tropical regions. One of the easiest behavioral signals obtainable from the PW dataset is that of zonal propagation direction. Through

the use of time-longitude plots, coherent signals of PW anomalies through time indicate the zonal propagation direction of individual events. Appendix A contains 42 figures of time-longitude plots (Hovmöller format) of the 3 to 8 day filtered PW data for various seasons and latitudes. Each individual figure is divided into four separate plots (a, b, c, d) for the same specified latitude, but for different seasons. Interpolated dataset days are listed as days missing at the top of each plot beneath the season and year title. Contoured regions represent periods in space and time with greater than +0.5 mm PW anomaly at the synoptic time scale (contour interval is 1.0 mm). Pattern of propagation direction and information on the intensity of specific patterns through various seasons becomes evident from viewing these plots. Horizontal gaps in coherence correspond to days in the filtered dataset that were linearly interpolated in the original dataset in order to apply the filtering process and therefore do not accurately represent the actual synoptic scale behavior for the time period.

Using both the time-longitude and PW standard deviation with longitude plots, it is possible to show synoptic origin regions, regions of coherent propagation and preferred zonal direction of propagation, and relative strength of the average signal of such behavior. To document such behavior, descriptions are made for similar seasons. Major differences in the variables are discussed according to observed characteristic seasonal values and locations.

SON

During this transitional season, the northern hemisphere already experiences predominant eastward motion at 30°N during every year of study

(Figs. A1a, b, c, d, A8a). Such movement appears to increase toward the latter part of the season in both intensity and coherence. Peaks in seasonally averaged standard deviation exist near 130°E (0.3 cm) and 80°W (0.23 cm) (Fig. 13a). A weak signal of westward-moving anomalies is present, especially during the earlier part of the season, and is generally confined to longitudes between the prime meridian and 120°W. This is also the region of least organized synoptic behavior.

Equatorward, a transition occurs before reaching 20°N, so that both eastward and westward motion are found during all years of study (Figs. A2a, b, c, d, A9a). Although westward motion is preferred in longitudes between the prime meridian and 120°W, some anomalously strong periods are present over parts of the entire Pacific and Indian Oceans. Eastward-moving anomalies appear to originate near the prime meridian and propagate over the Indian Ocean, some of which remain coherent across the entire Pacific Ocean (nearly completing a path around the world). A similar pattern exists at 10°N (Figs. A3a, b, c, d, A10a).

Along the equator, westward motion dominates the signal for all longitudes, except between 120°E and the prime meridian, where eastward-moving anomalies exist (Figs. A4a, b, c, d, A11a). The westward-moving signals remain coherent further westward toward the Indian Ocean at 10°S, although a hint of easterly motion remains just east of the prime meridian (Figs. A5a, b, c, d, A12a). In addition, a clear signal of eastward-moving anomalies is present in a narrow zone from about 40°W to the west coast of South America (80°W). A broad region of weaker anomalies (generally less than 0.15 cm) stretches from about 160°W to 90°W longitude, with an associated minimum in standard deviation (less than 0.10 cm), with a minimum of 0.05 cm near 120°W

(Fig. 13a). This minimum in PW anomalies exists over the western extension of the cold Peruvian Current.

The transition from westward to dominant eastward-moving anomalies occurs between 10°S and 20°S. Only a hint of westward motion exists at 20°S during the years of study (Figs. A5a, b, c, d, A12a). A region of weak anomalies remains between 140°W and 80°W, with synoptic standard deviation near 0.12 cm (Fig. 13a). At the southernmost latitude of the study region (30°S), the time-longitude plots are dominated by strong, fast eastward-moving anomalies at every longitude for all study years (Figs. A6a, b, c, d, A13a). Peaks in synoptic standard deviation are found near 160°E and 60°W, where values exceed 0.25 cm (Fig. 13a).

DJF

Anomaly motion is predominantly eastward through all longitudes at 30°N during boreal winter (Figs. A8b, c, d, A15a, b, c, d). Only sporadic westward-moving signals are present at various longitudes. As during SON, average peaks in synoptic variation exist near 130°E and 80°W, where standard deviation values reach 0.30 and 0.25 cm respectively (Fig. 13b). At 20°N, a westward-moving signal becomes more obvious, primarily during the early part of the season in the western hemisphere (Figs. A9b, c, d, A16a, b, c, d). A peak in the average synoptic standard deviation occurs at 120°E with a value exceeding 0.20 cm (Fig. 13b).

Zonal propagation at 10°N has characteristics of both westward- and eastward-moving anomalies, with eastward-moving coherent signals appearing strongest between 20°W and 40°E (Figs. A10b, c, d, A17a, b, c, d). Other eastward motion is noted interspersed in westward-moving anomalies at

different longitudes. Otherwise, the westward-moving anomalies appear to have stronger spatial coherence and greater magnitude than eastward-moving anomalies at this latitude. A similar pattern exists at the equator, with the exception of a slightly enhanced eastward-moving signal between 80°W and 40°W (Figs. A11b, c, d, A18a, b, c, d). The weak but persistent slow eastward-moving anomaly appears again along the equator through all longitudes during the 1985/1986 season (Fig. A11b).

Both eastward and westward motion occur at 10°S, with some years showing more motion in one direction than the other (Figs. A12b, c, d, A19a, b, c, d). The 1982-83 and 1987-88 seasons demonstrate enhanced eastward-moving anomalies (Figs. A12d, A19c). A region of diminished anomalous activity occurs between 140°W and 80°W, where synoptic standard deviation dips to an average of about 0.12 cm (Fig. 13b). A similar situation exists at 20°S, with eastward-moving activity dominating during the first third of the season and more frequent westward-moving anomalies during the season's last third (Figs. A13b, c, d, A20a, b, c, d). The center of the diminished activity shifts eastward from near 120°W at 10°S to near 100°W at 20°S, although the surrounding region encompasses about the same longitudinal span. Peaks in the synoptic standard deviation field are found near 120°E and 140°E, as well as at 60°W, with values exceeding 0.25 cm at the first two peaks and approaching 0.25 cm at the third (Fig. 13b).

Motion at 30°S is predominantly eastward at all longitudes (Fig. A14b, c, d, A21a, b, c, d). Only a hint of westward motion is found within a region of decreased activity west of South America. Otherwise, the transition from westward- to eastward-moving anomalies occurs between 20°S and 30°S during austral summer. Again, as with SON, peaks in synoptic variation exist

near 160°E and 60°W, with standard deviation exceeding 0.25 cm in both locations (Fig. 13b).

MAM

At the northernmost latitude (30°N), eastward motion predominates through all latitudes (Fig. A22a, b, c, d, A29a, b). Only a few hints of westward-moving activity appears scattered through space and time during each of the study years. A single coherent maximum can commonly be tracked for longer than one complete global circuit. Although the eastward zonal propagation dominates at 20°N, an increase in the westward component is observed, especially toward the latter part of the season (Figs. A23a, b, c, d, A30a, b). Sharp peaks in synoptic standard deviation at 30°N exist near 130°E and 80°W, with values near 0.35 and 0.25 cm respectively (Fig. 13c). These peaks do not exist at 20°N, and individual maxima do not remain coherent for as long a track.

The transition to westward motion over most longitudes occurs between 20°N and 10°N. Westward-moving anomalies at 10°N appear at all longitudes east of about 40°E and west of about 10°W (Figs. A24a, b, c, d, A31a, b), although eastward motion prevails early in the seasons of some years. Strong eastward motion dominates between 10°W and 40°E.

During some years, motion at the equator is predominantly westward (1981, 1982, 1984, 1989) (Figs. A25a, b, d, A32b), while other years portray a strong eastward-moving component (1983, 1988) (Figs. A25c, A32a). In both cases, however, eastward motion is enhanced between the prime meridian and 40°E and increased slightly from 80°W to 40°W. A hint of decreased anomalous activity appears in the middle of the season from 120°W to 80°W during every year and from the dateline to 120°W for all years except 1983 (Fig.

A25c). Corresponding standard deviation plots reveal the center of minimal activity to be located near 100°W, where values dip below 0.1 cm (Fig. 13c). A similar pattern is portrayed at 10°S, with the exception that the region of decreased activity is shifted eastward to longitudes between 120°W and 80°W (Figs. A26a, b, c, d, A33a, b).

A transition from predominantly westward-moving to eastward-moving activity for all longitudes at 20°S generally occurs near the middle of the season (Figs. A27a, b, c, d, A34a, b), although 1983 and 1988 demonstrate generally eastward-moving activity throughout the entire season (Figs. A27c, A34a). Such a seasonal transition is no longer noted at 30°S, where eastward motion is observed during the entire period for all years (Figs. A28a, b, c, d, A35a, b). Only a hint of westward-moving anomalies is noted toward the beginning of the years of this season. Synoptic standard deviation peaks near 150°E at both latitudes (0.23 cm) and near 60°W at 20°S (0.23 cm) and at 130°W (0.25 cm) and 40°W (0.27 cm) at 30°S (Fig. 13c).

JJA

Even at the northernmost latitude (30°N), evidence of westward motion exists, although it is generally confined to the western hemisphere and the eastward-moving anomaly signal remains stronger at most longitudes (Figs. A29c, d, A36a, b, c, d). Synoptic standard deviation of PW during boreal summer is considerably lower than in other seasons at this latitude, with magnitudes below 0.2 cm everywhere except near 80°E and 130°E (Fig. 13d). The westward-moving signal becomes stronger at 20°N, especially during the latter half of the season (Figs. A30c, d, A37a, b, c, d). Eastward motion persists from the prime meridian into the Indian Ocean (except for 1989) (Fig. A37d).

Westward-moving anomalies penetrate west of the dateline at 10°N (Figs. A31c, d, A38a, b, c, d). Only between the prime meridian and 60°E is there found evidence of eastward-propagating anomalies. A similar pattern exists at the equator, with variation in intensity and frequency of anomalous events (Figs. A32c, d, A39a, b, c, d). A notable exception in pattern emerges during 1985, where the weak but very persistent eastward-moving anomaly is present through the entire period for all longitudes (Fig. A39b).

Clear evidence of a region of subtropical subsidence appears between 140°W and 80°W, where anomalous PW and standard deviation signals are diminished at 10°S (Fig. A33c, d, A40a, b, c, d). Westward propagation dominates the signal at nearly all longitudes, except near the prime meridian, where eastward-moving anomalies are observed. The signal of subsidence is weaker at 20°S, and a transition from westward to eastward zonal propagation occurs somewhere between 10°S and 20°S (Figs. A34c, d, A41a, b, c, d). Almost all zonal propagation at 30°S is from west to east (Figs. A35c, d, A42a, b, c, d) and average standard deviation increases to greater than 0.15 cm for almost all longitudes (Fig. 13d).

The synoptic time scale is dominated by easily recognizable persistent, repeatable, long-lived propagating anomalies. Over extended time periods, most regions possess similar synoptic behavior in nearly every year. The direction of zonal propagation of these anomalies is affected by season, especially at latitudes bordering the transition between tropical and midlatitude processes. During JJA and SON, the northern hemisphere transition from easterly to westerly motion occurs between 30°N and 20°N. In DJF and MAM, the transition is not as clear over the spatial domain, but it occurs equatorward of the summer and fall transition latitudes. Similarly, the southern hemisphere

latitude of transition from easterly to westerly motion occurs near 20°S during DJF and MAM, while this critical latitude shifts equatorward during JJA and SON to between 20°S and 10°S.

Eastward zonal propagation appears enhanced across the African continent, especially between the equator and 20°N. A similar tendency is noted over the South American continent (equator to 30°S). Motion west of these continents seems to have an enhanced westward component. This pattern is enhanced on a seasonal cycle and becomes more evident during each hemisphere's summer season.

Notwithstanding these plots indicate some genesis region of westward-propagating anomalous activity, most regions seem to prefer westward or eastward propagation. Most interesting from these plots is that any single anomalous event propagating in either zonal direction is capable of existing at almost anywhere during any season between the latitudinal transition zones from predominantly westward to predominantly eastward motion (near 20°N and 20°S). Specific anomalous events often demonstrate continuity of a signal exceeding +0.5 mm PW anomaly for more than 120° of longitude, commonly from 20,000 - 40,000 km. However, there are preferred seasons when the zonal propagation is more likely to be from one direction than the other at a specific longitude.

The next chapter focuses on the persistent synoptic behavior of broad geographical regions.

CHAPTER V

REGIONAL CHARACTERISTICS OF SYNOPTIC SCALE BEHAVIOR

A. DETERMINING STUDY REGIONS AND METHODS FOR STUDY

Focusing on regional patterns of tropical synoptic scale activity allows a view of behavior associated with identifiable tropical convergence zones. Regional variations in tropical behavior are observed at various locations and seasons from the time-longitude plots in Appendix A and from the global climate shown in Figs. 3-13. Characteristic patterns of zonal propagation apparently differ markedly both regionally and seasonally. This chapter documents the behavior of PW anomalies within regions associated with the convergence zones.

Two tools have been developed for the study of synoptic scale activity within the selected study regions: Composited time-longitude plots of filtered PW data and lag correlation plots for individual and climatological seasons. Composited Hovmöller plots (over many synoptic events) show the preferred seasonal zonal propagation direction, zonal structure, and average intensity of associated activity centered on the regional focal point. Lag correlation plots identify temporally evolving anomaly fields and reveal the spatial structure and extent of anomalies in the PW field.

Each region is first discussed with respect to the pattern in the seasonally composited time-longitude plots consisting of "strong" anomalous PW events (in excess of +2.0 mm anomalies at the focal point). These patterns are described, including climatologically preferred direction and speed of zonal propagation, frequency, and zonal and temporal coherence of the climatological synoptic

scale event. Propagation is synthesized in a global plot of preferred direction between 15°N and 15°S for all four seasons. Second, a discussion of the spatial pattern in the seasonally composited time lag correlation fields is given to identify the spatial domain of the climatological anomalous event, reinforce the results for the preferred direction of zonal propagation, and discus teleconnective patterns that are evident.

B. REGIONAL ZONAL PROPAGATION

Figures 14 through 20 display composited Hovmöller plots of positive filtered PW anomalies. Each occurrence of an anomaly exceeding +2.0 mm at the selected regional focal point constitutes an event, and is centered at day zero on the plot. A mean Hovmöller plot of all events within the seasonal climatology is constructed for the 16-day period centered on day zero and the predetermined regional and seasonal focal point. Shaded area represents a land surface type. Latitudes vary seasonally along each focal longitude, so the shaded land surface varies in the seasonal plots as well. All events in the 24 season climatology are included.

ITCZ

The focal point at 145°W attains its most poleward latitude during boreal fall, reaching 15°N. Figure 14 reveals a footprint of westward propagation at about 9 ms^{-1} in the climatological composite of strong events for MAM, JJA, and SON. The SON signal is the most coherent, originating near 125°W and continuing beyond the dateline, to at least 155°E. There are additional hints of the signal all the way to the South American coast. Periodicity of anomalous

SON (15.0N)
(37 Events)

(a)

DJF (10.0N)
(47 Events)

(b)
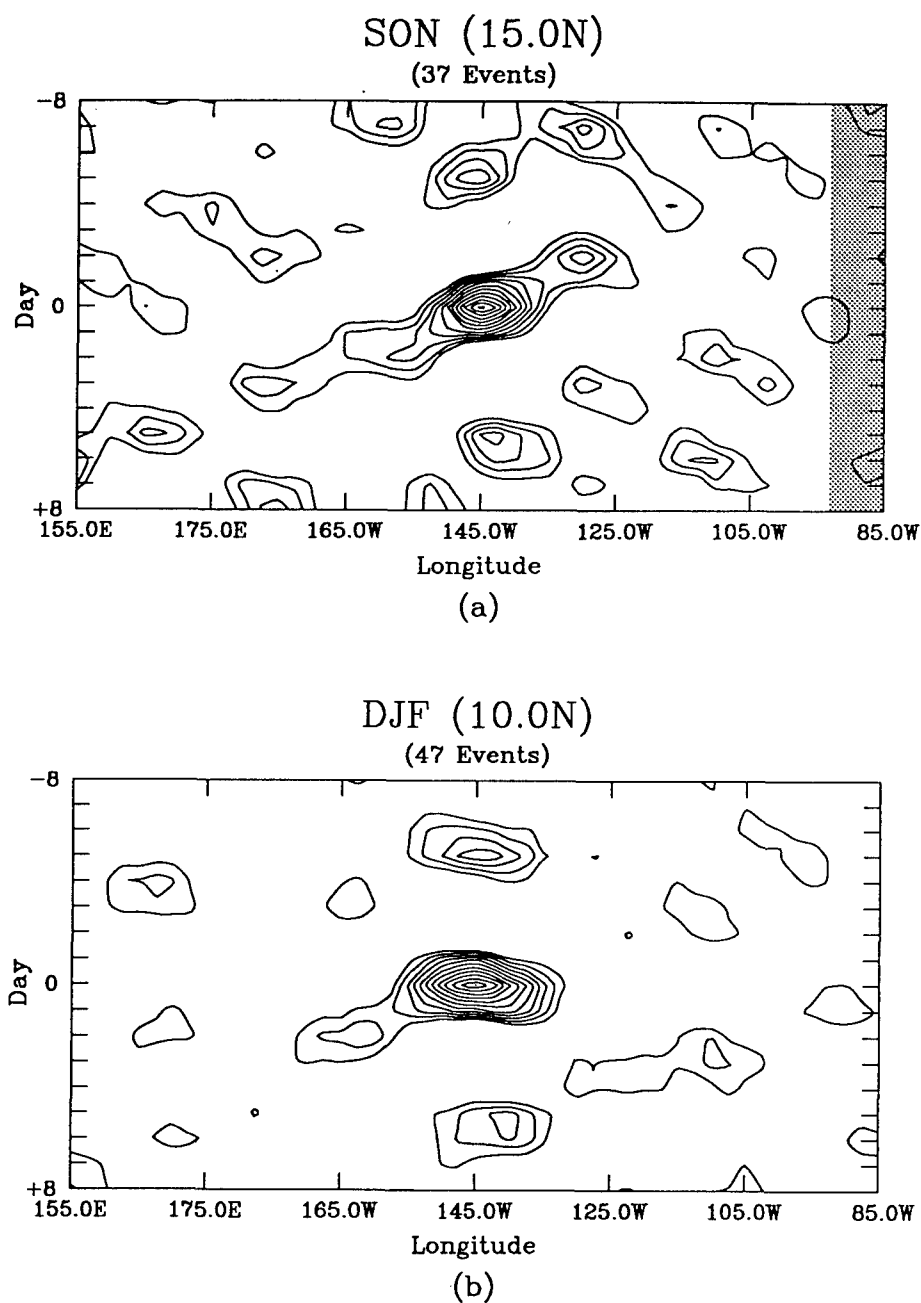
FIG. 14. Composite of synoptic scale events exceeding +2.0 mm PW anomaly in the 3 to 8 day time filtered PW dataset for the North Pacific ITCZ at 145°W for (a) SON at 15°N, (b) DJF at 10°N, (c) MAM at 10°N, and (d) JJA at 12.5°N. Shading denotes land, which varies because the central latitude is seasonally dependent. Lowest contour is +0.25 mm with an interval of 0.25 mm.

MAM (10.0N)

(25 Events)

(c)

JJA (12.5N)

(35 Events)

(d)

FIG. 14. Cont.

SON (15.0S)
(31 Events)

(a)

DJF (17.5S)
(48 Events)
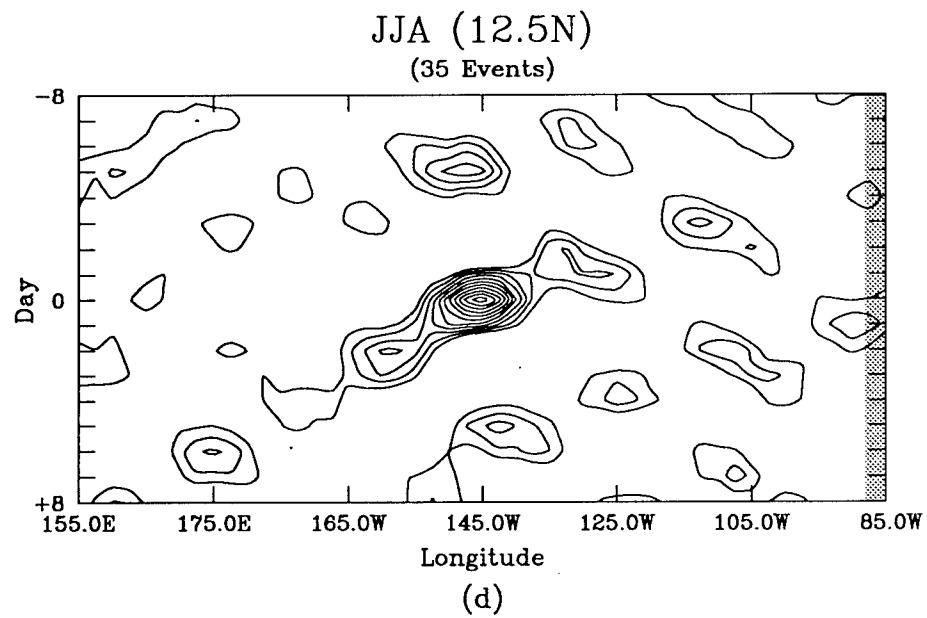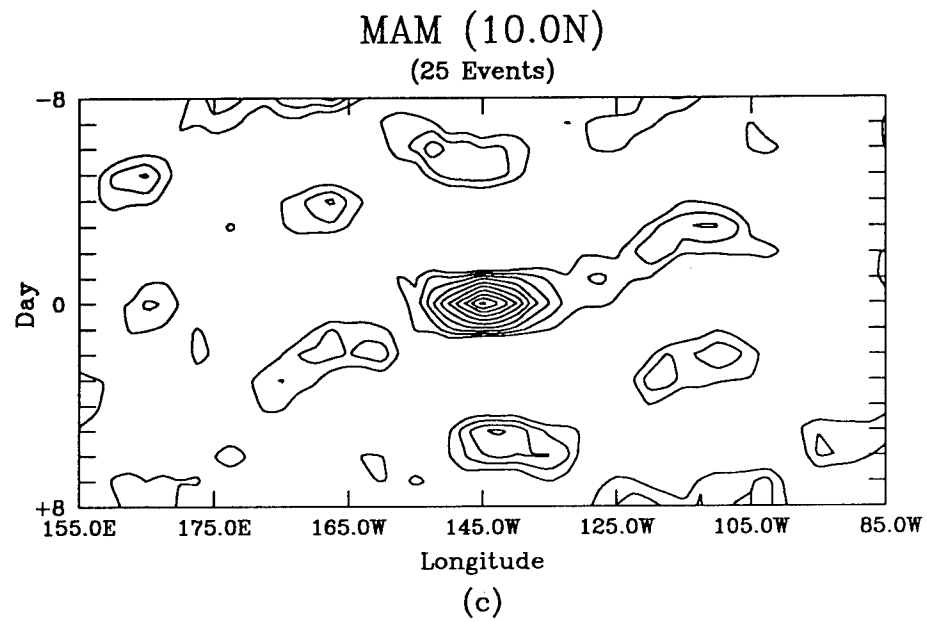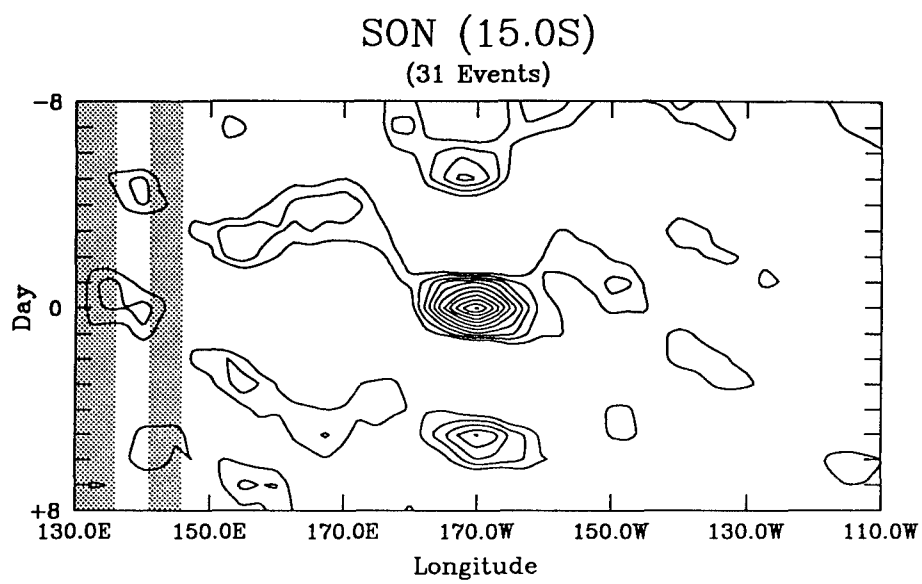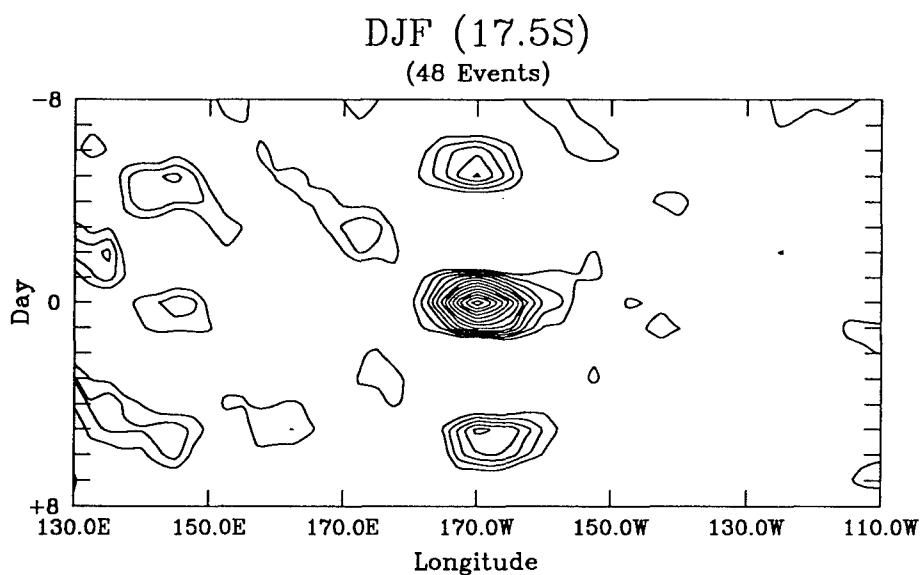
(b)

FIG. 15. As in Fig. 14, except for the SPCZ at 170°W for (a) SON at 15°S, (b) DJF at 17.5°S, (c) MAM at 12.5°S, and (d) JJA at 15°S.

MAM (12.5S)
### (26 Events)

(c)

JJA (15.0S)
(38 Events)

(d)

FIG. 15. Cont.

SON (12.5N)
(39 Events)

(a)

DJF (7.5N)
(34 Events)

(b)
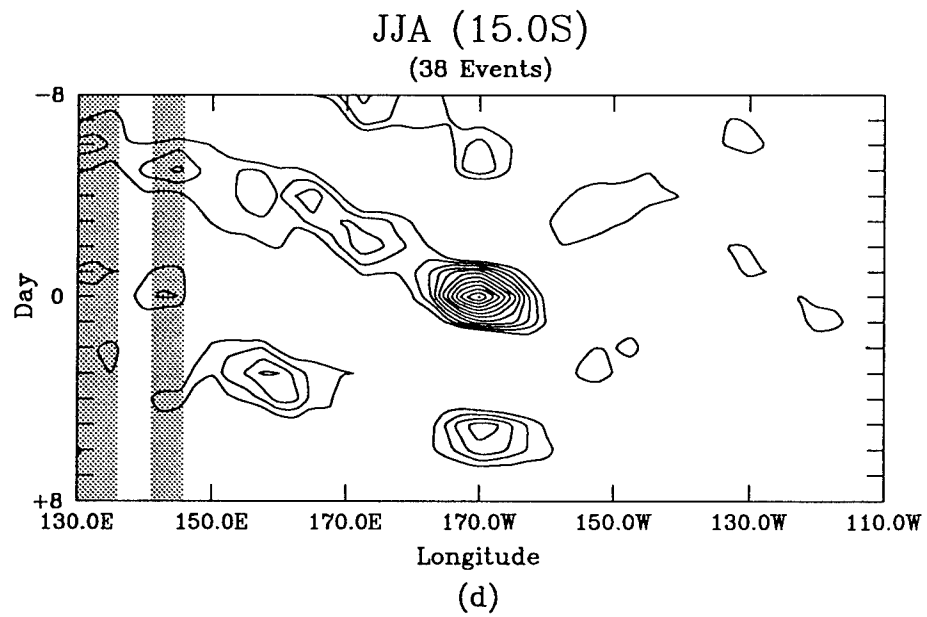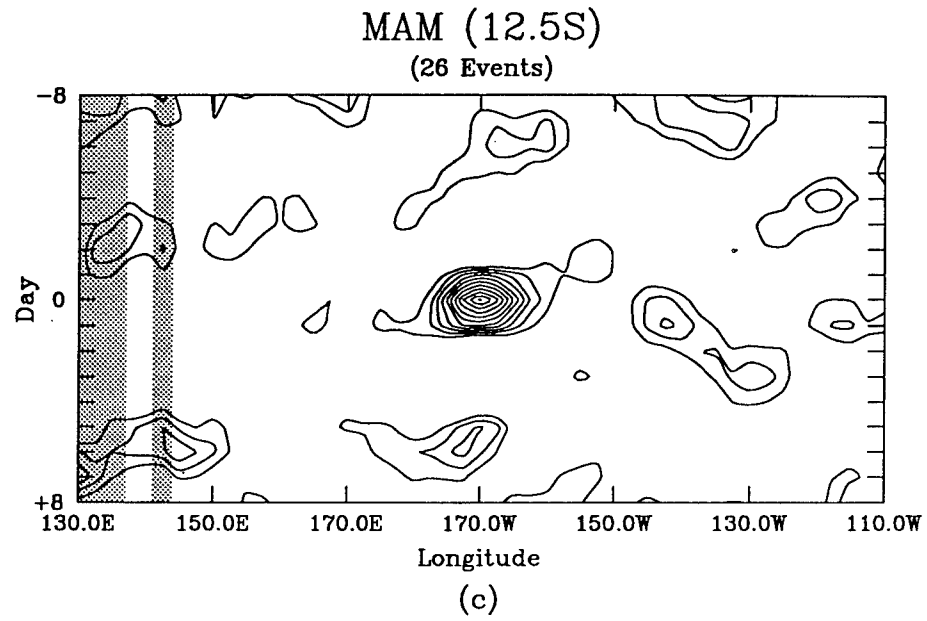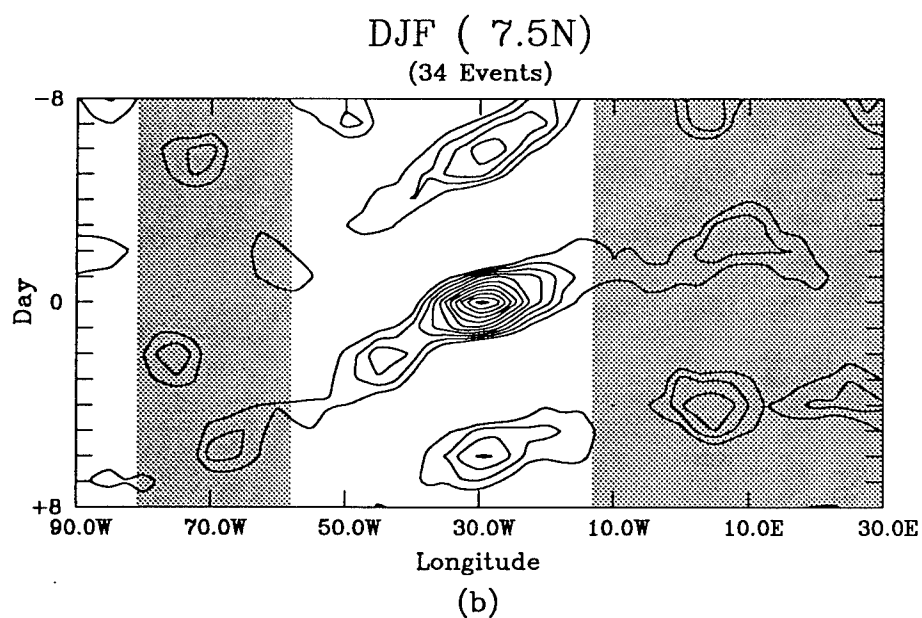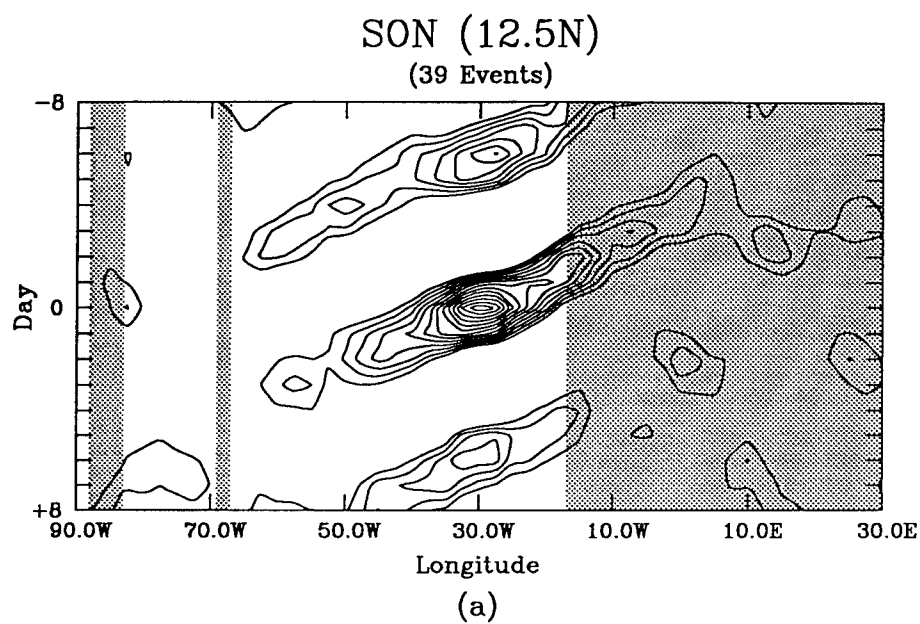
FIG. 16. As in Fig. 14, except for the North Atlantic ITCZ at 30°W for (a) SON at 12.5°N, (b) DJF at 7.5°N, (c) MAM at 7.5°N, and (d) JJA at 12.5°N.

MAM (7.5N)
(30 Events)

(c)

JJA (12.5N)
(33 Events)

(d)

FIG. 16. Cont.

SON (12.5N)
(50 Events)

(a)

DJF (7.5N)
(59 Events)

(b)
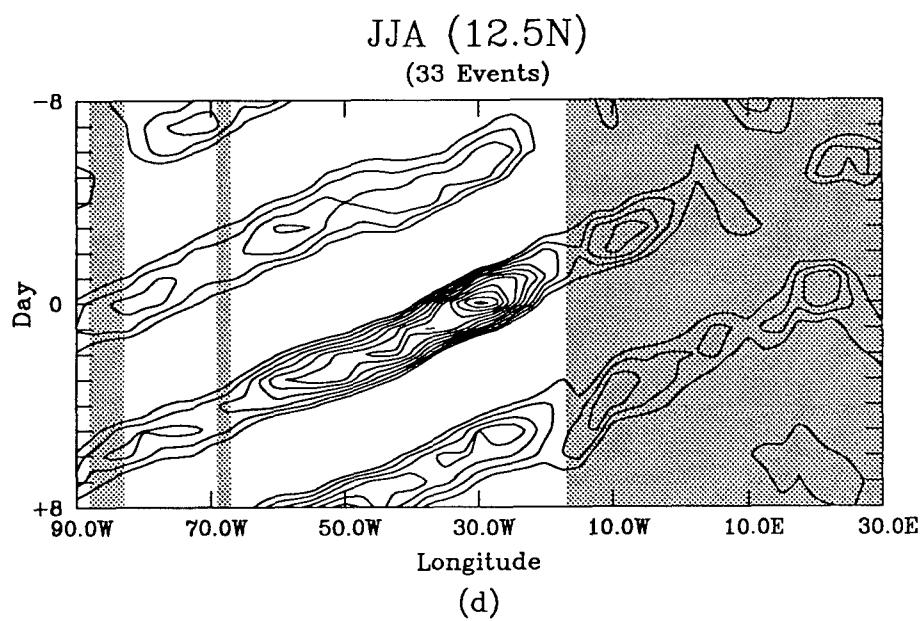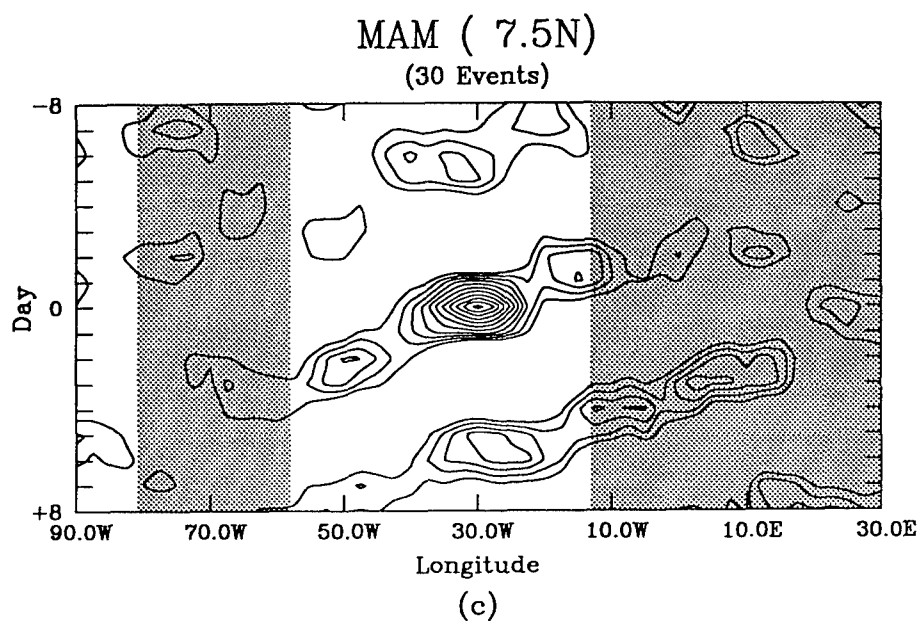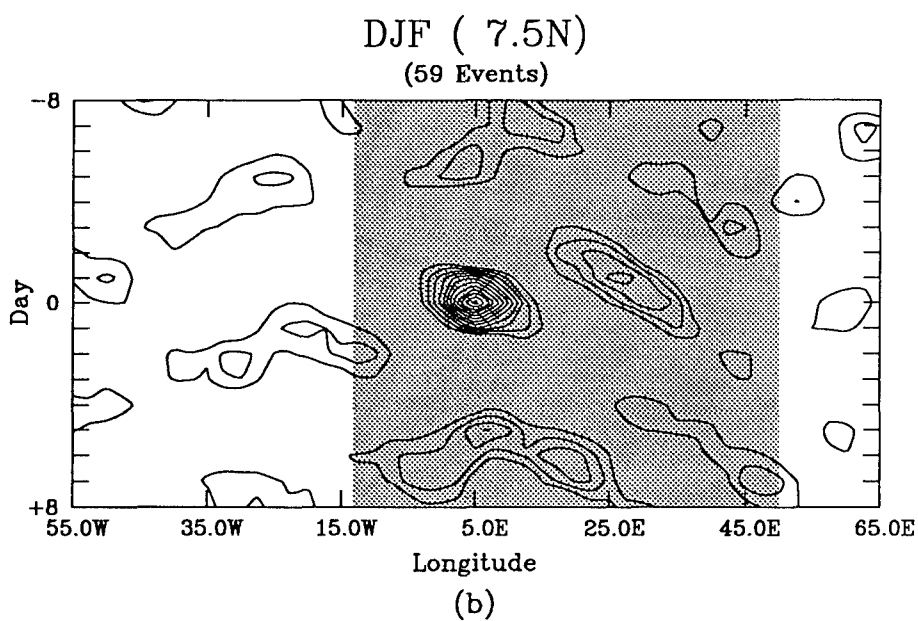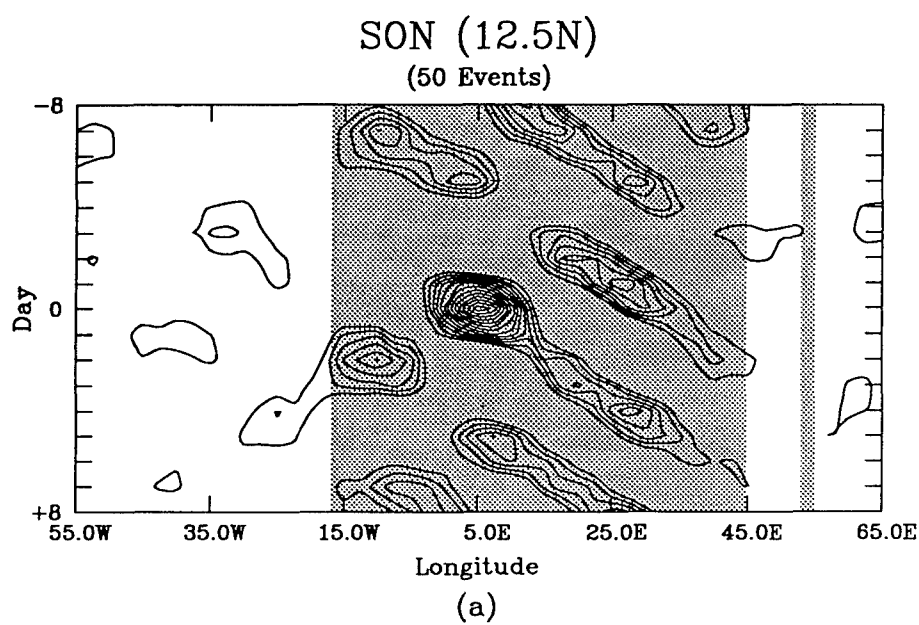
FIG. 17. As in Fig. 14, except for the Sahel region at 5°E for (a) SON at 12.5°N, (b) DJF at 7.5°N, (c) MAM at 12.5°N, and (d) JJA at 15°N.

MAM (12.5N)
(78 Events)

(c)

JJA (15.0N)
(72 Events)

(d)

FIG. 17. Cont.

SON (2.5N)
(18 Events)

(a)

DJF (2.5S)
(33 Events)

(b)
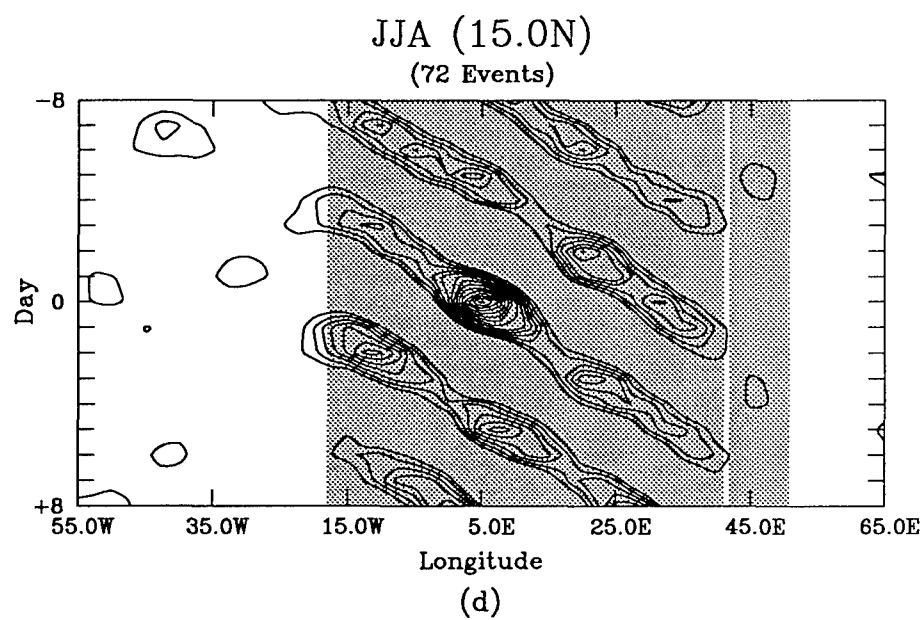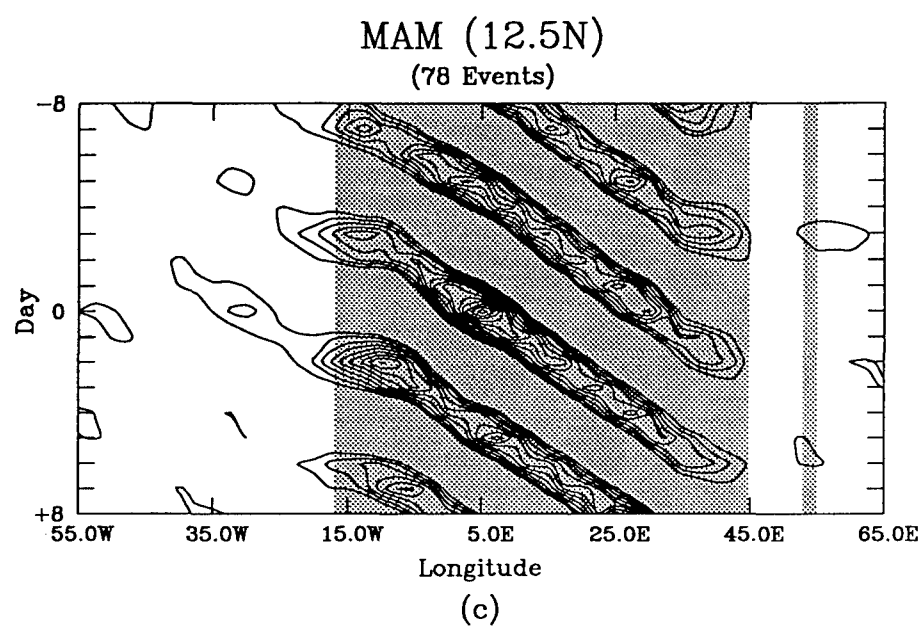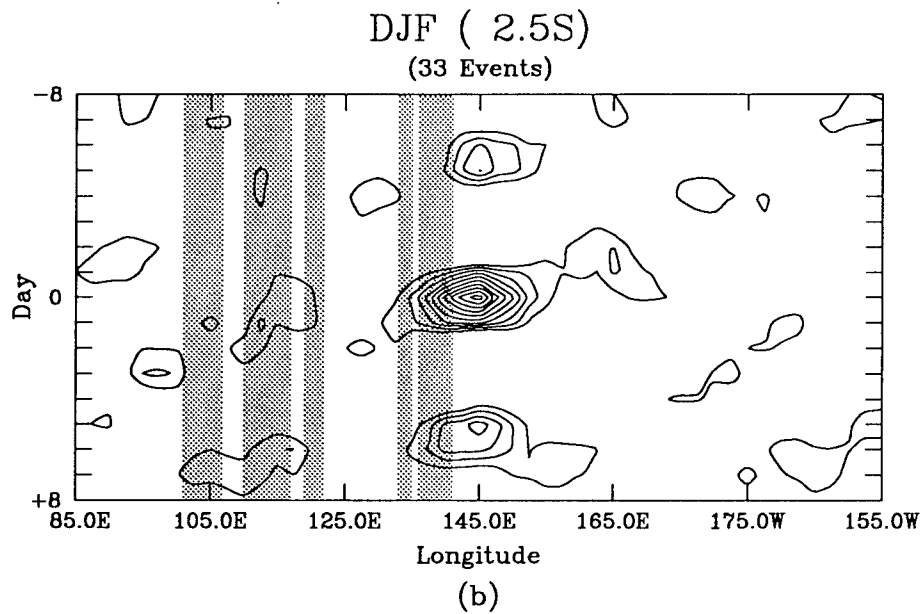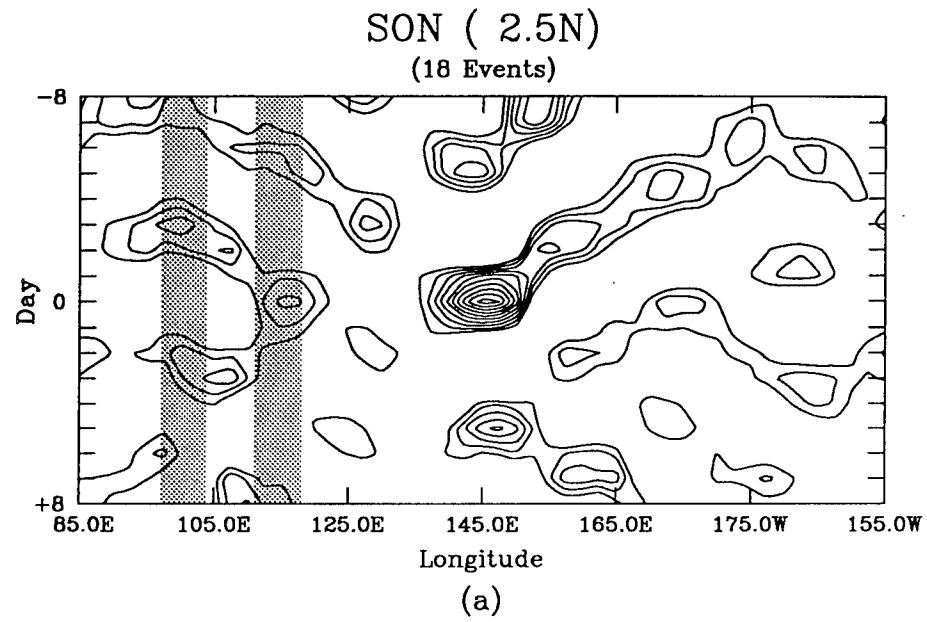
FIG. 18. As in Fig. 14, except for the Pacific warm pool at 145°E for (a) SON at 2.5°N, (b) DJF at 2.5°S, (c) MAM at 2.5°S, and (d) JJA at 2.5°N.

MAM (2.5S)
(18 Events)

(c)

JJA (2.5N)
(22 Events)

(d)

FIG. 18. Cont.

SON (7.5S)
(29 Events)

(a)

DJF (12.5S)
(33 Events)

(b)
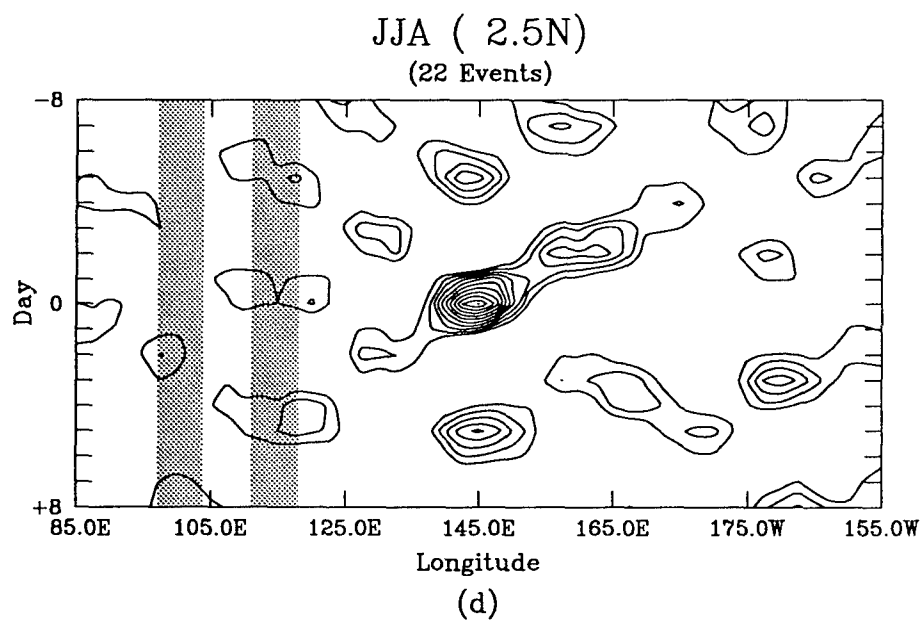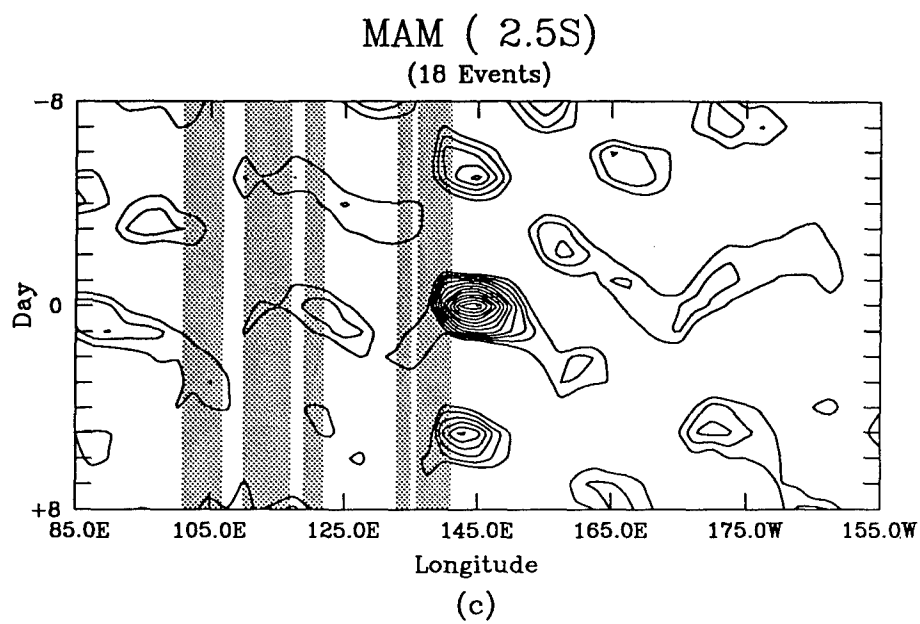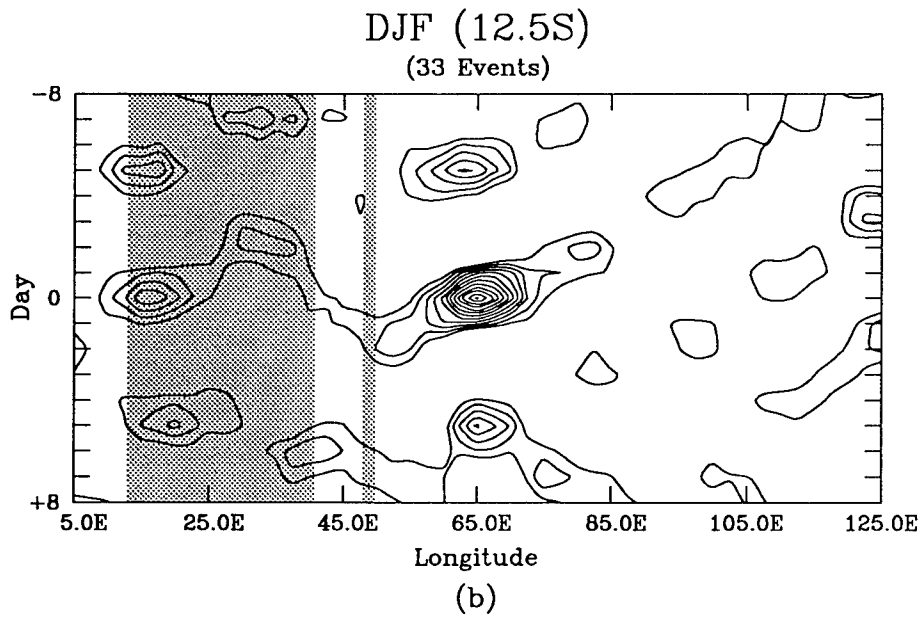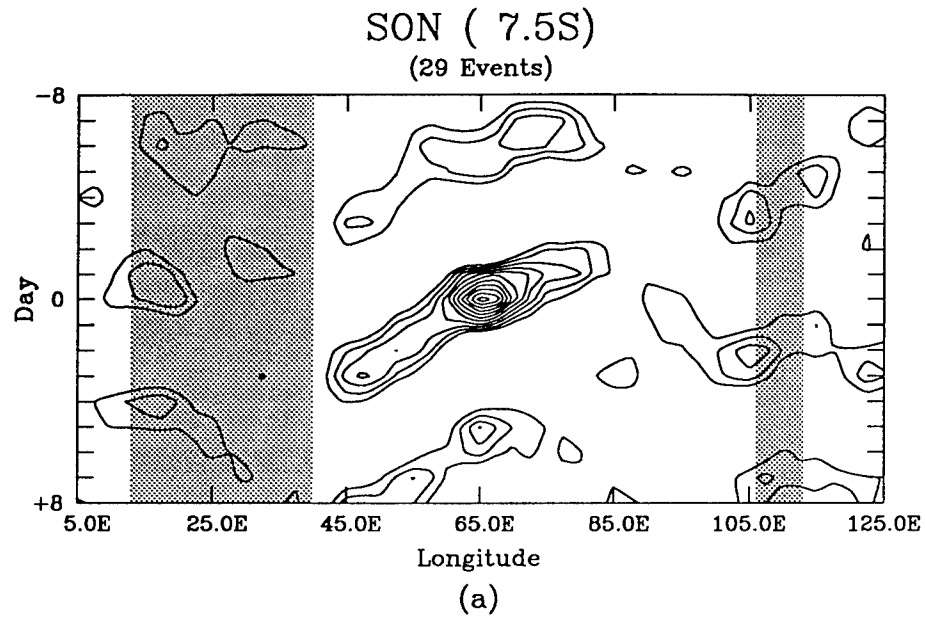
FIG. 19. As in Fig. 14, except for the South Indian ITCZ at 65°E for (a) SON at 7.5°S, (b) DJF at 12.5°S, (c) MAM at 10°S, and (d) JJA at 7.5°S.

MAM (10.0S)
(26 Events)

(c)

JJA (7.5S)
(21 Events)

(d)
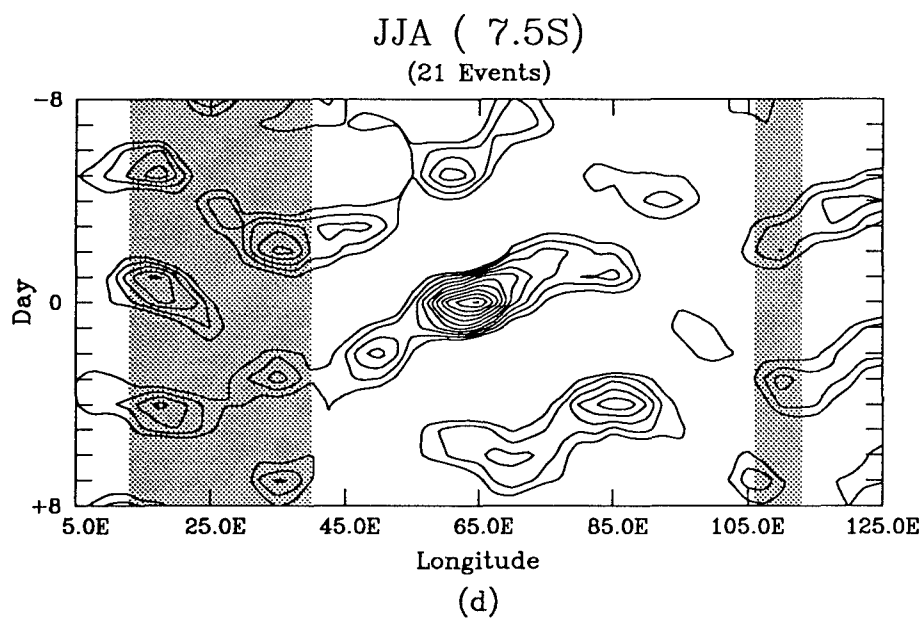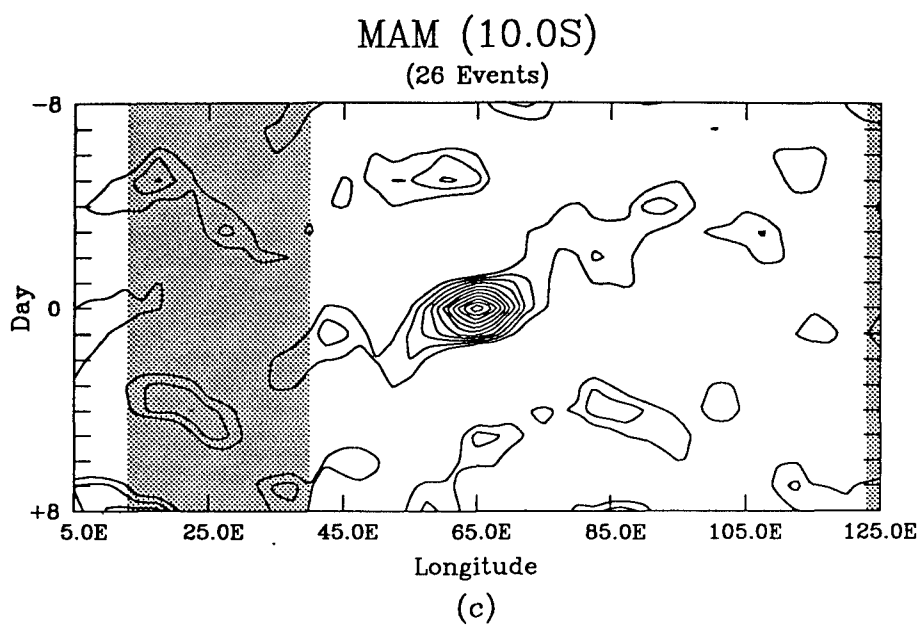
FIG. 19. Cont.
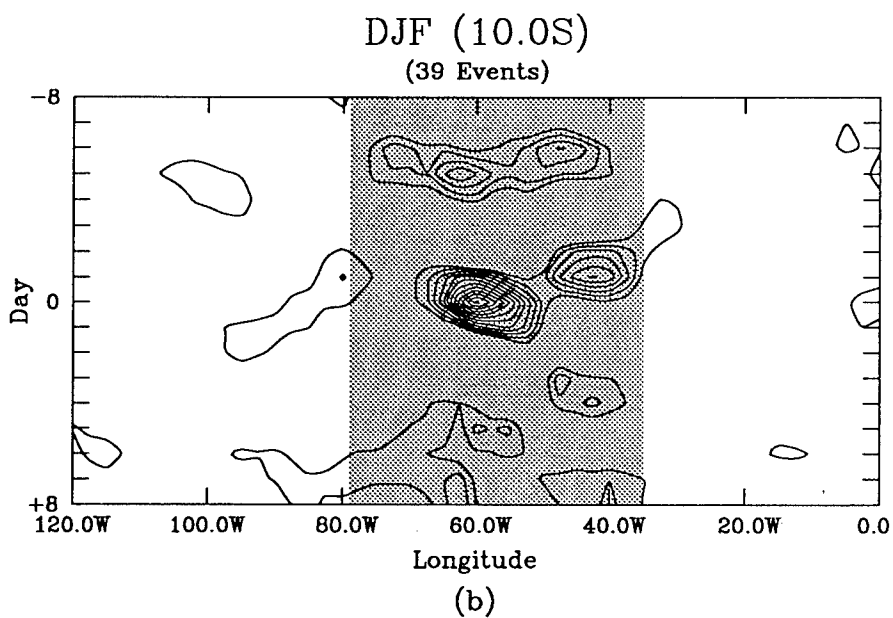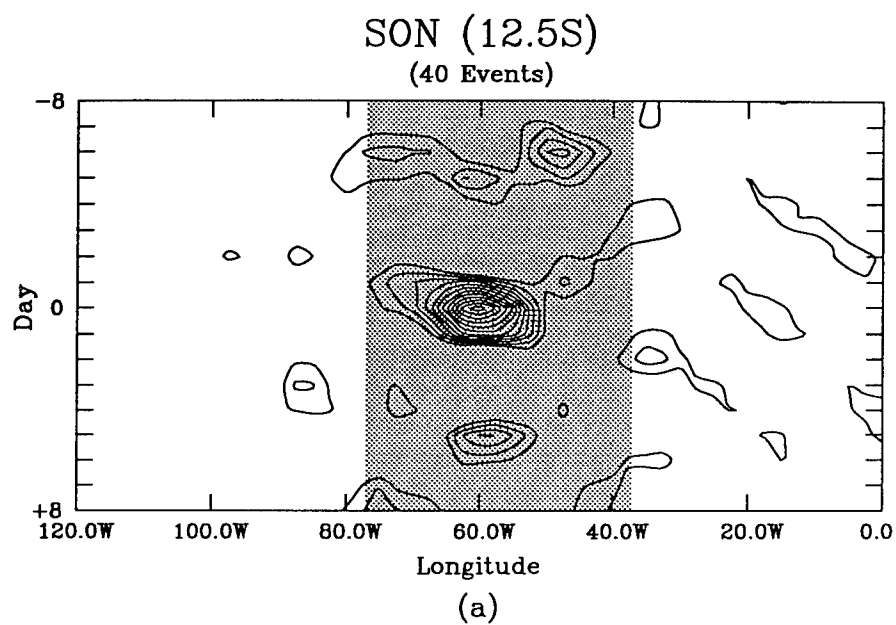
FIG. 20. As in Fig. 14, except for the Amazon region at 60°W for (a) SON at 12.5°S, (b) DJF at 10°S, (c) MAM at 12.5°S, and (d) JJA at 12.5°S.

MAM (12.5S)
(52 Events)

(c)

JJA (12.5S)
(41 Events)

(d)
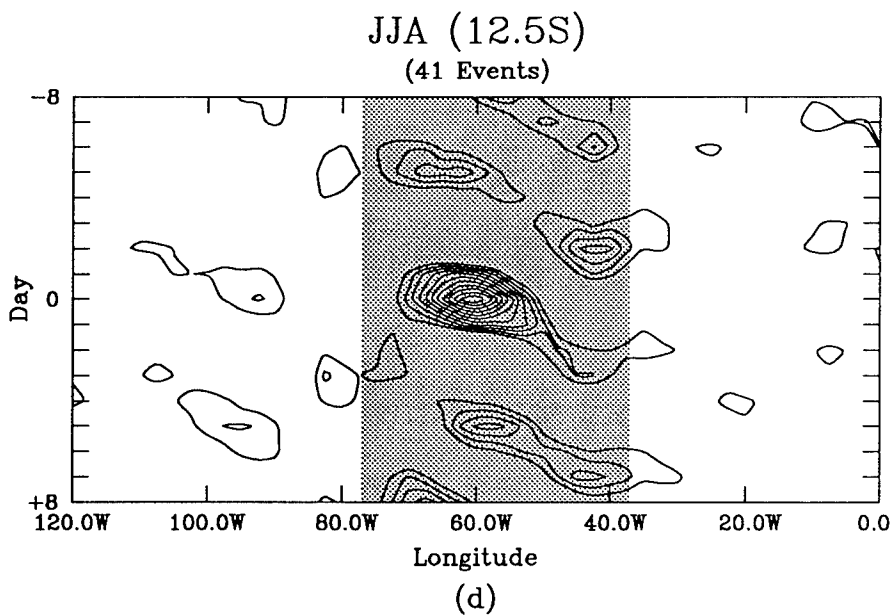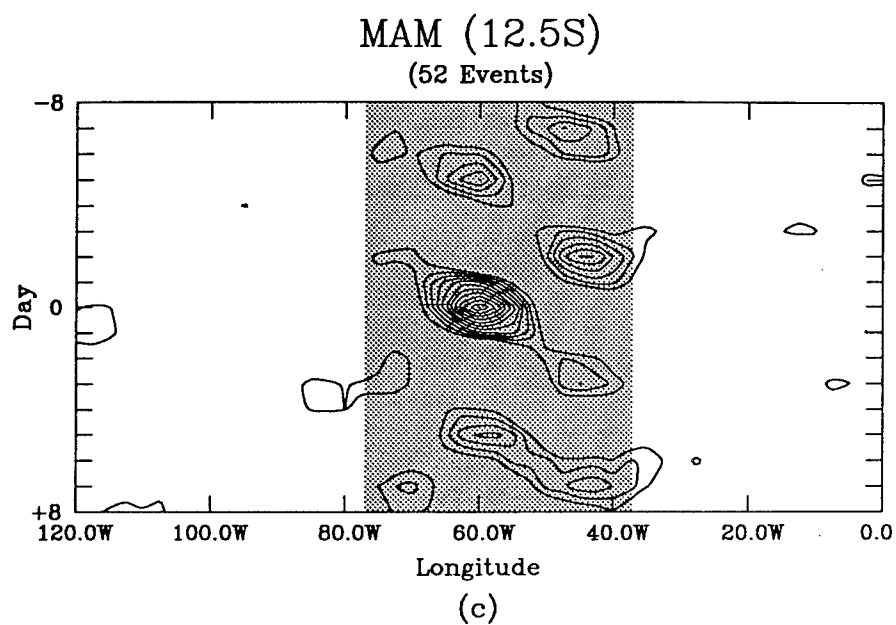
FIG. 20. Cont.

peaks at the focal longitude during all seasons in this region is approximately 5 days with a zonal length scale of about 5,000 km. Evidence of eastward motion is present, especially in the JJA and SON composites across the eastern half of the plot domains. The appearance of this eastward component appears to be the result of the annual cycle more than a latitudinal shifting of the focal point. Although the stronger events appear to favor westward propagation, the background pattern reveals eastward motion at a period of 4 to 4 1/2 days and a speed of 7 ms-1. No clear pattern of propagation behavior is identifiable at 10°N during boreal winter (Fig. 14b). Zonal propagation during this season assumes both eastward and westward phases during different events, leaving no signal of preferred zonal propagation direction. Hence, a clear bullseye pattern appears centered at day 0 and the focal point. Interestingly, this focal latitude, which corresponds to the maximum signal in the PW frequency field, is located at the transition between eastward motion to the south and westward motion to the north, which is shown later in this chapter. The resulting composite reveals the existence of both directions of motion.

SPCZ

Motion appears to favor the eastward propagation between 12.5°S and 17.5°S at 170°W. The strongest eastward signal occurs during JJA, when motion through the focal point remains intact from the eastern coast of northern Australia to near 160°W. Motion at the western edge of the region appears to propagate at near 15 ms^{-1}, but slows to approximately 7 ms^{-1} between 160°E and 160°W. This signal slows to 6 ms^{-1} during austral spring, and sporadic westward zonal propagation exists as well (Fig. 15a). Periodicity of anomalous maxima at the focal point during both austral spring and summer is about five

days. Any signal of preferred zonal propagation is difficult to determine during austral summer, although Fig. 15c hints toward a slight favoring of westward zonal propagation through the focal point at 12.5°S during austral fall. Constructive interference between events propagating in both zonal directions yields a bullseye signature at the center of the climatological time-longitude plot. Periodicity of anomalous maxima at the focal point is close to 5 1/2 days for both austral fall and winter.

NACZ

Strong coherence is evident in the time-longitude climatology during all seasons. Figure 16 reveals a strong westward propagating footprint from the west coast of Africa into the Caribbean Sea. These events, which propagate at 8 to 10 ms^{-1}, are so strong and repeatable, that they are well defined both before and after the defining event. They appear regularly at a 6-day interval and have a zonal wavelength of 6,000 km. The signal is weakest during DJF (Fig. 16b) and MAM (Fig. 16c), when the focal longitude shifts equatorward to 7.5°N, but the seasonal difference is more accountable for this signal change than is the latitudinal shift of the focal point. During JJA, the most coherent signal exists, as events that originate near the north African coast remain intact west of 90°W (Fig. 16d).

Sahel

Perhaps the strongest and clearest signal of all regions is located across Sahel Africa. Clear eastward propagation exists during all seasons, weakest during boreal winter (Fig. 17b) and strongest during boreal spring (Fig. 17c) and

summer (Fig. 17d). These events, which propagate at a speed of 7 ms^{-1}, originate near the west coast of north Africa and remain coherent across the entire land region to the east coast of the African continent. Periodicity of events is about five days, with a zonal wavelength between 2,500 and 3,000 km. Some evidence exists west of the north African west coast that the same source responsible for these eastward-moving anomalies also is associated with the westward-moving events that cross the Atlantic Ocean along the NACZ. Seasonal changes in the footprint characteristics of the composites are most attributable to the annual cycle rather than latitudinal variation of the focal point.

WPWP

Figure 18 shows evidence of propagation in both zonal directions during all seasons in this region, although a preference toward a westward tendency is observed in all seasons except MAM. Since the focal latitude is within 2.5° of the equator, the westward-propagating signal of near 9 ms^{-1} is consistent with the mixed Rossby-gravity mode response documented along the equator. However, although the footprint for the composite of stronger PW anomalies remains westward during these seasons, evidence for eastward propagation persists in the domains of the JJA and SON plots, consistent with this seasonal signal found along the ITCZ. Westward-propagating events during these seasons originate near the dateline and propagate to just west of the focal longitude, where the signal disappears. The periodicity of anomalous nodes along the focal longitude occurs at about a 5-day interval.

SICZ

With the focal latitude varying from 7.5°s to 12.5°S along 65°E longitude, predominant westerly motion prevails throughout all seasons (Fig. 19). Point of origin appears to be located near 85°E and the footprints remain coherent to near 45°E at their western edge. Hints of easterly motion across India are found, especially during MAM and JJA. The speed of westward propagation is about 10 ms^{-1} with a periodicity of close to 5 days.

Amazon

With the focal latitude remaining near 12.5°S during all seasons, evidence of eastward propagation emerges for all seasons across the western half of South America. The strongest eastward signal appears during MAM (Fig. 20c) and JJA (Fig. 20d), where it exists across all but extreme eastern South America. The SON (Fig. 20a) and DJF (Fig. 20b) composites hint toward some westward-moving anomalies originating near 35°W and propagating to just east of the focal longitude. The origin for eastward-moving anomalies appears to be near the west coast of South America. Propagation of these eastward-moving anomalies is near 9 ms^{-1} with a period of 5 days.

Temporal coherence and zonal propagation of synoptic scale behavior vary latitudinally and seasonally within each region. Some patterns are identifiable from this research. Both of these characteristics follow an annual cycle. For all the northern hemisphere regions, the weakest signal is found during the winter season. Over the oceans (except the SPCZ), the clearest signal occurs during summer, when westward zonal propagation prevails and

the temporal and longitudinal coherent signals are strongest. In the SPCZ, the strongest signal is seen during the wintertime, when eastward propagation is evident. Over the Sahel, the strongest signal is evident during spring, where anomalous activity occurs at a nearly constant interval of 4.75 days and propagation direction is strongly eastward. The Amazon region, on the other hand, has its strongest signal of eastward propagation during austral fall and winter.

Only two regions exhibit signals with clear and repetitive behavior: the NACZ (westward-moving) and the Sahel (eastward-moving). However, previous studies using other data sources have documented coherent behavior in some of the regions which lack clarity in the composites of the PW anomalies. The Hovmöller plots in Appendix A offer an explanation as to why this is the case. The composites for each region include events propagating both eastward and westward as well as events demonstrating little propagation. In order to reduce the confusion of these ambiguous results, it is necessary to refine the definition of eastward and westward propagating events and explore each region event by event to identify a consistent pattern.

Events exceeding +2.0 mm PW anomaly can display westward, neutral, eastward, or even both westward and eastward propagation at a particular focal point during most seasons. The composite of these events of opposing patterns yields an ambiguous footprint of climatological behavior. To understand the components present in the composites, it is necessary to identify all events that exhibit similar propagation characteristics. Five categories are listed to describe the events: coherent westward and eastward, favored westward and eastward, and neutral. A "coherent" event is defined as one that passes through a regional focal point maintaining the same propagation direction for a minimum of 30° of longitude. A "favored" event need only suggest a preferred

direction of zonal propagation (coherent for less than 30° of longitude). Other events demonstrating ambiguous or unclear patterns are defined as "neutral." Table 2 summarizes the statistics of events per season occurring at each focal point and for all seasons according to these criteria.

Most notable from Table 2 is the high percentage of neutral events at every focal point and for every season. It is possible that these events are a major source of ambiguity in the climatological Hovmöller plots. Also, in some regions during certain seasons, the number of coherent and favored westward and eastward-propagating events is roughly equal. Note that these situations tend to correspond well with the ambiguous Hovmöller plots (Figs. 14b, 15b, 15c, 18b, 18c, and 20b). Additionally, not all eastward or westward-propagating features for a particular focal point and season have the same speed of propagation. Only the NACZ and Sahel regions demonstrated a fairly event-consistent propagation speed. The result of all these factors is a weak signal for some of the Hovmöller composites. It is evident that these composites can only suggest a preferred zonal direction and propagation speed of events in most cases, since more than the climatologically suggested patterns of events actually occur within all of these focal regions and seasons.

Using the Hovmöller composites to characterize the preferred zonal direction of propagation, it appears that stronger anomalies favor westward motion within focal regions over the ocean near the equator; for those over land, the preference appears to be eastward propagation. However, a notable background eastward propagation is observed in the boreal summer and fall season composites across the Pacific Ocean (Figs. 14a, 14d, 18a, and 18d). Obvious differences exist in synoptic scale propagation between regions.

TABLE 2. Average number of events per season for each region and season for behavior classified into the five categories: coherent westward, favored westward, neutral, favored eastward, and coherent eastward. A coherent event demonstrates zonal coherence at +0.25 mm or higher in the same direction over 30° of longitude. Favored events suggest westward or eastward propagation. Neutral events show ambiguous or no clear propagation direction.

Region	Season	Coherent Westward	Favored Westward	Neutral	Favored Eastward	Coherent Eastward
ITCZ	SON	2.6	1.4	1.8	0.2	0.6
	DJF	1.7	0.4	3.0	1.0	0.6
	MAM	1.2	0.7	1.0	0.8	0.5
	JJA	2.5	0.7	2.2	0.2	0.3
SPCZ	SON	0.2	1.0	2.4	0.4	2.2
	DJF	1.0	0.6	3.0	0.4	1.9
	MAM	0.5	0.5	2.7	0.2	0.5
	JJA	0.8	0.3	3.0	0.2	2.0
NACZ	SON	3.8	1.2	2.6	0.0	0.2
	DJF	1.9	0.7	1.7	0.6	0.0
	MAM	2.2	0.5	1.2	0.5	0.7
	JJA	4.5	0.3	0.5	0.0	0.2
Sahel	SON	1.6	0.4	2.8	1.2	4.0
	DJF	0.9	0.7	3.4	1.4	2.0
	MAM	0.0	0.2	1.8	2.3	8.7
	JJA	0.5	0.7	2.2	2.8	5.8
WPWP	SON	1.0	0.4	1.2	0.6	0.4
	DJF	1.3	0.1	2.6	0.0	0.7
	MAM	0.5	0.2	1.5	0.2	0.7
	JJA	1.5	0.8	1.3	0.0	0.0
SICZ	SON	2.6	0.4	2.6	0.2	0.0
	DJF	1.6	0.4	2.1	0.3	0.3
	MAM	1.2	1.0	1.5	0.5	0.2
	JJA	1.3	0.7	1.2	0.3	0.0
Amazon	SON	0.4	0.2	4.2	1.2	2.0
	DJF	0.6	0.6	2.0	1.7	0.7
	MAM	0.7	1.2	2.8	2.5	1.5
	JJA	0.3	0.5	2.3	1.8	1.8

C. SEASONAL COMPOSITES OF STRONG PW ANOMALIES

Although Appendix A provides a detailed global view of zonal propagation, this section offers a summary of zonal propagation for stronger anomalous PW events; namely, those exceeding +2.0 mm in amplitude. The seasonal composites of preferred zonal propagation around the global tropics between 15°N and 15°S are generated using information obtained from time-longitude composites generated for every 2.5° latitude along each of the seven focal longitudes. These composites offer a view of the longitude of origin of certain types of propagation behavior for each of the four seasons.

Figure 21 contains four seasonal plots of the predominant direction of propagation of PW anomalies for the tropics between 15°N and 15°S identified by the time-longitude composites of PW anomalies exceeding +2.0 mm in amplitude. Each seasonal plot contains one half of the tropics: The top centered on the Pacific Ocean, and the bottom centered on Africa. These two parts of each plot extend through all longitudes between 15°N and 15°S. Regions dominated by eastward (westward) motion are heavily (lightly) shaded. Regions without shading indicate that no preferred zonal propagation direction can be determined from the time-longitude composites.

The SON composite of preferred direction (Fig. 21a) indicates a large region of westward propagation across the equatorial and South Pacific from near 120°W to the west Pacific warm pool as well as one extending from the west coast of North Africa into the Caribbean and northern South America. A narrow band of westward propagation extends from the Pacific south of the Hawaiian Islands to east of the Philippines. Two smaller areas of westward propagation are present in the eastern hemisphere: One at the northern edge of the plot from the Bay of Bengal to the Gulf of Aden and the other across the

SON Composite

(a)

DJF Composite

(b)
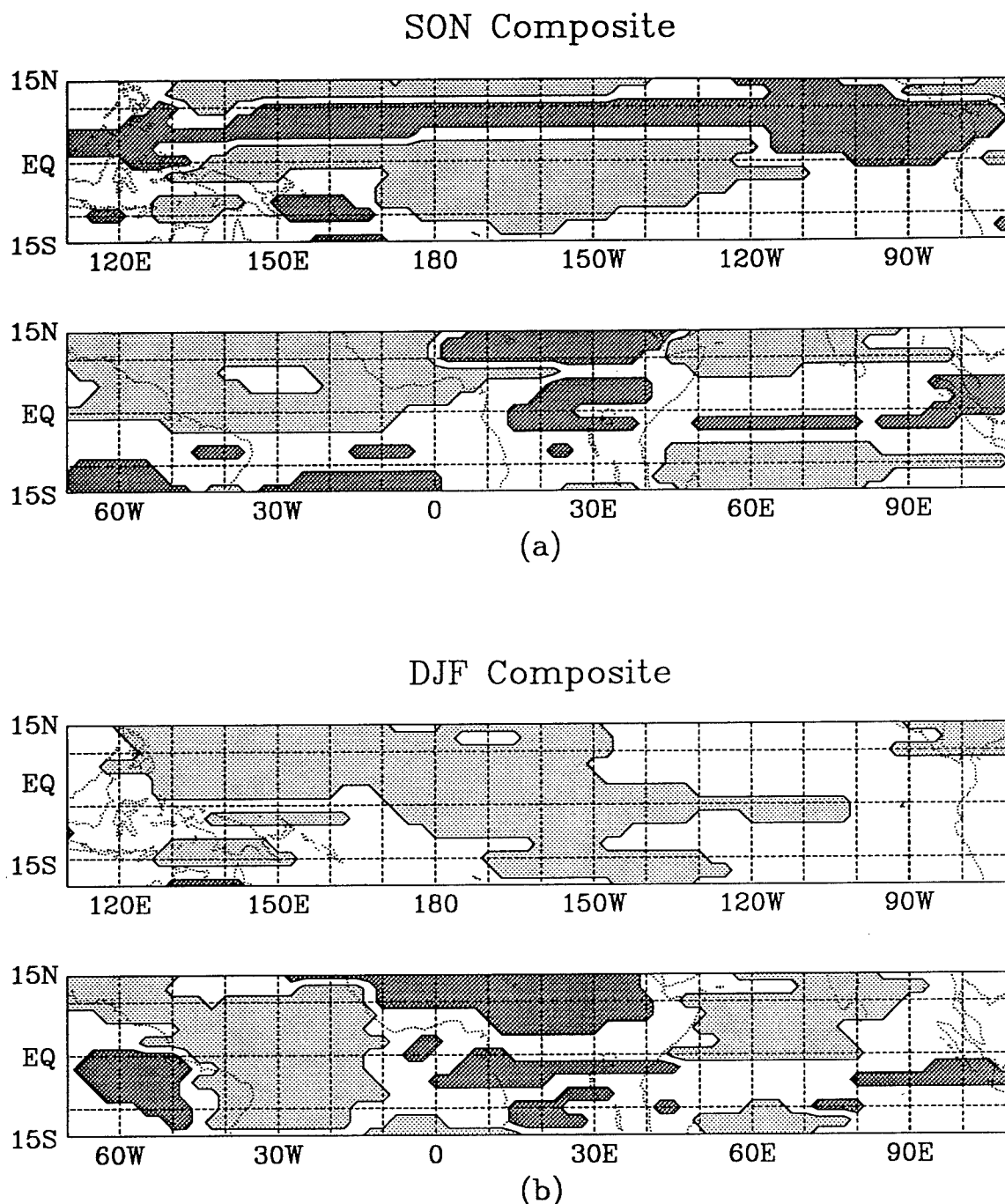
FIG. 21. Seasonal summaries of preferred direction of zonal propagation for PW anomalies exceeding +2.0 mm as suggested by Hovmöller composites. Seasonal plots are for (a) SON, (b) DJF, (c) MAM, and (d) JJA. Light (dark) shading represents regions with preferred westward (eastward) propagation. Unshaded regions have no clear preference.

MAM Composite

(c)

JJA Composite

(d)
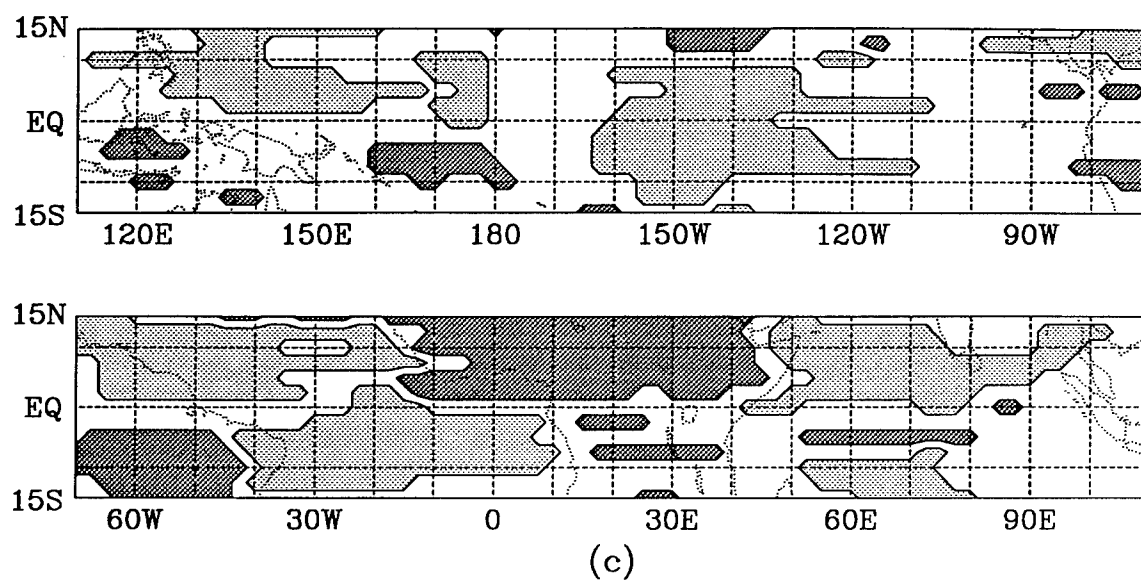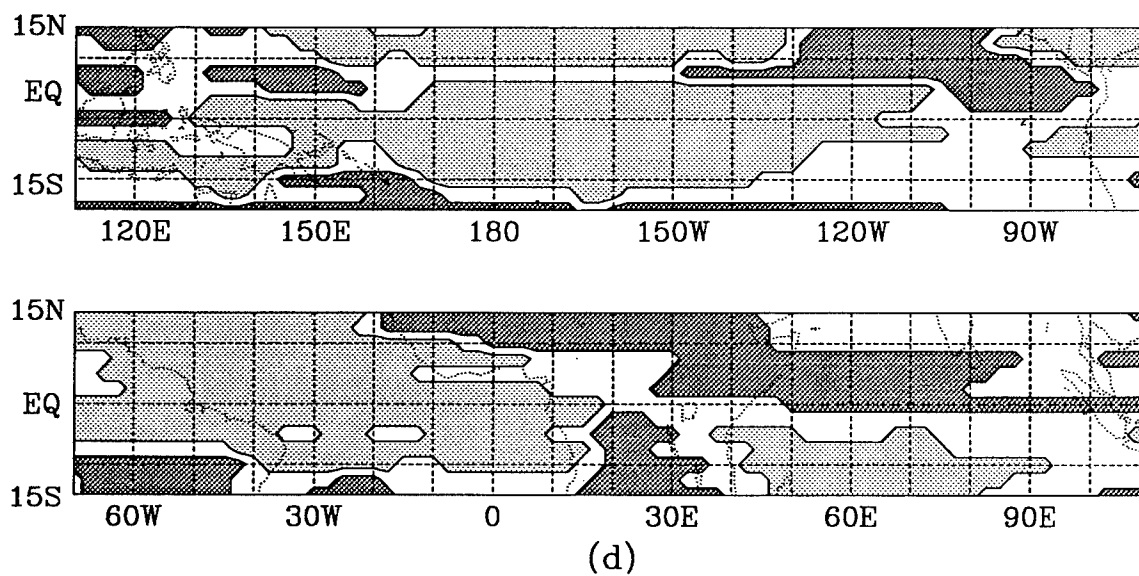
FIG. 21. Cont.

South Indian Ocean. The most conspicuous region of eastward propagation extends from near Indonesia eastward across the Pacific near 7.5°N to the west coast of northern South America. Other regions exist across equatorial and Sahel Africa, central South America, and across the South Atlantic.

Figure 21b shows a predominant region of westward motion from the Central Pacific to the warm pool region during DJF. Westward propagation covers almost the entire Atlantic Ocean region and increases in coverage over the Indian Ocean during this season. Evidence of eastward propagation across the Pacific and South Atlantic disappears, but remains over South America and across equatorial and Sahel Africa.

The MAM composite indicates that a preferred direction of zonal propagation of PW anomalies is not as evident during spring across the Pacific Ocean (Fig. 21c). Only the immediate warm pool region north of the equator and the central Pacific east of 160°W exhibit a clear tendency for westward propagation during this season. Westward motion remains evident across the North and South Atlantic and across the North Indian Ocean. Eastward motion regions remain evident across central South America and Sahel Africa.

The JJA composite (Fig. 21d) portrays westward motion across the Pacific Ocean, except for a region of eastward propagation in the east Pacific near 7.5°N between 150°W and the west coast of northern South America, and one in the west Pacific near 7.5°N between 130°E and 160°E. Westward propagation dominates the entire Atlantic region north of 10°S and across the South Indian Ocean. Evidence of eastward propagation extends near the southern boundary of the plot from 100°E to 100°W as well as in central South America, central southern Africa, and from Sahel Africa across the Indian Ocean along and just north of the equator.

For all seasons, regions of preferred westward propagation of strong anomalies persist across the equatorial and southern central Pacific Ocean and the Atlantic Ocean, while eastward propagation occurs across central South America and across Africa near 10°N. Other regions exhibit no continuously preferred zonal propagation direction.

Motion near 7.5°N across the Pacific appears to have two preferred modes: one during DJF and MAM, and the other during JJA and SON. During Boreal winter and spring, motion along this band is mainly westward. A transition to neutral and even eastward motion occurs through boreal summer and fall, when a continuous band of eastward propagation extends across the entire Pacific Ocean (Fig. 21a). Figure 22 presents the SON Hovmöller composite of +2.0 mm and greater anomalous PW events at 145.0°W for (a) 7.5°N and (b) the equator. Dominant eastward motion occurs at 7.5°N, while clear westward propagation is present along the equator. The pattern at 15.0°N is similar to that at the equator for this longitude (not shown).

Westward motion across the equatorial and North Atlantic Ocean appears to originate near the west coast of North Africa during all seasons. The longitude of origin remains near 20°W for all seasons except SON, when it shifts east to near the prime meridian. Westward propagation across the South Atlantic originates near the coast of southern Africa during MAM and JJA, but originates farther to the west at about 10°W during DJF. No evidence for westward propagation exists across this area during SON. Westward propagation across the North Indian Ocean originates in the Bay of Bengal and extends to the east coast of Africa for all seasons except JJA, when motion becomes eastward near and just north of the equator.

SON (7.5N)
(28 Events)

(a)

SON (0.0)
(18 Events)

(b)
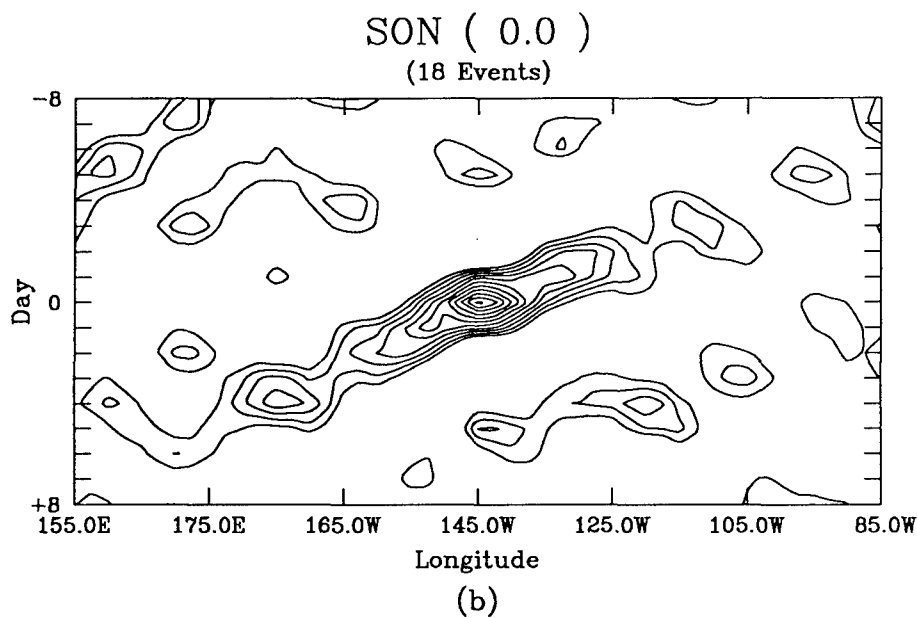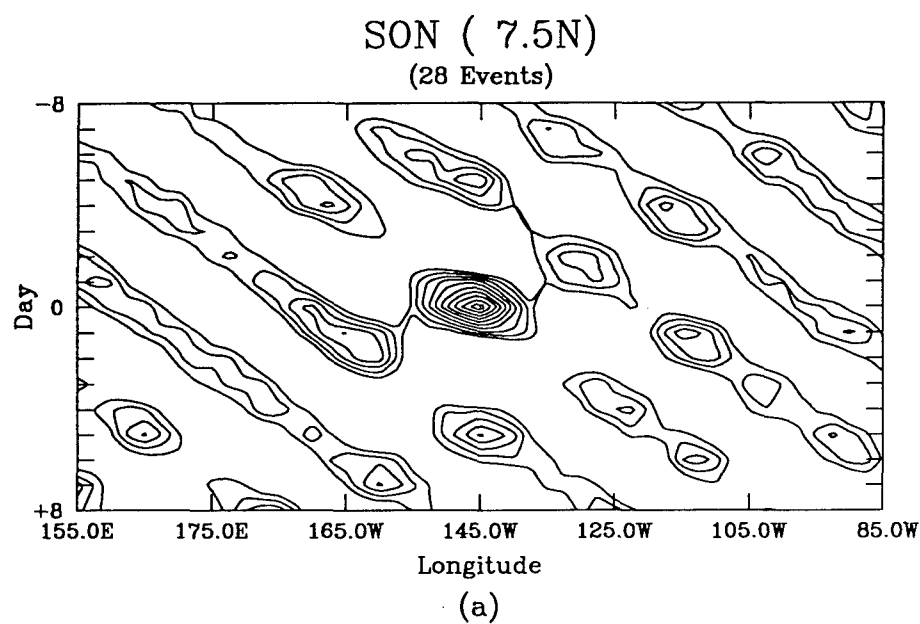
FIG. 22. Composite of synoptic scale events exceeding +2.0 mm PW anomaly in the 3 to 8 day time filtered PW dataset at 145°W for SON at (a) 7.5°N and (b) the equator. Lowest contour is +0.25 mm with an interval of 0.25 mm.

D. SPATIAL COHERENCE OF COMPOSITED ANOMALIES

Composites of anomalous events plotted through time offer some information regarding the zonal coherence of regional behavior. Such plots, spatially constrained to this dimension, do not provide understanding of the longitudinal nor the spatial extent of anomalous PW behavior. To understand the spatial coherence of such events, it is necessary to employ composites of time lag correlation for each region on a seasonal basis. The base points for all correlation are the same as the focal points assigned to each respective region and season. Appendix B contains plots of the composited lag correlations through time over the regional domain of each region during all four seasons. Each figure consists of three separate plots: the top plot contains day -1 lag correlation, the middle plot presents day 0 correlation, and the bottom plot displays day +1 lag correlation. Heavy shading represents regions where $r \geq 0.2$, while light shading indicates areas of $r \leq -0.2$. Heavy shading occurs where an area is climatologically likely to have anomalously high synoptic-scale PW values when the focal point area has high synoptic-scale PW values. Areas of light shading represent regions that are behaviorally anticorrelated to the focal point.

A discussion of spatial coherence and correlation patterns of synoptic scale fluctuations of PW is provided through the use of these figures. Teleconnective patterns are identifiable over the spatial domain of the study regions. Each region is discussed during all four seasons.

ITCZ

The SON lag correlation plot of 3 to 8 day filtered PW data for a climatological boreal fall (Fig. B1) reveals a slight westward propagation of the r $\geq$ 0.2 region through time. This region, which is about 800 km in diameter on day -1, is located slightly east of the focal point. It becomes elongated and centered west of the focal point by day +1. A meridionally oriented region of r $\leq$ -0.2 exists some 4000 km to the west on day 0, spanning near the dateline from the equator to 25°N. A hint of reversal in the direction of zonal propagation appears in Fig. B2, as the region of positive correlation around the focal point progresses eastward through time. Relatively little pattern in the correlation field is detectable during boreal winter. Little if any evidence exists supporting propagation of the coherent region around the focal point during MAM in Fig. B3. Days -1, 0, and +1 all demonstrate a bullseye pattern surrounding the focal point. The JJA lag correlation composite, however, exhibits a clear west-northwestward propagation pattern through time (Fig. B4). A region of negative correlation (r $\leq$ -0.2) exists over and surrounding the Hawaiian Islands on day -1 and day 0. Only weak teleconnective patterns are visible in the JJA and SON lag correlation plots.

SPCZ

A slight southeastward progression of positive lag correlations through time during austral spring is seen in Fig. B5. A negatively correlated region located to the west of the focal point propagates eastward through time from east of New Caledonia to near Fiji. The austral summer lag correlation composite reveals no zonal propagation, but possibly an equatorward shift of

the r ≥ 0.2 region surrounding the focal point (Fig. B6). Figure B7 only hints at a south-southeastward propagation through the focal point during DJF. The best signal of zonal propagation in this region appears during austral winter, when a clear signal of eastward motion through time is evident (Fig. B8). Almost no teleconnective patterns are retrievable from the seasonal lag correlation plots in this region.

NACZ

The region of r ≥ 0.2 surrounding the focal point has greater area in the North Atlantic as compared to Pacific Ocean focal regions. During boreal fall, the radius of the r ≥ 0.2 region extends at more than 1,000 km from its center (Fig. B9). Clear westward motion through time exists with this feature, and hints of a wavetrain are present. Persistent regions of negative correlation (r ≤ -0.2) remain approximately 2700 km to the west and 2200 km to the east of the westward-propagating r ≥ 0.2 region. The boreal winter season composite of time lag correlation in Fig. B10 shows the weakest signal for this region in both zonal propagation and teleconnective pattern; still, westward propagation of about 3 ms^{-1} is evident. The MAM composite in Fig. B11 indicates more of a northward than a westward propagation through time. A hint of wavetrain propagation is present from the regions of r ≤ 0 about 2500 km east and west of the correlation maximum. Another persistent teleconnective region of negative correlation is found on along the west coast of South America. The boreal summertime pattern reveals a dipole of a positive correlation maximum near the focal point and a negative maximum about 2700 km to the west (Fig. B12). Propagation of this field through time is westward at about 6 ms^{-1}. A second

region of negative correlation about 2200 km east of the focal point is consistent with a wavetrain propagation pattern.

Sahel

Of all the study regions, this one demonstrates the greatest spatial pattern of teleconnectivity. During boreal fall, the meridionally elongated focal point correlation maximum is sandwiched between two meridionally elongated regions of negative correlation located about 1600 km to each side (Fig. B13). This pattern extends from the west coast of North Africa to the Saudi Arabian peninsula. A secondary wavetrain pattern is found in the southern hemisphere from South America to South Africa, with alternating regions of positive and negative correlation. The pattern suggests a link between anomalously wet periods over the focal point region and South America, where an area of positive correlation exists through time. Propagation of anomalous behavior is eastward at 5 ms^{-1}. Figure B14 reveals a much weaker pattern for boreal winter than that observed during SON, but the signal of eastward propagation persists. The southern hemisphere wavetrain pattern disappears while the one across Africa remains only slightly apparent. The African wavetrain reappears strongly during MAM in the form of meridionally elongated regions of alternating positive and negative correlation, with the main track across Sahel Africa and a secondary one across the southern part of the continent (Fig. B15). Propagation direction remains eastward at about 6 ms^{-1}. The boreal summer pattern across the Sahel region (Fig. B16) remains consistent with the spring and fall patterns, with a wavetrain pattern extending from the west coast of North Africa eastward to the Saudi Arabian peninsula.

WPWP

Although the SON lag correlation fields hint at a wavetrain pattern, the signal is weak (Fig. B17). Propagation appears to be mainly meridional, with the $r \geq 0.2$ region moving southward through time. Any pattern almost disappears in DJF and MAM (Figs. B18 and B19). Propagation or teleconnective patterns are difficult to find during these seasons. However, a fairly strong signal of westward propagation exists in the JJA lag correlation composite in Fig. B20. Hints of a teleconnective pattern also appear, but are weak.

SICZ

Propagation appears fairly westward during all seasons except MAM, when little evidence of propagation is found During all seasons, the radius of the $r \geq 0.2$ region approaches 700 km on day 0 and is shorter on the other days. The SON composite reveals a region of negative correlation 1800 km west of the correlation maximum (Fig. B21). Figure B22 indicates slow westward propagation and little teleconnectivity for DJF. The austral fall plot (Fig. B23) hints only at the wavetrain pattern across Africa observed in the Sahel region plots, which is better seen in the JJA composites (Fig. B24).

Amazon

Figure B25 shows an enlarged region of positive correlation values surrounding the correlation center point on day 0 and much smaller regions of positive correlation a day before and after. This pattern continues through all

the seasons. The SON composite indicates 3 ms^{-1} east-southeastward propagation across the Amazon Basin. An eastward-propagating wavetrain is apparent in the Pacific Ocean near 10°N. In the austral summer composite, wavetrain patterns diminish, but propagation retains its eastward component and 3 ms^{-1} propagation speed (Fig. B26). The MAM and JJA composites indicate possible wavetrain propagation across the Amazon Basin, with eastward propagation at the focal point during austral fall (Fig. B27) and southeastward propagation during austral winter (Fig. B28). Also evident during these seasons is the western edge of the eastward-propagating north African wavetrain.

These data show that spatial coherence and teleconnectivity of behavior are both regionally and somewhat seasonally dependent. The pattern in the Pacific and Indian Ocean focal regions reveal little if any correlation over a large spatial domain and at best weak teleconnective patterns. Patterns of spatial coherence in these regions are generally circular with radii of about 700 km on day 0. Such results suggest that synoptic scale behavior does not have a single preferred mode of propagation; rather, both eastward and westward propagation occur through the 24 month climatology, rendering this type of plot less useful for defining synoptic activity.

On the other hand, the NACZ, Sahel, and Amazon regions demonstrate seasonally enhanced teleconnective patterns. In the NACZ region, areas of anomalously high PW associated with synoptic scale behavior appear related to other regions of anomalously low PW through both time and space on each side of the focal point during boreal summer and fall. Spatial coherence of positive correlation about the focal point at day 0 has a circular pattern with a radius of about 1000 km. In the Sahel region composites, the teleconnective

pattern extends over several wavelengths and appears in both hemispheres in the Sahel region composites during boreal fall. An apparent link between anomalously high PW on the synoptic time scale is suggested to exist during this season between the regional focal point over Sahel Africa and over South America. The correlation pattern associated with anomalous events is meridionally elongated, extending several thousand kilometers in the meridional direction and about 1500 km in the zonal. Greatest meridional elongation occurs during MAM, while the DJF plot appears more circular in nature. The Amazon region demonstrates a lesser elongation of the correlation region associated with the point of correlation, but the region remains somewhat meridionally elongated, stretching through about 20° of longitude by 10° of latitude. The JJA plot is least elongated. The pattern indicates the possible presence of a wavetrain during all seasons, especially seen in the MAM composite. For the NACZ, Sahel, and Amazon regions, synoptic behavior appears well linked in both time and space to other synoptic scale events.

A comparison between the seasonal Hovmöller and time-lag correlation composite plots for all focal points reveals that both forms of data present the same general information about synoptic scale behavior. Both estimate the same preferred zonal direction of propagation and similar propagation rates of synoptic events for specific regions and seasons. Both estimate the same zonal wavelengths for synoptic scale behavior in the NACZ and Sahel regions (which are the only regions that have a strong enough signal in either field to estimate such a parameter). Knowing this information, further research will rely upon either the seasonal Hovmöller or time-lag correlation composites to describe differences in synoptic scale behavior.

CHAPTER VI

SCALE INTERACTION BETWEEN SYNOPTIC AND LONGER TIME SCALES

The focus of the study now shifts to interaction between synoptic scale activity and behavior on longer time scales. Although it is possible that there exist links between the synoptic and almost any other longer time scales, previous studies have determined likely interaction between synoptic and both intraseasonal and interannual atmospheric variations. Following these traditional avenues, the two scale interactions chosen for this study are synoptic/intraseasonal and synoptic/interannual. Previous chapters have extracted information from this dataset about the synoptic scale. This chapter demonstrates the lack of a link between the synoptic and intraseasonal scales and suggests a connection between the synoptic and interannual scales over the Pacific and Indian Ocean regions.

A. INTRASEASONAL/SYNOPTIC SCALE INTERACTION

To extract information on the intraseasonal scale, the TOVS-generated PW dataset is time filtered to emphasize the temporal band between 30 and 60 days. The resulting data highlight behavior at the loosely defined intraseasonal time scale. Figures 23 and 24 contain filtered time series of PW for two different nine-month periods at the intraseasonal time scale (dashed line) and the synoptic time scale (solid line) for individual points representing the previously defined seven study regions. Latitudes for the focal points are determined by using an annual average of the seasonal latitudinal locations and are listed in

each of the plot descriptions. Figure 23 covers the period from June of 1983 through February 1984 and Fig. 24 contains data for May through November of 1989.

A casual look at these figures reveals neither a phase nor an amplitude relationship of intraseasonal behavior between any of the focal regions, nor any pattern between the synoptic and intraseasonal amplitudes for either time period. Yet all regions show a modest signal of oscillation in the PW field at the intraseasonal time scale. The time series plots for every region reveal at least one peak and trough exceeding 1.5 mm in amplitude, with some reaching 3 mm or greater in certain regions over the time series. Periods of more active and less active intraseasonal variations in the PW anomaly are also visible in the time series for all areas; again, these more and less active periods appear spatially unrelated.

Synoptic scale variations appear to have similar patterns of spatial and temporal relationship as those observed on the intraseasonal scale. The amplitude of the synoptic scale events is greater than the intraseasonal events, exceeding 4.0 mm in several focal regions during the time series periods. Any relationship between the amplitude of synoptic scale events during opposite intraseasonal phases cannot be determined from a casual observation of the time series plots. To determine qualitative differences in the amplitudes of synoptic scale activity during positive versus negative phases of the intraseasonal oscillation, it is necessary to compute the average regional amplitude for a synoptic scale event occurring during each intraseasonal phase. For this process, a positive (negative) intraseasonal phase is designated by periods of time when the intraseasonally filtered PW values exceed 0.5 mm (are below -0.5 mm) in value. Each synoptic scale peak amplitude occurring during the opposite and negative intraseasonal phases for
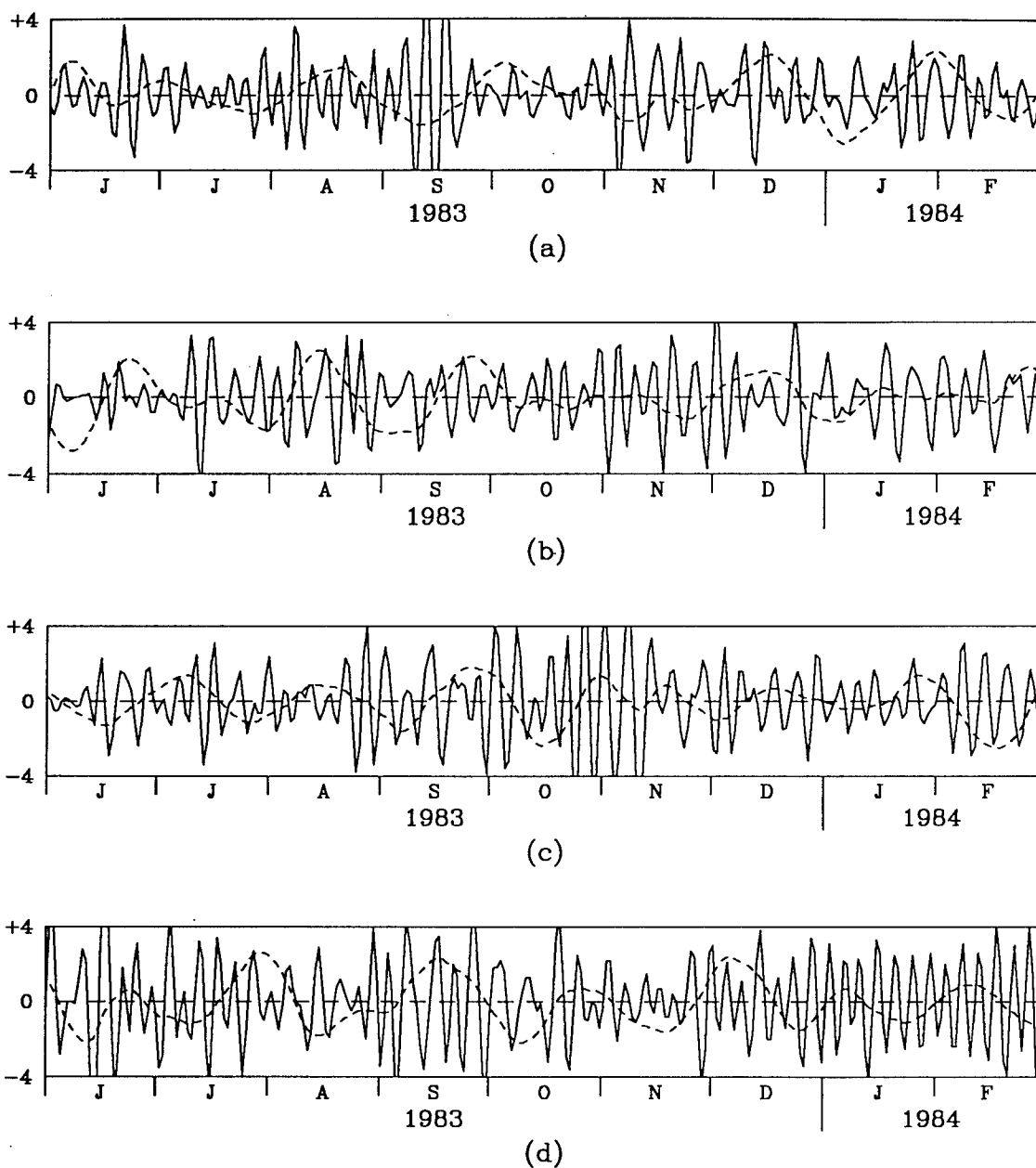
FIG. 23. Time series of synoptic (solid line) and intraseasonal (dashed line) filtered PW observations in mm from June 1983 through February 1984 for (a) 12.5°N, 145°W, (b) 15°S, 170°W, (c) 10°N, 30°W, (d) 12.5°N, 5°E, (e) 0°, 145°E, (f) 10°S, 65°E, and (g) 12.5°S, 60°W (units in mm).

(e)

(f)

(g)
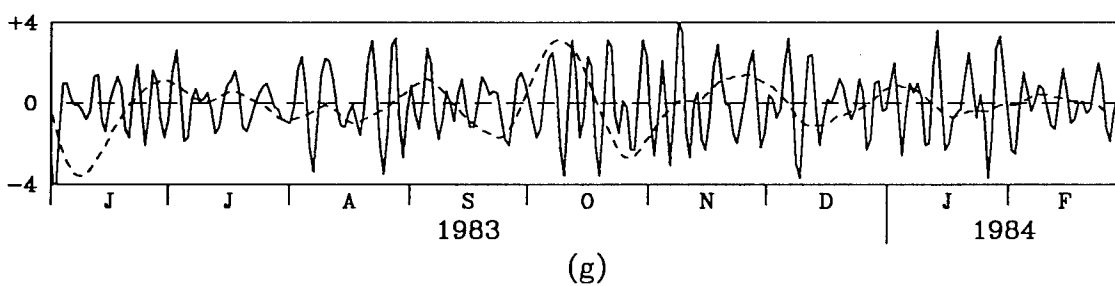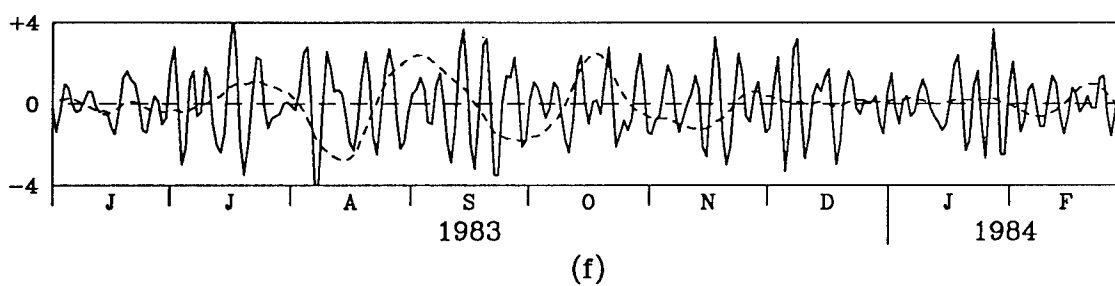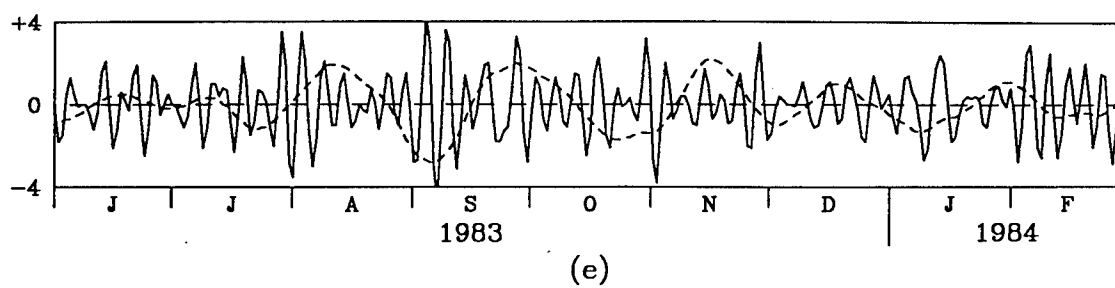
FIG. 23. Cont.
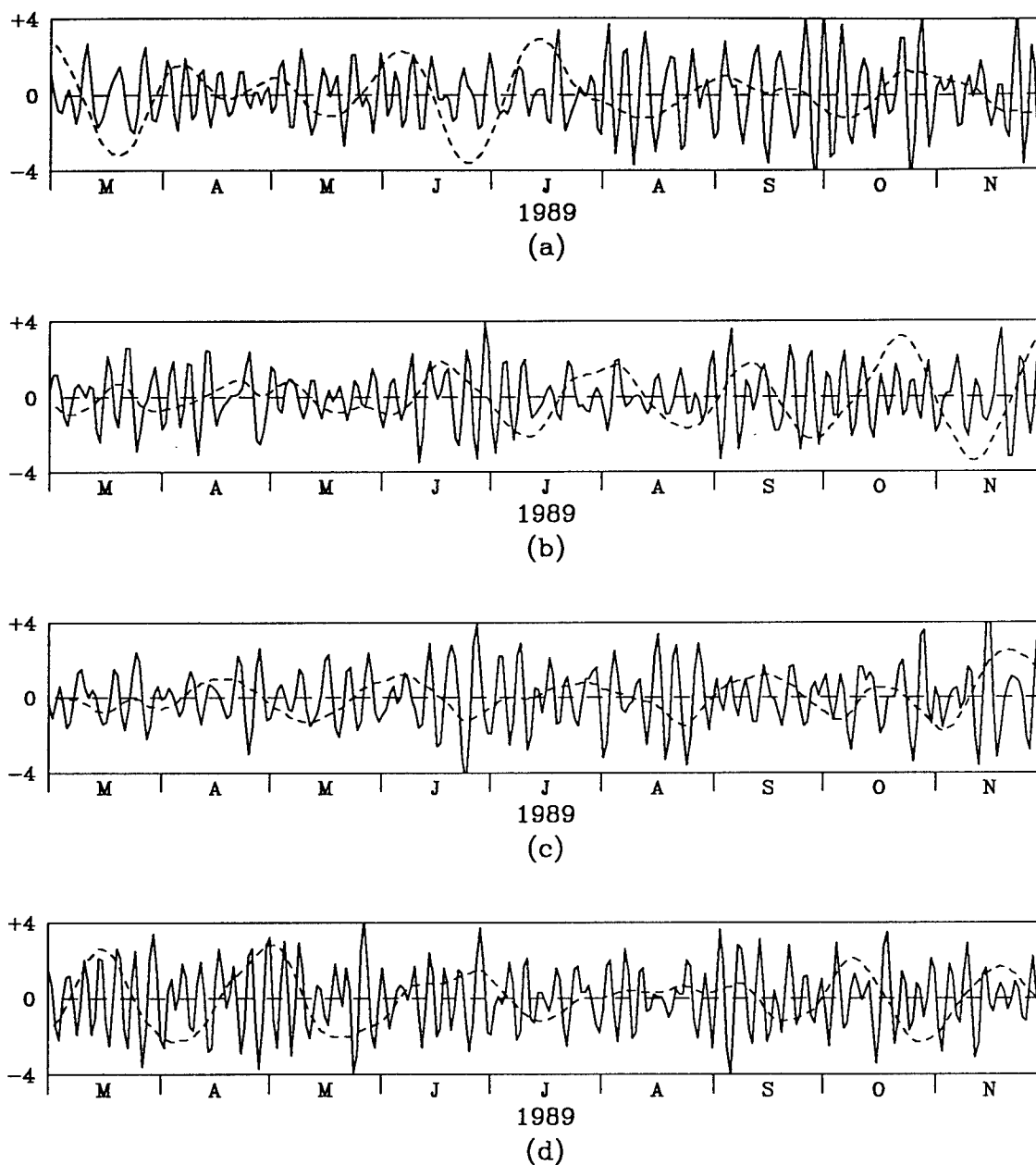
FIG. 24. As in Fig. 23, except from March through November 1989.

(e)

(f)

(g)
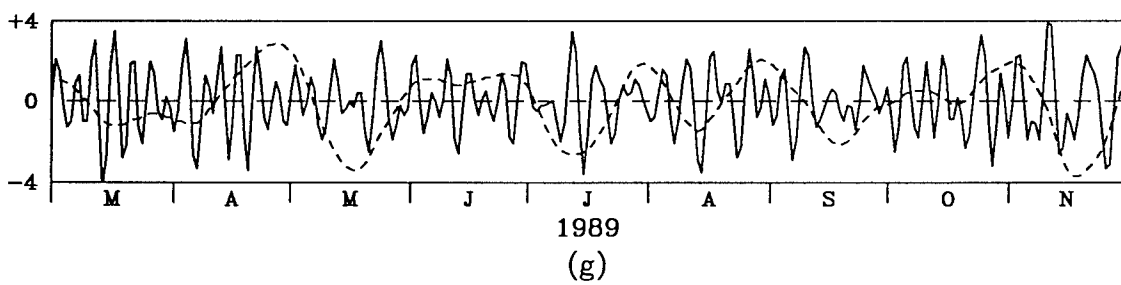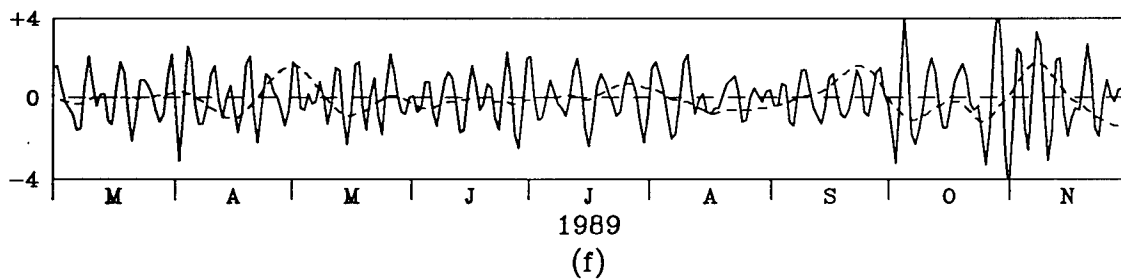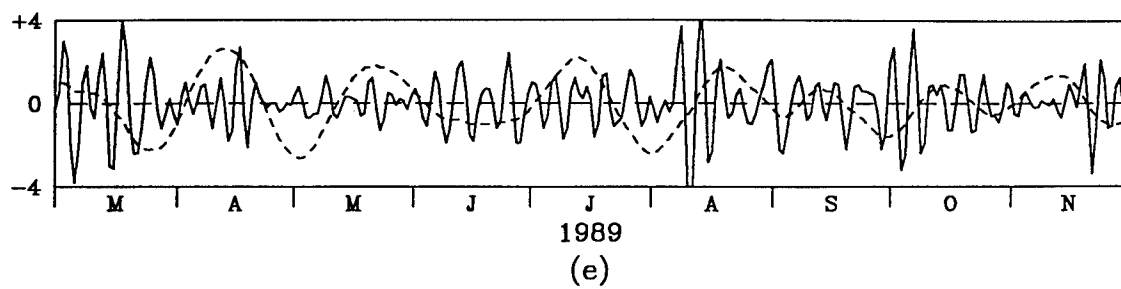
FIG. 24. Cont.

the two periods plotted in Figs. 23 and 24 is documented to calculate both a positive and negative phase average. Table 3 presents the results of this calculation, listing the average amplitude of a synoptic scale event during a positive and negative intraseasonal phase for all seven focal regions. From these results, the magnitude of synoptic scale events appears unrelated to the phase of the intraseasonal oscillation as identified by the filtered PW data. Seasonal Hovmöller composite plots of synoptic scale events exceeding +1.0 mm anomaly during opposite phases of the intraseasonal oscillation reveal similar zonal propagation patterns and characteristics during all seasons for all regions in this study. Figures 25 through 28 contain these seasonal Hovmöller composites for the west Pacific warm pool region (an area noted by some studies for synoptic/intraseasonal scale interactions). These plots are similar to those contained in Figs. 14 through 20, except that each mean Hovmöller plot contains anomalies exceeding +1.0 mm instead of +2.0 mm PW anomaly. The figures contain two plots: the top shows the plot for synoptic events occurring during the positive phase of the 30 to 60 day filtered PW data ($\geq$ +0.5 mm) and the bottom is for events during the negative phase ($\leq$ -0.5 mm). Only the JJA plot reveals any noticeable difference between the synoptic behavior occurring during positive and negative intraseasonal signal of the PW data (Fig. 28). During the negative phase of this season, stronger synoptic scale events appear better behaved and more spatially coherent than those during the positive intraseasonal phase. The overall pattern of propagation remains similar between the two categories of events. However, in none of the other regions during any season is there found any more obvious a difference in the behavior of synoptic scale events occurring during the negative and positive intraseasonal phases.

TABLE 3. Average amplitude in mm of a 3 to 8 day filtered temporal PW peak value during both positive and negative periods of the 30 to 60 day filtered PW data (exceeding +0.5 mm and less than -0.5 mm) for all regions and seasons.

Region	Location	Positive (+0.5 mm)	Negative (-0.5 mm)
ITCZ	(12.5°N, 145.0°W)	1.69 mm	1.86 mm
SPCZ	(15.0°S, 170.0°W)	1.80 mm	1.72 mm
NACZ	(10.0°N, 30.0°W)	1.66 mm	1.97 mm
Sahel	(12.5°N, 5.0°E)	2.49 mm	2.31 mm
WPWP	(0.0, 145.0°E)	1.51 mm	1.59 mm
SICZ	(10.0°S, 65.0°E)	1.62 mm	1.58 mm
Amazon	(12.5°S, 60.0°W)	2.00 mm	1.97 mm

All results of this part of the study suggest an inconclusive relationship between the behavior of synoptic scale events occurring during opposite phases of the signal of intraseasonal variation in the synoptically and intraseasonally filtered PW datasets. The differences in the behavior of synoptic scale events occurring during these opposite behaviors appear nominal. Both the amplitudes and zonal propagation characteristics of synoptic anomalies reveal nothing noteworthy about possible scale interaction between these two time scales. No conclusive evidence of differences in the behavior of synoptic scale anomalies occurring during opposite intraseasonal phases is found in any of the regions or seasons. Whatever interaction between these two time scales does exist is not found by this comparison.

SON (2.5N)

Positive Phase (5 Events)

(a)

Negative Phase (11 Events)
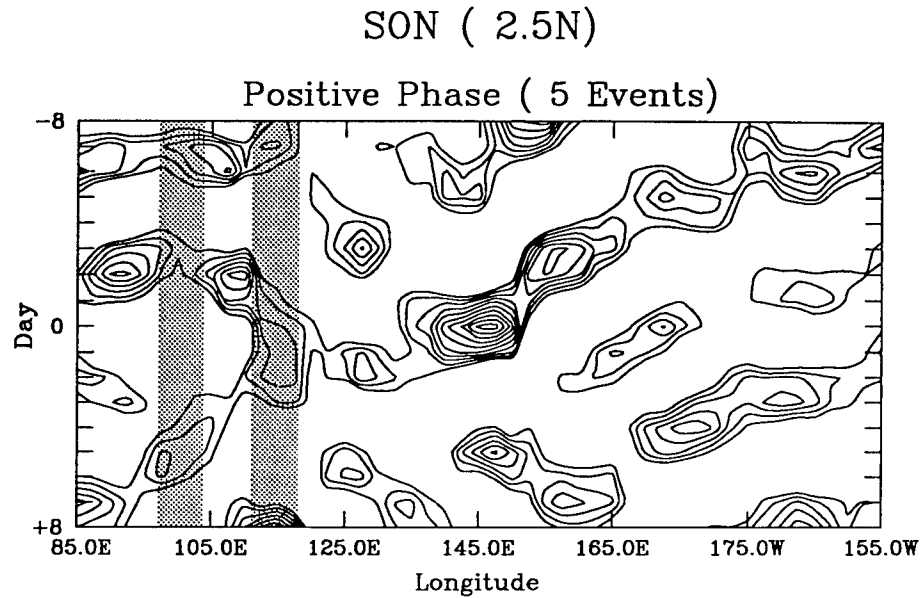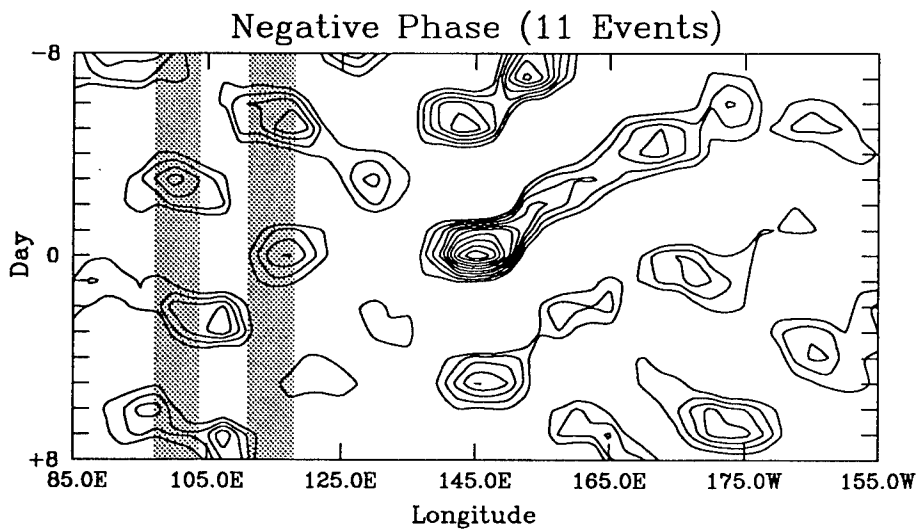
(b)

FIG. 25. Seasonal Hovmöller composite of all synoptic scale PW anomalies exceeding +1.0 mm at 2.5°N, 145°E for 5 SON seasons during (a) positive and (b) negative intraseasonal phases as determined by the 30 to 60 day filtered PW data. A positive (negative) phase is defined as a period of time over which the intraseasonal PW exceeded (were less than) the average period value by at least +0.5 mm (-0.5 mm).
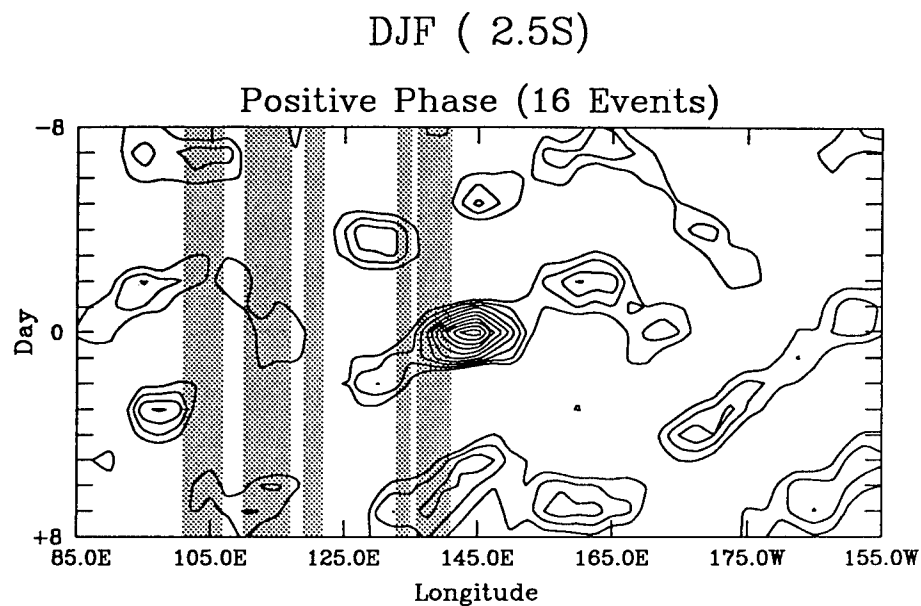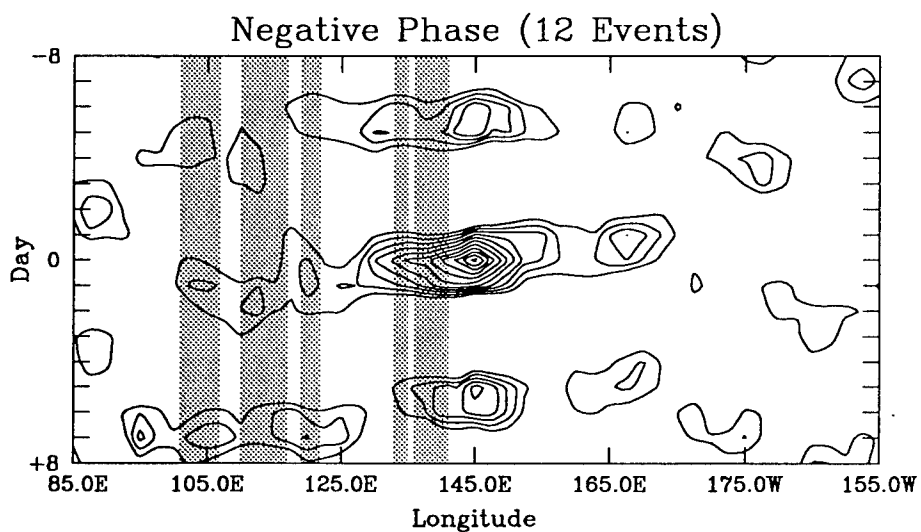
FIG. 26. As in Fig. 25, except at 2.5°S, 145°E for 7 DJF seasons.

MAM (2.5S)

Positive Phase (8 Events)

(a)

Negative Phase (10 Events)

(b)
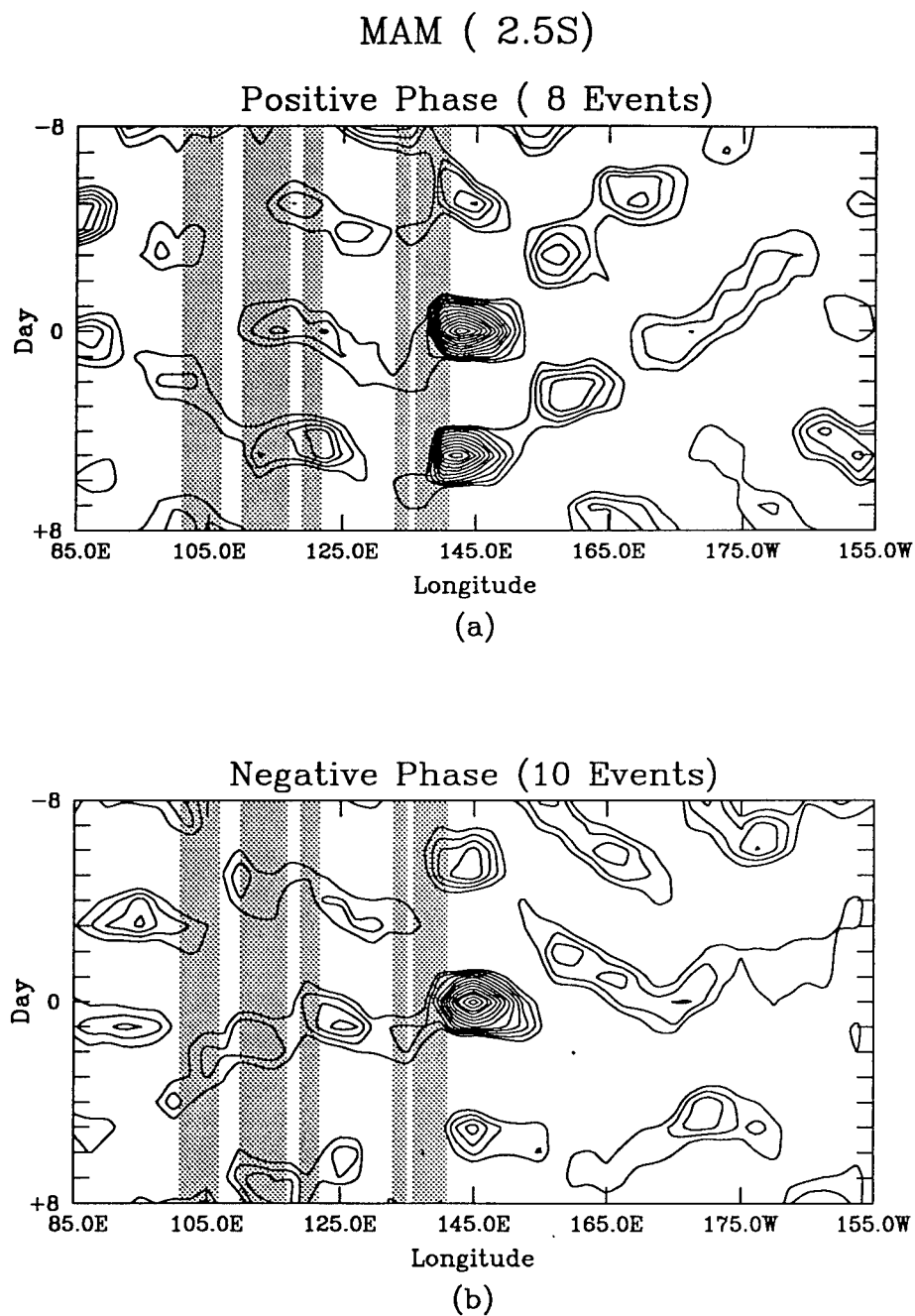
FIG. 27. As in Fig. 26, except for 6 MAM seasons.

JJA (2.5N)

Positive Phase (10 Events)

(a)

Negative Phase (12 Events)

(b)
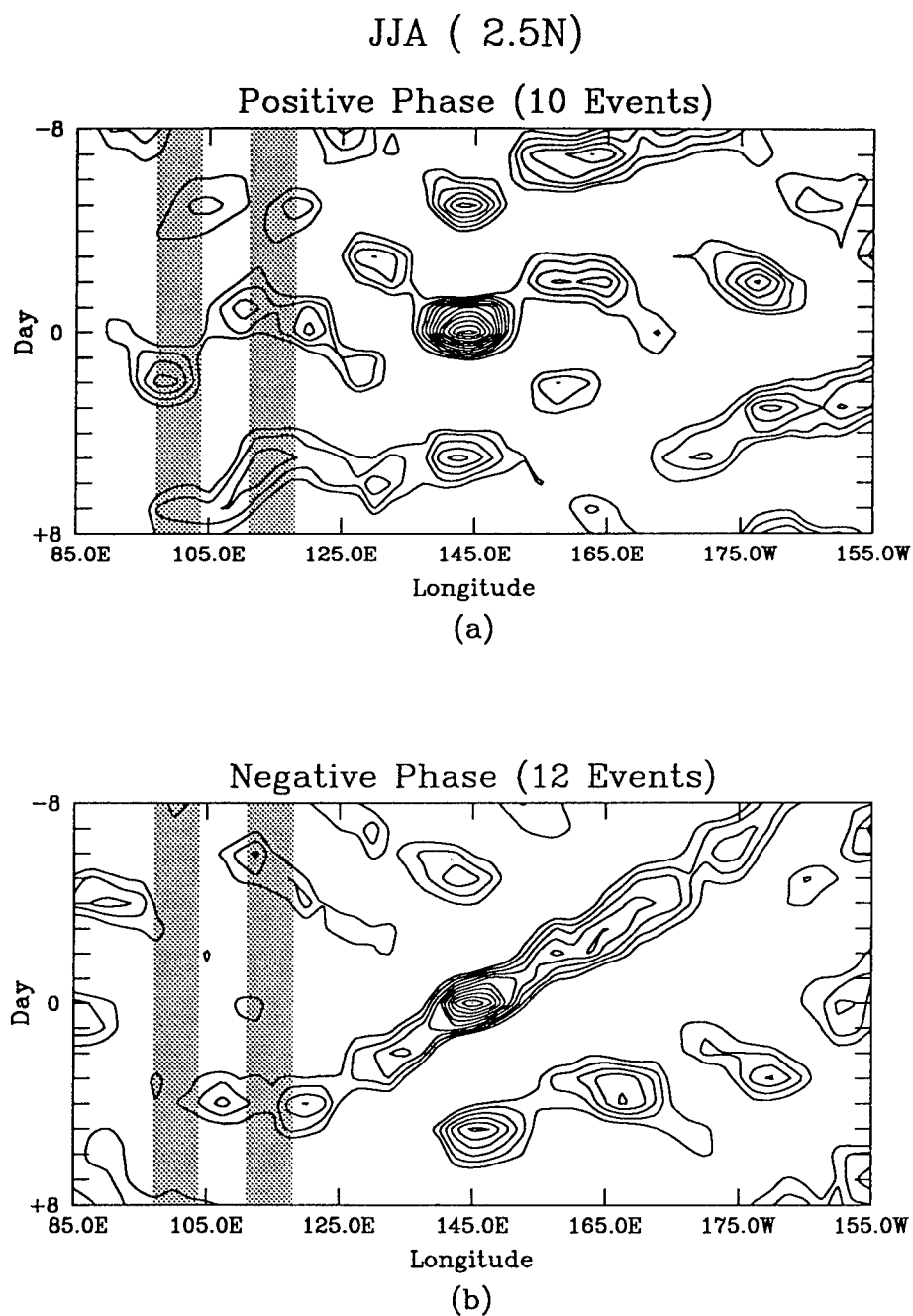
FIG. 28. As in Fig. 25, except for 6 JJA seasons.

B. INTERANNUAL/SYNOPTIC SCALE INTERACTION

Information about interannual behavior cannot be extracted through the filtering of the PW dataset; instead, warm and cold phases of interannual variation (ENSO) must be identified by independent data sources. The variable used for this identification is the area-averaged sea surface temperature anomaly in the El Niño 1 and 2 regions as indicated the Climate Diagnostics Bulletin (1995). These two regions cover the ocean area between 90°W and the west coast of South America from the equator to 10°S. For this scale interaction comparison, a warm (cold) ENSO phase is defined to be a period of at least six consecutive months with SSTs at least 0.5 degrees C above (below) the climatological average. By these criteria, warm phases occurred between the summers of 1982 and 1983 and from the end of 1986 through the fall of 1987, while cold phases existed from the end of 1984 through the fall of 1985 and between the beginning and end of 1988. To obtain useful information about synoptic scale events during opposite ENSO phases, it is necessary to conduct seasonal comparisons of warm and cold phase behavior. Lack of continuous or complete data limits comparison seasons to MAM 1983 and SON 1987 for warm phase periods and MAM and SON 1988 for cold phase periods.

Seasonal lag correlation plots of warm and cold phase events reveal noticeable differences in zonal propagation behavior in some regions. Appendix C (Figs. C1 through C28) contains lag correlation plots for warm phase (MAM 1983 and SON 1987) and cold phase (MAM 1988 and SON 1988) periods of ENSO (similar to Appendix B). Each figure contains correlation data lagged through time with the focal point on day zero. Darker (lighter) shading indicates areas where $r \geq 0.2$ ($r \leq -0.2$).

A comparison between warm and cold phase events during similar seasons reveals a clear difference in the propagation direction and pattern of synoptic scale activity for most of the regions. In fact, the propagation characteristics of synoptic scale activity appear to change dramatically during these two opposite phases of ENSO. Table 4 lists the propagation directions and speeds of synoptic scale behavior during warm and cold ENSO phases as indicated by the composite time-lag correlation plots in Appendix C. The zonal direction of propagation changes between warm and cold phases in the ITCZ, SPCZ, and SICZ regions during their respective spring season (Figs. C1 and C2, C5 and C6, and C23 and C24) and in the WPWP region during both the spring and fall comparisons (Figs. C17 through C20). Additionally, noticeable changes in propagation behavior occur in the ITCZ, SPCZ, and SICZ regions during their respective fall seasons (Figs. C3 and C4, C7 and C8, and C21 and C22). The NACZ, Sahel, and Amazon regions maintain similar propagation patterns with only minor variations in speed and direction, regardless of the ENSO phase (Figs. C9 through C12, C13 through C16, and C25 through C28).

Although a comparison between only two separate seasons consisting of a warm and cold ENSO phase does not constitute a climatology, the differences in the synoptic propagation characteristics between the opposite phases of the interannual variation are too large to be ignored. The regions having clearly different synoptic scale behavior during these two time periods are located over the Indian and Pacific Ocean regions, with the greatest differences observed over the west Pacific warm pool. The PW data thus identify a relationship between the synoptic and interannual time scales.

TABLE 4. Propagation direction and speed in ms⁻¹ of synoptic scale PW anomalies +1.0 mm or greater in amplitude during warm and cold interannual phases as determined by seasonal lag correlation composites for all regions and seasons. Question marks indicate ambiguous or unclear propagation patterns.

Region	Season	WARM PHASE		COLD PHASE	
		Direction	Speed	Direction	Speed
ITCZ	MAM	SW	11 ms⁻¹	E	3 ms⁻¹
	SON	SE	10 ms⁻¹	???	???
SPCZ	MAM	W	3 ms⁻¹	E	3 ms⁻¹
	SON		0 ms⁻¹	SE	6 ms⁻¹
NACZ	MAM	N	3 ms⁻¹	???	???
	SON	W	3 ms⁻¹	WSW	9 ms⁻¹
Sahel	MAM	ESE	6 ms⁻¹	E	7 ms⁻¹
	SON	ENE	7 ms⁻¹	E	6 ms⁻¹
WPWP	MAM	W	10 ms⁻¹	ESE	6 ms⁻¹
	SON	SE	6 ms⁻¹	WSW	5 ms⁻¹
SICZ	MAM		0 ms⁻¹	SE	8 ms⁻¹
	SON	ENE	4 ms⁻¹	W	4 ms⁻¹
Amazon	MAM	E	1 ms⁻¹	E	6 ms⁻¹
	SON	E	4 ms⁻¹	SE	4 ms⁻¹

It is important to note that the method used for studying scale interactions in this research has some important limitations. First and most critical, the time scales for the study were defined as having set bounds of periodicity. For example, the "synoptic" scale is defined as behavior demonstrating three to eight day periodicity, while "intraseasonal" variations are set by 30 to 60 day periodicity bounds. Such values for defining these scales were determined by considering periods that have greater power in the power spectrum and interesting behavior as documented by previous studies. However, scale interaction in the atmosphere does not limit itself to set windows

of time spectra. For a detailed investigation of this research topic, a better method to use is wavelet analysis, as was performed by Schroeder and McGuirk (1996). This analysis method allows a view of interaction between two or more behavioral time scales and the behavior associated with them. Figure 29 is a plot of positive and negative PW anomalies through time and by periodicity. Note how relative extrema in the anomaly magnitude tend to prefer certain time scales; however, there is not a dominant time scale. Instead, peak PW magnitudes vary around a central preferred time scale value. For this location and time period, coherent variations occur at about 45 days (ISO), 22 days, 10-12 days, and 5-7 days. Such a plot is able to show why the concepts of "synoptic" and "intraseasonal" scale must consider a certain time window of phenomena. Additionally, the plot can show links in behavior on different time scales. Periods of unusually active or inactive anomalous activity at one time scale can easily be compared to that at another preferred time scale to identify possible scale interactions at various geographical locations. As a final point, it is noteworthy that, at this point in space, it is common for a wide range of scales to achieve a positive or negative extremum simultaneously.
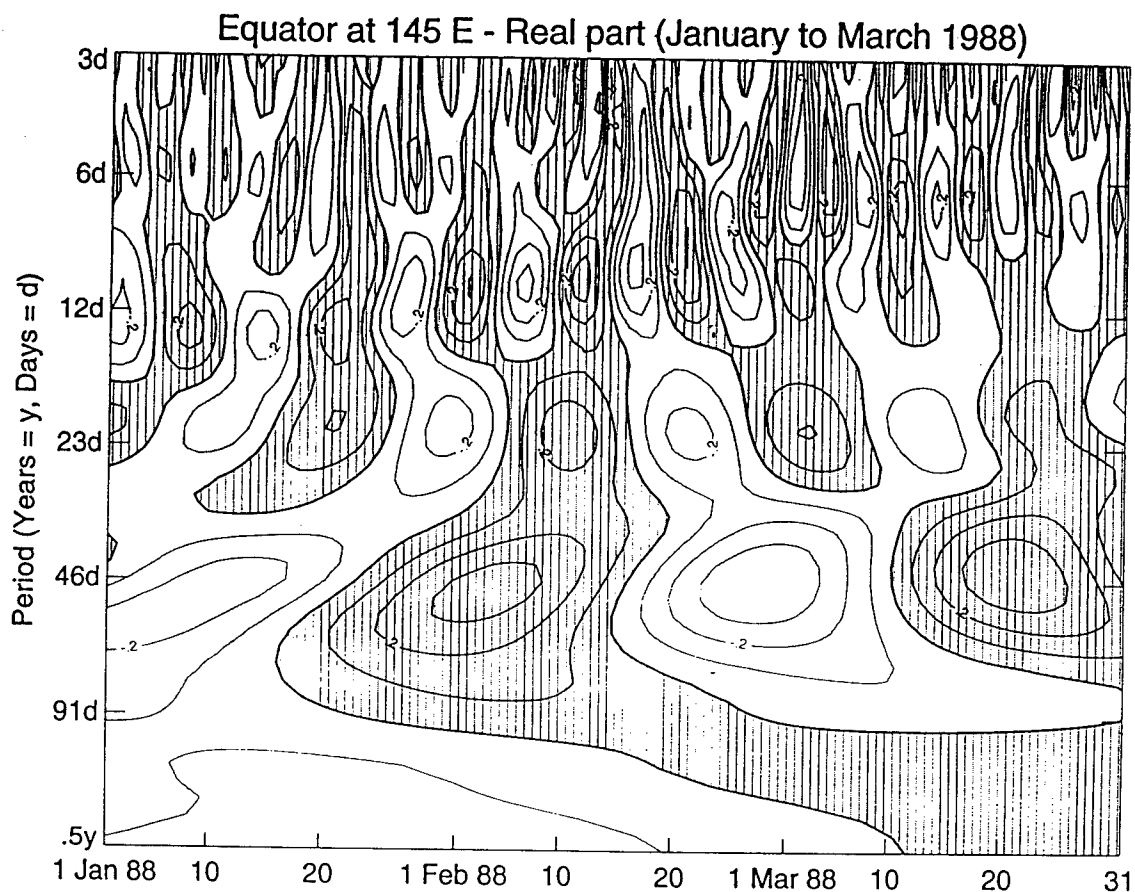
FIG. 29. Real part of wavelet components of daily PW values at 0°, 145°E from January through March 1988. Contour values along a horizontal line depict the instantaneous amplitudes with a constant period. Events with periodicities ranging from 3 to 182 days are represented in both positive (shaded) and negative (unshaded) phases.

CHAPTER VII

A COMPARISON BETWEEN PW AND OLR

Some of the results in this research provide information not obtained from studies that have relied on OLR data. Clearly the PW and OLR signals do not identify the same atmospheric characteristics. A brief comparison of these two types of data provides a better understanding as to why differences in results exist.

An OLR dataset of 2.5° by 2.5° daily gridded brightness temperature values from November 1988 through May 1990 is used for the comparison. This dataset contains only one day of missing data, which is filled in by using interpolated values from one day before and after the missing day. The dataset is then time filtered at the synoptic time scale using three and eight days as the filter bounds. After excluding the first and last few months of the filtered OLR data, an entire year of daily values exists for comparison with the filtered synoptic-scale PW data.

Appendix D contains 14 figures, each consisting of two seasonal Hovmöller comparisons of coherent synoptic scale behavior between PW anomalies and negative OLR anomalies (figures D1 through D14). Plots are prepared for each 10° latitude between 30°N and 30°S. Positive PW anomalies are contoured at an interval of 1.0 mm, starting from the lowest contour at +0.5 mm. Negative OLR anomalies are contoured at an interval of 10 Wm^{-2} with the first contour set at -5 Wm^{-2}.

Both PW and OLR identify coherent events and zonal propagation. Zonal propagation of anomalous events at 30°N and 30°S (Figs. D1, D2, D13, and D14) appears to be represented in a similar manner by both forms of data.

Each indicates a general eastward motion of events, although the OLR anomalies are less spatially coherent. A major difference with the OLR plots is the seasonally occurring signal of large regions lacking anomalous events, especially in the JJA plot at 30°N (Fig. D2). Although the anomalous PW signal remains coherent across the entire globe at this latitude for JJA, the OLR plot shows large areas almost void of anomalously low OLR values across the entire Pacific and Atlantic Oceans, and across Africa.

The 20°N and 20°S plot comparisons reveal that the OLR and PW plots indicate opposite directions and different speeds of zonal propagation across certain longitudes (Figs. D3, D4, D11, and D12). Again, the OLR plots contain large regions void of anomalously low OLR values, while the PW plots maintain spatial coherence through all longitudes. OLR plots at 10°N and 10°S reveal substantially greater anomaly magnitudes over most longitudes as compared to more poleward latitudes (Figs. D5, D6, D9, and D10). These plots indicate that the lowest anomalies and best spatial coherence occur during their respective summer and fall seasons. The PW Hovmöller plots show no major difference in the amplitude of anomalous behavior as compared to other latitudes, and coherence remains through all longitudes. At the equator, the patterns of coherence of anomalous events between PW and OLR data seem unrelated in the direction of zonal propagation of anomalous events (Figs. D7 and D8). The OLR plot is almost void of coherent behavior across the central and eastern Pacific during all seasons and across the Atlantic Ocean during JJA and SON. The magnitude of OLR anomalies remains higher than those at 20° and 30°, but is lower than those found at 10°.

The PW data has a clear advantage over the OLR data in terms of spatial coherence. It is true that the OLR data can identify synoptic scale activity as long as it is associated with convection; but once the associated convection

ceases, OLR loses track of the features. If convective activity is not associated with synoptic scale phenomena, the OLR data cannot identify them; hence the large longitudinal regions void of any coherent signal in the seasonal Hovmöller plots of synoptic scale OLR anomalies. The PW data, on the other hand, identify and track coherent anomalous synoptic scale behavior across the entire globe during all seasons, whether or not associated with convection. This advantage allows the PW data to find and study synoptic scale events perhaps never before identified or documented by previous studies.

A correlation between synoptically filtered PW and OLR data offers a more qualitative view concerning the relationship of results obtained from these two independent sources. Figures 30 through 33 display the spatial pattern of the seasonally averaged correlation coefficient between PW and OLR data for each of the four seasons from MAM 1989 to DJF 1989/1990 for the entire grid region from 30°N to 30°S. Each figure is divided into two plots: the top centered on the Pacific Ocean from longitudes 110°E to 70°W, and the bottom centered on the African continent including longitudes from 70°W to 110°E. Darker (lighter) shading corresponds to areas having positive (negative) seasonally averaged correlation coefficients between synoptically filtered PW and OLR data. Seasonal grid average correlation coefficients range from between -0.135 during DJF to -0.195 for JJA. From this pattern, a weak but distinct relationship between positive PW anomalies and negative OLR anomalies is present over the majority of the grid domain. Noteworthy is a region of positive correlation located over the Pacific warm pool, Amazon, equatorial Africa, and oceanic convergence zone regions for all seasons. Such a signal may indicate a problem with the interpolation algorithms for obtaining PW data in regions that frequently experience convective activity, or a bias in either variable with respect to the signals they

Correlation Coefficient of PW with OLR Data
DJF 1989/1990
Grid Average r = −.135
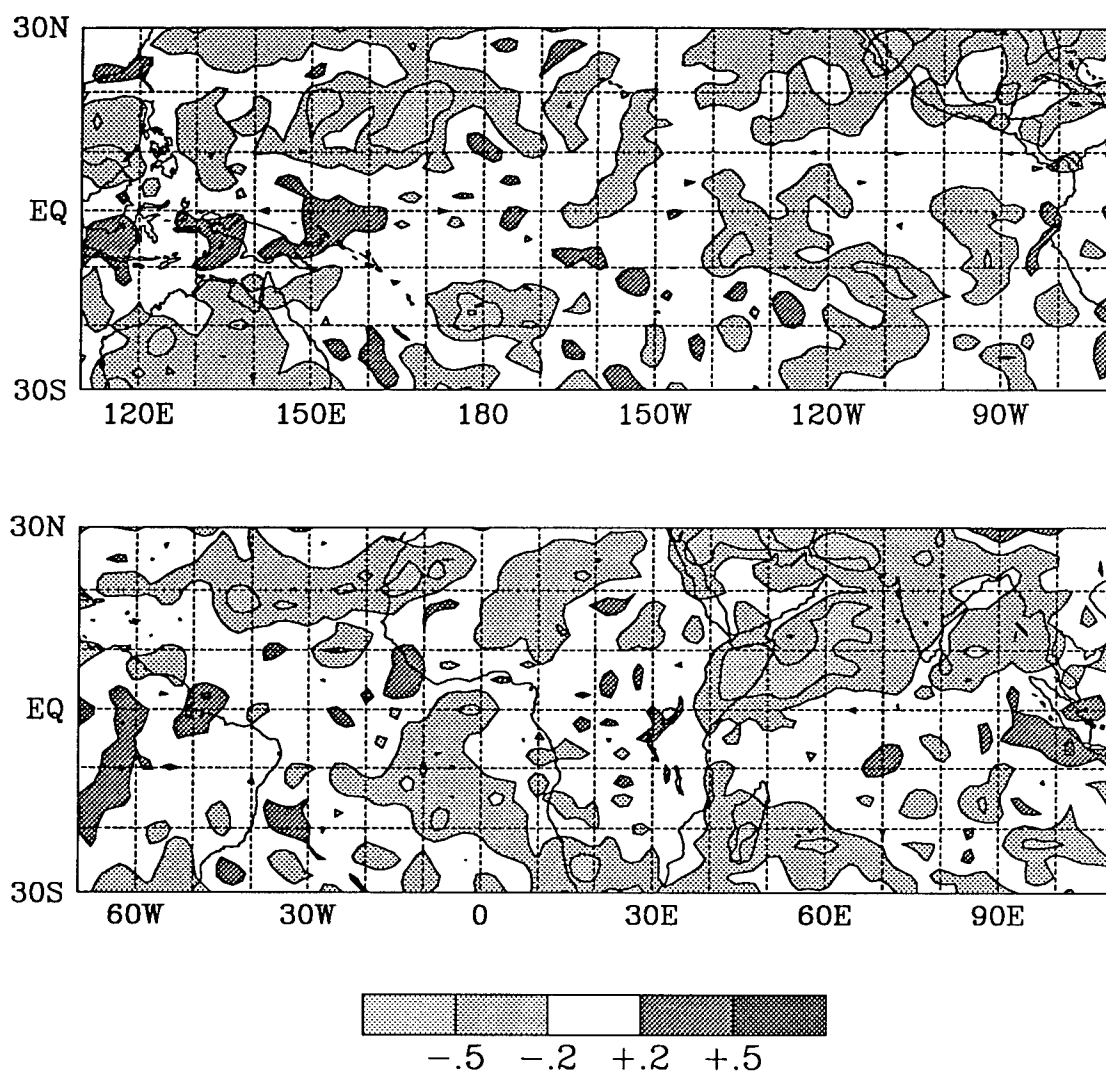
FIG. 30. Seasonally averaged correlation coefficient between synoptically filtered PW and OLR data for SON 1989. Lighter (darker) shading indicates regions of negative (positive) correlation. Contour interval is as according to bar graph.

Correlation Coefficient of PW with OLR Data
MAM 1989
Grid Average r = −.153

−.5 −.2 +.2 +.5
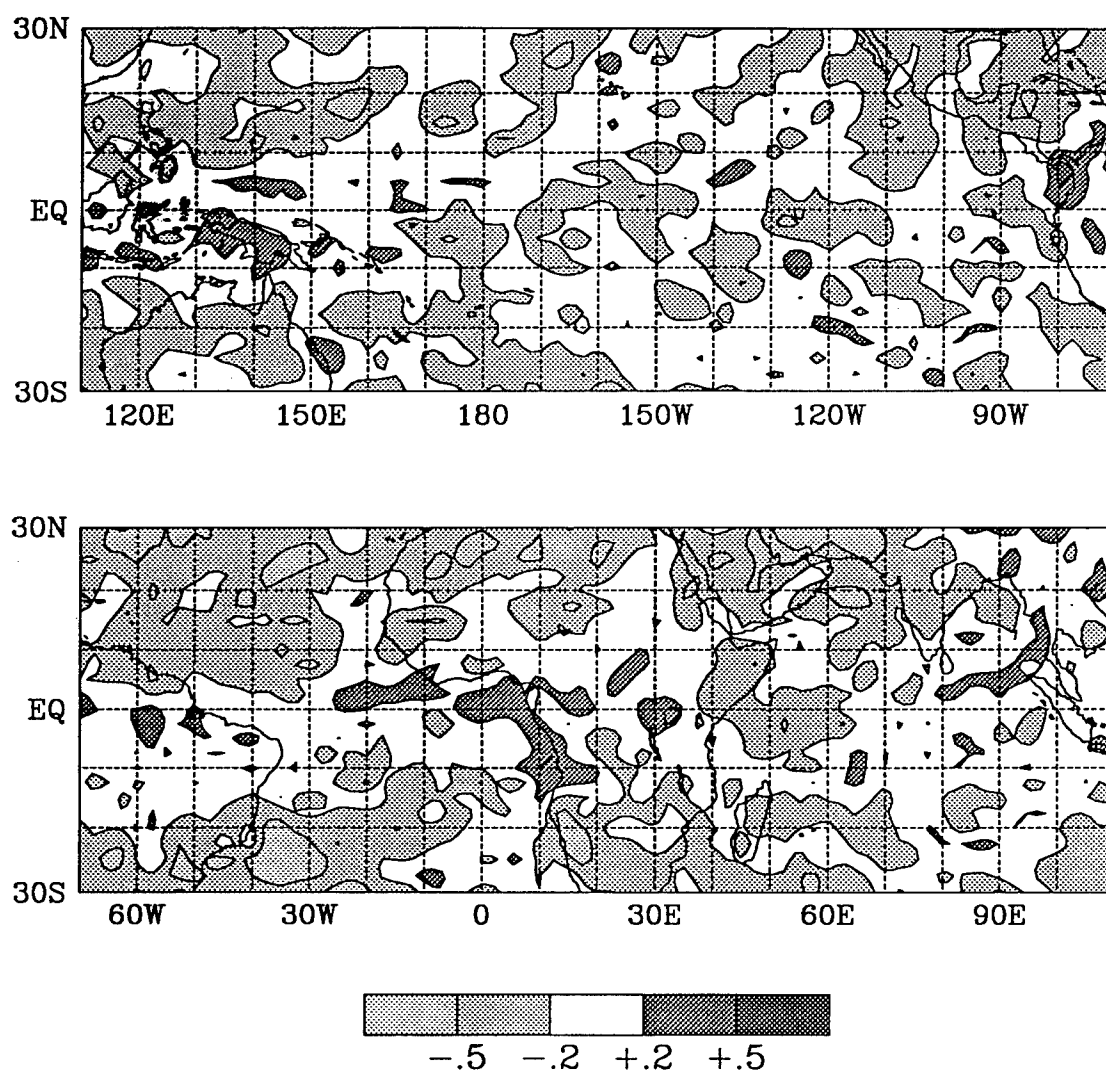
FIG. 31. As in Fig 30, except for DJF 1989/1990.

Correlation Coefficient of PW with OLR Data
JJA 1989
Grid Average r = −.195
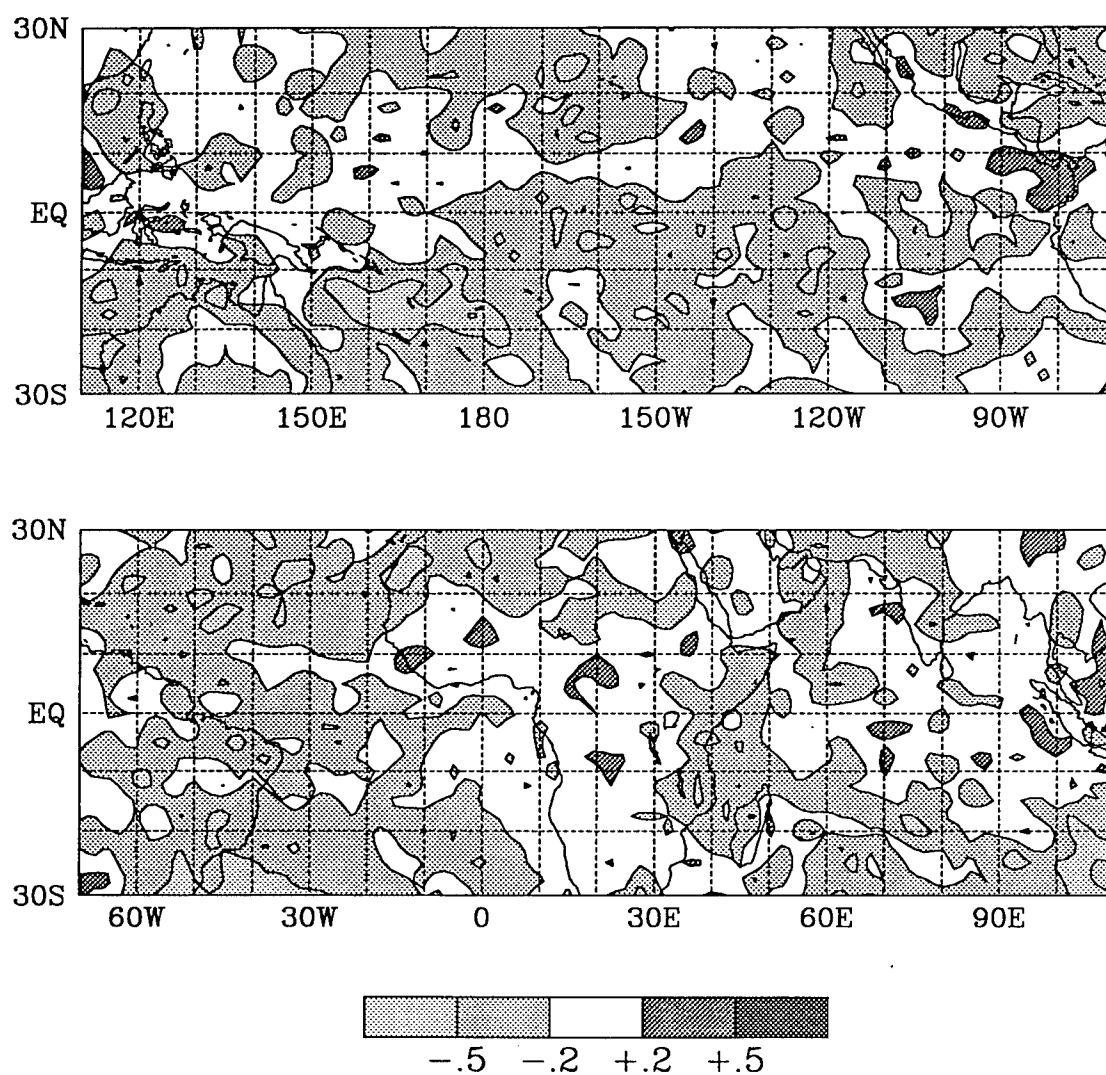
FIG. 32. As in Fig. 30, except for MAM 1989.

Correlation Coefficient of PW with OLR Data
SON 1989
Grid Average r = −.190
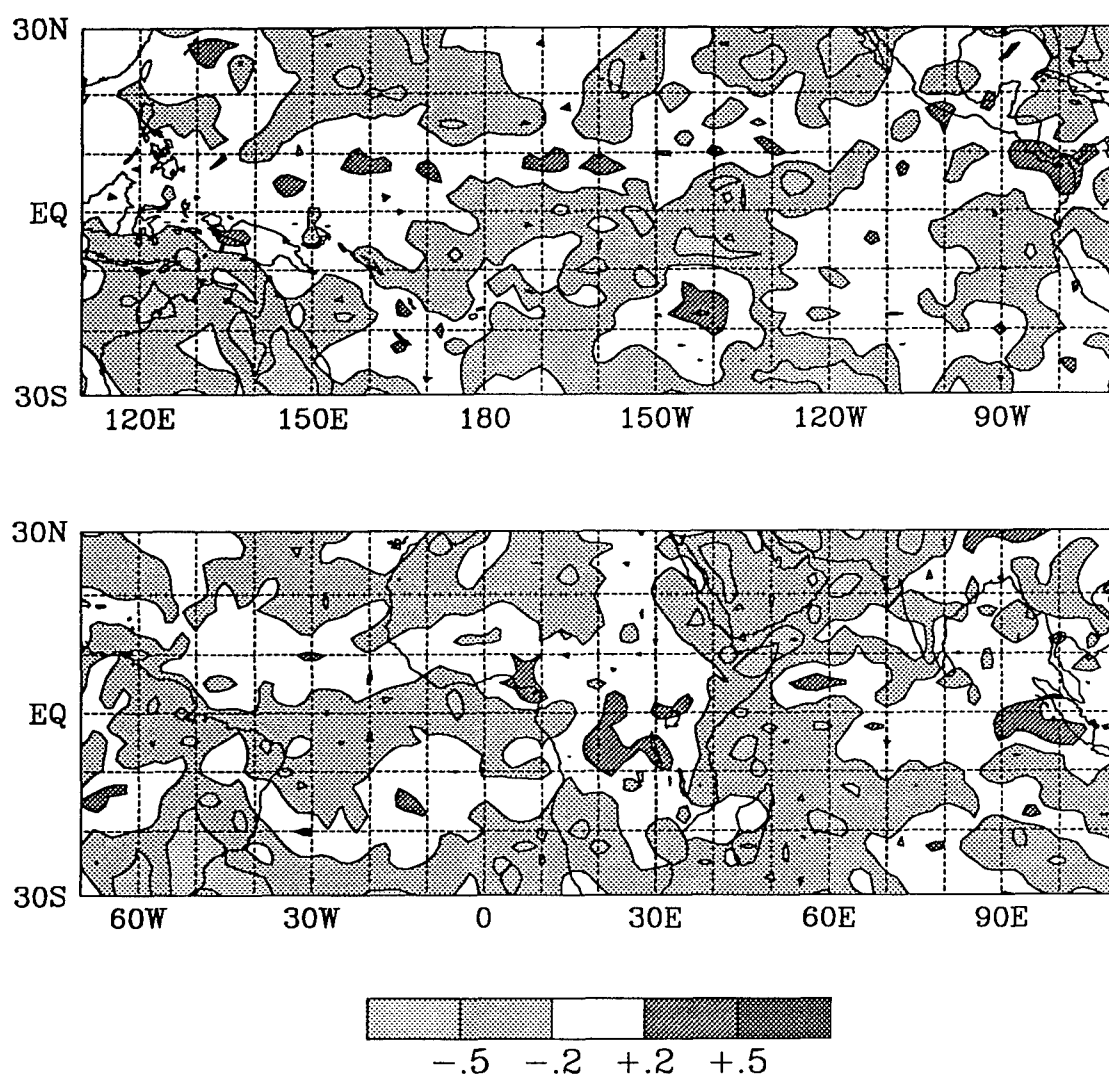
FIG. 33. As in Fig. 30, except for JJA 1989.

are trying to detect. These biases, though small, imply anomalous convection in anomalously dry regions or suppressed convection in anomalously moist areas.

The correlation between synoptically filtered PW and OLR data over each season is not too impressive when averaged over the entire grid domain; but it is easy to see regional variations in the value of the correlation coefficient. The next step in this section is to compare PW and OLR data using seasonal Hovmöller composites of synoptic events, as used in previous chapters. Since the comparison involves data from only one season, the composite includes all events that exceed +1.0 mm anomaly in the synoptically filtered PW data, so that several events are included. The composites of the filtered PW data are compared with the composite of the synoptically filtered OLR data from the same event days. Appendix E contains 28 figures (figures E1 through E28) of Hovmöller composite plots for (a) PW data and (b) OLR data for the tropical convective regions.

The regional differences in the values of the PW/OLR correlation coefficient are evident when comparing the seasonal Hovmöller composites of PW and OLR data. Although most regions demonstrate some coherence in the seasonal OLR Hovmöller composites, anomalies of OLR do not necessarily share the same phase or propagation direction as are found in the corresponding PW Hovmöller composite. The Sahel, WPWP, SICZ, and Amazon regions demonstrate this behavior for all seasons (Figs. E13 through E16, E17 through E20, E21 through E24, and E25 through E28). The correlation in the SPCZ region appears to almost exist (Figs. E5 through E8), while a fairly clear relationship between the PW and OLR composites is seen in the ITCZ region (Figs. E1 through E4). The best PW/OLR correlation found in this study is in the NACZ region (Figs. E9 through E12).

Generally the Hovmöller plots of PW and OLR data identify two distinctly different phenomena. With extended regions of weak activity in the OLR plots, it is clear that OLR presents synoptic scale information that is somehow associated with convective activity. There are two reasons that could explain this lack of correlation between the filtered OLR and PW data. As has been observed by past studies, anomalously low OLR readings are not always an indicator of active convection; these low values can be associated with the cirrus blowoff area associated with convection. Persistent cirrus can distort any correlation tendency between OLR and PW. Also, it is quite possible that signals in the PW field are not necessarily associated with convective activity, especially over land areas. In such an instance, areas with anomalously high PW would tend to be collocated with average OLR readings. Since the plots of these two different data reveal different propagation characteristics, it appears that the synoptic scale anomalies in the PW field are not necessarily related to the convective activity found in the OLR data. This result is expected somewhat, since OLR is normally a signal of upper tropospheric activity, while PW variations often indicate characteristics of the lower troposphere.

The major advantage PW data has over OLR data is spatial coherence. The OLR data can identify activity on the synoptic scale activity only when convection can be triggered, which excludes most land areas, regions of cooler ocean surfaces, regions of subtropical subsidence, and perhaps even within the convectively active regions on occasion. This limitation severely diminishes the spatial coherence of the OLR anomaly signal. The PW data, on the other hand, can identify and track coherent anomalous synoptic scale behavior across the entire globe during all seasons, whether or not associated with convection. Presumably, PW will be disturbed anytime the tropical boundary layer is disturbed (thickened or depressed). Also, PW is a much more persistent parcel

trajectory than is a convective cloud. These advantages allow PW data to maintain a signal of synoptic scale events perhaps never before identified or documented by previous studies.

CHAPTER VIII

SUMMARY AND CONCLUSIONS

Synoptic scale behavior of the global tropics has been examined through time filtered TOVS-estimated precipitable water. The study first documented general variability and propagation characteristics of synoptic scale PW anomalies of the global tropics for various latitudes and seasons. Further investigation determined the necessity for study on a regional scale and described the method for selecting the focal regions to be explored. Regional differences in synoptic scale behavior are most easily recognized in seasonal Hovmöller composites and time-lag correlation plots. A comparison between synoptically and intraseasonally filtered PW data as well as between synoptic behavior occurring during warm and cold ENSO phases provides insight into possible scale interactions and their regionally differing characteristics. A final comparison between patterns in synoptic activity as revealed by PW and OLR data attempts to identify reasons for the results obtained from the use of the TOVS-generated PW dataset.

The initial step in this research process was to establish the areas where synoptic variations are likely to occur. Since preferred convergence zones have been noted to be latitudinally oriented regions of relatively high convective activity and PW maxima, the TOVS-generated PW dataset was used to locate their preferred seasonal latitudinal locations. A useful method for portraying their position was found by identifying the maximum values of the frequency of occurrence of relative PW maxima between 27.5°N and 27.5°S. Over the global tropics, a semi-continuous band of elevated frequency values associated with the various regional convergence zones extend through almost

all longitudes. Seasonal plots reveal a migration of several degrees of latitude of convergence zones, as well as seasonal fluctuations in their apparent strength over an annual cycle, in agreement with results by Gruber.(1972). The intertropical convergence zone (ITCZ) appears the strongest feature in the plot, extending across the entire Pacific from the warm pool region to the west coast of South America. The North Atlantic convergence zone (NACZ) appears as a continuation of the ITCZ along the north coast of South America to over equatorial Africa. The South Indian convergence zone (SICZ) is an extension of the NACZ region from the east coast of Africa into the central Indian Ocean south of the equator. A second convergence region in the Pacific (SPCZ) extends from the warm pool east-southeastward across the central Pacific south of the equator.

Another method of using the PW data, expected to be useful for identifying convergence zones, was poorly correlated with these convergence zones. Interestingly, this method, which is the location of maximum synoptic scale standard deviation of PW, does not collocate spatially with the latitudes of the convergence zones. However, its signal offers some important insights into tropical synoptic scale behavior. A band of slightly elevated standard deviation values stretches across the Pacific a few degrees north of the apparent ITCZ location. A relative minimum of variation exists along the equator through almost all longitudes. Values of synoptic scale variation increase dramatically in the poleward direction from near 30° latitude in both hemispheres. The actual latitude where this increase begins varies with region and hemisphere, but it is generally found from between 10° and 25° away from the equator. This boundary likely indicates the latitudinal extent of midlatitude synoptic scale influences within the tropical regions. The North Pacific appears to be free of midlatitude behavior south of 20°N, while the South Pacific shows signs of

eastward propagation as far north as 10°S in the west. The magnitude of synoptic scale PW standard deviation is higher over land than over ocean regions. This result suggests greater daily changes in atmospheric PW in regions where atmospheric moisture is not constantly maintained by an ocean surface.

Temporal and spatial coherence of PW anomalies is easily seen by viewing the synoptic PW anomalies in Hovmöller format. PW anomalies may be perturbations in the height of the boundary layer resulting from moisture convergence. Some of these perturbations are very continuous in space and time: once they are created, they do not easily disappear. These particular anomalies remain persistent and coherent over large space and long time intervals. Individual anomalies are sometimes traceable around the entire globe or even longer. They extend through many synoptic time scales and are amazingly coherent when compared to other signals of synoptic scale behavior, such as OLR. This incredible coherence in the PW anomaly field is not easily explainable considering the numerous interactions of behavior in the tropical atmosphere. The presence of continents, midlatitude interactions, and scale interactions all act to influence and change the coherent structure of synoptic activity; yet, the atmosphere somehow tends to remember these perturbations in the PW field, or reinforce their structure once they become established. Such coherence, which extends through as many as 20 or more synoptic time scales, cannot be explained from the current understanding of the tropical atmosphere. A major genesis region of these anomalies appears to be in the Gulf of Guinea, where PW anomalies diverge into the preferred eastward mode across Sahel Africa and the westward mode across the North Atlantic. Throughout much of the tropics, evidence supports the simultaneous existence of both an eastward and a westward propagation mode. Whatever the forcing mechanism

is in the tropical atmosphere, it responds in a varying degree of combination of these two dominant modes throughout the entire tropical region. Seasonal Hovmöller composites of synoptic scale PW anomalies exceeding +2.0 mm performed along the focal longitudes reveal these modal response combinations. In the Pacific ITCZ, SPCZ, west Pacific warm pool, South Indian Ocean, and Amazon basin regions, composites show evidence of both behavioral modes occurring through the seasonal climatology. The individual westward and eastward modes are best seen in the NACZ and Sahel regional composites respectively, where very strong and repetitive unimodal behavior occurs. The westward mode has a propagation speed of about 10 ms^{-1} and has a zonal wavelength of approximately 6,000 km, while the eastward mode has zonal wavelength of about 2,700 km and a propagation speed of 7 ms^{-1}. Both of these modes are present with varying intensities according to latitude and season, with the eastward mode enhanced by land masses. The eastward mode is also enhanced along 7.5°N across the Pacific Ocean during the SON season. Although the westward mode remains evident along this latitude, the eastward mode is more dominant for latitudes between 5°N and 12.5°N during this time of year.

Previous work about tropical normal modes has not documented the existence of both an eastward and westward mode at the synoptic time scale. Takayabu (1994) did identify both a westward and an eastward propagating behavioral mode in the OLR field; however, those particular behaviors are associated with the gravity modes (time scales of about 1 1/2 days), which fail to account for the phenomena documented in this research. Expected normal mode behavior explains the predominantly westward propagation along the equator as a mixed Rossby-gravity wave response, which agrees with Liebmann and Hendon (1990), who document a westward-propagating 850 mb

wind anomaly field with a spectral peak of 4 days as a Rossby-gravity mode. However, the eastward mode appears to be an unprecedented result. Since this eastward mode is enhanced off-equator, it is not a Kelvin response. The time scale of this mode does not allow for a gravity mode explanation. Instead, a normal mode response consistent with this observation is an eastward-moving Rossby-gravity mode.

Lag correlation plots reveal the same bimodal behavior across the various tropical regions indicated by the Hovmöller composites. Regions not experiencing a single behavioral mode (Pacific and Indian Ocean regions) lack spatial coherence and propagation pattern, while a wavetrain pattern is evident in the North Atlantic and Sahel Africa regions, where the westward and eastward modes dominate respectively. Propagation appears well behaved and quite regular in these quasi-unimodal regions.

Even though the general propagation behavior can be described by normal mode behavior, two problems exist with this explanation. First, the propagation in both the eastward and westward modes appears to be independent of Doppler shifting -- for example, the propagation speed does not appear to depend upon the zonal wind speed. PW anomalies maintain their propagation speed notwithstanding their location in the tropics. Since significant changes in wind direction and speed are seen in tropical climatological wind fields, this makes a normal mode explanation of these behaviors difficult. Furthermore, although PW perturbations are more likely to exist in the lower troposphere, they may in actuality be found at any vertical level. This makes it impossible to define the level of "advecting wind" in the explanation. Second, the two unique modal signals show no consistent cross-equatorial coupling. The strong eastward signal visible at 7.5°N across the Pacific Ocean during boreal fall is not balanced by a similar signal at 7.5°S

during austral fall. Such inconsistencies cannot be explained from the normal mode paradigm.

No conclusive evidence supports interaction between the synoptic and intraseasonal time scales in these respective time scale filtered PW fields. Since previous work has documented a clear difference in synoptic scale OLR anomalies during moist and dry ISO phases (Murakami et al. (1986); Lau (1993); Chen, et al. (1996)), there must be a difference in the origin of the PW and OLR signals. Synoptic PW anomalies remain coherent regardless of the occurrence of convective activity: the ISO causes no visible change in the synoptic PW field; this feature is only evident in the anomalous OLR field when convective activity responds to its presence. Convective activity may, however, originate from the PW anomalies during the wet ISO phase. Furthermore, it is possible that convective activity results at the point of constructive interference between PW anomalies propagating in the opposite normal mode directions. Evidence supporting interaction between the synoptic and interannual scales is seen through the directional reversal of synoptic PW anomaly propagation between warm and cold ENSO phases in the Pacific and Indian Ocean regions.

A comparison between the PW and OLR signals reveals only a slight negative correlation. Grid-averaged seasonal correlation coefficients ranging from -0.135 to -0.195 suggest at best a weak relationship between high PW anomalies and anomalously low OLR anomalies at the synoptic time scale. Regional correlation coefficient values range from greater than +0.2 to less than -0.5, with the highest values typically found over the west Pacific warm pool and convergence zone regions. These convectively active regions indicate a slight positive correlation between OLR and PW anomalies at the synoptic time scale. Since the PW signal is temperature dependent, these areas of observed cooler

temperatures associated with large scale convective activity may result in lower regional PW values.

After considering all of these findings, PW remains preferable to OLR for studying behavior in the tropical atmosphere. Individual PW anomalies are traceable over great distances as compared to OLR anomalies. The synoptic PW field is evident regardless of convective activity, and the values of PW have no ambiguities with respect to cirrus effects.

In summary, tropical synoptic scale behavior is extremely coherent through space and time. This coherence of this behavior in PW is much greater than in OLR. Two modes of synoptic scale behavior dominate the tropics: eastward and westward, the eastward being enhanced by land areas and seasonal cycle. However, signs of each mode are present to various degrees at nearly all latitudes. Interaction between synoptic behavior and the ISO is not evident in the PW field; instead, convection is more prevalent during the wet phase of the ISO, and may originate from the already present PW anomalies. The comparison between PW and OLR support this finding, as OLR does not spatially correlate with PW at the synoptic time scale.

REFERENCES

Branstator, G., 1983: Horizontal Energy Propagation in a Barotropic Atmosphere with Meridional and Zonal Structure. *J. Atmos. Sci.*, **40**, 1689-1708.

Cadet, D.L., 1983: Mean Fields of Precipitable Water over the Indian Ocean during the 1979 Summer Monsoon from TIROS-N Soundings and FGGE Data. *Tellus*, **35B**, 329-345.

___, and S. Greco, 1987: Water Vapor Transport over the Indian Ocean during the 1979 Summer Monsoon. Part I: Water Vapor Fluxes. *Mon. Wea. Rev.*, **115**, 653-663.

Chao, W.C., and S.-J. Lin, 1994: Tropical Intraseasonal Oscillation, Super Cloud Clusters, and Cumulus Convection Schemes. *J. Atmos. Sci.*, **51**, 1282-1297.

Chen, S.S., R.A. Houze Jr., and B.E. Mapes, 1996: Multiscale Variability of Deep Convection in Relation to Large-Scale Circulation in TOGA COARE. *J. Atmos. Sci.*, **53**, 1380-1409.

Chen, T.-C., and M.-C. Yen, 1994: Interannual Variation of the Indian Monsoon Simulated by the NCAR Community Climate Model: Effect of Tropical Pacific SST. *J. Climate*, **7**, 1403-1415.

Chung, H., 1993: Atmospheric Moisture Fields Derived by Satellite Observations over the Tropical Pacific Ocean. PhD. Dissertation, Dept. of Meteorology, Texas A&M University, College Station, TX, 77843, 168 pp.

Climate Analysis Center, NOAA, 1995: Equatorial Pacific SST Anomaly for Nino 1+2. *Climate Diagnostics Bulletin*. Washington, D.C.

Dunn, G.E., 1940: Cyclogenesis in the Tropical Atlantic. *Bull. Amer. Meteor. Soc.*, **6**, 133-146.

Gruber, A., 1972: Fluctuations in the Position of the ITCZ in the Atlantic and Pacific Oceans. *J. Atmos. Sci.*, **29**, 193-197.

Hatfield, E., 1994: Precipitable Water Structure in Tropical Systems as Estimated from TOVS. M.S. Thesis, Dept. of Meteorology, Texas A&M University, College Station, TX, 77843, 127 pp.

Hayashi, Y.-Y., and T. Nakazawa, 1989: Evidence of the Existence and Eastward Motion of Superclusters at the Equator. *Mon. Wea. Rev.*, **117**, 236-243.

Hayes, P.M., 1988: Active Modes of the Pacific ITCZ. M.S. Thesis, Dept. of Meteorology, Texas A&M University, College Station, TX, 77843, 90 pp.

Hsu, H.-H., B.J. Hoskins, and F.-F. Jin, 1990: The 1985'86 Intraseasonal Oscillation and the Role of the Extratropics. *J. Atmos. Sci.*, **47**, 823-839.

Khalsa, S.J.S., and E.J. Steiner, 1988: A TOVS Dataset for Study of the Tropical Atmosphere. *J. Appl. Meteor.*, **27**, 851-862.

Kiladis, G.N., and K.M. Weickmann, 1992a: Circulation Anomalies Associated with Tropical Convection during Northern Winter. *Mon. Wea. Rev.*, **120**, 1900-1923.

___, and ___, 1992b: Extratropical Forcing of Tropical Pacific Convection during Northern Winter. *Mon. Wea. Rev.*, **120**, 1924-1938.

Lau, K.-H., 1993: Relationship between Synoptic-Scale Transient Activity and Summertime Intraseasonal Fluctuations in the Asiatic Monsoon Region. *East Asia and Western Pacific Meteorology and Climate*, W.J. Kyle and C.P. Chang, Eds., World Scientific Publishing Co., 621 pp.

___, and N.-C. Lau, 1990: Observed Structure and Propagation Characteristics of Tropical Summertime Synoptic Scale Disturbances. *Mon. Wea. Rev.*, **118**, 1888-1913.

Lau, K.-M., and P.-H. Chan, 1985: Aspects of the 40-50 Day Oscillation during the Northern Winter as Inferred from Outgoing Longwave Radiation. *Mon. Wea. Rev.*, **113**, 1889-1909.

___, and C.-P. Chang, 1987: Planetary Scale Aspects of the Winter Monsoon and Atmospheric Teleconnections. *Monsoon Meteorology*, C.-P. Chang and T.N. Krishnamurti, Eds., Oxford University Press, 544 pp.

___, and L. Peng, 1987: Origin of Low-Frequency (Intraseasonal) Oscillations in the Tropical Atmosphere. Part I: Basic Theory. *J. Atmos. Sci.*, **44**, 950-972.

___, and H. Wu, 1994: Large Scale Dynamics Associated with Super Cloud Cluster Organization over the Tropical Western Pacific. *J. Meteor. Soc. Japan*, **72**, 481-496.

Li, L., and T.R. Nathan, 1994: The Global Atmospheric Response to Low-Frequency Tropical Forcing: Zonally Averaged Basic States. *J. Atmos. Sci.*, **51**, 3412-3426.

Li, T., and B. Wang, 1994: The Influence of Sea Surface Temperature on the Tropical Intraseasonal Oscillation: A Numerical Study. *Mon. Wea. Rev.*, **122**, 2349-2362.

Liebmann, B., and H.H. Hendon, 1990: Synoptic-Scale Disturbances near the Equator. *J. Atmos. Sci.*, **47**, 1463-1479.

Lin, R.-Q., and D.R. Mock, 1986: A Test of the ECMWF Model in Tropical Synoptic-Scale Diagnosis. *Mon. Wea. Rev.*, **114**, 1519-1538.

Madden, R.A., and P.R. Julian, 1972: Description of Global-Scale Circulation Cells in the Tropics with a 40-50 Day Period. *J. Atmos. Sci.*, **29**, 1109-1123.

Matsuno, T., 1966: Quasi-Geostrophic Motions in the Equatorial Area. *J. Meteor. Soc. Japan*, **44**, 25-43.

McGuirk, J.P., A.H. Thompson, and L.L. Anderson, Jr., 1989: Synoptic Scale Moisture Variation over the Tropical Pacific Ocean. *Mon. Wea. Rev.*, **117**, 1076-1091.

___, ___, and N.R. Smith, 1987: Moisture Bursts over the Tropical Pacific Ocean. *Mon. Wea. Rev.*, **115**, 787-798.

Murakami, T., 1980: Temporal Variations of Satellite-Observed Outgoing Longwave Radiation over the Winter Monsoon Region. Part I: Long-Period (15-30 day) Oscillations. *Mon. Wea. Rev.*, **108**, 408-426.

___, and T. Nakazawa, 1985: Tropical 45 Day Oscillations during the 1979 Northern Hemisphere Summer. *J. Atmos. Sci.*, **42**, 1107-1122.

___, L.-X. Chen, and A. Xie, 1986: Relationship among Seasonal Cycles, Low-Frequency Oscillations, and Transient Disturbances as Revealed from Outgoing Longwave Radiation Data. *Mon. Wea. Rev.*, **114**, 1456-1465.

Nakazawa, T., 1986: Intraseasonal Variations of OLR in the Tropics During the FGGE Year. *J. Meteor. Soc. Japan*, **64**, 18-33.

___, 1988: Tropical Super Clusters within Intraseasonal Variations over the Western Pacific. *J. Meteor. Soc. Japan*, **66**, 823-839.

Riehl, H., 1945: Waves in the Easterlies and the Polar Front in the Tropics. Dept. of Meteorology, University of Chicago, Misc. Rept. 17, Chicago, 79 pp.

___, 1948: On the Formation of Typhoons. *J. Meteor.*, **5**, 247-264.

Sadler, J.C., 1967: On the Origin of Tropical Vortices. *Proc. of the Working Panel on Tropical Dynamical Meteorology*, NWRF 12-1167-132, Navy Weather Research Facility, Monterey, 39-76.

Salby, M.L., and H.H. Hendon, 1994: Intraseasonal Behavior of Clouds, Temperature, and Motion in the Tropics. *J. Atmos. Sci.*, **51**, 2207-2224.

Schroeder, S.R., and J.P. McGuirk, 1996: Wavelet Analysis Applied to a Long-Period Data Base of Precipitable Water Derived from TOVS. *Proc. of the 8th Conference on Satellite Meteorology and Oceanography*, Atlanta, GA, 1996, 83-84.

Smith, W.L., H.M. Woolf, C.M. Hayden, D.Q. Wark, and L.M. McMillin, 1979: The TIROS-N Operational Vertical Sounder. *Bull. Amer. Meteor. Soc.*, **60**, 1177-1187.

Steiner, E.J., and S.J.S. Khalsa, 1987: Sea Surface Temperature, Low-Level Moisture, and Convection in the Tropical Pacific, 1982-1985. *J. Geophys. Rea.*, **92**, 14,217-224.

Stephens, G.L., 1990: On the Relationship between Water Vapor over the Oceans and Sea Surface Temperature. *J. Climate*, **3**, 634-645.

Strager, C.S., 1989: Origins of Convective Activity over Panama. M.S. Thesis, Dept. of Meteorology, Texas A&M University, College Station, TX, 77843, 101 pp.

Takayabu, Y.N., 1994a: Large-Scale Cloud Disturbances Associated with Equatorial Waves. Part I: Spectral Features of the Cloud Disturbances. *J. Meteor. Soc. Japan*, **72**, 433-448.

___, 1994b: Large-Scale Cloud Disturbances Associated with Equatorial Waves. Part II: Westward-Propagating Inertio-Gravity Waves. *J. Meteor. Soc. Japan*, **72**, 451-465.

Thepenier, R.-M., and D. Cruette, 1981: Formation of Cloud Bands Associated with the American Subtropical Jet Stream and Their Interaction with Midlatitude Synoptic Disturbances Reaching Europe. *Mon. Wea. Rev.*, **109**, 2209-2220.

Wang, X.-L., and T. Murakami, 1988: Intraseasonal Disturbance Activity before, during, and after the 1982-83 ENSO. *J. Atmos. Sci.*, **45**, 3754-3770.

Webster, P.J., 1973: Temporal Variations of Low-Latitude Zonal Circulations. *Mon. Wea. Rev.*, **101**, 803-816.

___, and H.-R. Chang, 1988: Equatorial Energy Accumulation and Emanation Regions: Impacts of a Zonally Varying Basic State. *J. Atmos. Sci.*, **45**, 803-829.

___, and J.R. Holton, 1982: Cross-Equatorial Response to Middle-Latitude Forcing in a Zonally Varying Basic State. *J. Atmos. Sci.*, **39**, 722-733.

Weickmann, K.M., and S.J.S. Khalsa, 1990: The Shift of Convection from the Indian Ocean to the Western Pacific Ocean during a 30-60 Day Oscillation. *Mon. Wea. Rev.*, **118**, 964-978.

Winton, S.E., 1991: Interactions of Tropical Synoptic-Scale Features as Viewed from a Satellite. M.S. Thesis, Dept. of Meteorology, Texas A&M University, College Station, TX, 77843, 96 pp.

Wittmeyer, I.L., and T.H. Vonder Haar, 1994: Analysis of the Global ISCCP TOVS Water Vapor Climatology. *J. Climate*, **7**, 325-333.

Yin, M., 1994: Information Content and Reliability of TOVS Estimates of Precipitable Water. M.S. Thesis, Dept. of Meteorology, Texas A&M University, College Station, TX, 77843, 108 pp.

APPENDIX   A

Synoptic Filtered Time-Longitude Plots at 30.0 N

SON 1983
Missing Oct 2-4, Nov 11

SON 1985
Missing Nov 18-23

(a)

(b)

SON 1987
Missing Sep 1-7

SON 1988
No Missing Days

(c)

(d)
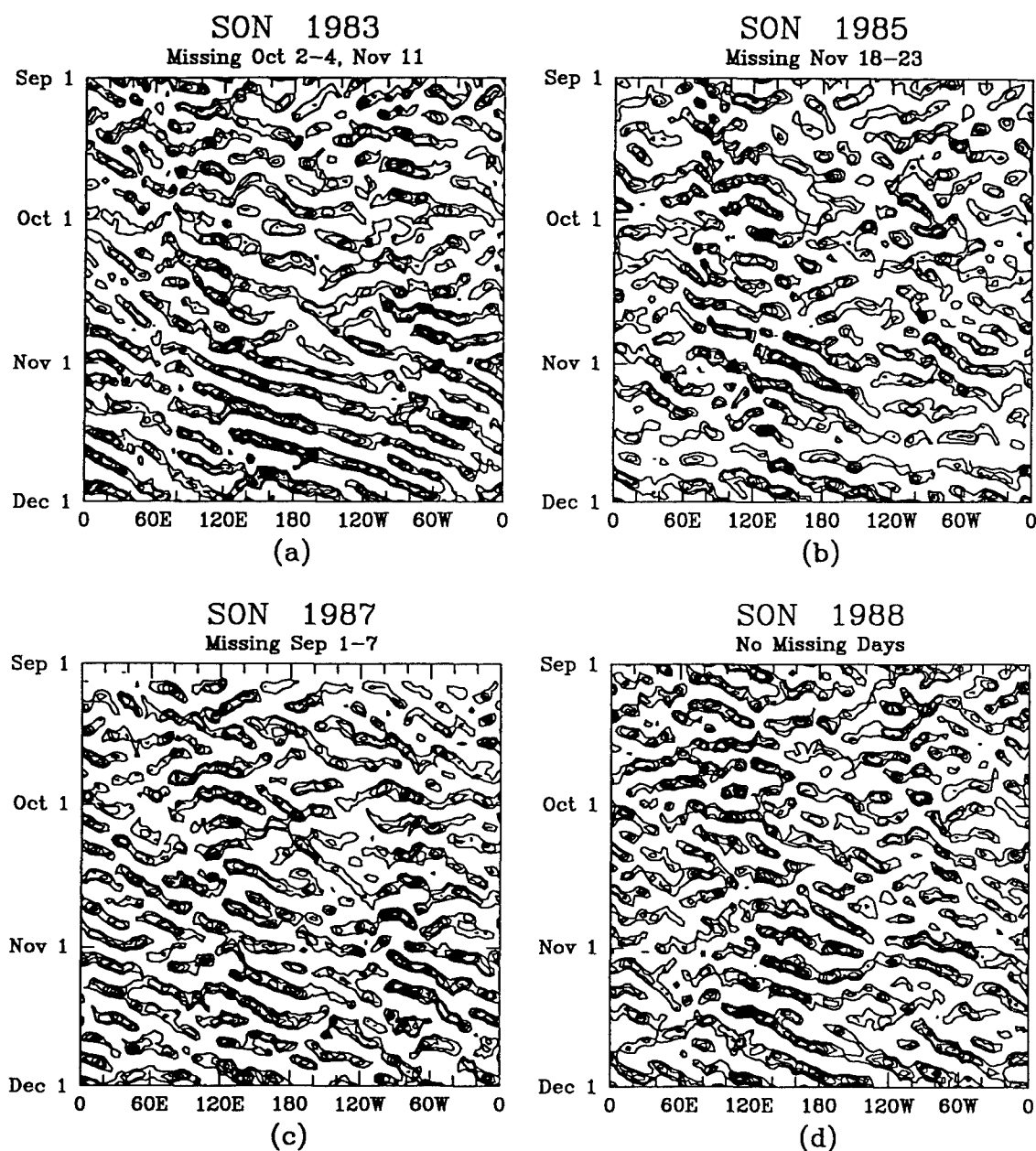
FIG. A1. Synoptic filtered time-longitude plots at 30°N for (a) SON 1983, (b) SON 1985, (c) SON 1987, and (d) SON 1988. Days missing from each period are listed on plots. Lowest contour plotted is +0.5 mm with an interval of 1.0 mm.

Synoptic Filtered Time−Longitude Plots at 20.0 N
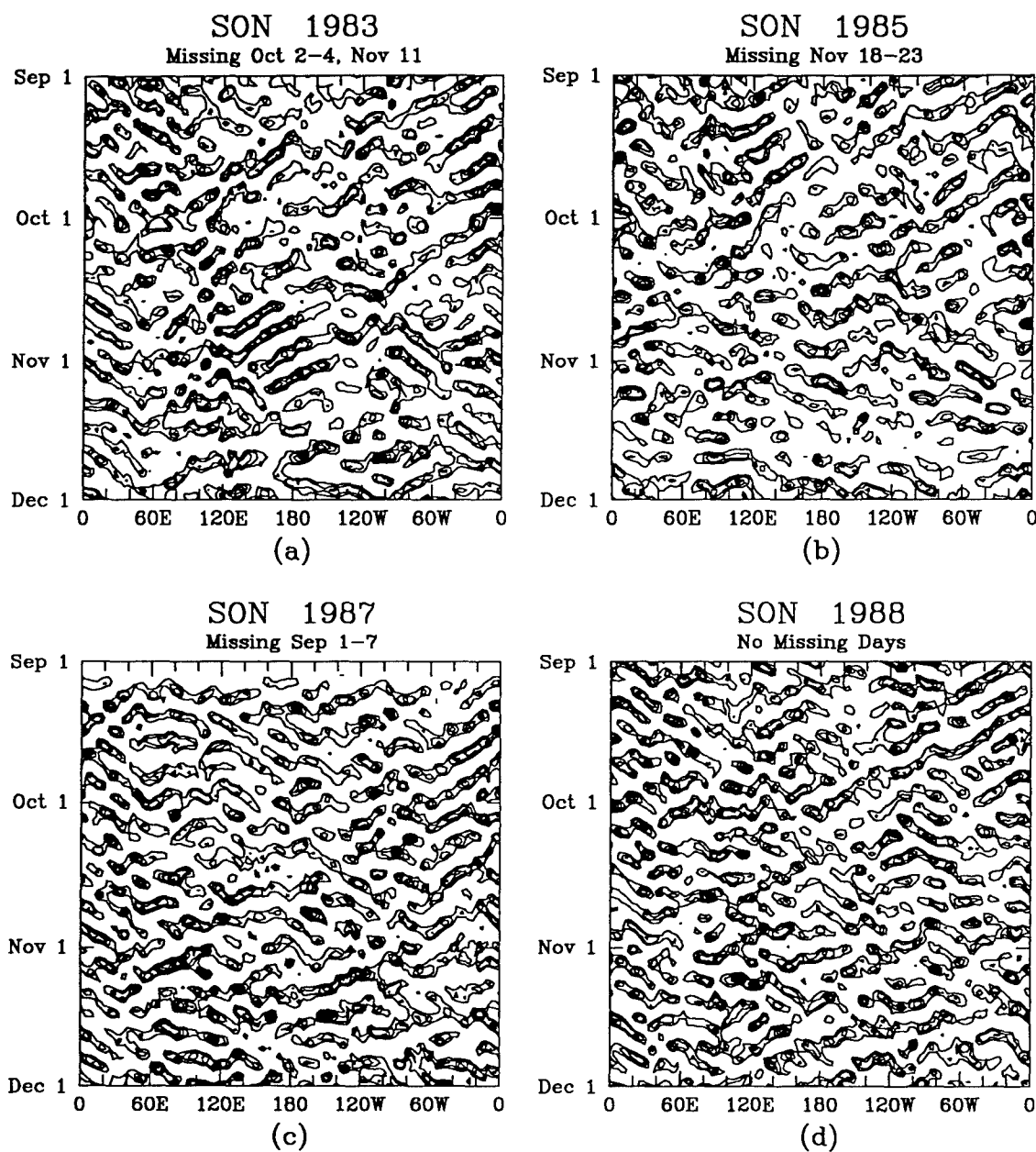
FIG. A2. As in Fig. A1, except at 20°N.

Synoptic Filtered Time–Longitude Plots at 10.0 N

SON 1983
Missing Oct 2–4, Nov 11

(a)

SON 1985
Missing Nov 18–23

(b)

SON 1987
Missing Sep 1–7

(c)

SON 1988
No Missing Days

(d)
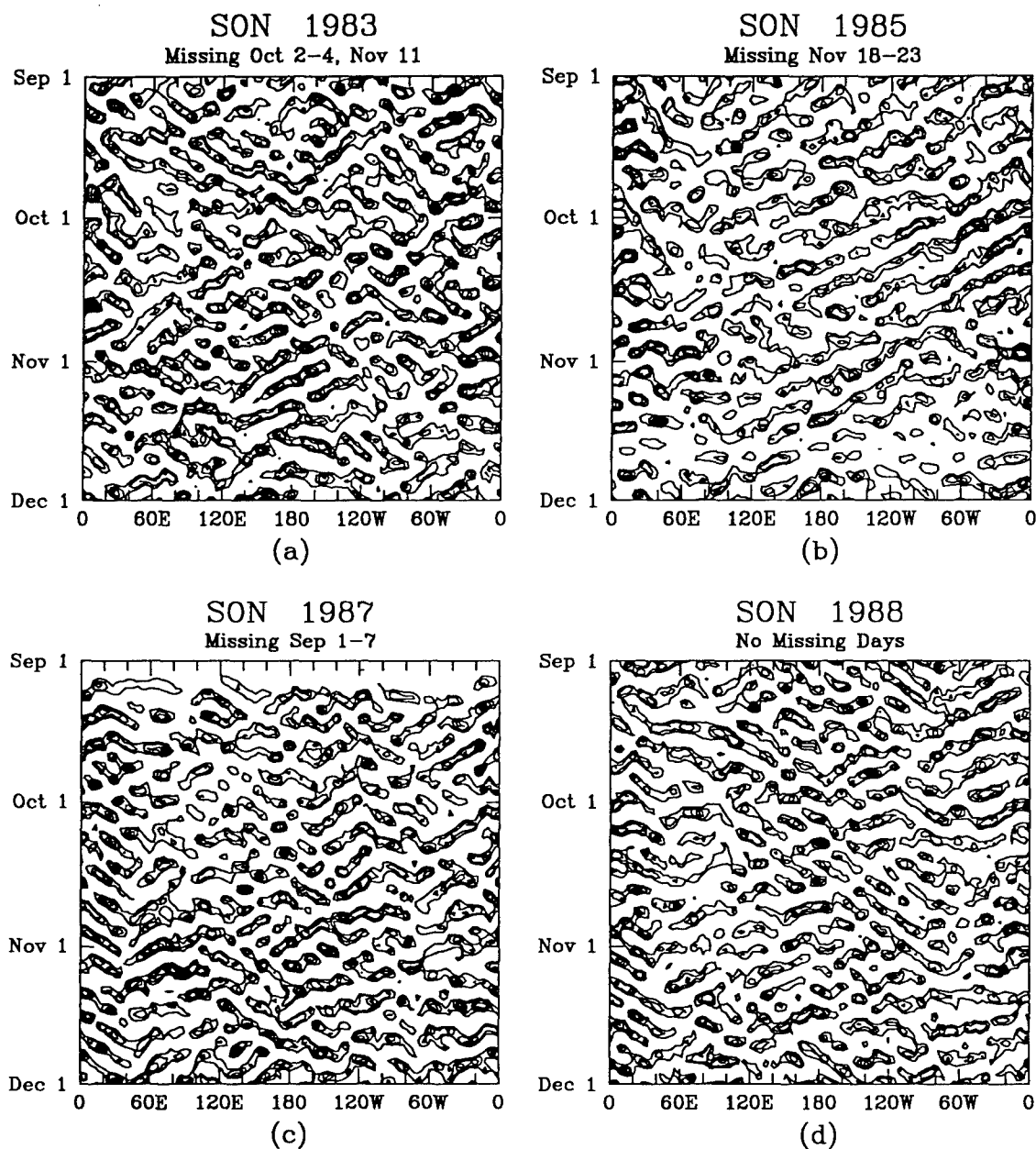
FIG. A3. As in Fig. A1, except at 10°N.

Synoptic Filtered Time—Longitude Plots at the EQ

SON 1983
Missing Oct 2–4, Nov 11

(a)

SON 1985
Missing Nov 18–23

(b)

SON 1987
Missing Sep 1–7

(c)

SON 1988
No Missing Days

(d)
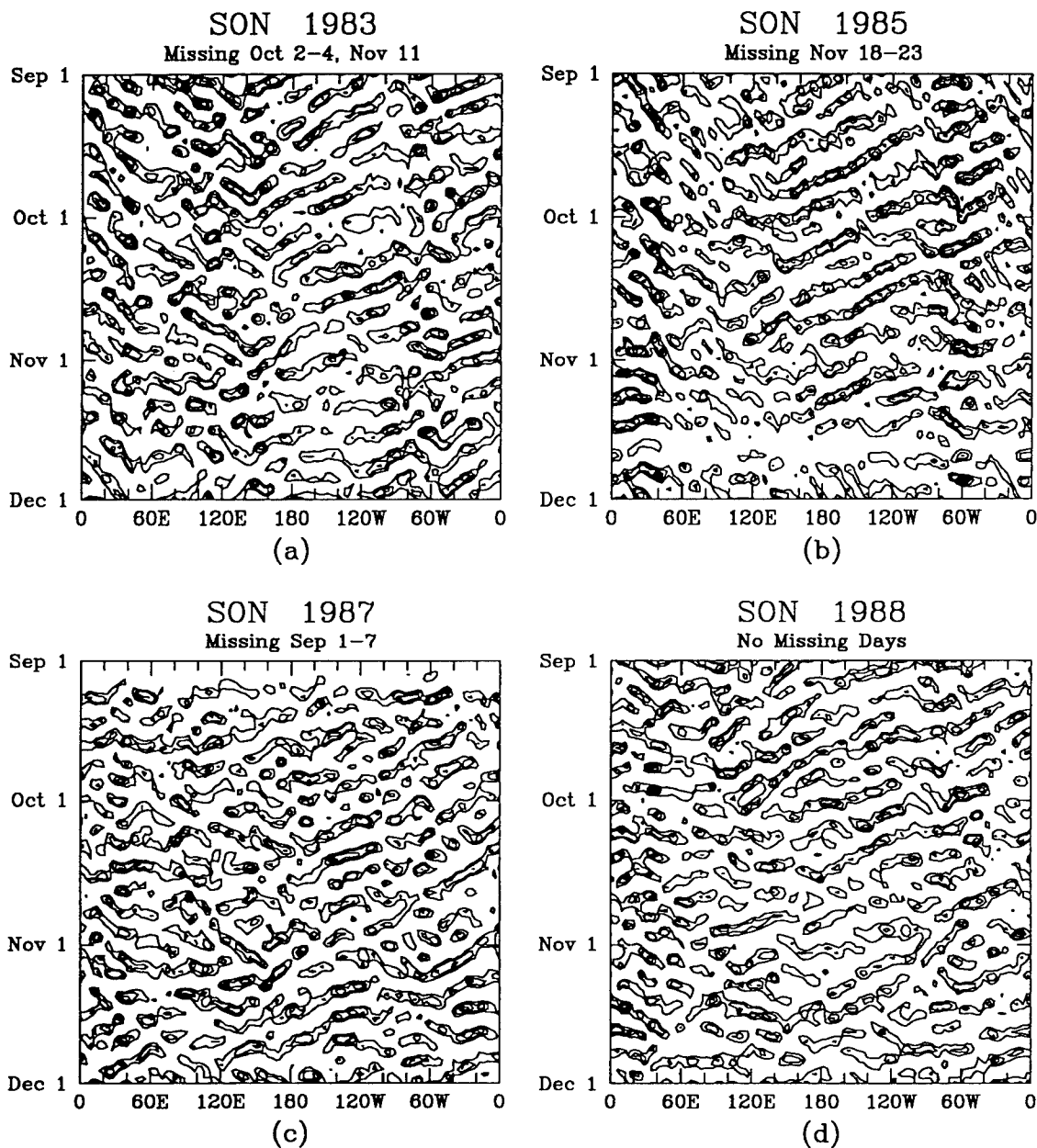
FIG. A4. As in Fig. A1, except at the equator.

Synoptic Filtered Time–Longitude Plots at 10.0 S
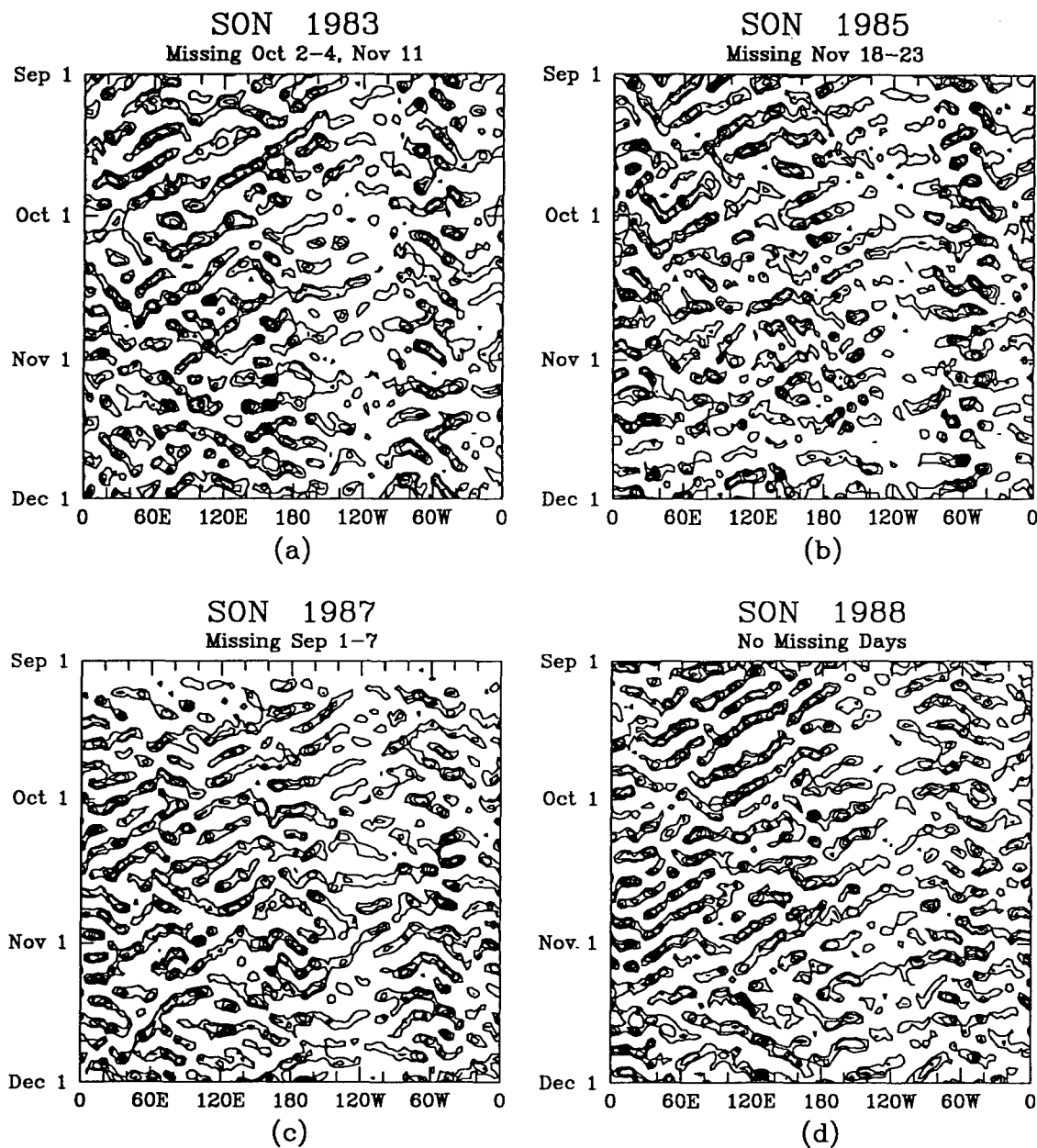
FIG. A5. As in Fig. A1, except at 10°S.

Synoptic Filtered Time–Longitude Plots at 20.0 S

SON 1983
Missing Oct 2–4, Nov 11

SON 1985
Missing Nov 18–23

(a)

(b)

SON 1987
Missing Sep 1–7

SON 1988
No Missing Days

(c)

(d)
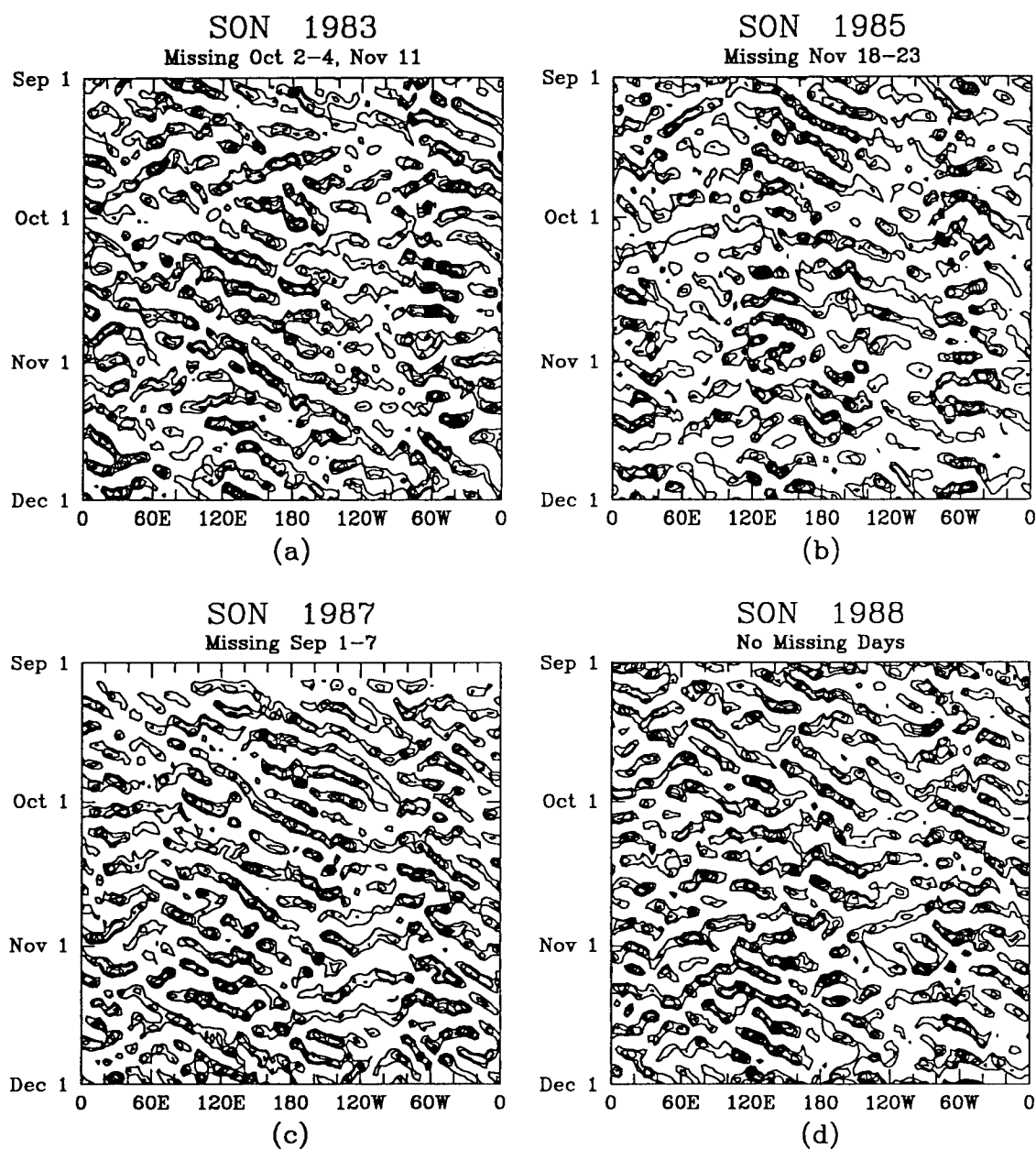
FIG. A6. As in Fig. A1, except at 20°S.

Synoptic Filtered Time–Longitude Plots at 30.0 S
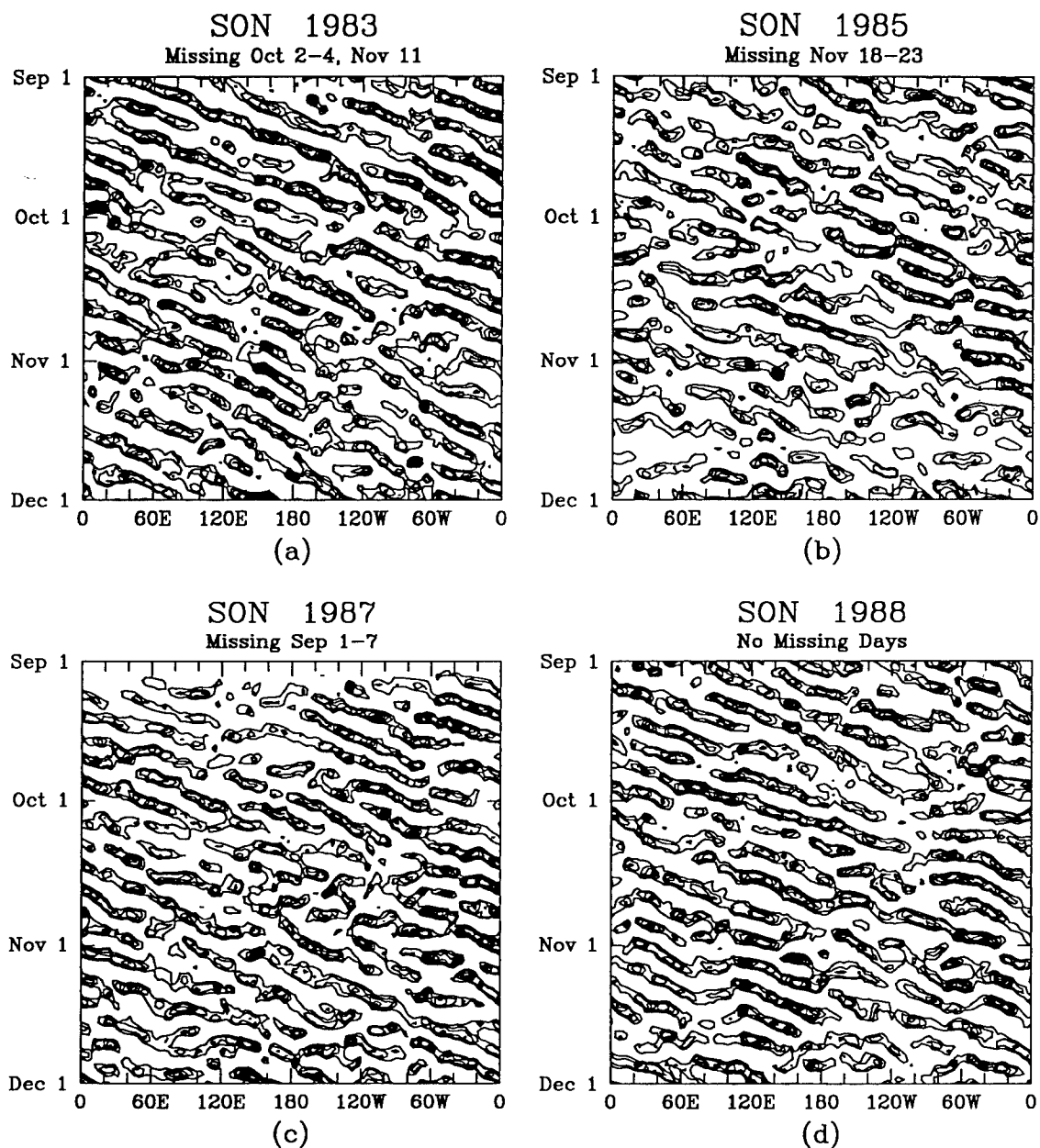
FIG. A7. As in Fig. A1, except at 30°S.

Synoptic Filtered Time–Longitude Plots at 30.0 N

SON 1989
Missing Oct 9

(a)

DJF 1980/1981
Missing Dec 31, Jan 18–24

(b)

DJF 1981/1982
Missing Dec 20, Jan 10

(c)

DJF 1982/1983
No Missing Days

(d)
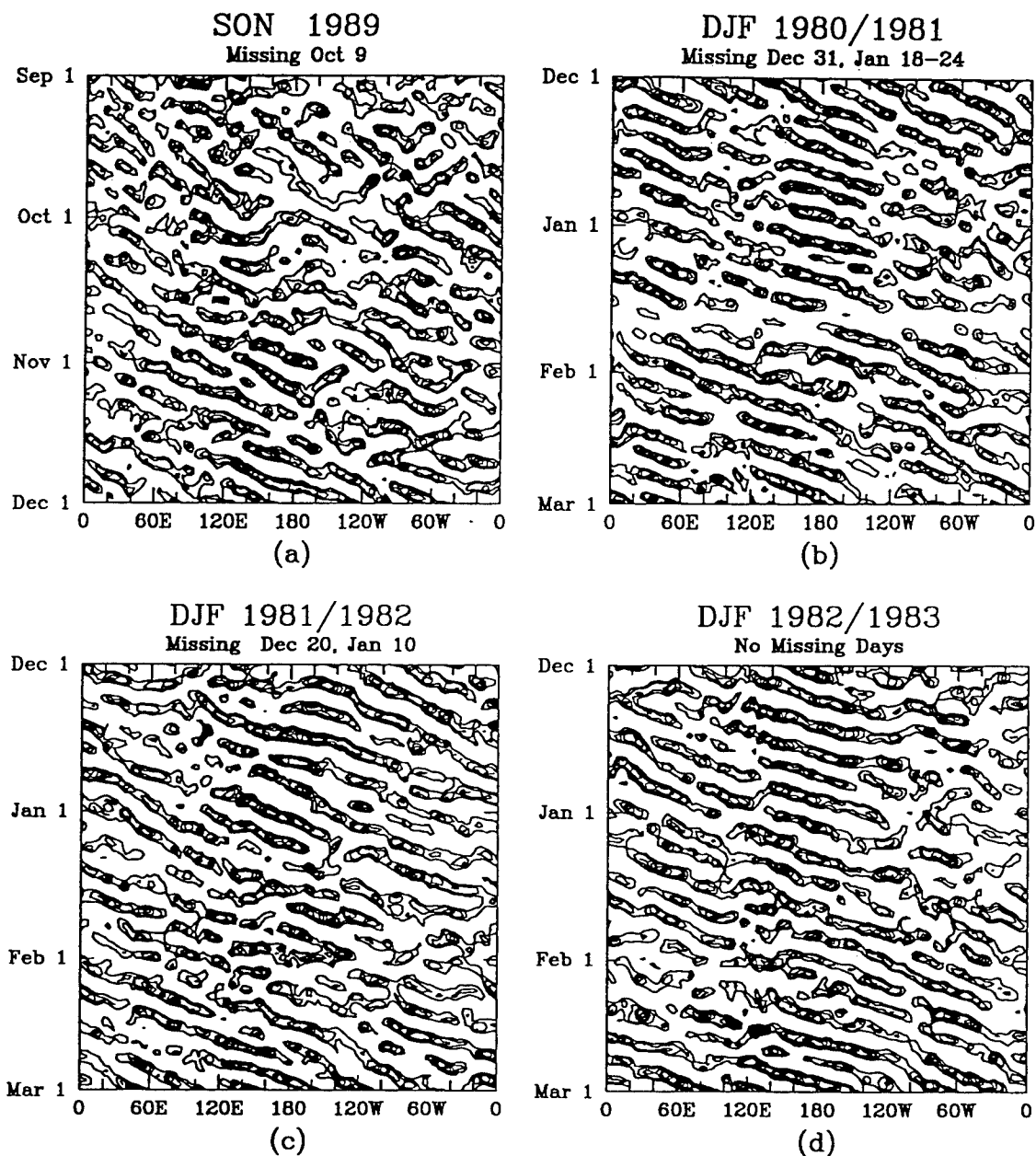
FIG. A8. As in Fig. A1, except for (a) SON 1989, (b) DJF 1980/1981, (c) DJF 1981/1982, and (d) DJF 1982/1983.

Synoptic Filtered Time–Longitude Plots at 20.0 N

SON 1989
Missing Oct 9

DJF 1980/1981
Missing Dec 31, Jan 18–24

DJF 1981/1982
Missing Dec 20, Jan 10

DJF 1982/1983
No Missing Days

(a)

(b)

(c)

(d)
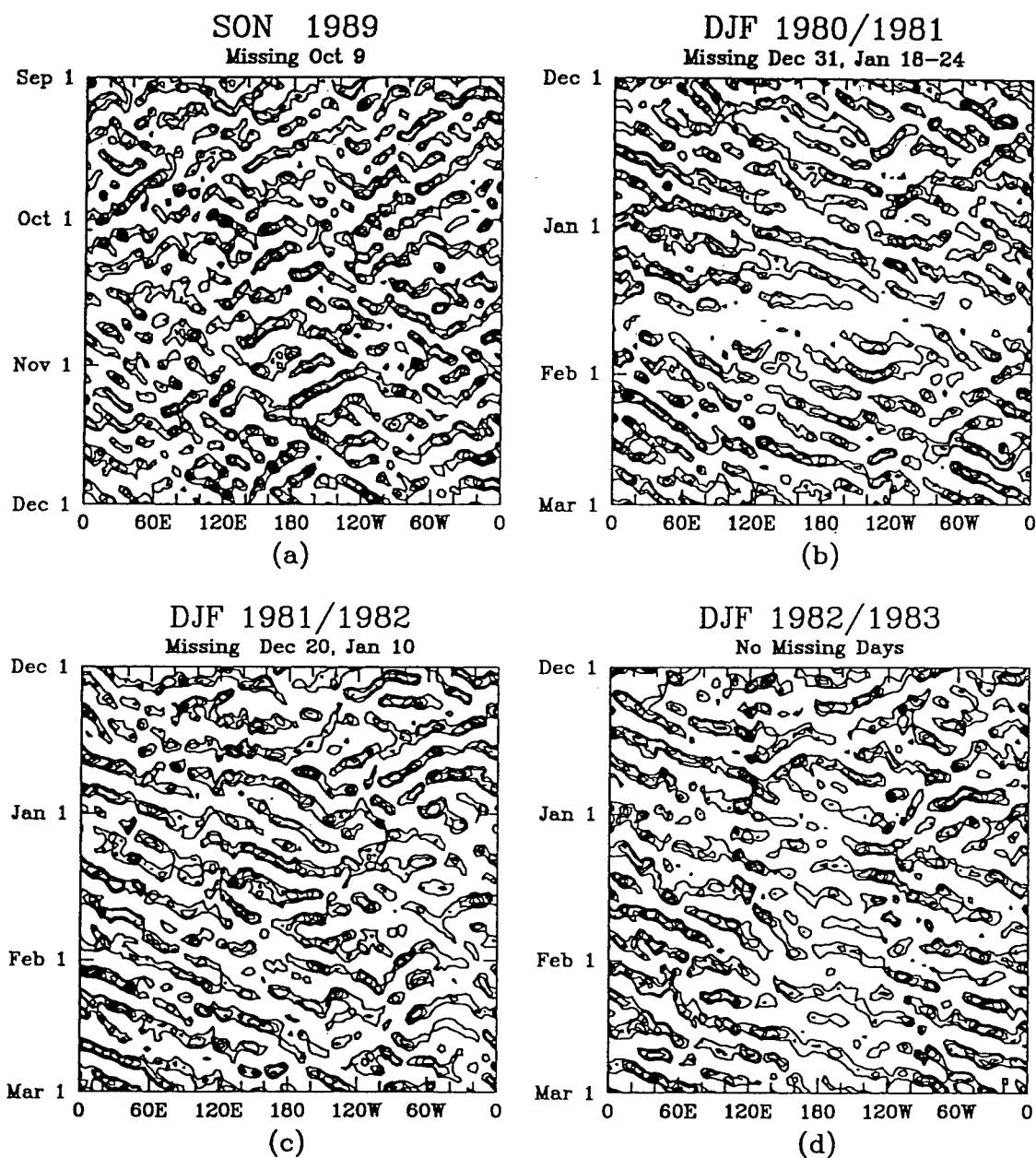
FIG. A9. As in Fig. A8, except at 20°N.

Synoptic Filtered Time–Longitude Plots at 10.0 N
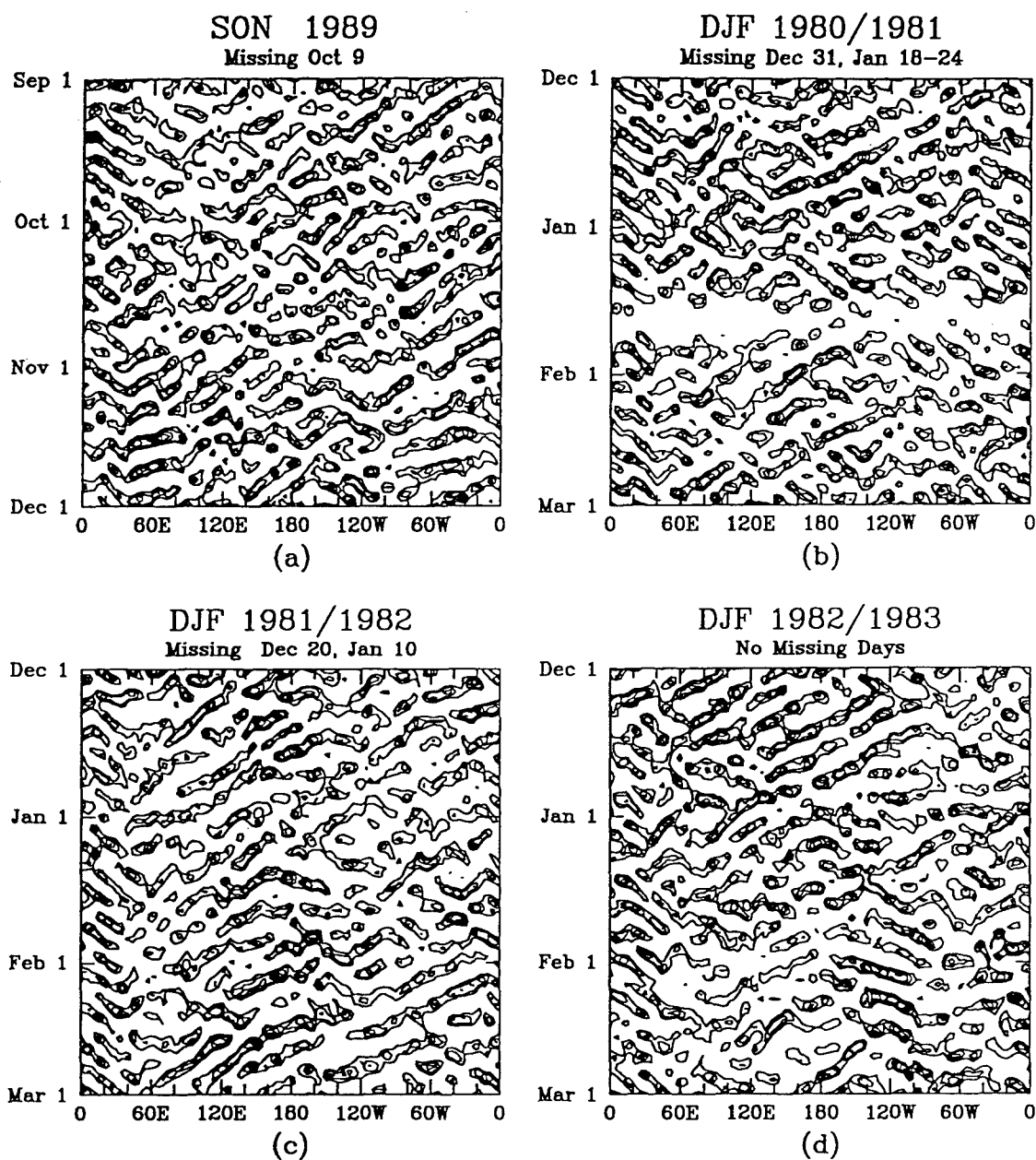
FIG. A10. As in Fig. A8, except at 10°N.

Synoptic Filtered Time–Longitude Plots at the EQ

SON 1989
Missing Oct 9

(a)

DJF 1980/1981
Missing Dec 31, Jan 18–24

(b)

DJF 1981/1982
Missing Dec 20, Jan 10

(c)

DJF 1982/1983
No Missing Days

(d)
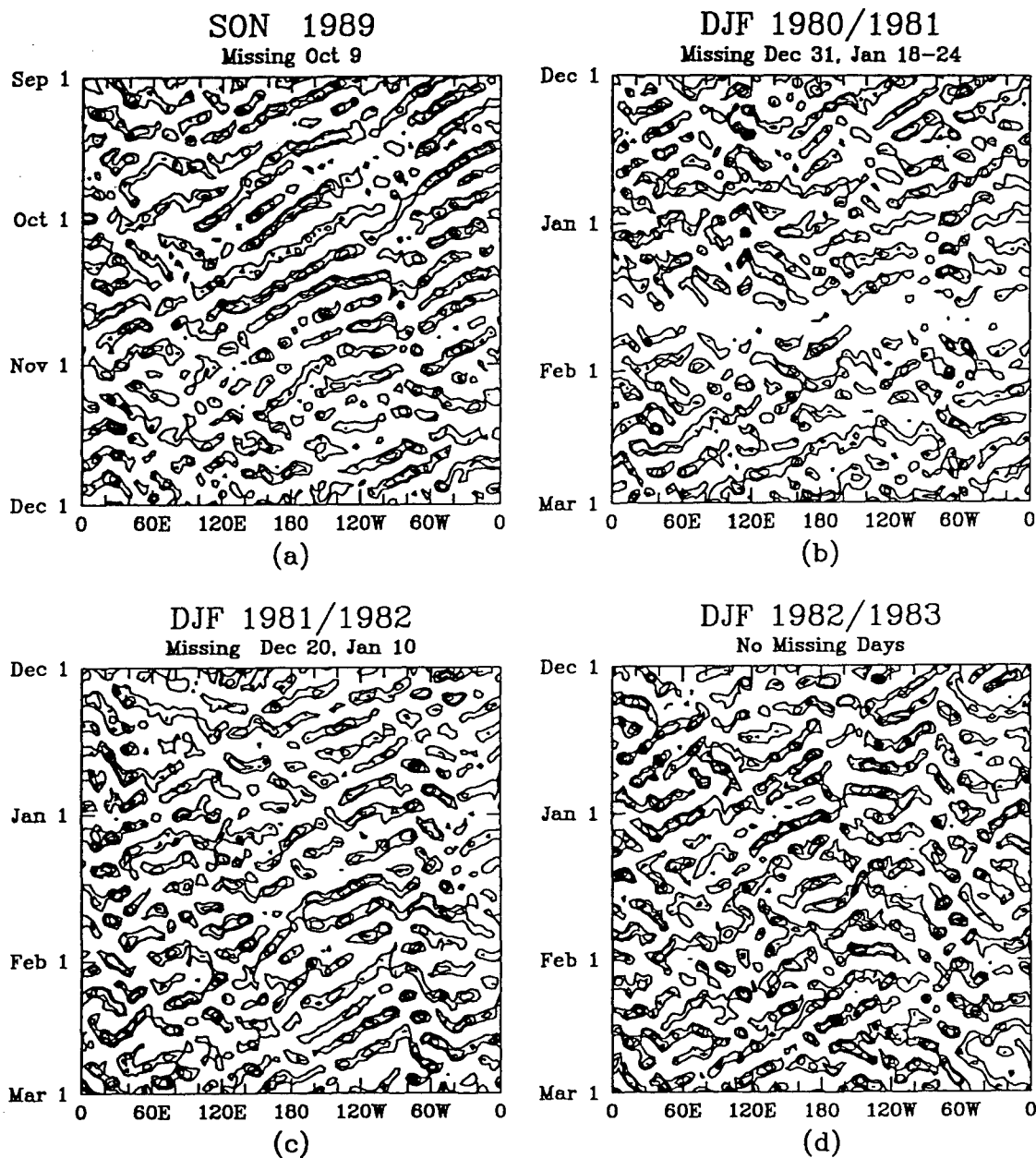
FIG. A11. As in Fig. A8, except at the equator.

Synoptic Filtered Time–Longitude Plots at 10.0 S

SON 1989
Missing Oct 9

(a)

DJF 1980/1981
Missing Dec 31, Jan 18–24

(b)

DJF 1981/1982
Missing Dec 20, Jan 10

(c)

DJF 1982/1983
No Missing Days

(d)
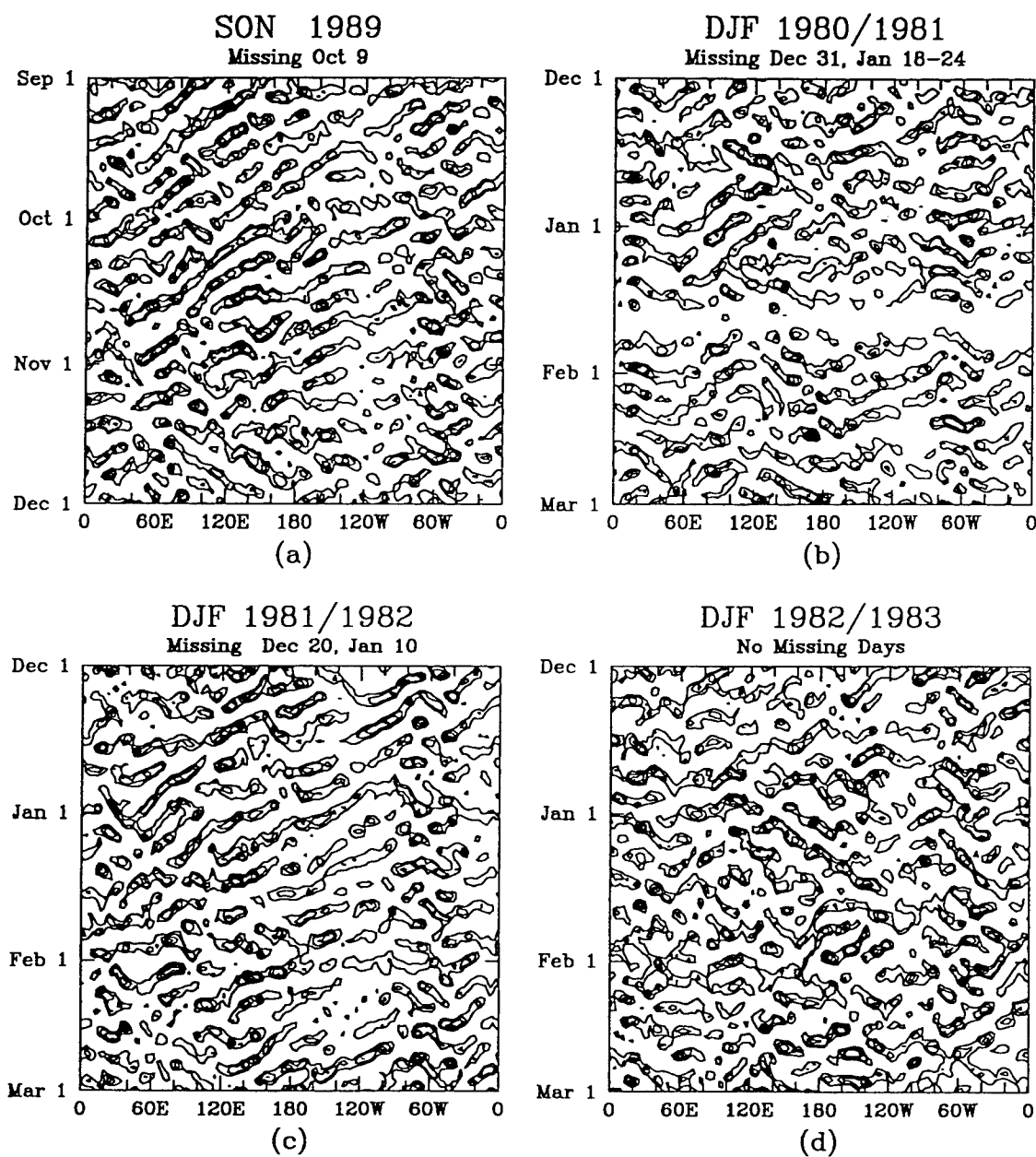
FIG. A12. As in Fig. A8, except at 10°S.

Synoptic Filtered Time—Longitude Plots at 20.0 S

SON 1989
Missing Oct 9

(a)

DJF 1980/1981
Missing Dec 31, Jan 18—24

(b)

DJF 1981/1982
Missing Dec 20, Jan 10

(c)

DJF 1982/1983
No Missing Days

(d)
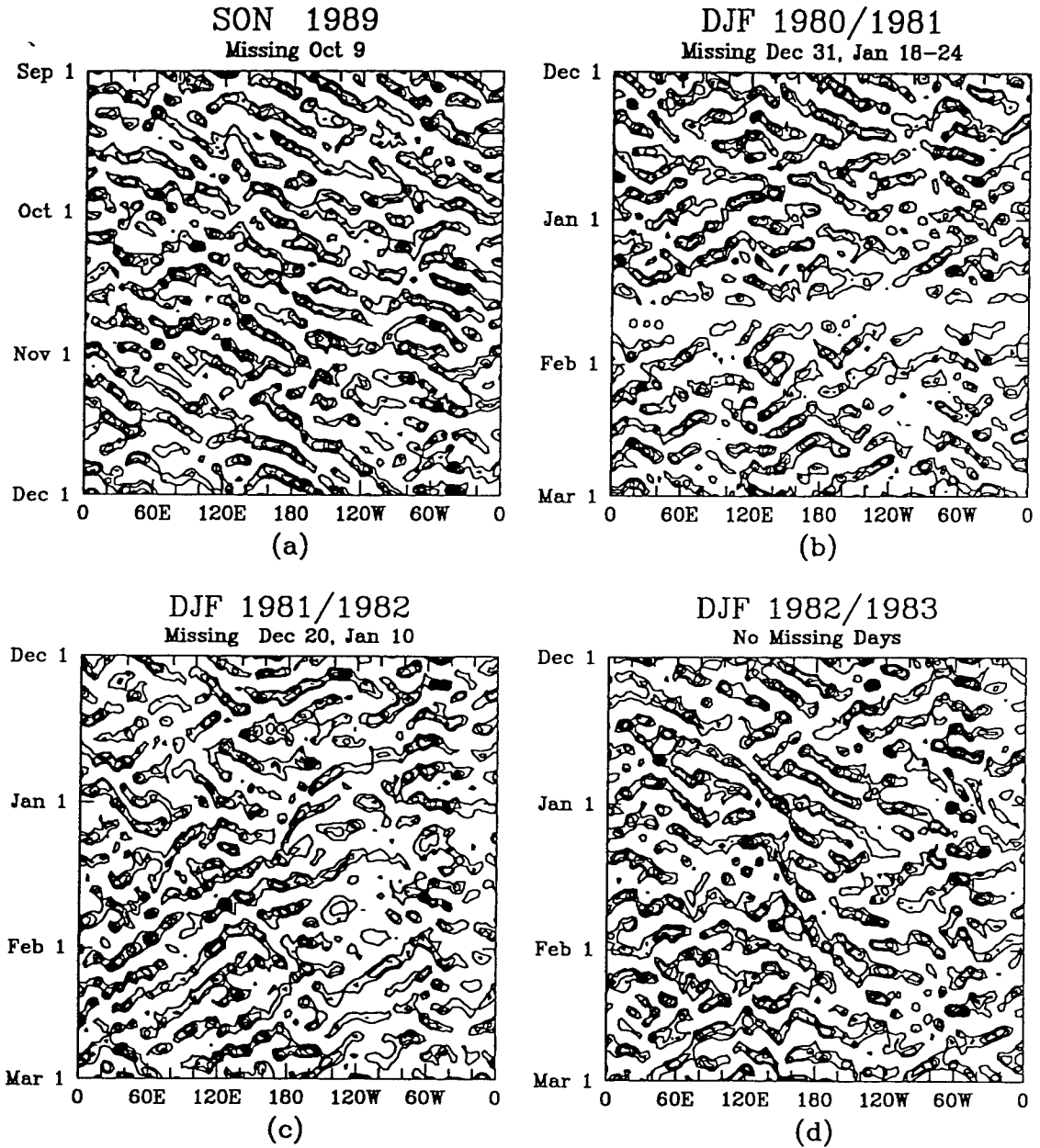
FIG. A13. As in Fig. A8, except at 20°S.

Synoptic Filtered Time—Longitude Plots at 30.0 S
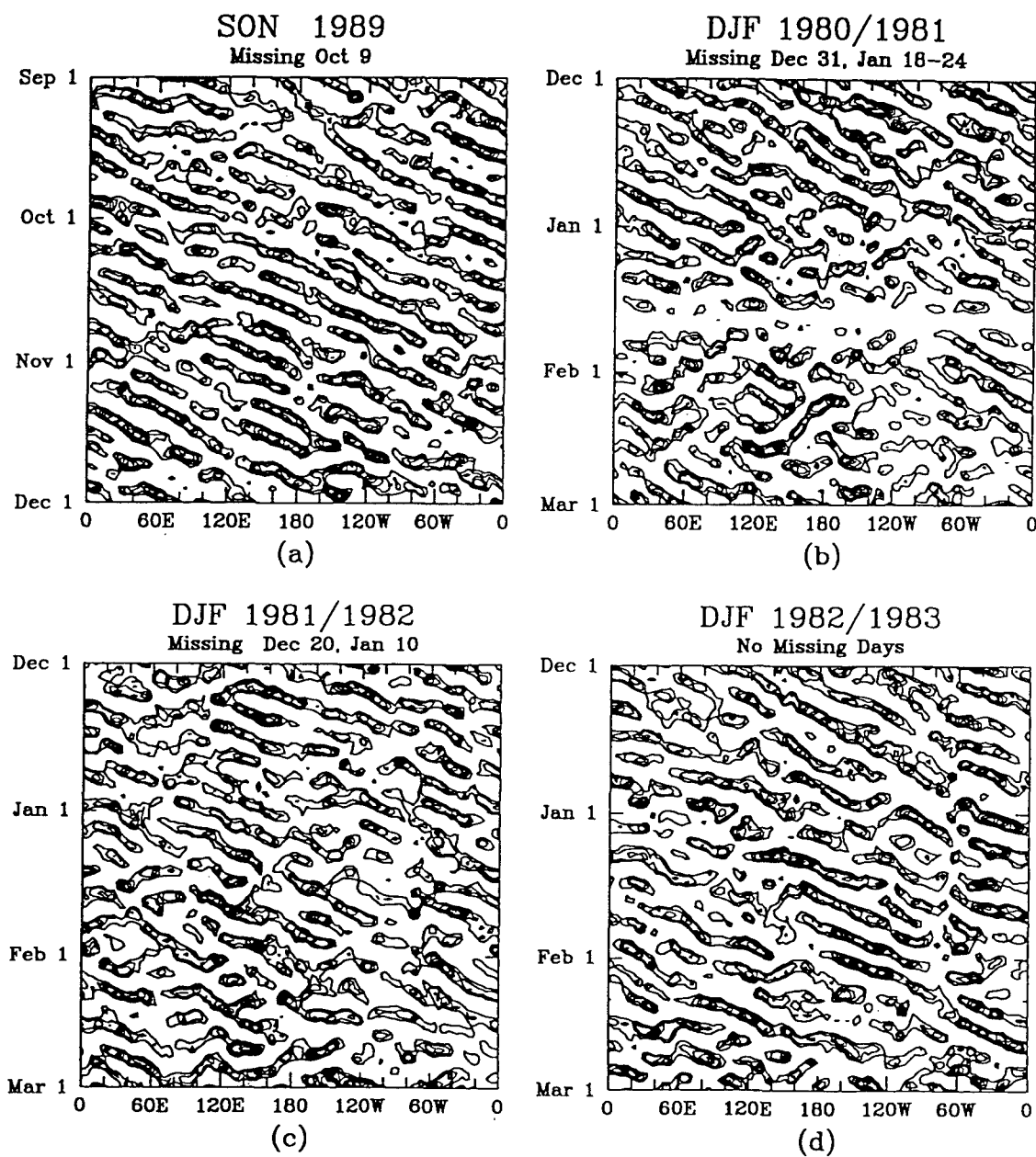
FIG. A14. As in Fig. A8, except at 30°S.

Synoptic Filtered Time–Longitude Plots at 30.0 N

DJF 1983/1984
No Missing Days

(a)

DJF 1985/1986
Missing Jan 2–3

(b)

DJF 1987/1988
Missing Jan 12

(c)

DJF 1989/1990
Missing Dec 14

(d)
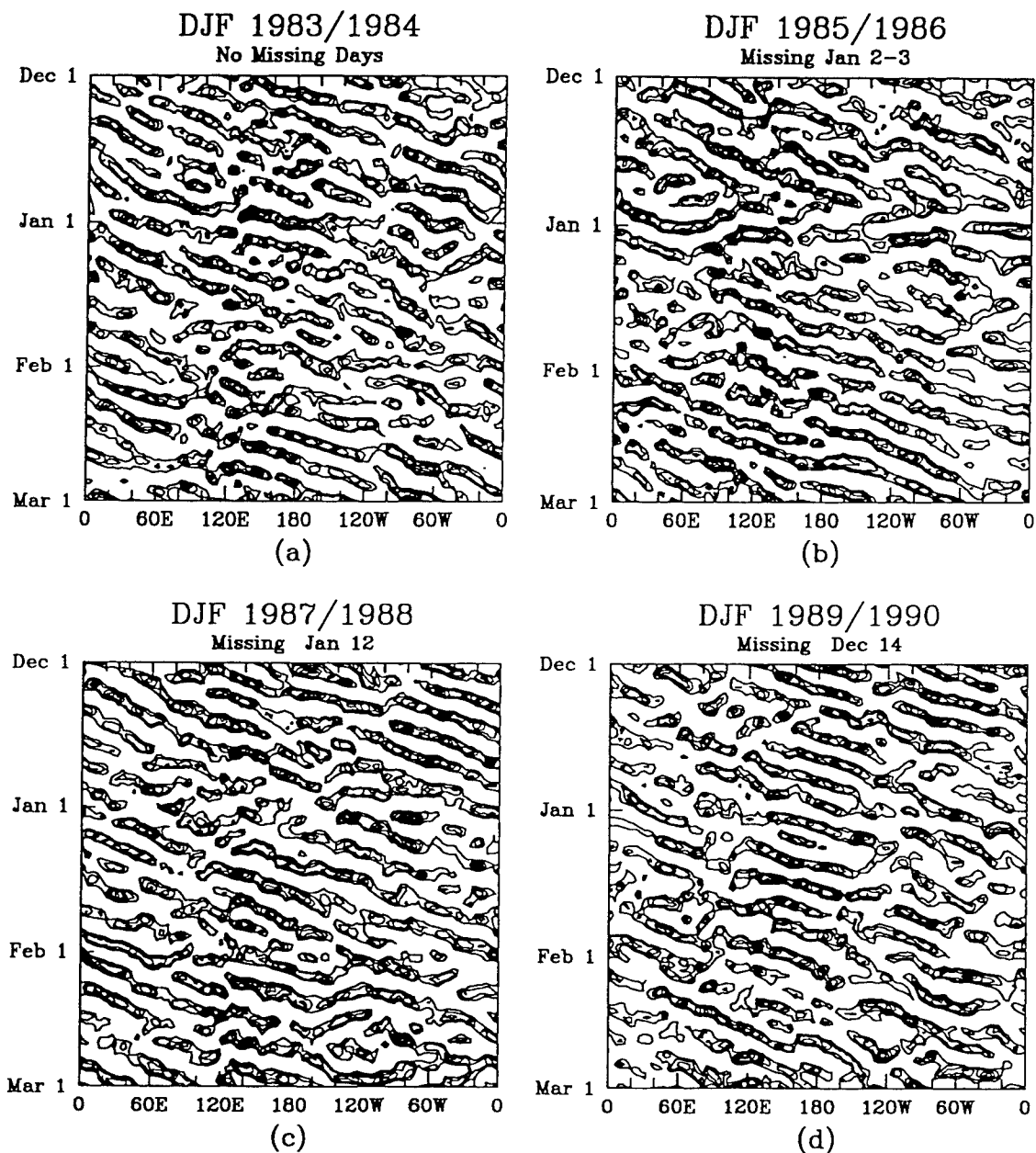
FIG. A15. As in Fig. A1, except for (a) DJF 1983/1984, (b) DJF 1985/1986, (c) DJF 1987/1988, and (d) DJF 1989/1990.

Synoptic Filtered Time–Longitude Plots at 20.0 N

DJF 1983/1984
No Missing Days

DJF 1985/1986
Missing Jan 2–3

(a)

(b)

DJF 1987/1988
Missing Jan 12

DJF 1989/1990
Missing Dec 14

(c)

(d)
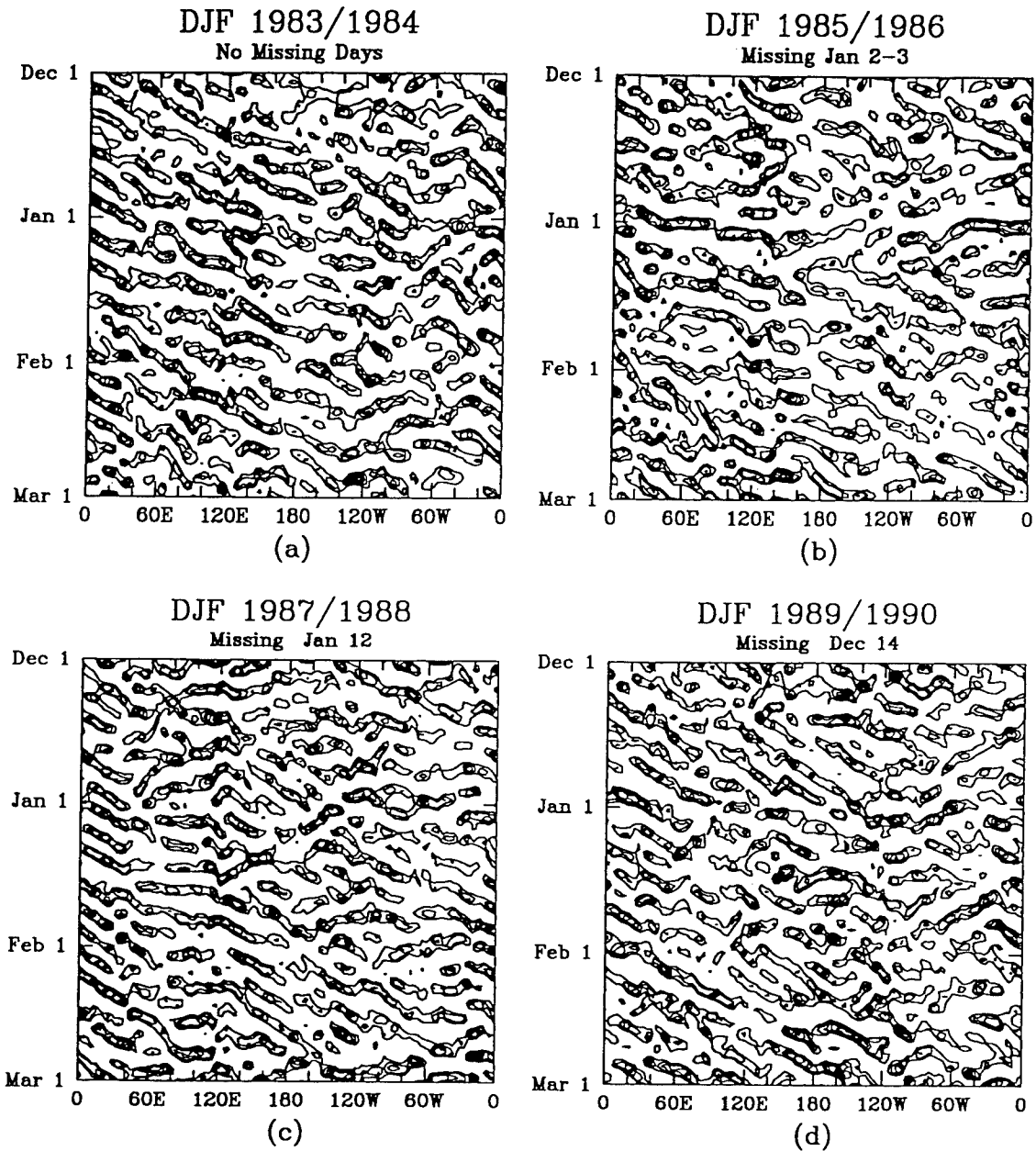
FIG. A16. As in Fig. A15, except at 20°N.

Synoptic Filtered Time–Longitude Plots at 10.0 N
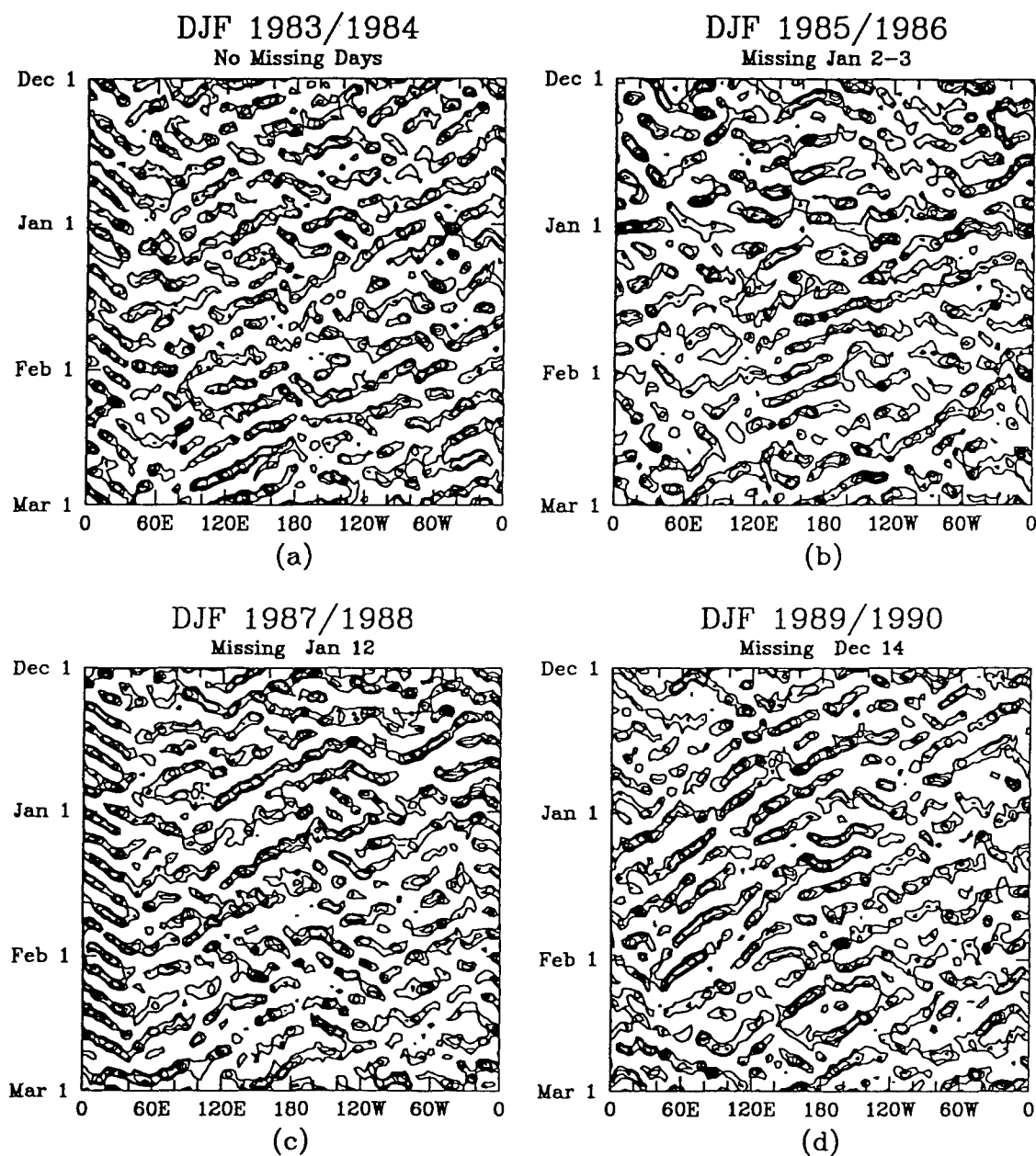
FIG. A17. As in Fig. A15, except at 10°N.

Synoptic Filtered Time–Longitude Plots at the EQ

DJF 1983/1984
No Missing Days

DJF 1985/1986
Missing Jan 2–3

(a)

(b)

DJF 1987/1988
Missing Jan 12

DJF 1989/1990
Missing Dec 14

(c)

(d)
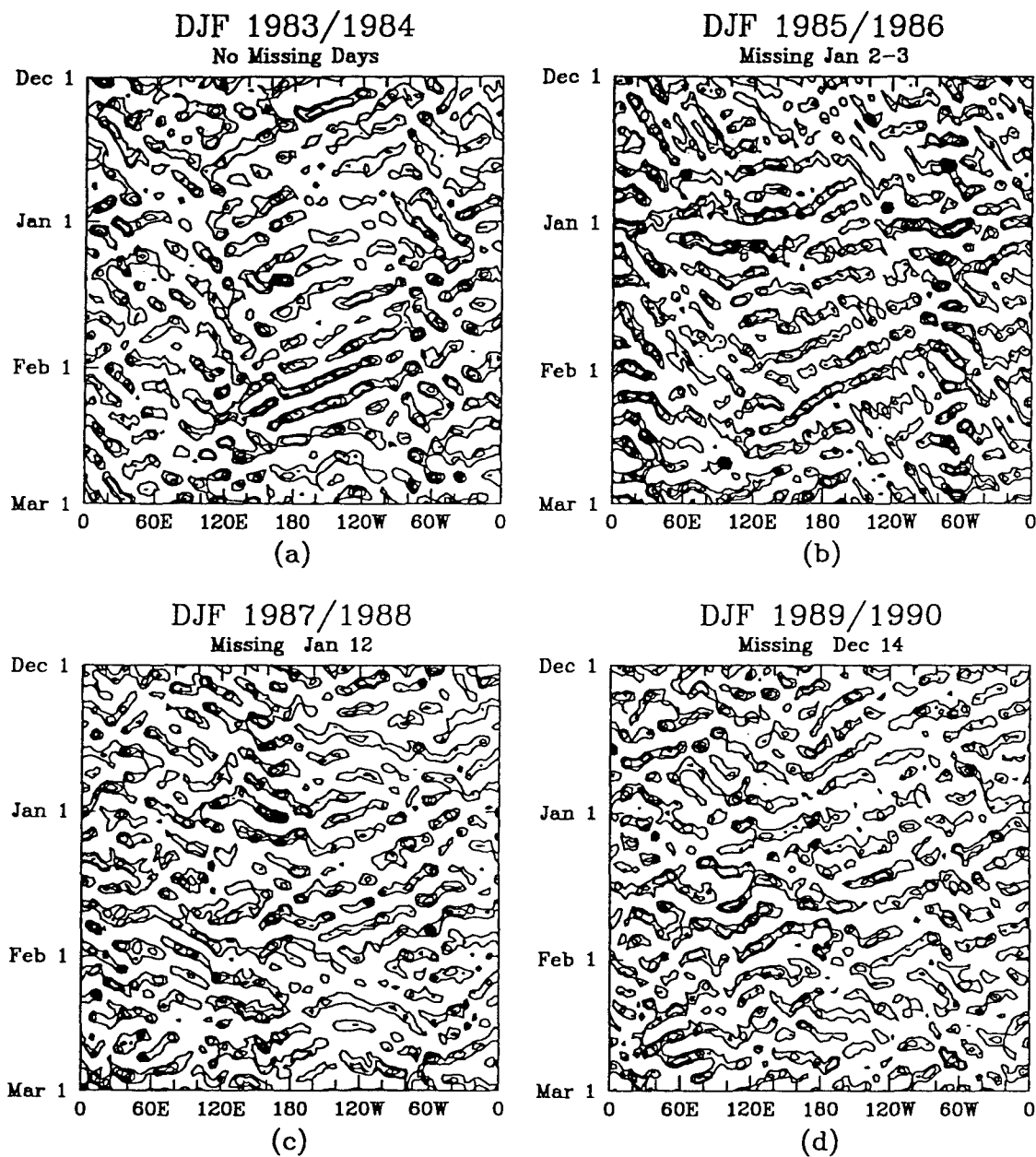
FIG. A18. As in Fig. A15, except at equator.

Synoptic Filtered Time–Longitude Plots at 10.0 S

DJF 1983/1984
No Missing Days

DJF 1985/1986
Missing Jan 2–3

(a)

(b)

DJF 1987/1988
Missing Jan 12

DJF 1989/1990
Missing Dec 14

(c)

(d)
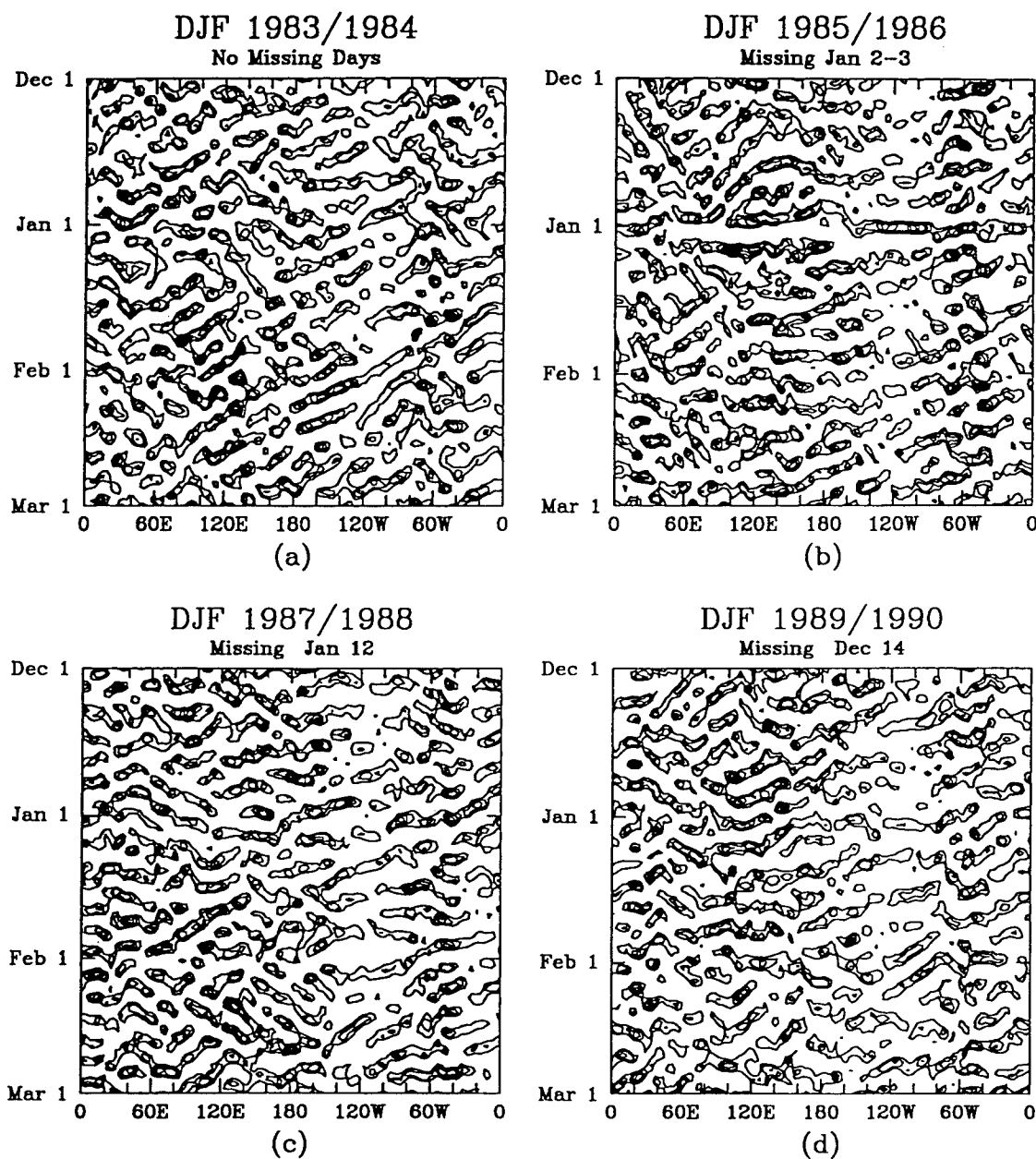
FIG. A19. As in Fig. A15, except at 10°S.

Synoptic Filtered Time–Longitude Plots at 20.0 S

DJF 1983/1984
No Missing Days

DJF 1985/1986
Missing Jan 2–3

(a)

(b)

DJF 1987/1988
Missing Jan 12

DJF 1989/1990
Missing Dec 14

(c)

(d)
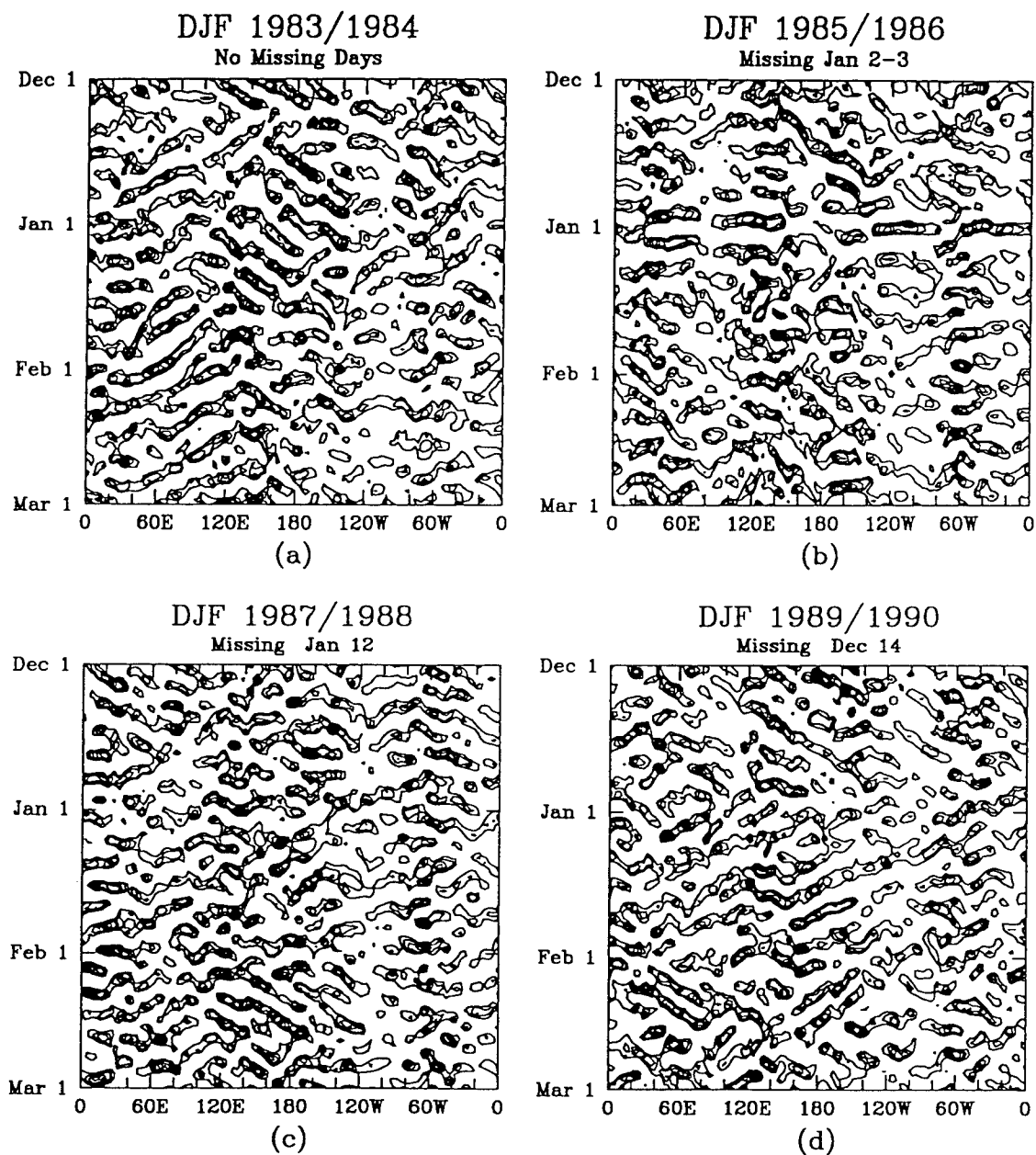
FIG. A20. As in Fig. A15, except at 20°S.

Synoptic Filtered Time−Longitude Plots at 30.0 S

DJF 1983/1984
No Missing Days

DJF 1985/1986
Missing Jan 2−3

DJF 1987/1988
Missing Jan 12

DJF 1989/1990
Missing Dec 14
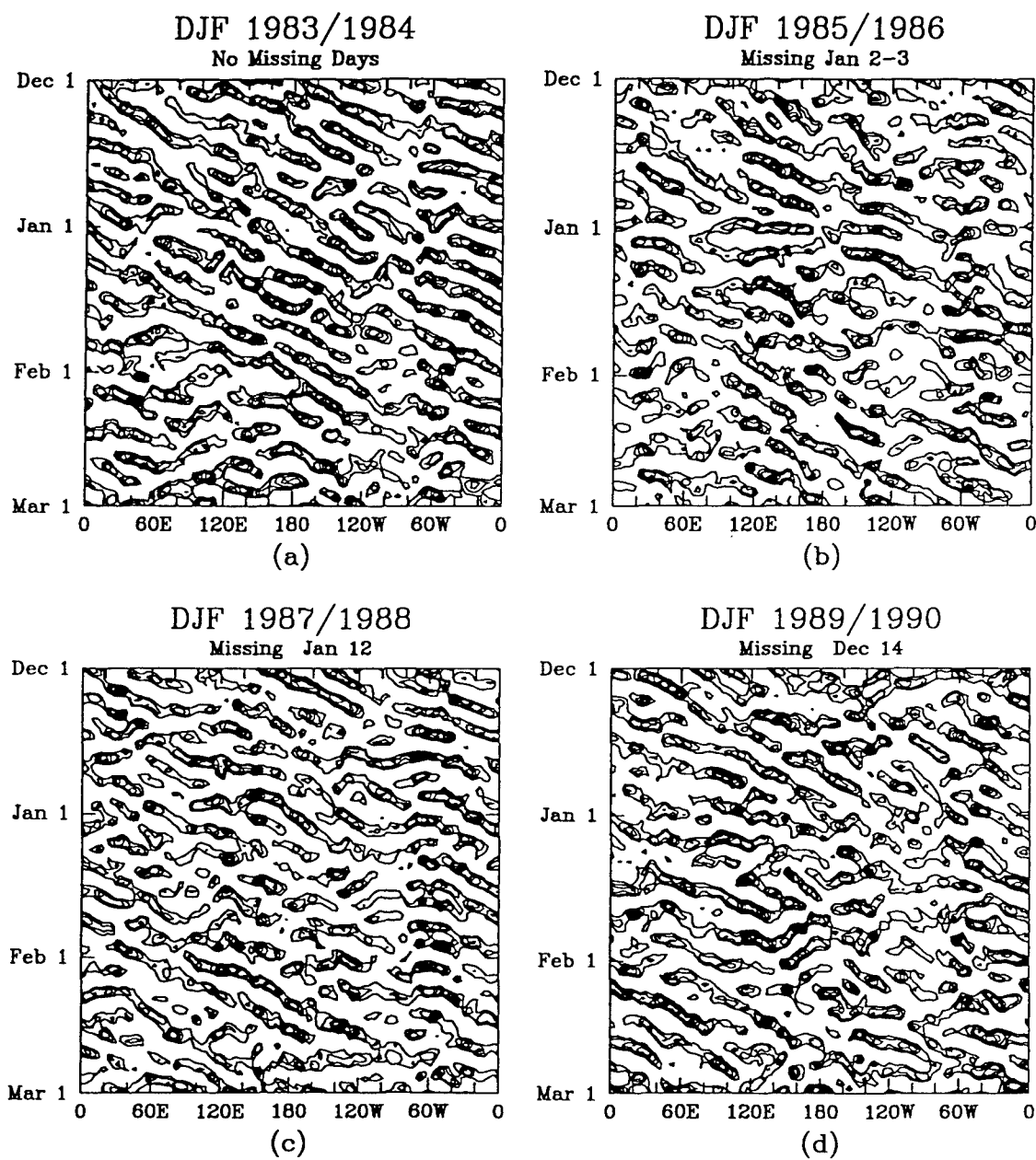
FIG. A21. As in Fig. A15, except at 30°S.

Synoptic Filtered Time—Longitude Plots at 30.0 N

MAM 1981
Missing Apr 19–24

MAM 1982
Missing May 7–8

(a)

(b)

MAM 1983
Missing May 22–28

MAM 1984
Missing May 20–26

(c)

(d)
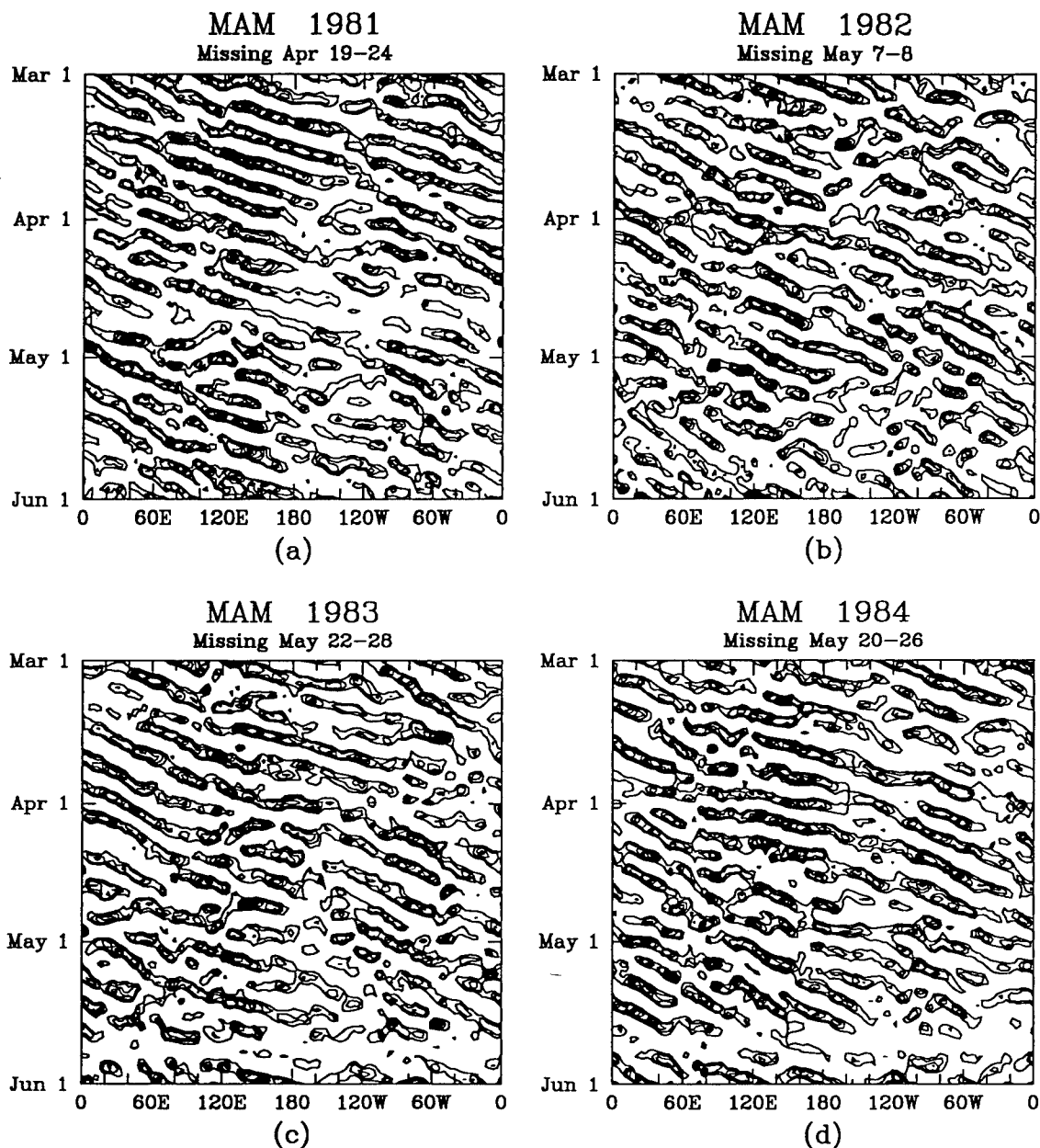
FIG. A22. As in Fig. A1, except for (a) MAM 1981, (b) MAM 1982, (c) MAM 1983, and (d) MAM 1984.

Synoptic Filtered Time−Longitude Plots at 20.0 N

MAM 1981
Missing Apr 19−24

(a)

MAM 1982
Missing May 7−8

(b)

MAM 1983
Missing May 22−28

(c)

MAM 1984
Missing May 20−26

(d)
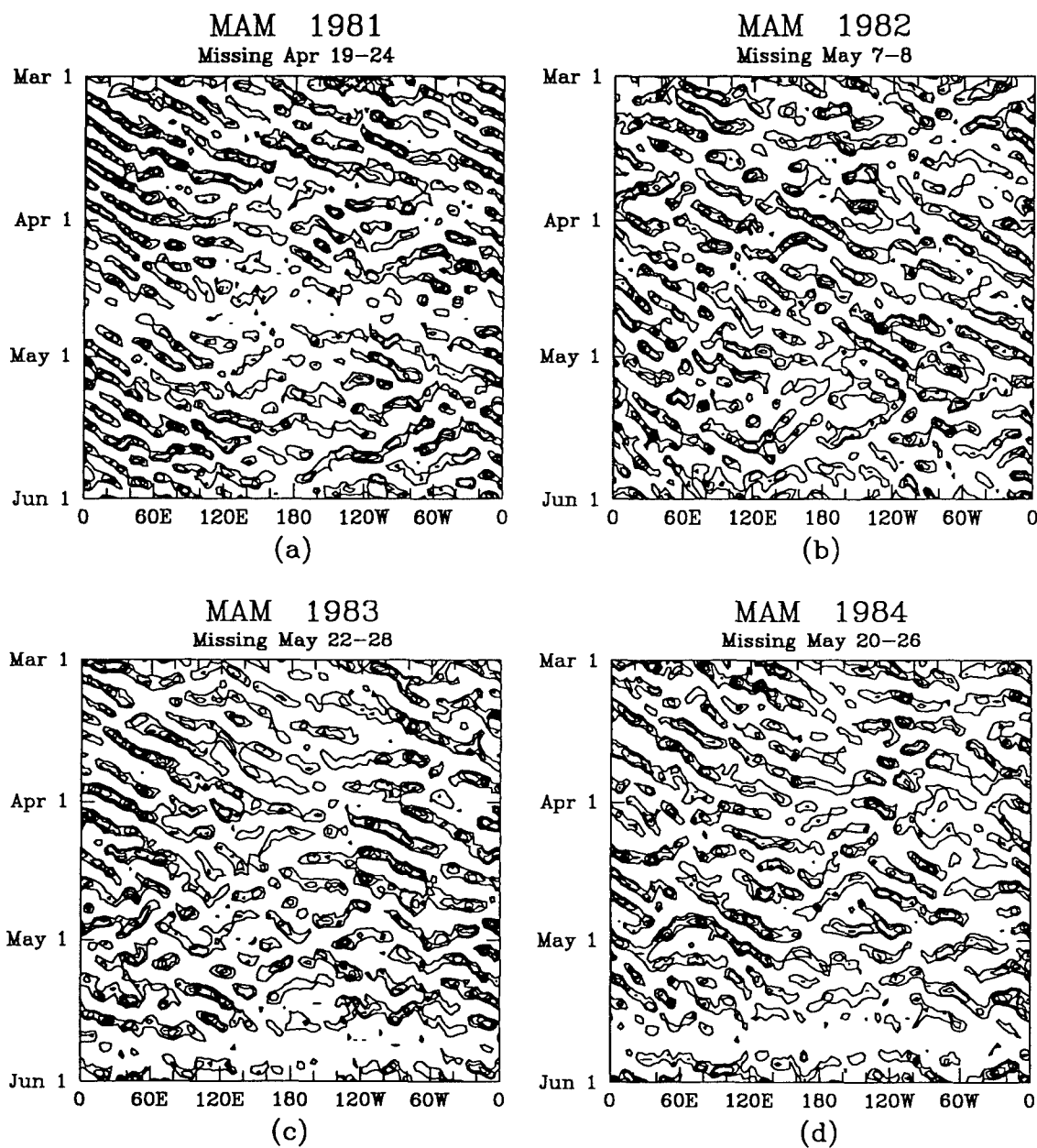
FIG. A23. As in Fig. A22, except at 20°N.

Synoptic Filtered Time–Longitude Plots at 10.0 N

MAM 1981
Missing Apr 19–24

(a)

MAM 1982
Missing May 7–8

(b)

MAM 1983
Missing May 22–28

(c)

MAM 1984
Missing May 20–26

(d)
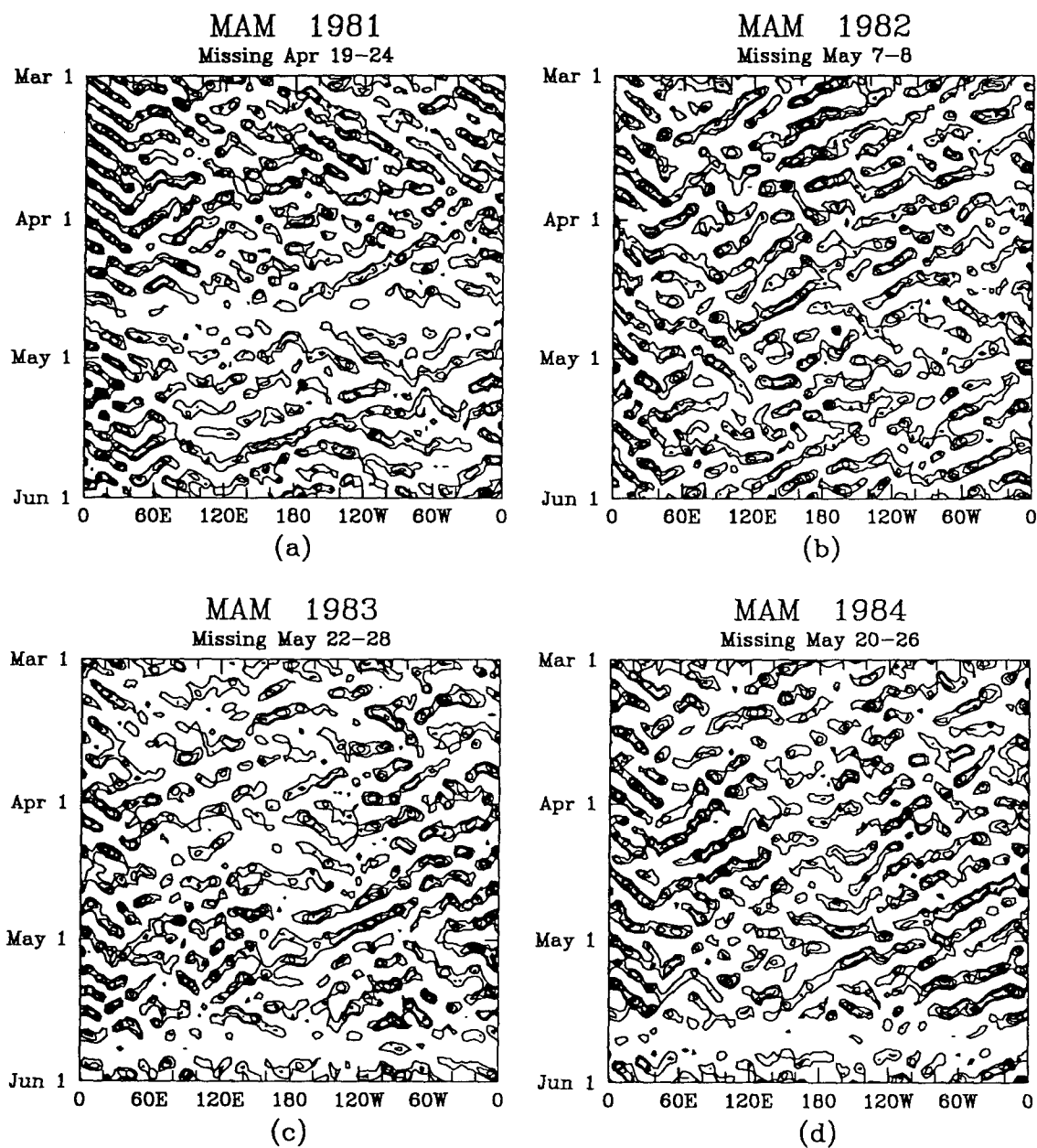
FIG. A24. As in Fig. A22, except at 10°N.

Synoptic Filtered Time−Longitude Plots at the EQ

MAM 1981
Missing Apr 19−24

MAM 1982
Missing May 7−8

(a)

(b)

MAM 1983
Missing May 22−28

MAM 1984
Missing May 20−26

(c)

(d)
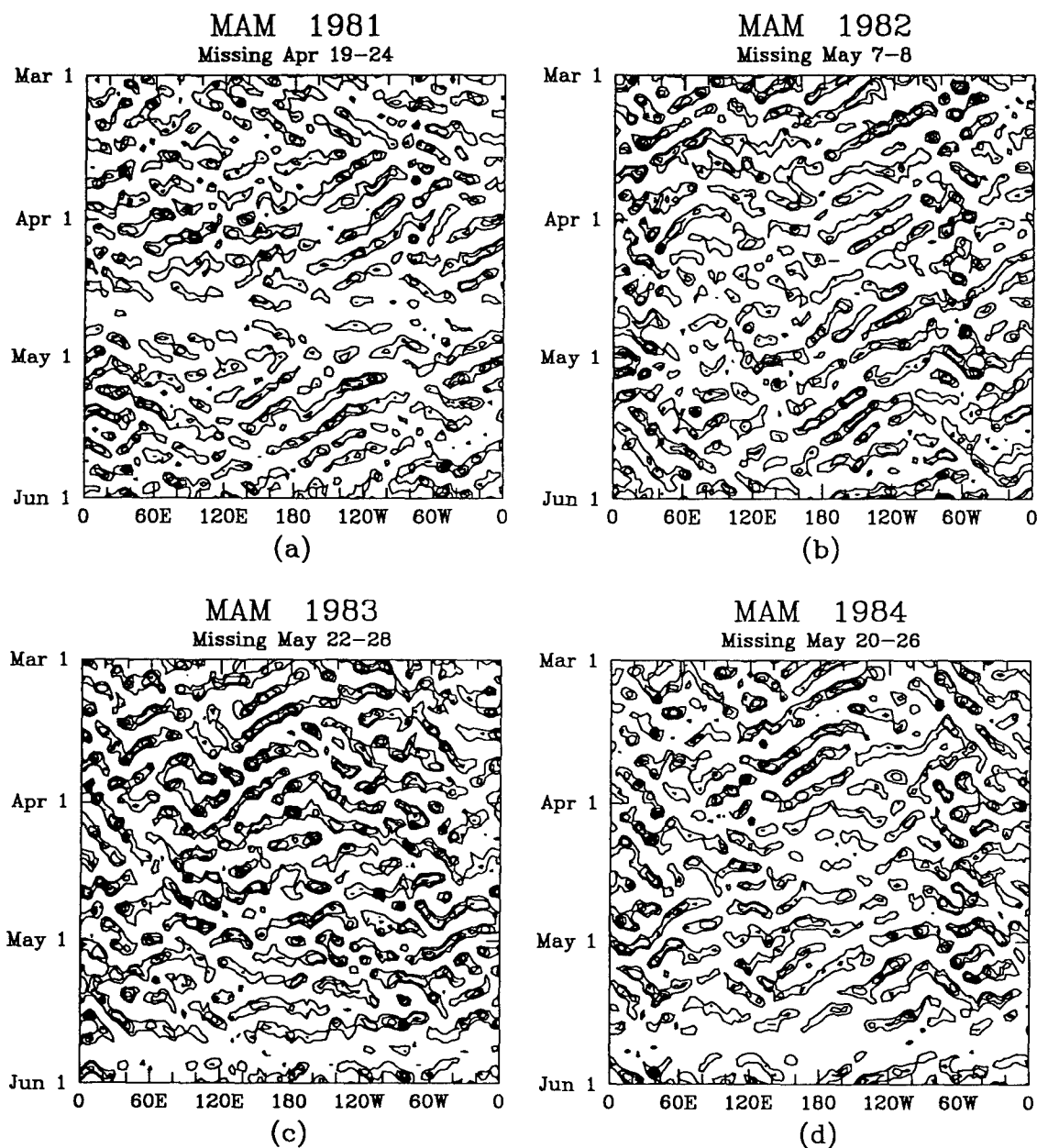
FIG. A25. As in Fig. A22, except at the equator.

Synoptic Filtered Time–Longitude Plots at 10.0 S
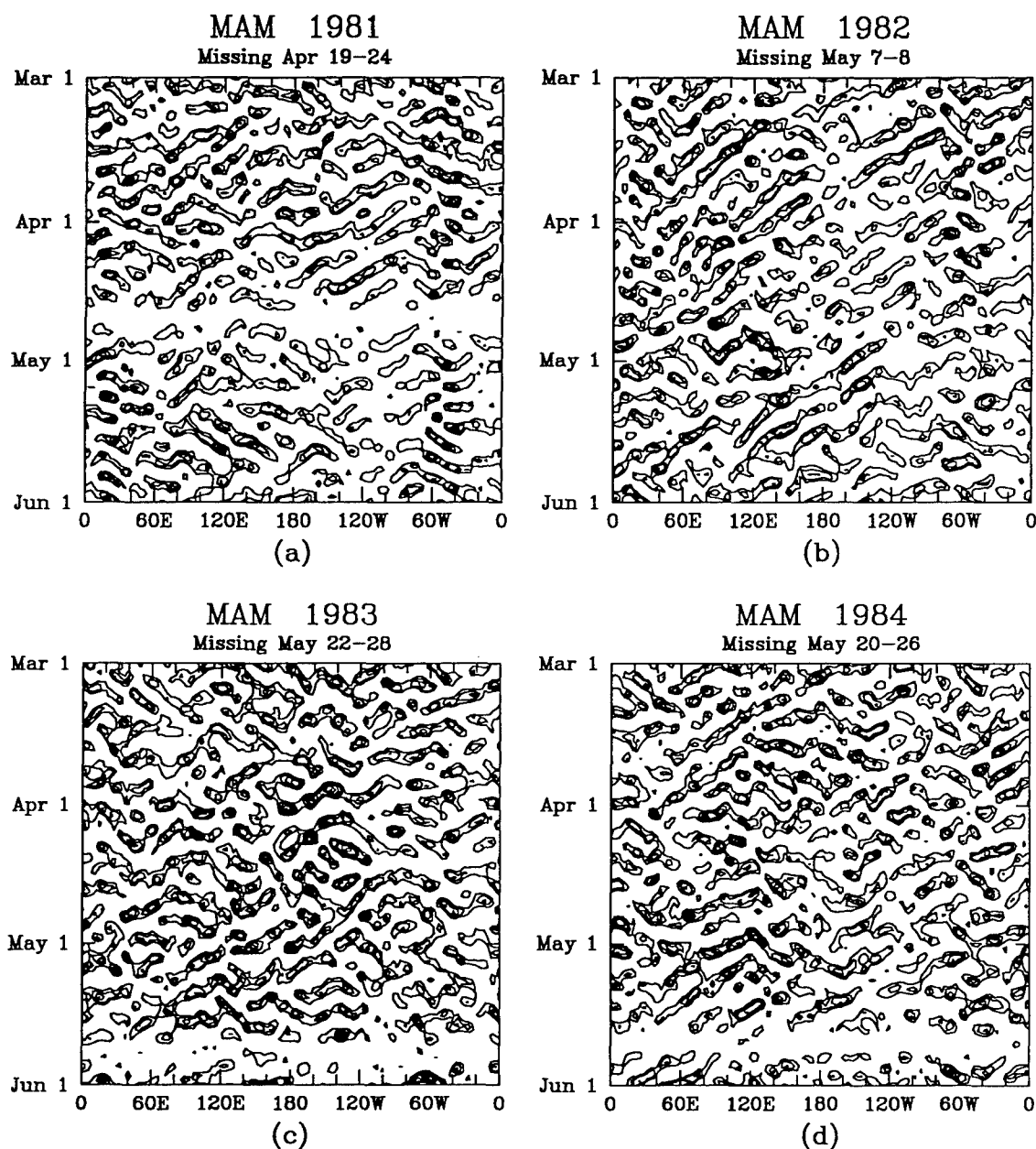
FIG. A26. As in Fig. A22, except at 10°S.

Synoptic Filtered Time–Longitude Plots at 20.0 S
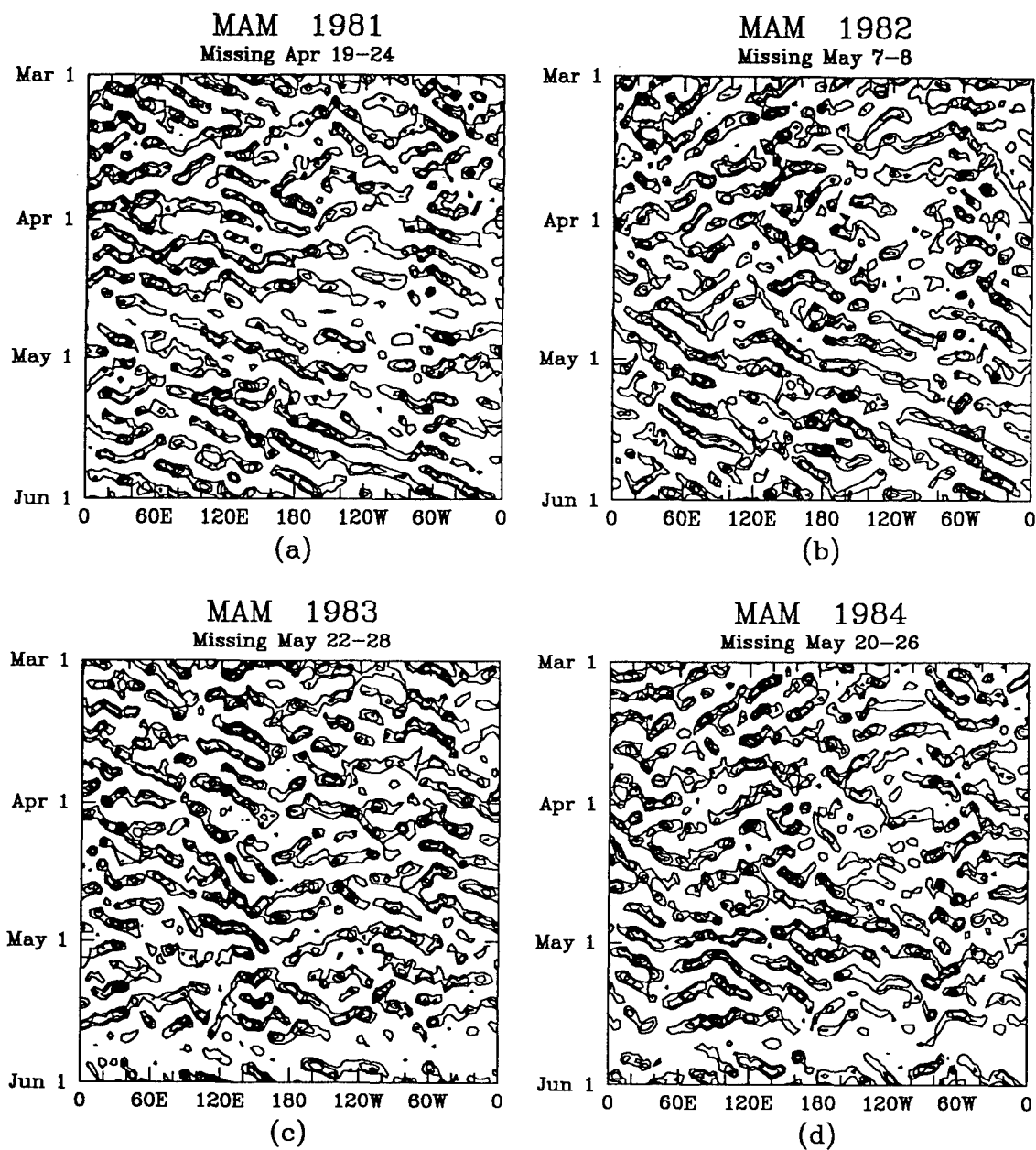
FIG. A27. As in Fig. A22, except at 20°S.

Synoptic Filtered Time–Longitude Plots at 30.0 S

MAM 1981
Missing Apr 19–24

MAM 1982
Missing May 7–8

(a)

(b)

MAM 1983
Missing May 22–28

MAM 1984
Missing May 20–26

(c)

(d)
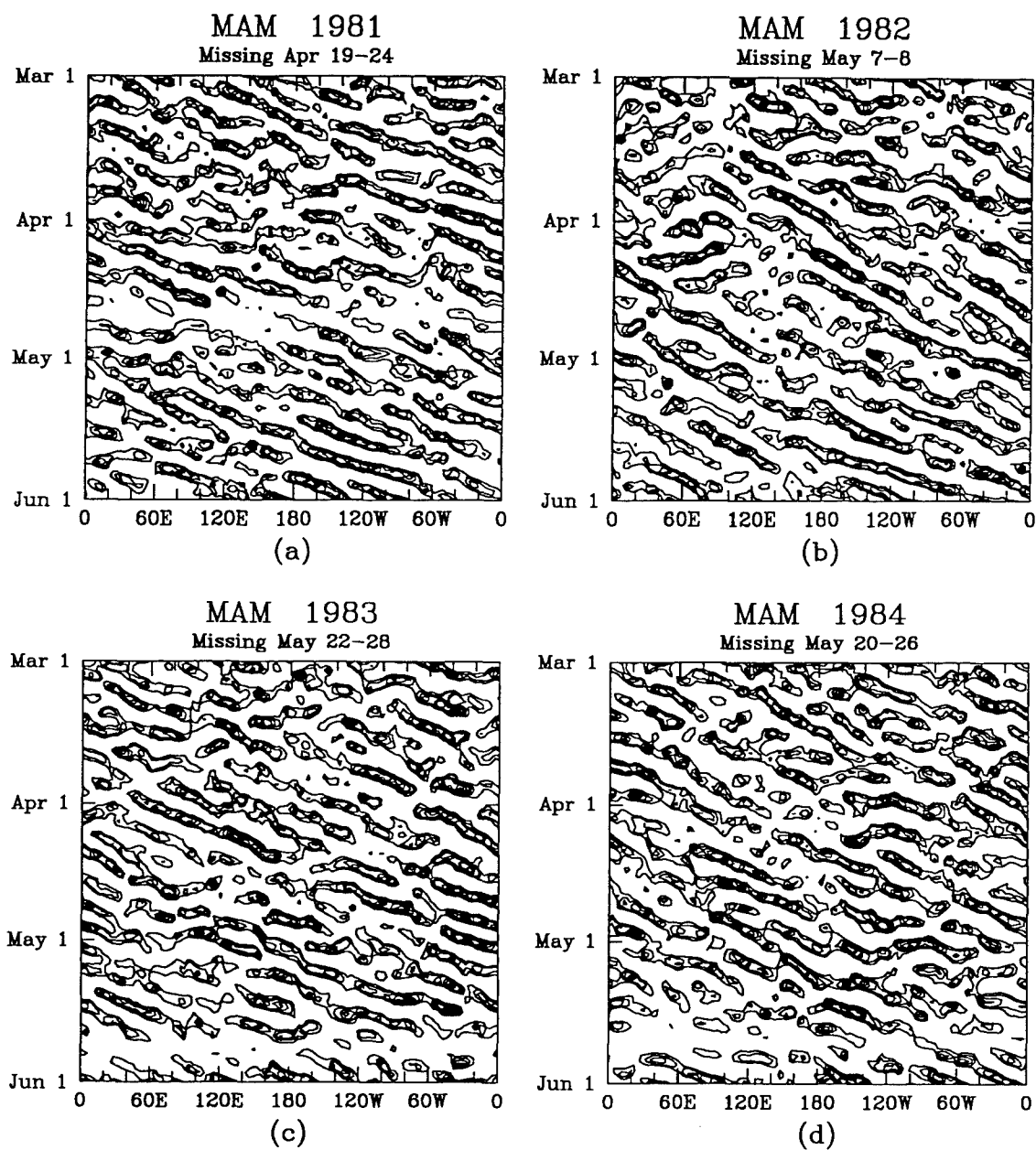
FIG. A28. As in Fig. A22, except at 30°S.

Synoptic Filtered Time−Longitude Plots at 30.0 N

MAM 1988
Missing Mar 29, Apr 5, 26, May 17

(a)

MAM 1989
No Missing Days

(b)

JJA 1981
Missing Aug 25−29

(c)

JJA 1982
No Missing Days

(d)
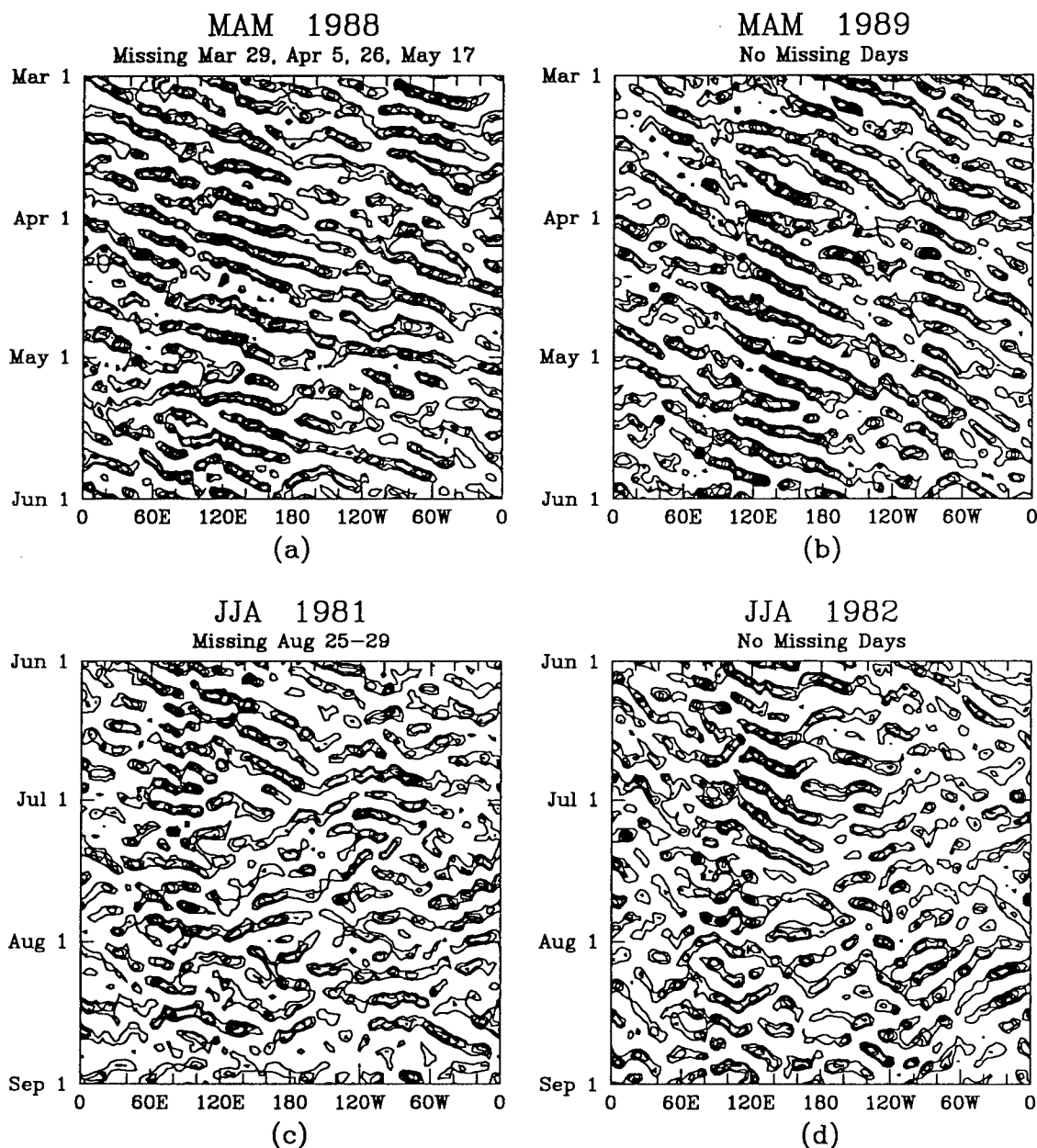
FIG. A29. As in Fig. A1, except for (a) MAM 1988, (b) MAM 1989, (c) JJA 1981, and (d) JJA 1982.

Synoptic Filtered Time–Longitude Plots at 20.0 N
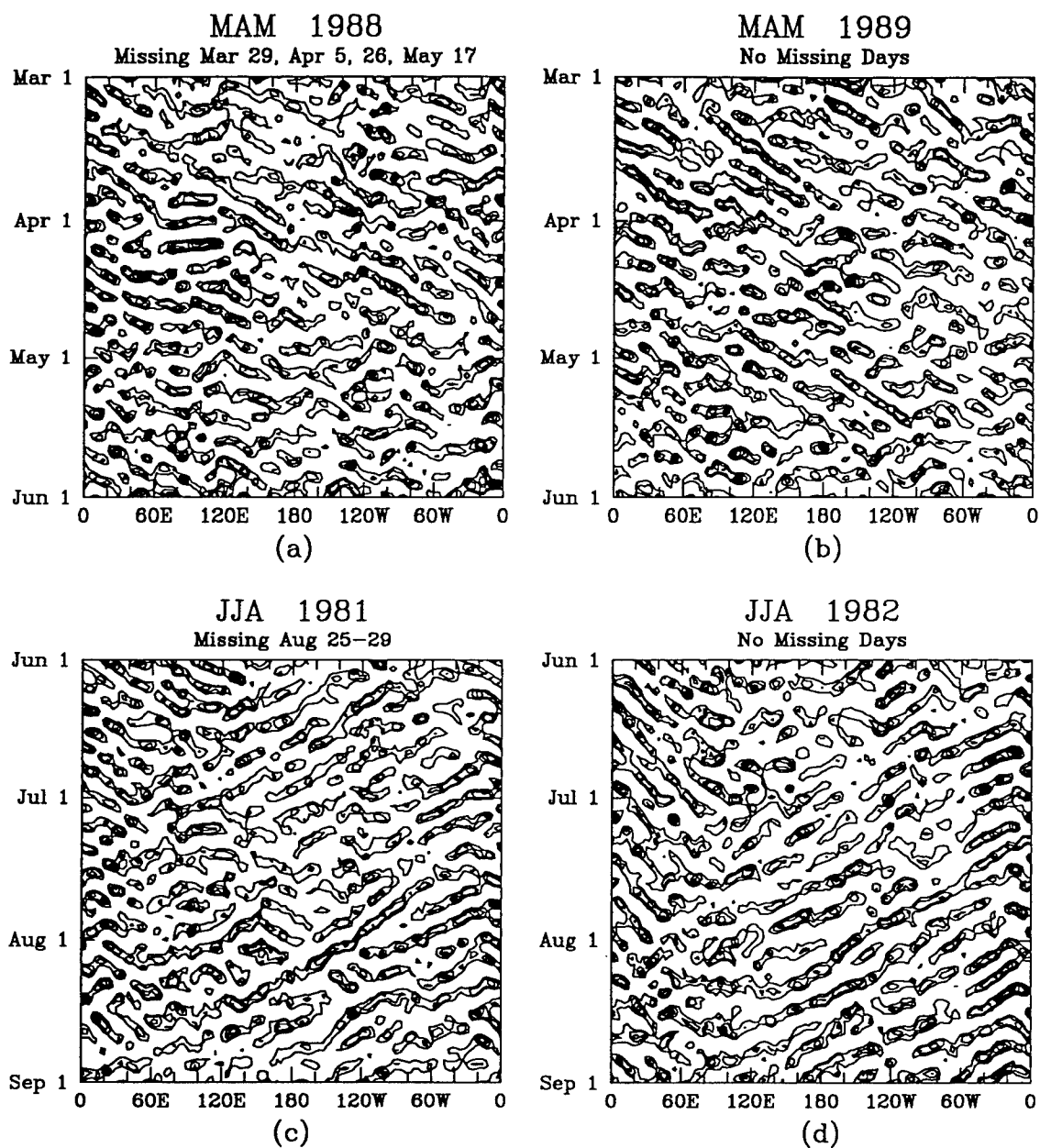
FIG. A30. As in Fig. A29, except at 20°N.

Synoptic Filtered Time–Longitude Plots at 10.0 N

MAM 1988
Missing Mar 29, Apr 5, 26, May 17

(a)

MAM 1989
No Missing Days

(b)

JJA 1981
Missing Aug 25–29

(c)

JJA 1982
No Missing Days

(d)
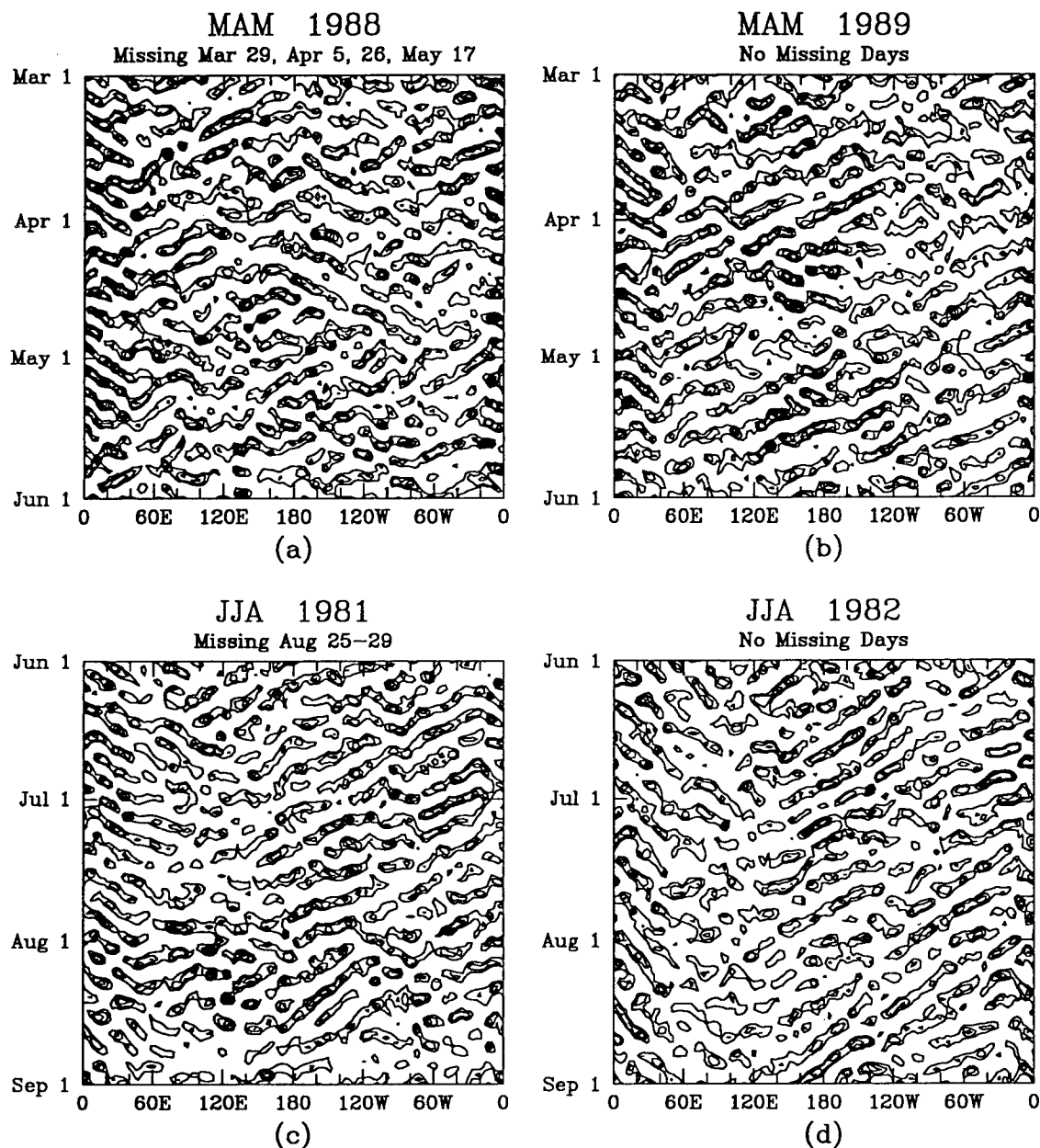
FIG. A31. As in Fig. A29, except at 10°N.

Synoptic Filtered Time−Longitude Plots at the EQ

MAM 1988
Missing Mar 29, Apr 5, 26, May 17

MAM 1989
No Missing Days

(a)

(b)

JJA 1981
Missing Aug 25−29

JJA 1982
No Missing Days

(c)

(d)
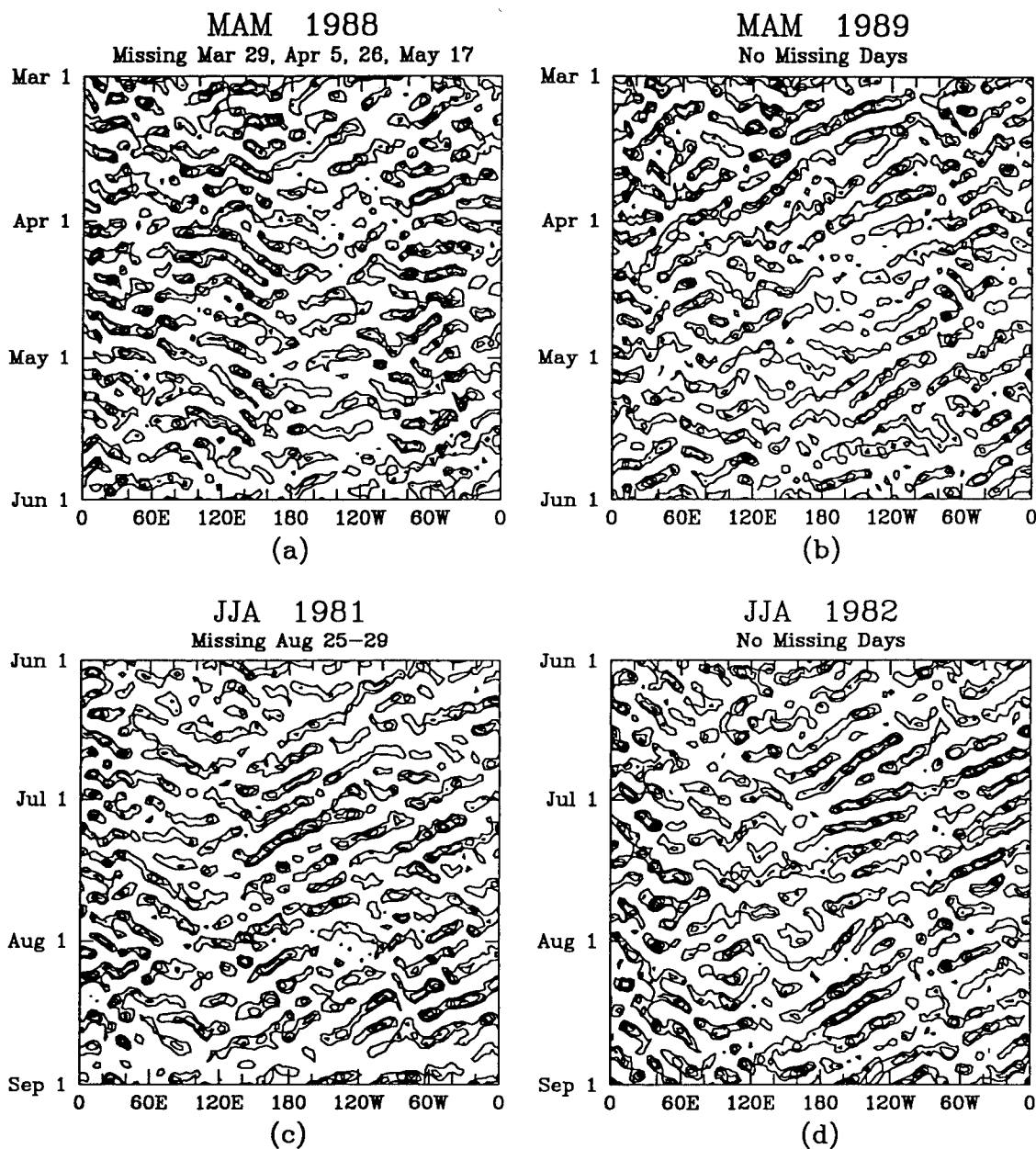
FIG. A32. As in Fig. A29, except at the equator.

Synoptic Filtered Time—Longitude Plots at 10.0 S

MAM 1988
Missing Mar 29, Apr 5, 26, May 17

(a)

MAM 1989
No Missing Days

(b)

JJA 1981
Missing Aug 25—29

(c)

JJA 1982
No Missing Days

(d)
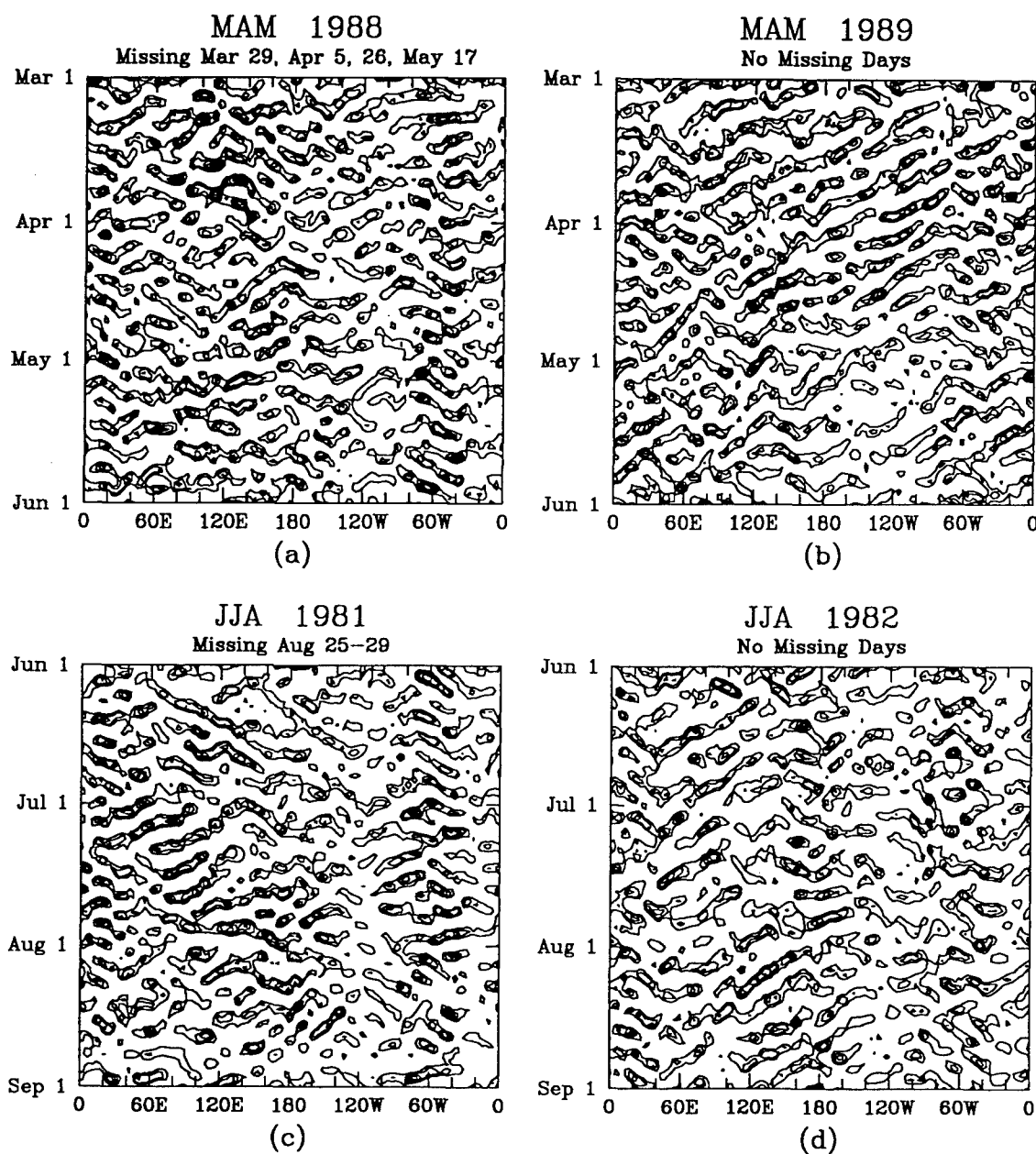
FIG. A33. As in Fig. A29, except at 10°S.

Synoptic Filtered Time–Longitude Plots at 20.0 S

MAM 1988
Missing Mar 29, Apr 5, 26, May 17

MAM 1989
No Missing Days

(a)

(b)

JJA 1981
Missing Aug 25–29

JJA 1982
No Missing Days

(c)

(d)
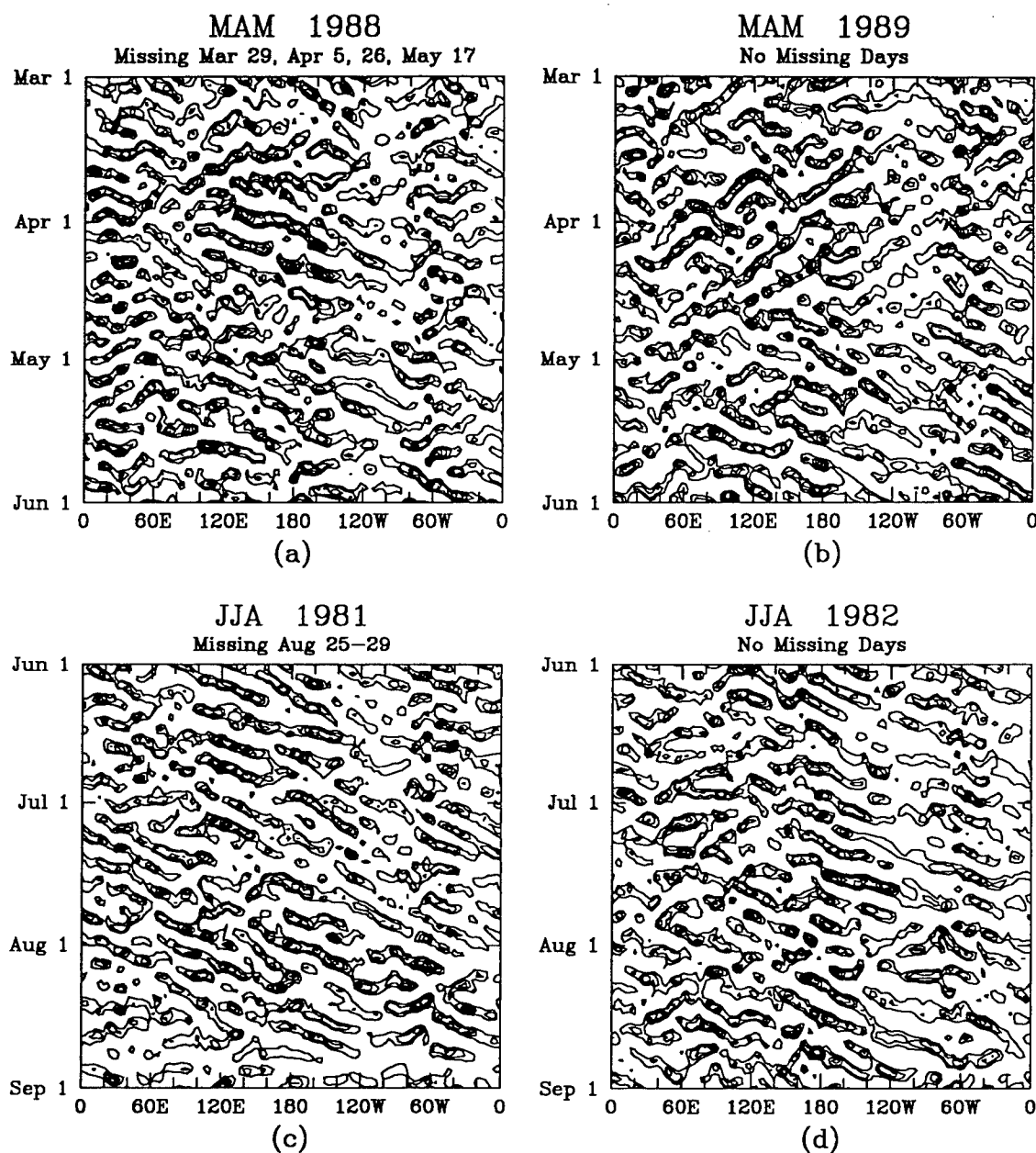
FIG. A34. As in Fig. A29, except at 20°S.

Synoptic Filtered Time–Longitude Plots at 30.0 S

MAM 1988
Missing Mar 29, Apr 5, 26, May 17

(a)

MAM 1989
No Missing Days

(b)

JJA 1981
Missing Aug 25–29

(c)

JJA 1982
No Missing Days

(d)
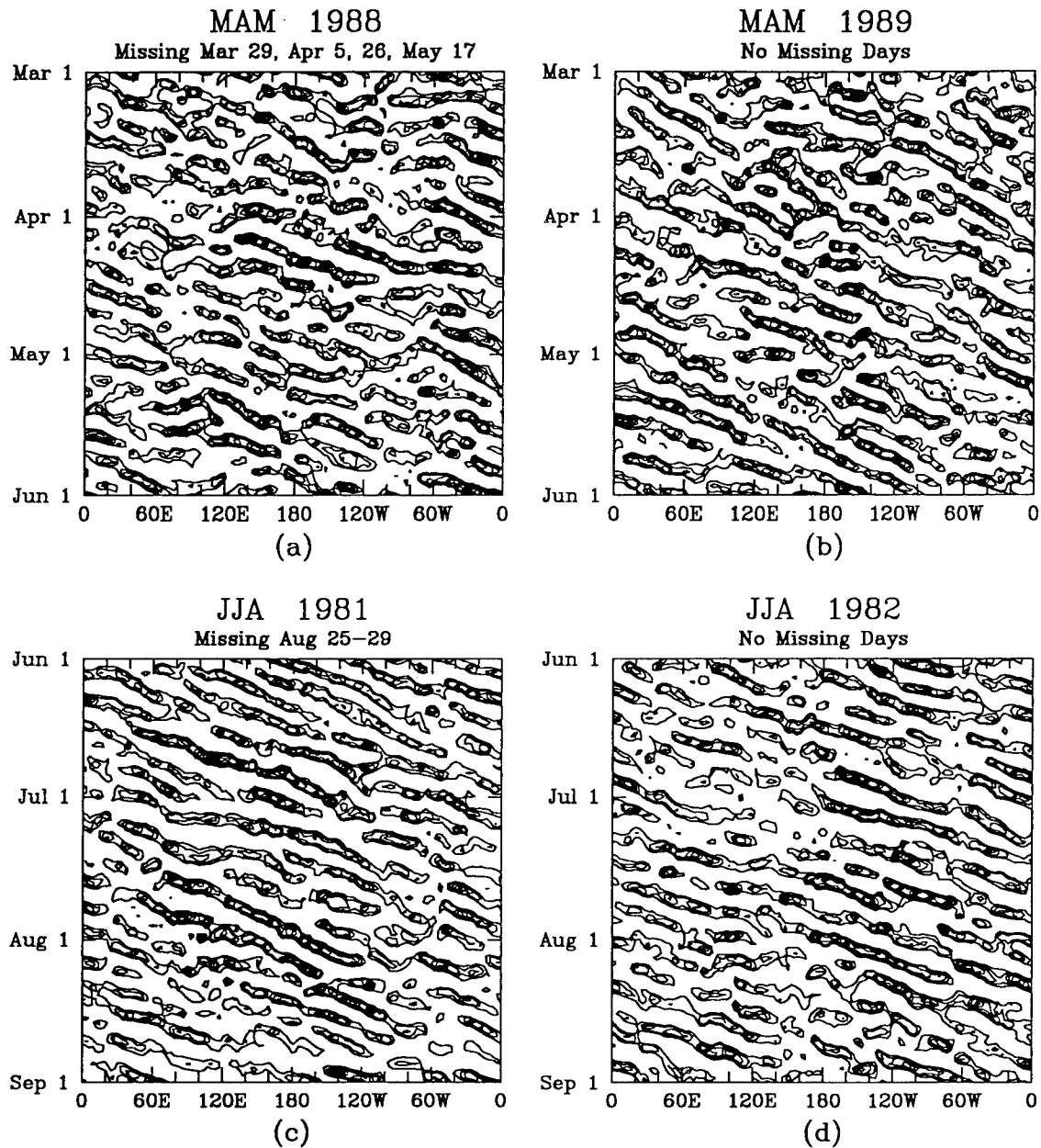
FIG. A35. As in Fig. A29, except at 30°S.

Synoptic Filtered Time–Longitude Plots at 30.0 N
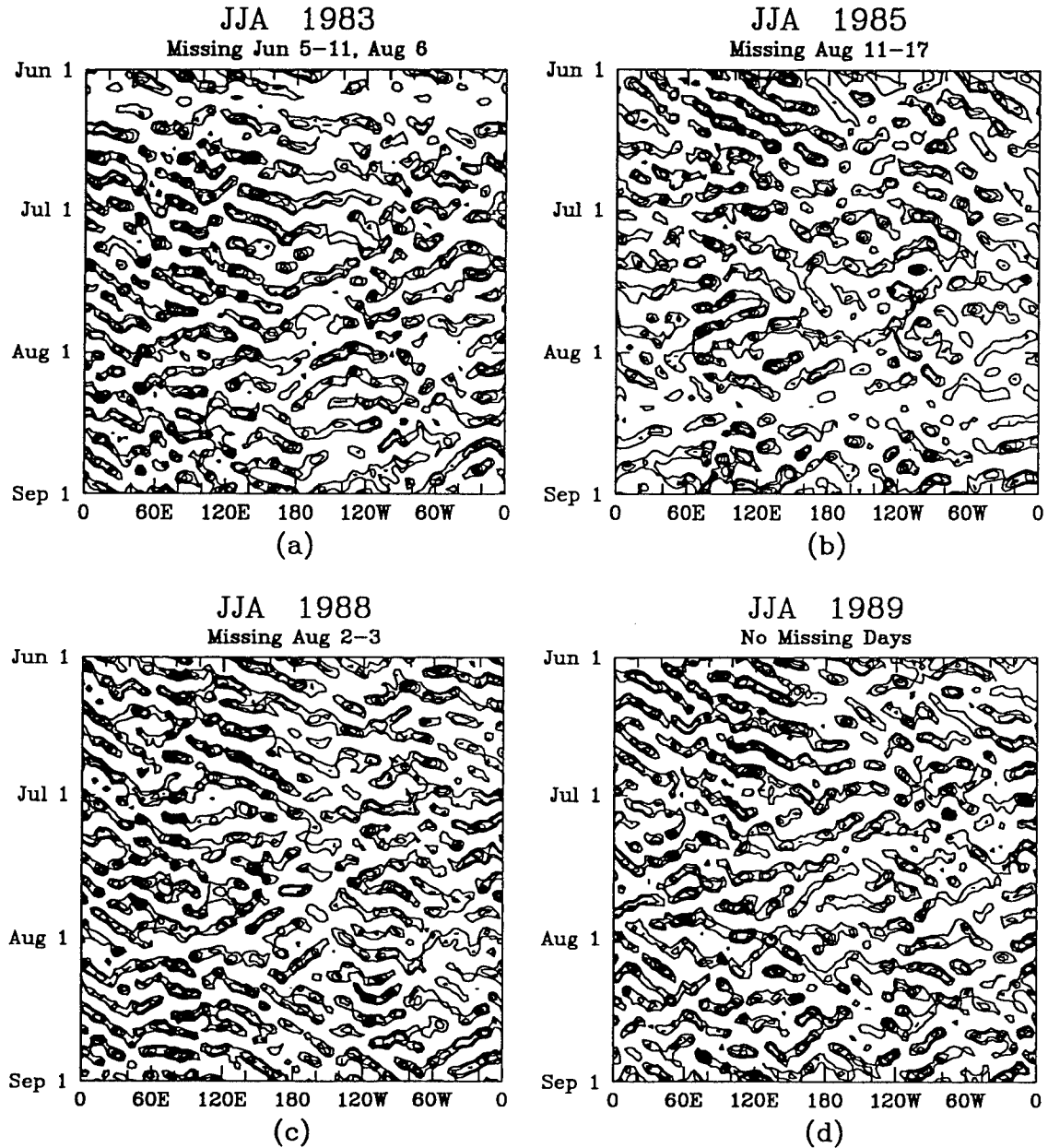
FIG. A36. As in Fig. A1, except for (a) JJA 1983, (b) JJA 1985, (c) JJA 1988, and (d) JJA 1989.

Synoptic Filtered Time−Longitude Plots at 20.0 N
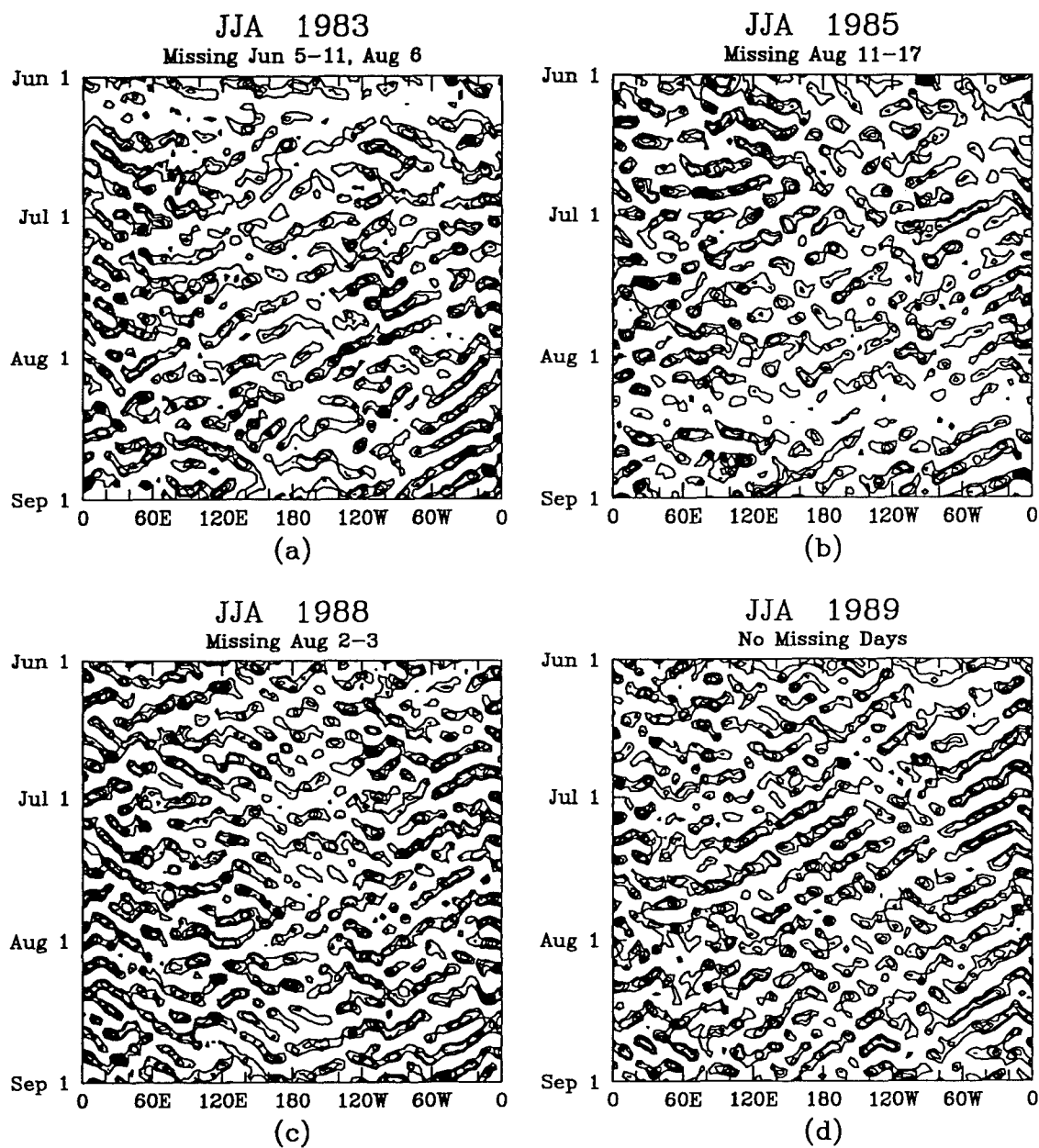
FIG. A37. As in Fig. A36, except at 20°N.

Synoptic Filtered Time–Longitude Plots at 10.0 N

JJA 1983
Missing Jun 5–11, Aug 6

JJA 1985
Missing Aug 11–17

(a)

(b)

JJA 1988
Missing Aug 2–3

JJA 1989
No Missing Days

(c)

(d)
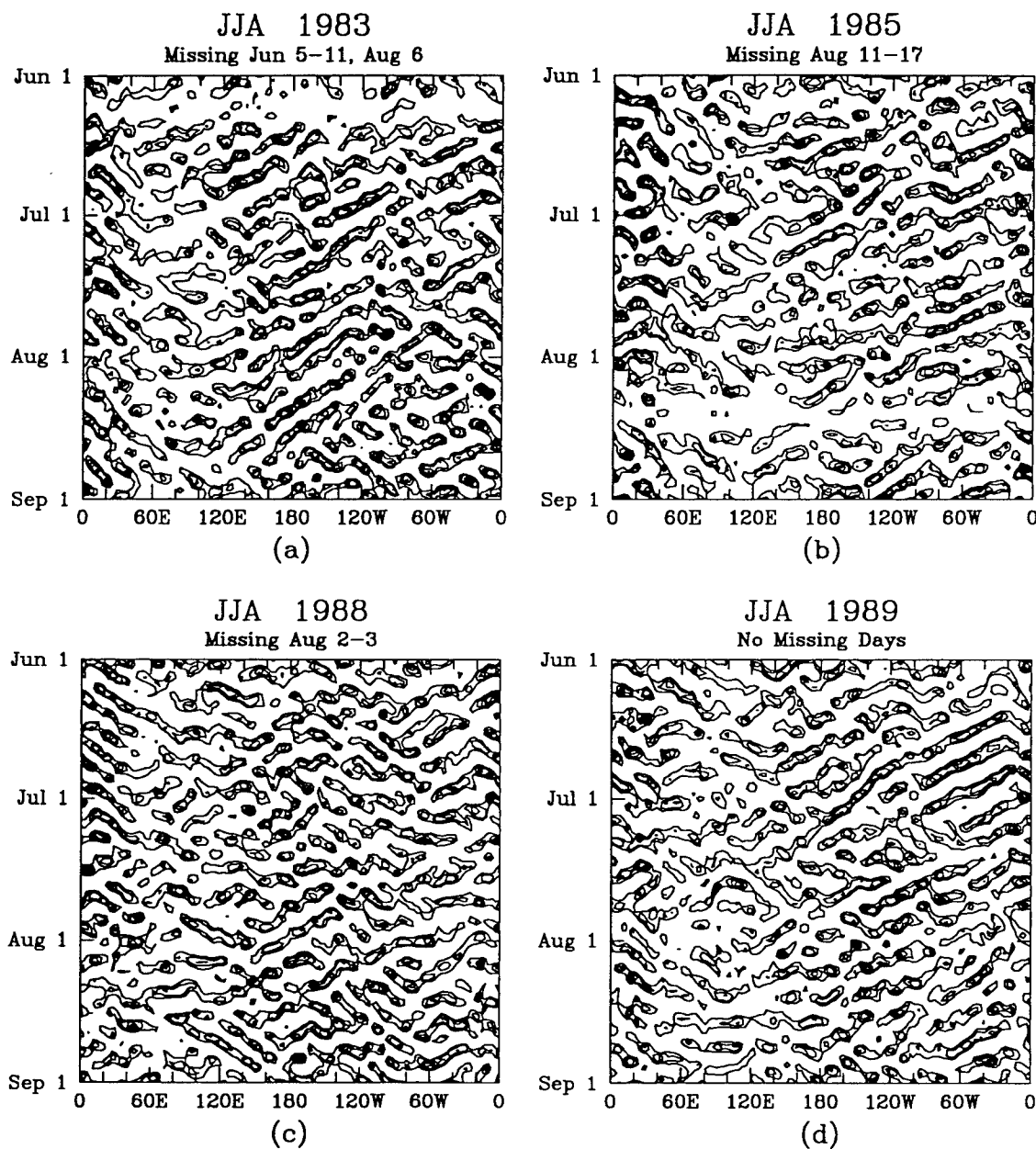
FIG. A38. As in Fig. A36, except at 10°N.

Synoptic Filtered Time–Longitude Plots at the EQ

JJA 1983
Missing Jun 5–11, Aug 6

(a)

JJA 1985
Missing Aug 11–17

(b)

JJA 1988
Missing Aug 2–3

(c)

JJA 1989
No Missing Days

(d)
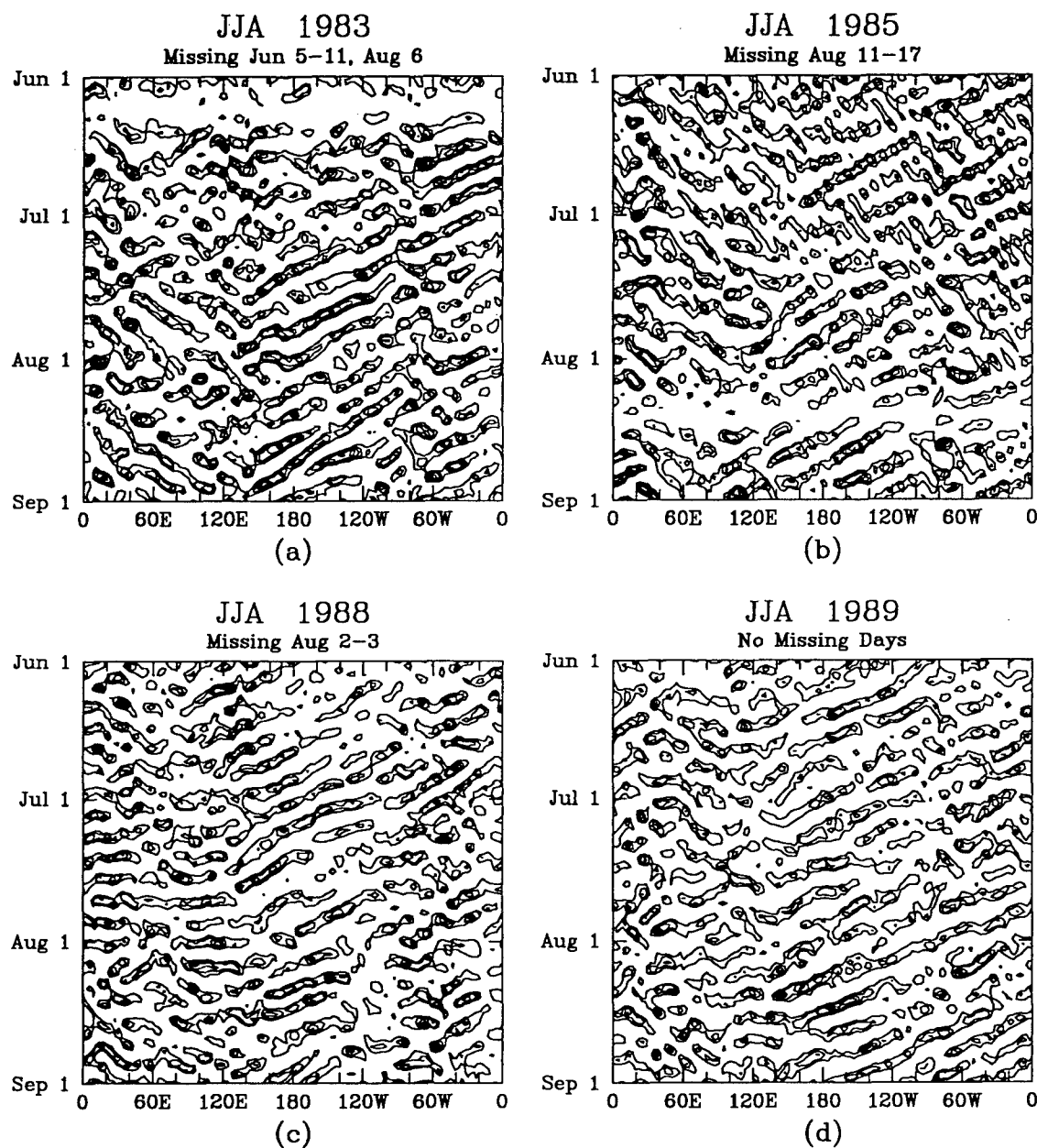
FIG. A39. As in Fig. A36, except at the equator.

Synoptic Filtered Time–Longitude Plots at 10.0 S

JJA 1983
Missing Jun 5–11, Aug 6

JJA 1985
Missing Aug 11–17

(a)

(b)

JJA 1988
Missing Aug 2–3

JJA 1989
No Missing Days

(c)

(d)
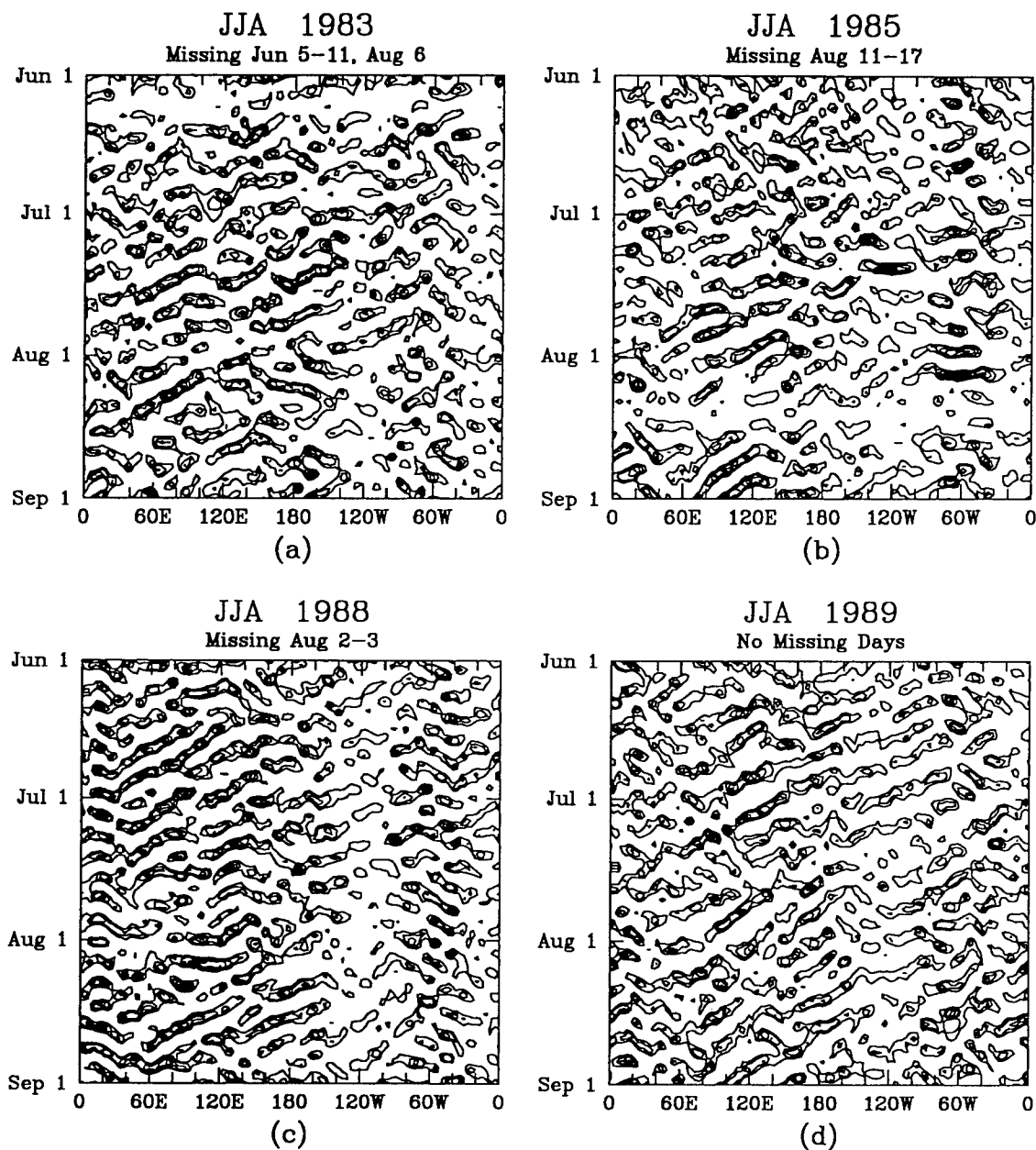
FIG. A40. As in Fig. A36, except at 10°S.

Synoptic Filtered Time−Longitude Plots at 20.0 S

JJA 1983
Missing Jun 5−11, Aug 6

(a)

JJA 1985
Missing Aug 11−17

(b)

JJA 1988
Missing Aug 2−3

(c)

JJA 1989
No Missing Days

(d)
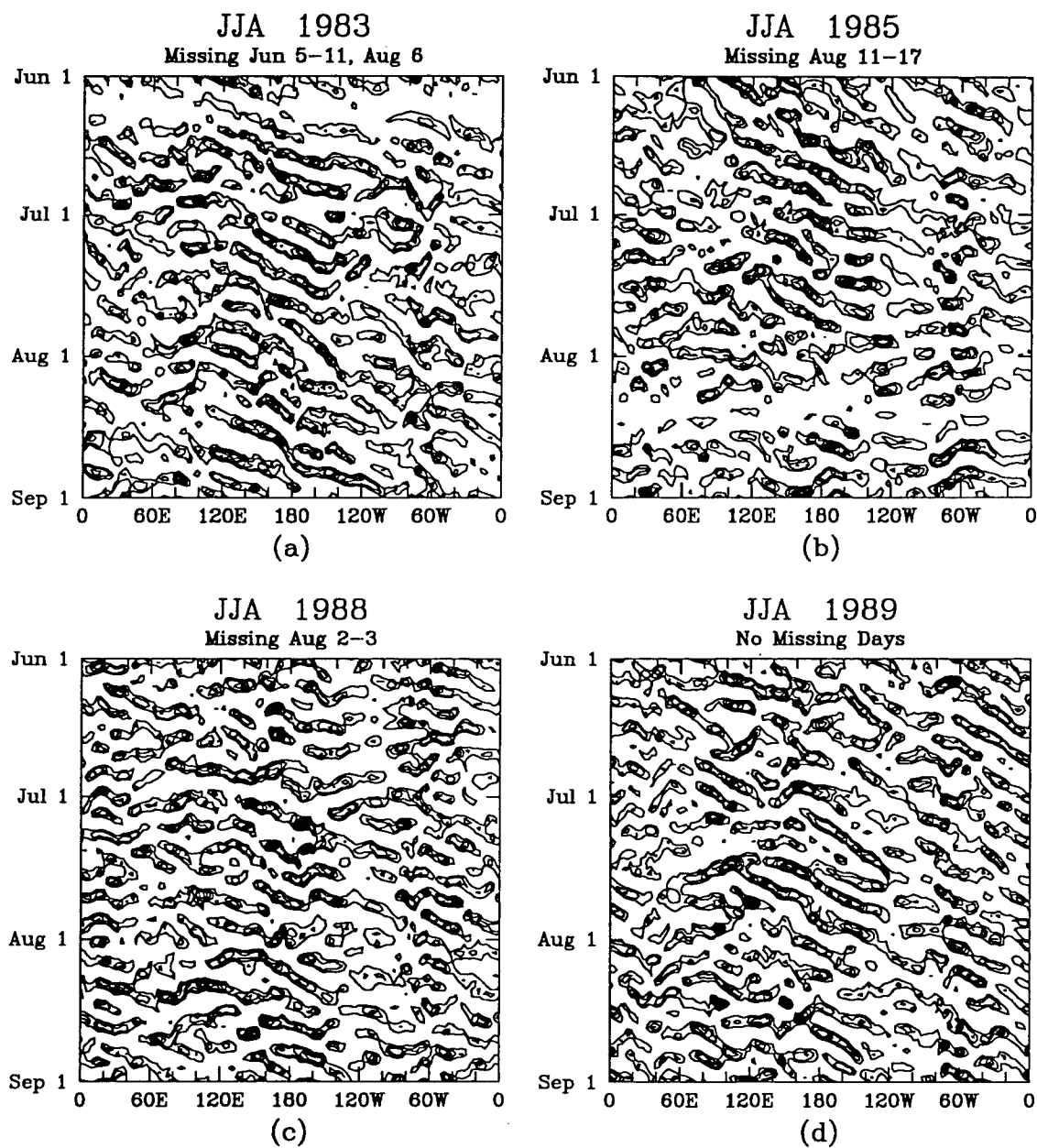
FIG. A41. As in Fig. A36, except at 20°S.

Synoptic Filtered Time–Longitude Plots at 30.0 S

JJA 1983
Missing Jun 5–11, Aug 6

(a)

JJA 1985
Missing Aug 11–17

(b)

JJA 1988
Missing Aug 2–3

(c)

JJA 1989
No Missing Days

(d)
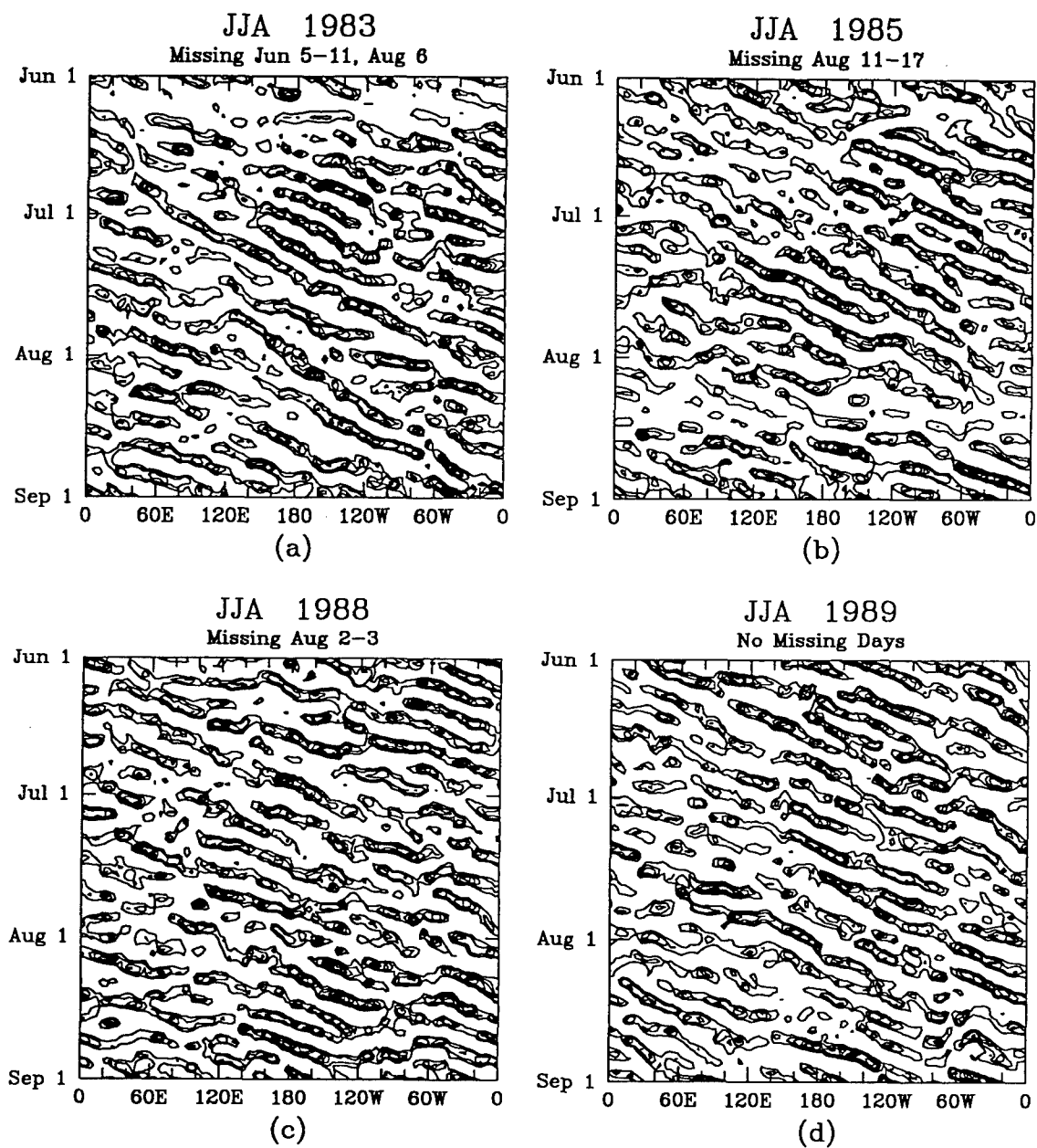
FIG. A42. As in Fig. A36, except at 30°S.

APPENDIX   B
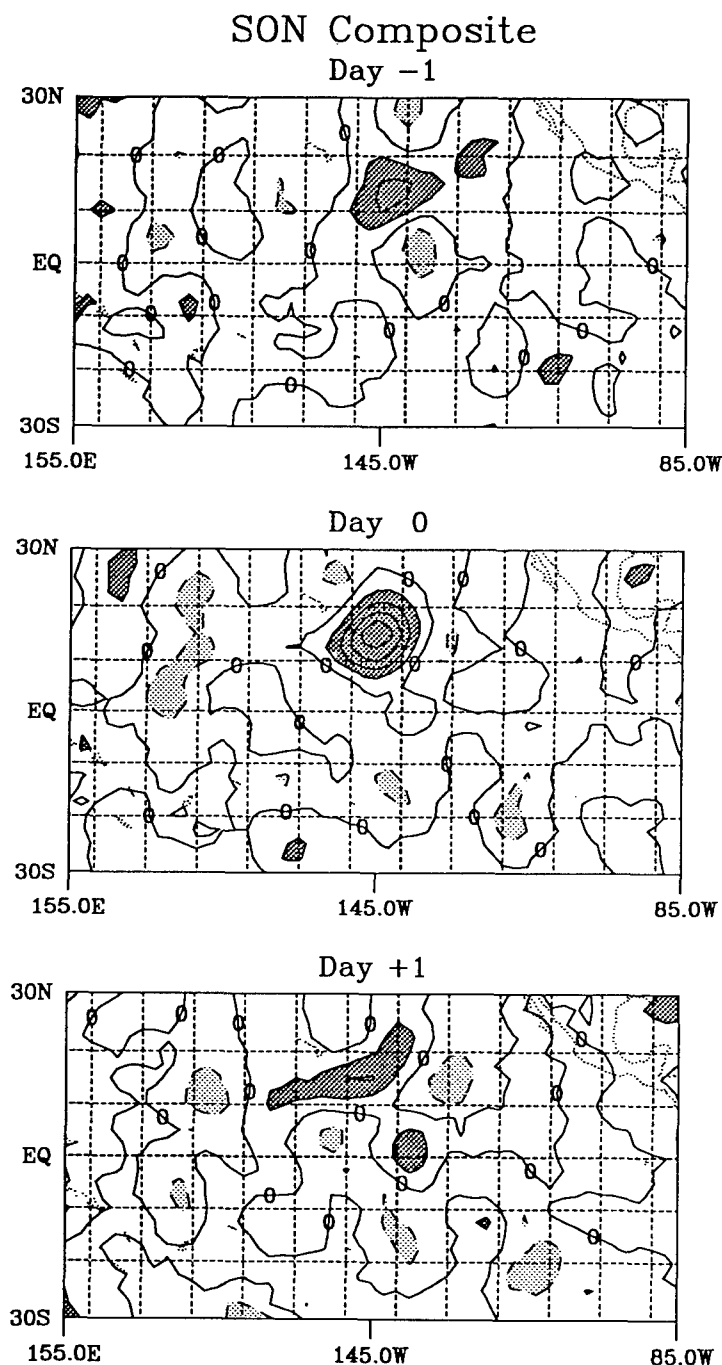
FIG. B1. Lag correlation coefficient between PW at the correlation point (15°N, 145°W) and all other grid points for 37 events exceeding +2 mm anomaly in the 3 to 8 day filtered PW dataset at 15°N, 145°W during five SON seasons. Middle panel is for simultaneous correlation: Top (bottom) panel leads (lags) the values at correlation point by one day. Contour interval is 0.2 with correlations ≥ 0.2 heavily shaded and ≤ -0.2 lightly shaded.
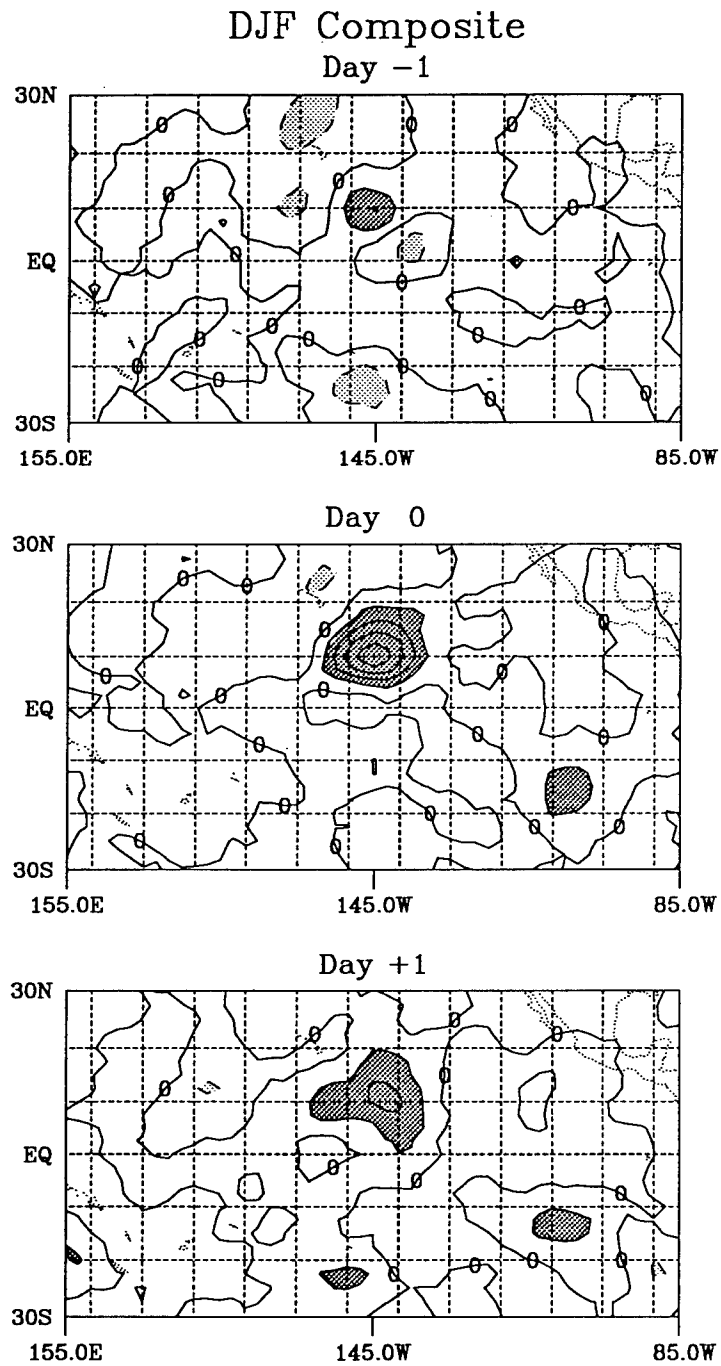
FIG. B2. As in Fig. B1, except at 10°N, 145°W for 47 events during seven DJF seasons.
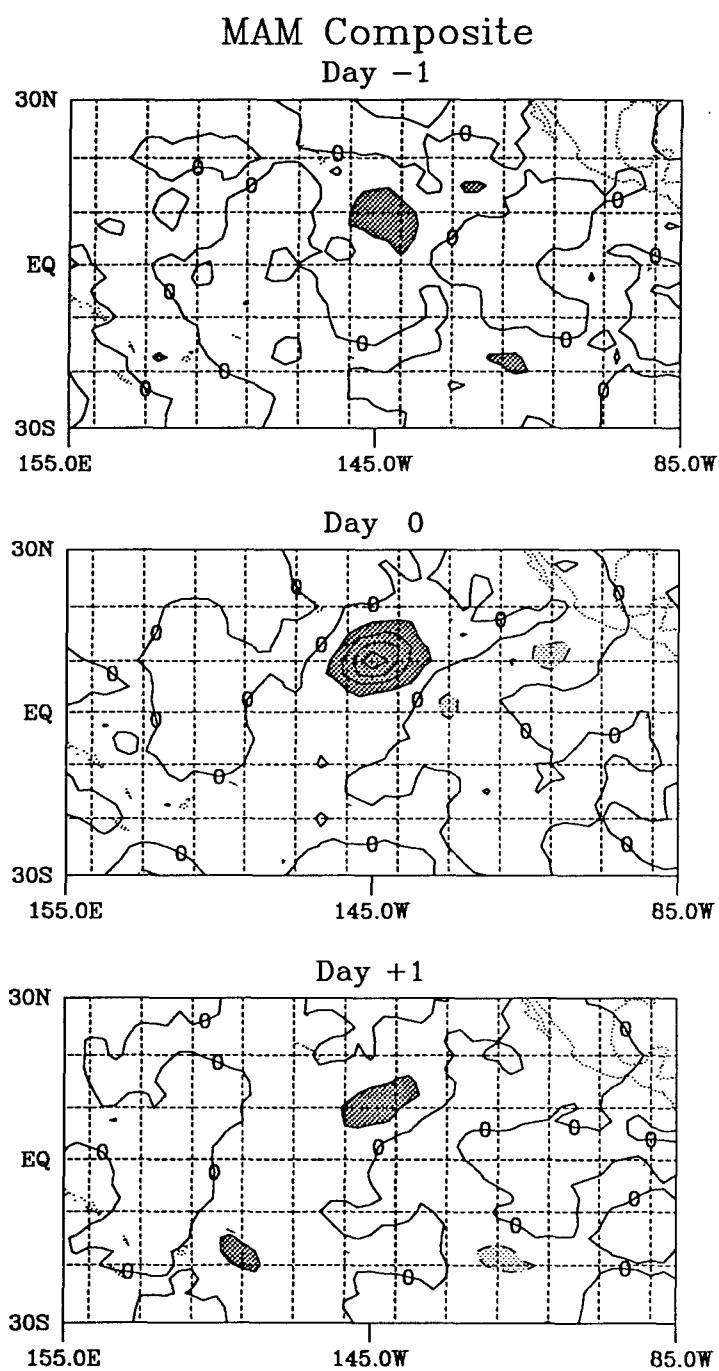
FIG. B3. As in Fig. B1, except at 10°N, 145°W for 25 events during six MAM seasons.

JJA Composite
Day −1

Day 0

Day +1
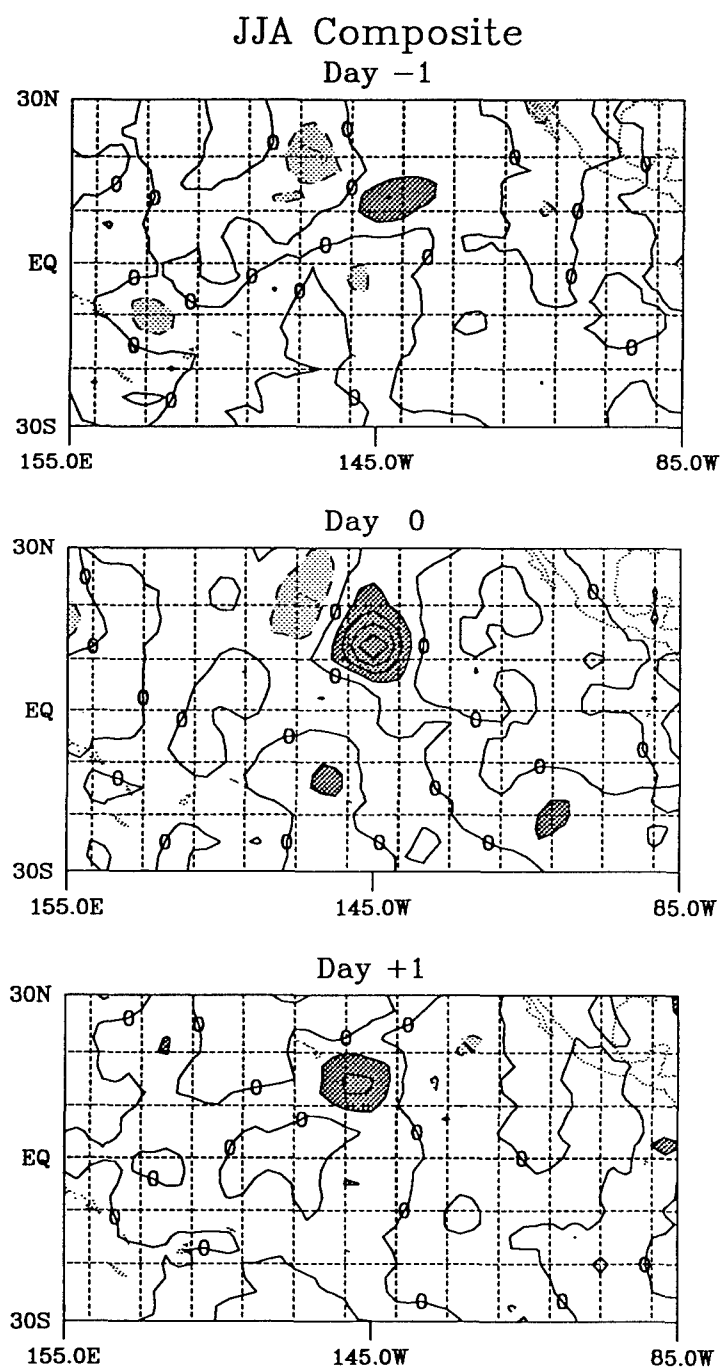
FIG. B4. As in Fig. B1, except at 12.5°N, 145°W for 35 events during six JJA seasons.
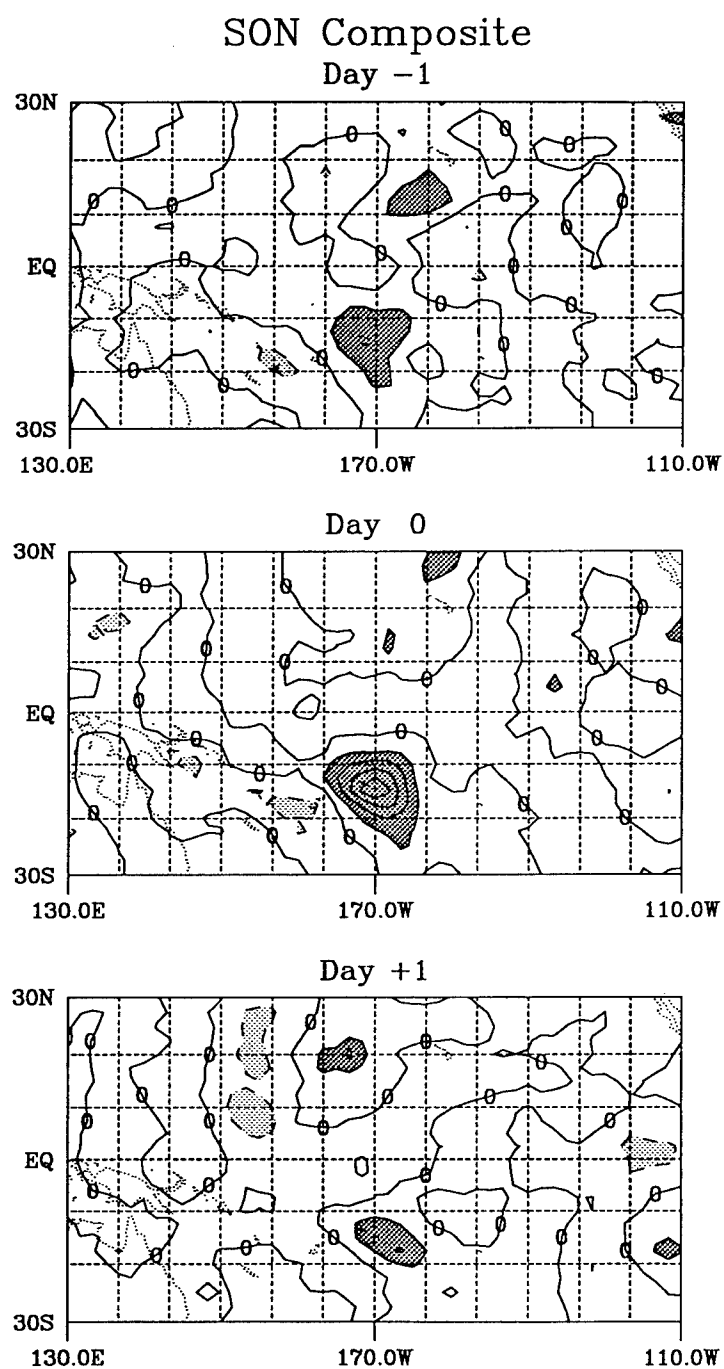
FIG. B5. As in Fig. B1, except for 31 events at 15°S, 170°W.

DJF Composite
Day −1

Day 0

Day +1
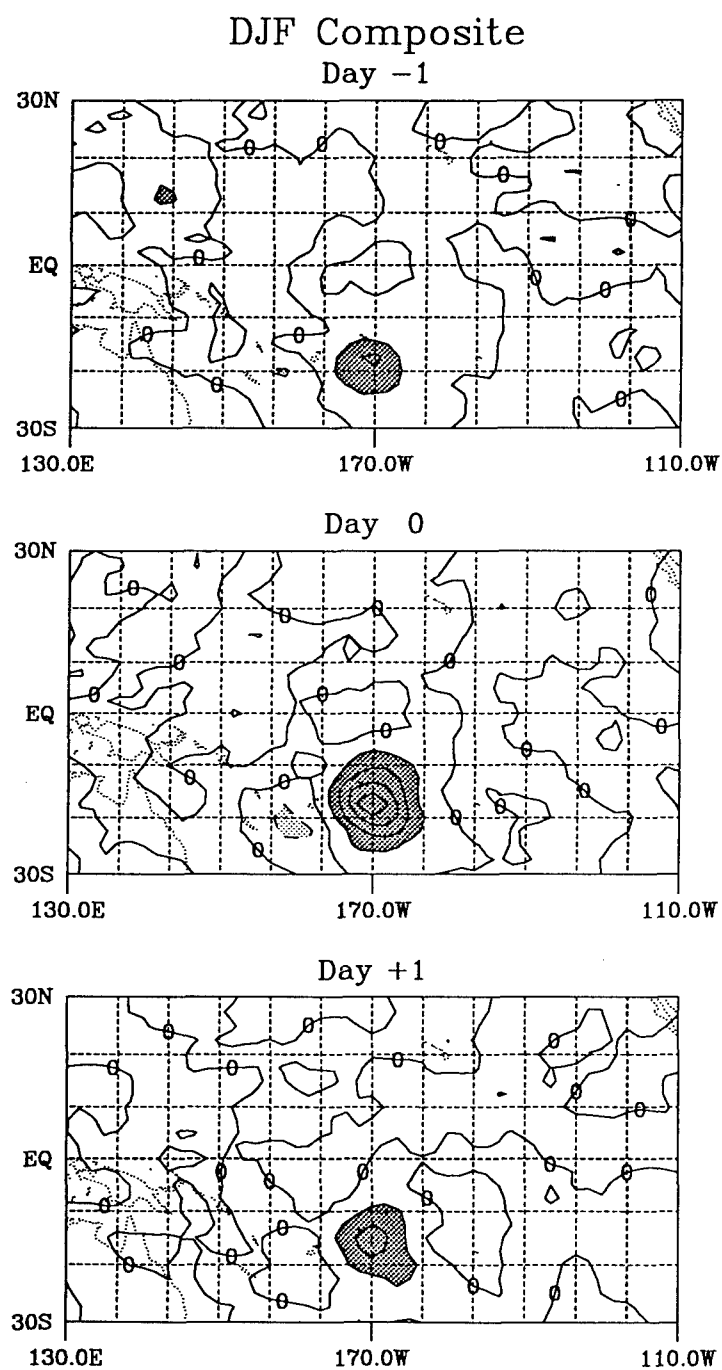
FIG. B6. As in Fig. B2, except for 48 events at 17.5°S, 170°W.
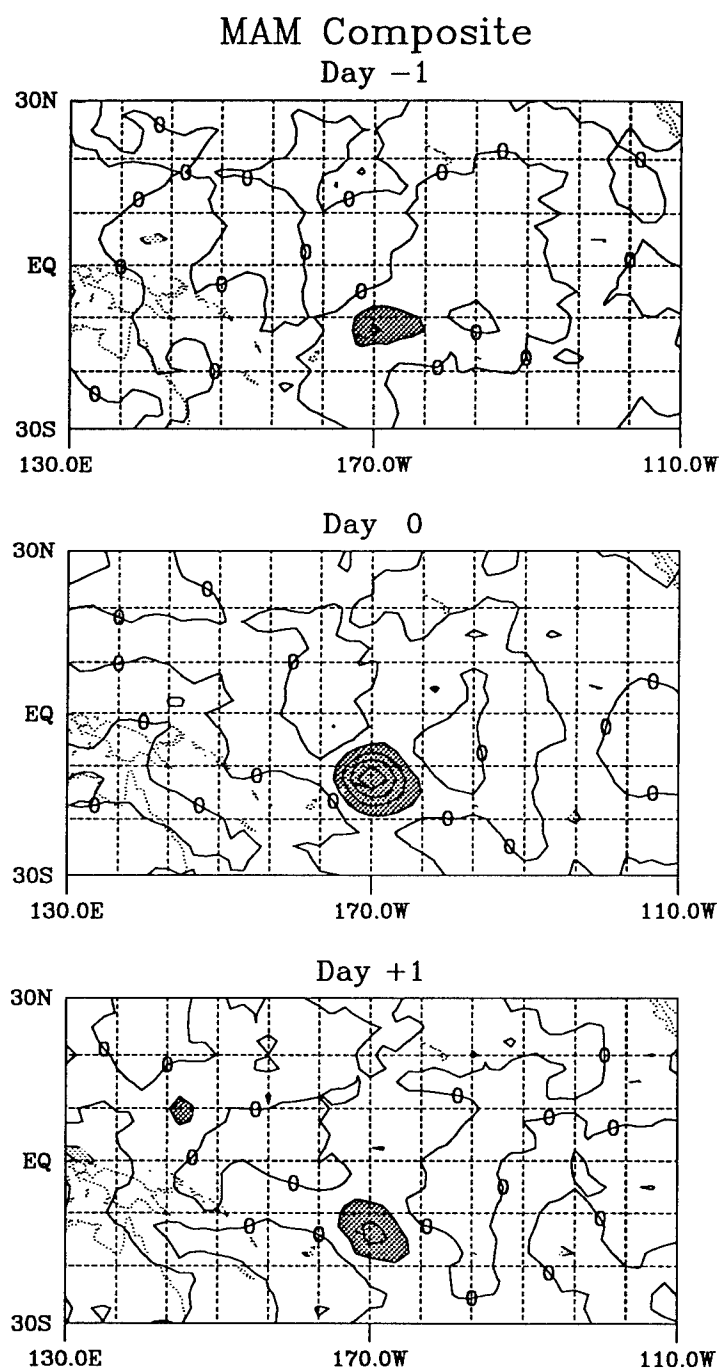
FIG. B7. As in Fig. B3, except for 26 events at 12.5°S, 170°W.

JJA Composite
Day −1

Day 0

Day +1
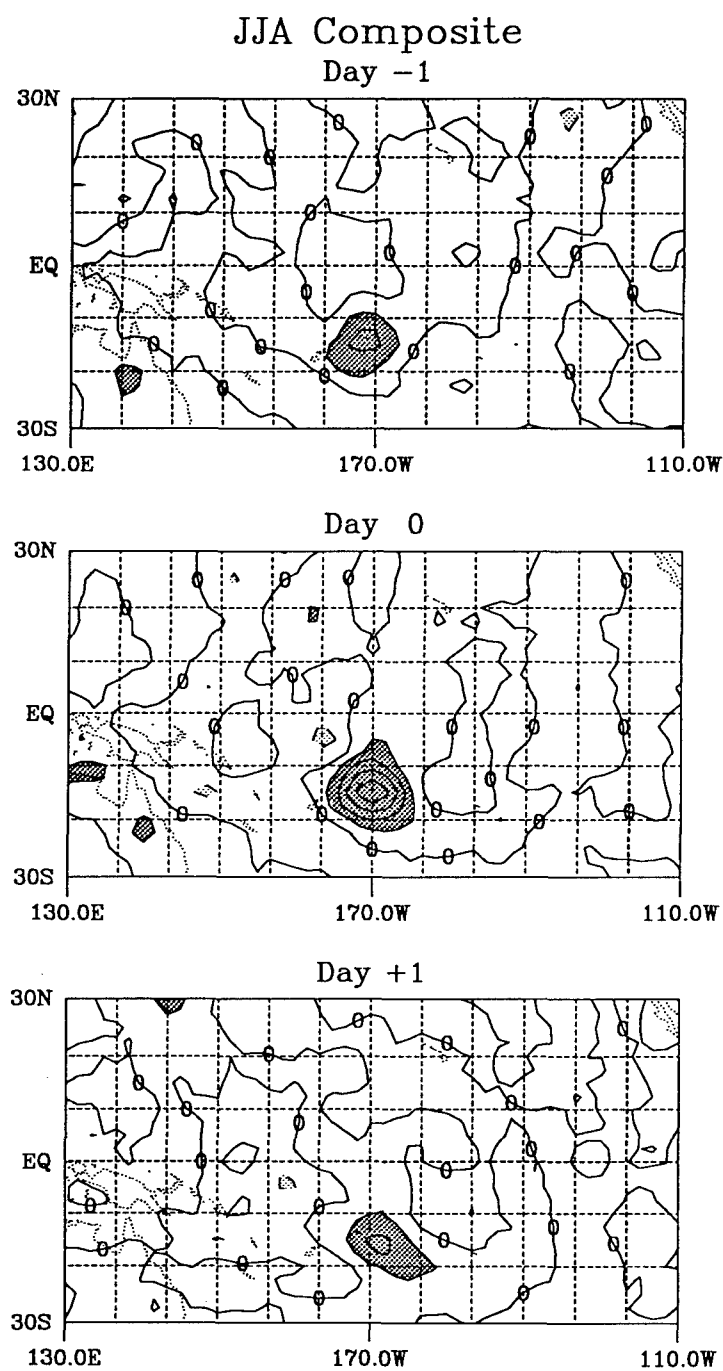
FIG. B8. As in Fig. B4, except for 38 events at 15°S, 170°W.

SON Composite
Day −1

Day 0

Day +1
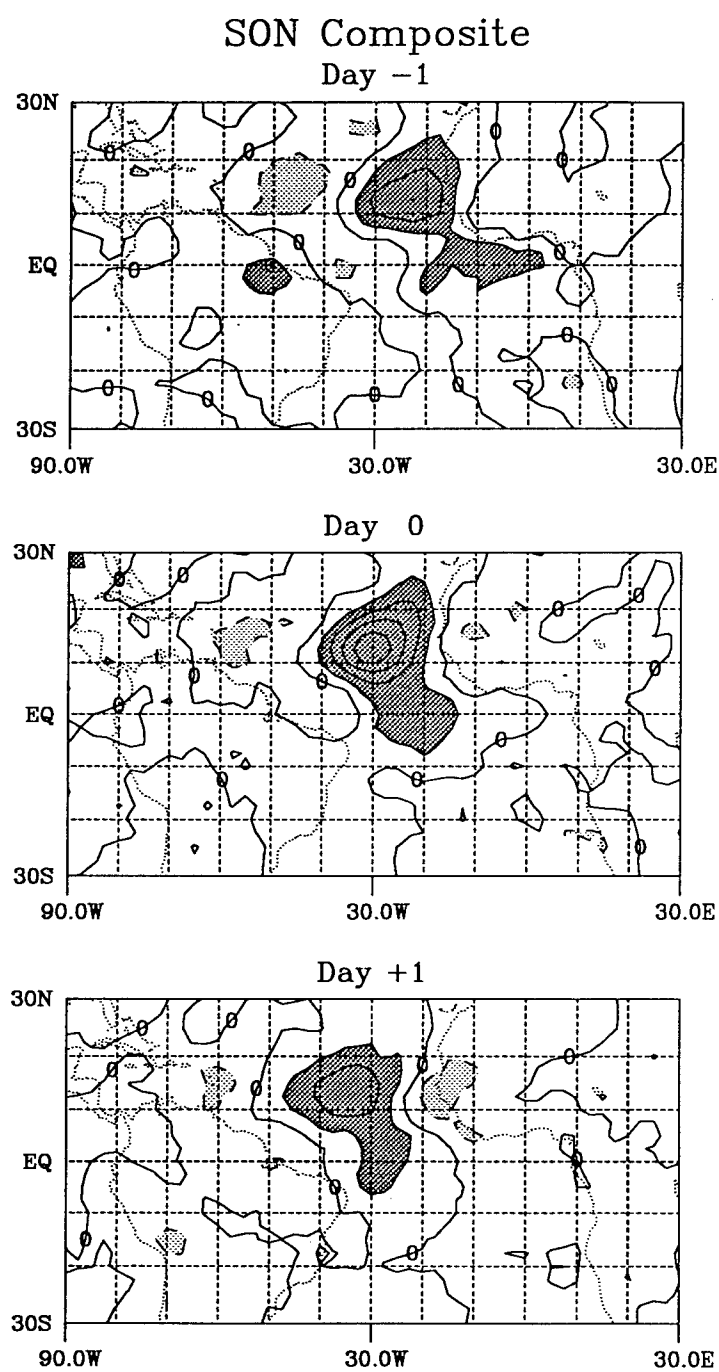
FIG. B9. As in Fig. B1, except for 39 events at 12.5°N, 30°W.

DJF Composite
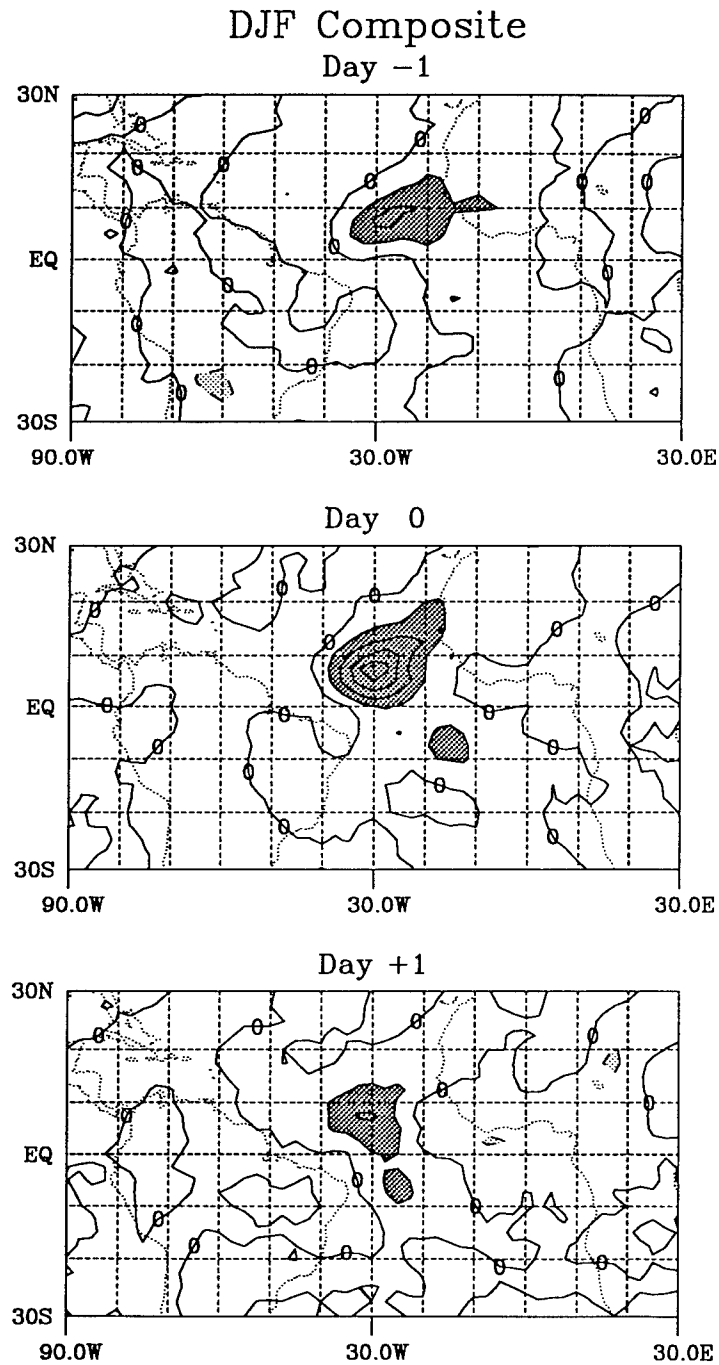
FIG. B10. As in Fig. B2, except for 34 events at 7.5°N, 30°W.
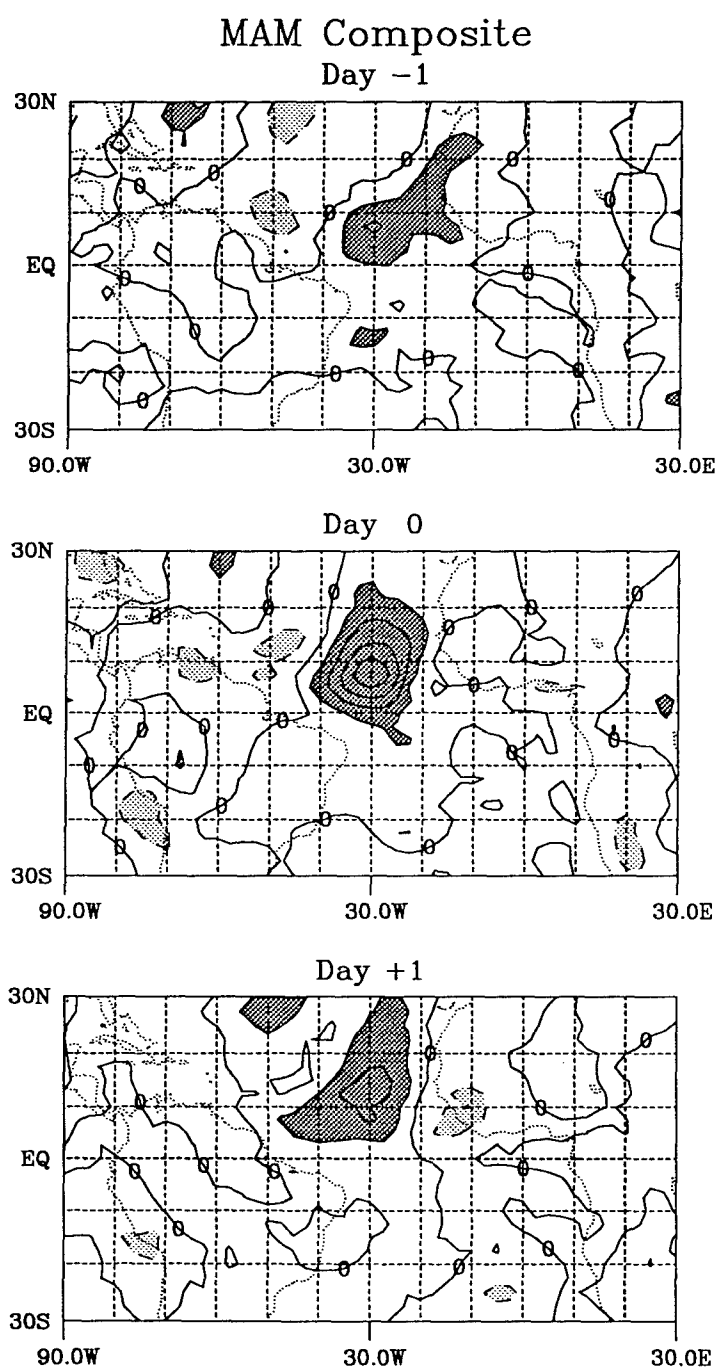
FIG. B11. As in Fig. B3, except for 30 events at 7.5°N, 30°W.
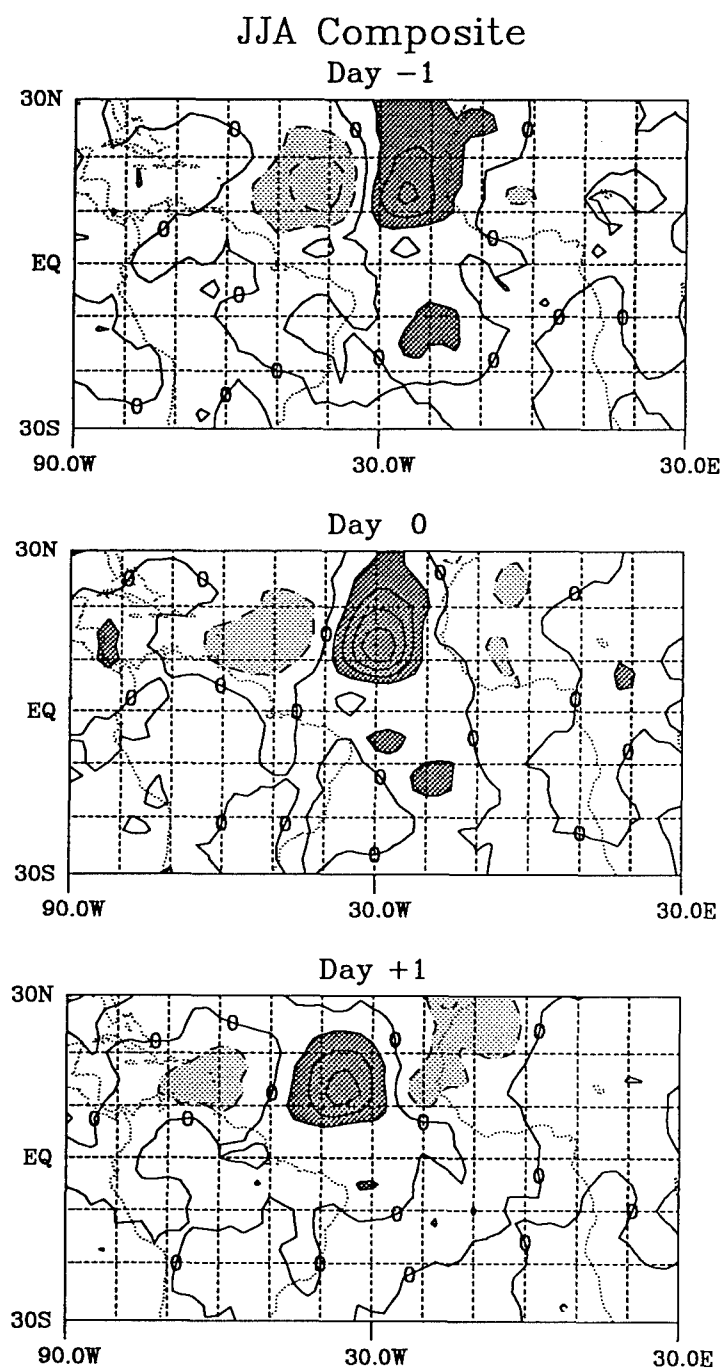
FIG. B12. As in Fig. B4, except for 33 events at 12.5°N, 30°W.

SON Composite

Day −1

Day 0

Day +1
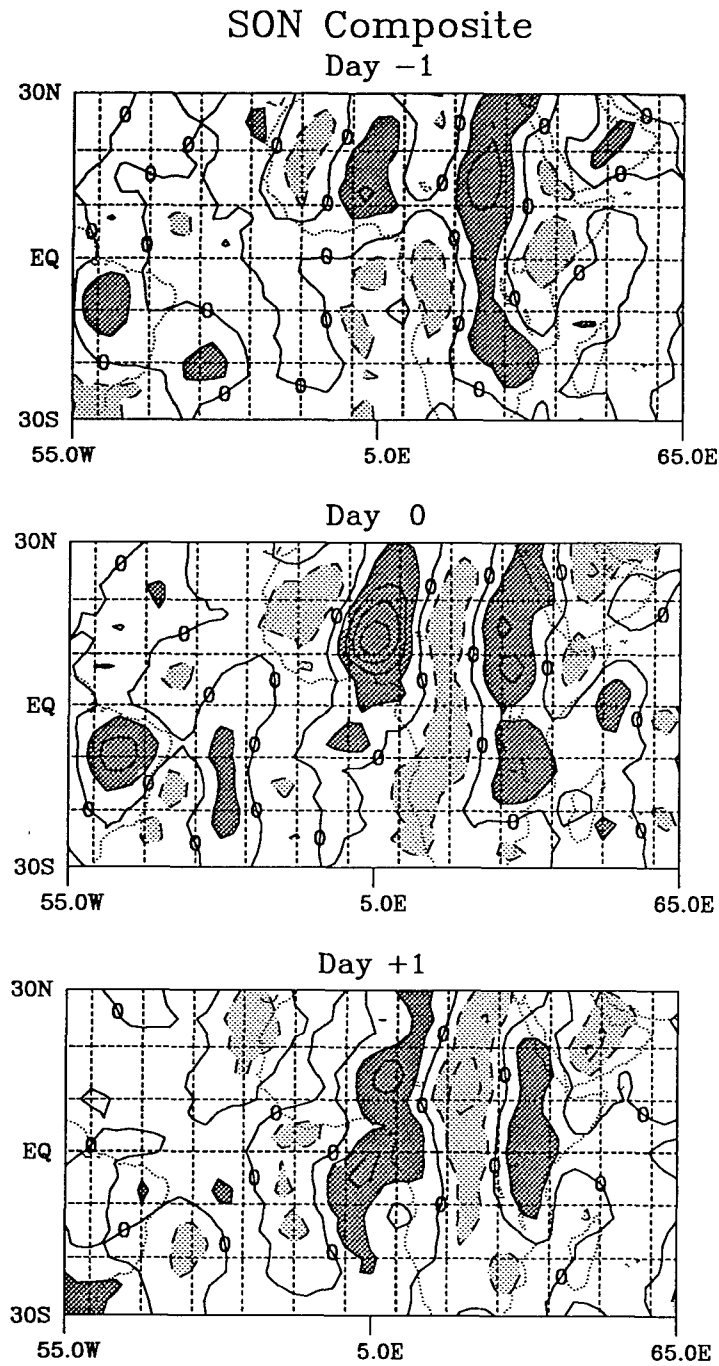
FIG. B13. As in Fig. B1, except for 50 events at 12.5°N, 5°E.

DJF Composite
Day −1

Day 0

Day +1
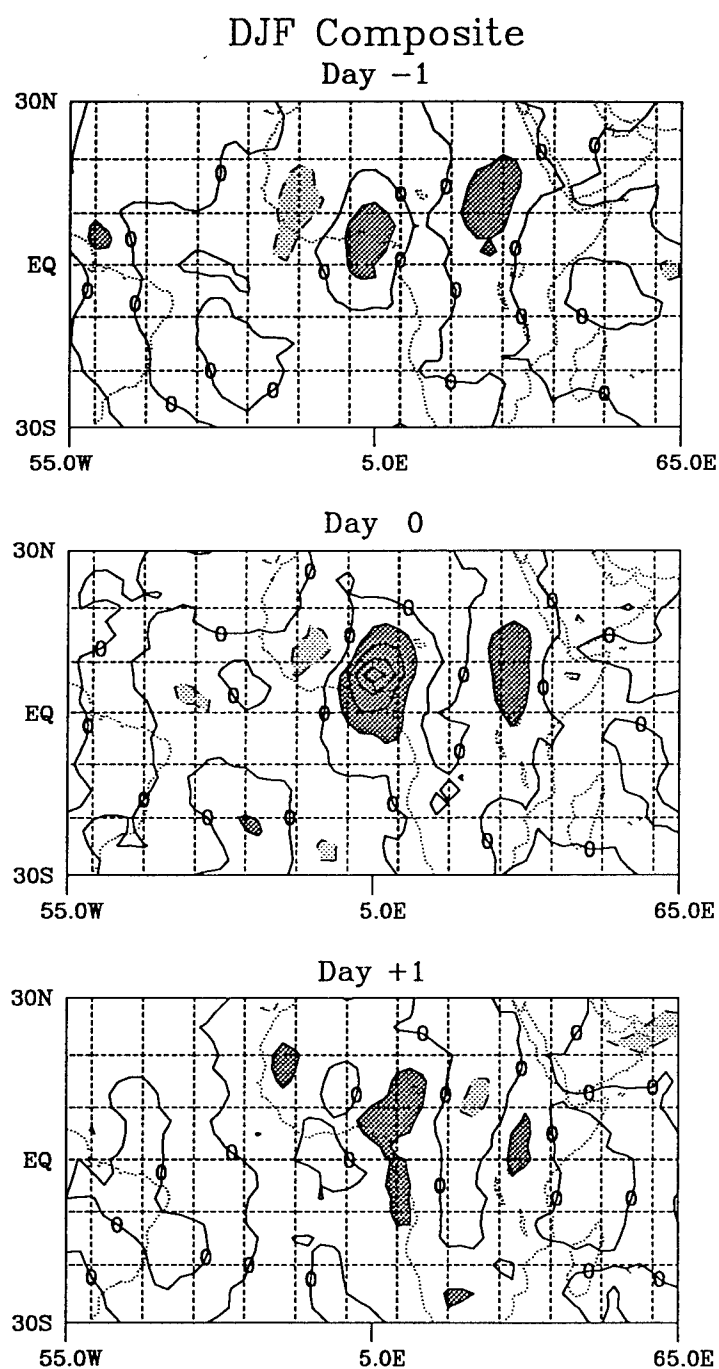
FIG. B14. As in Fig. B2, except for 59 events at 7.5°N, 5°E.
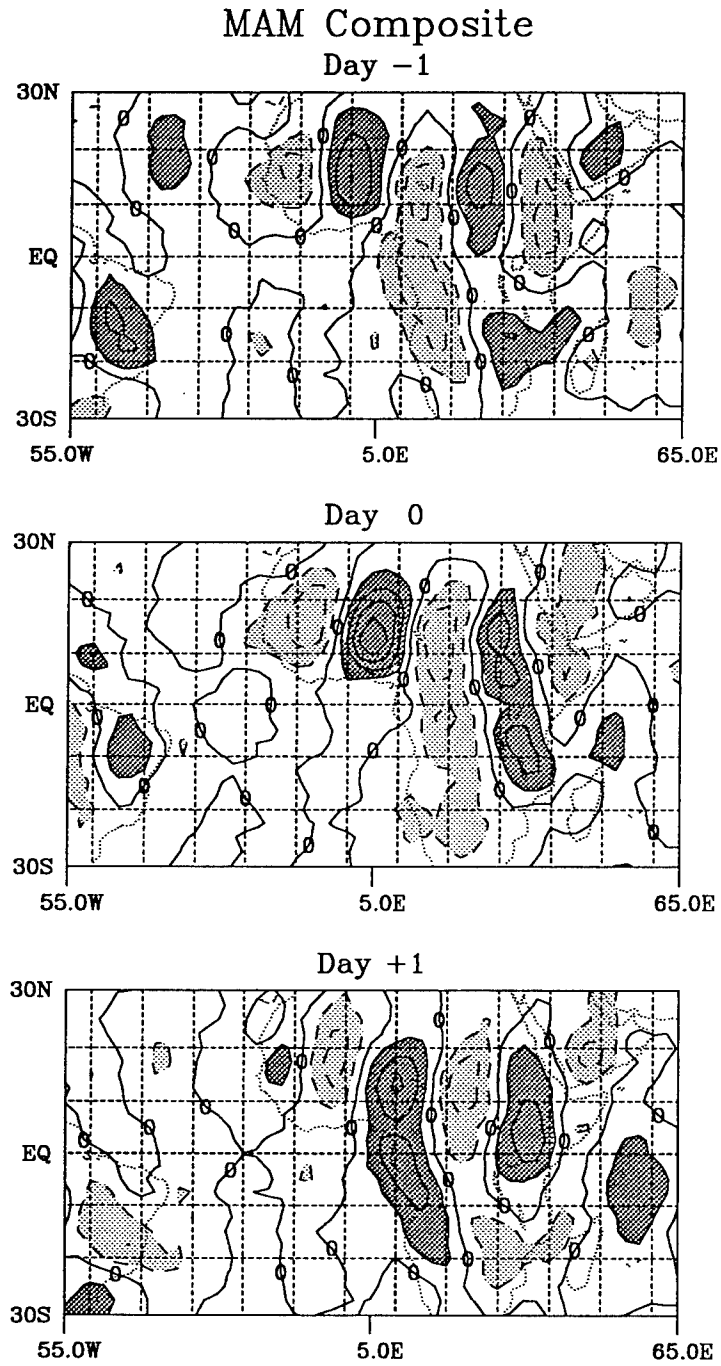
FIG. B15. As in Fig. B3, except for 78 events at 12.5°N, 5°E.

JJA Composite

Day −1

Day 0

Day +1
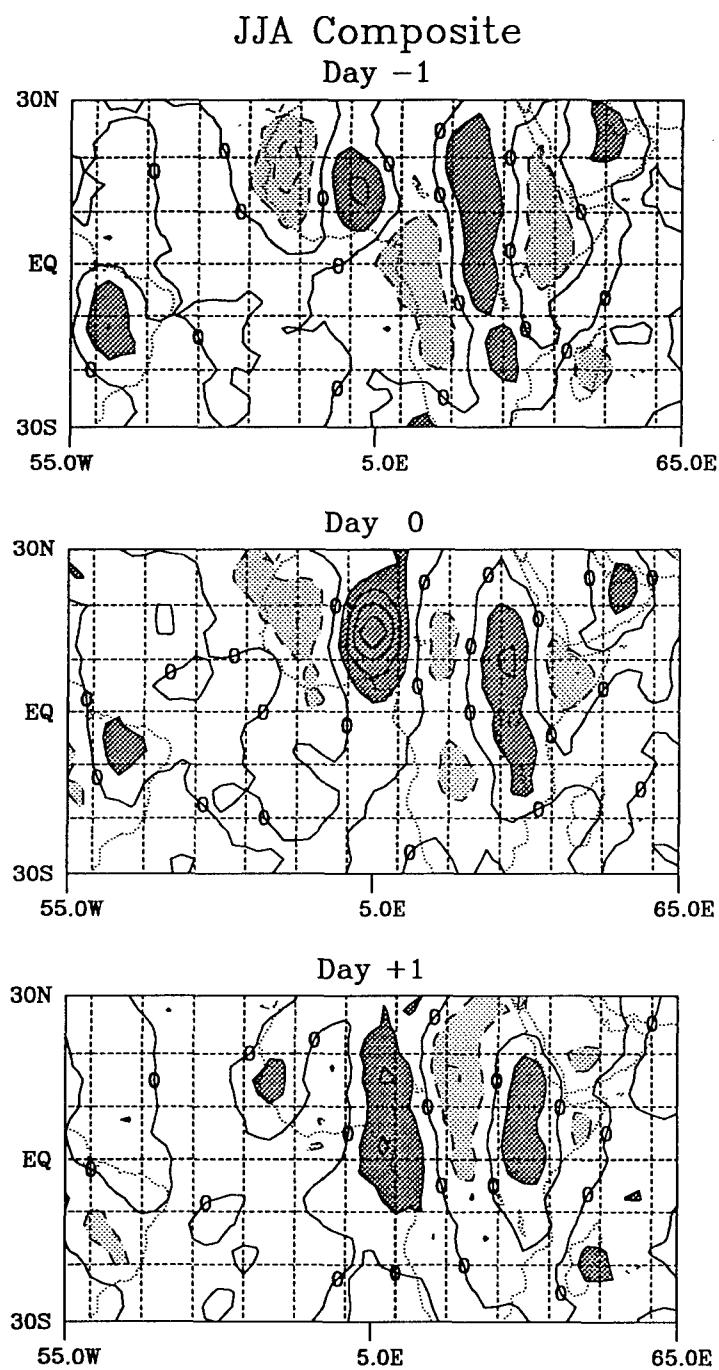
FIG. B16. As in Fig. B4, except for 72 events at 15°N, 5°E.
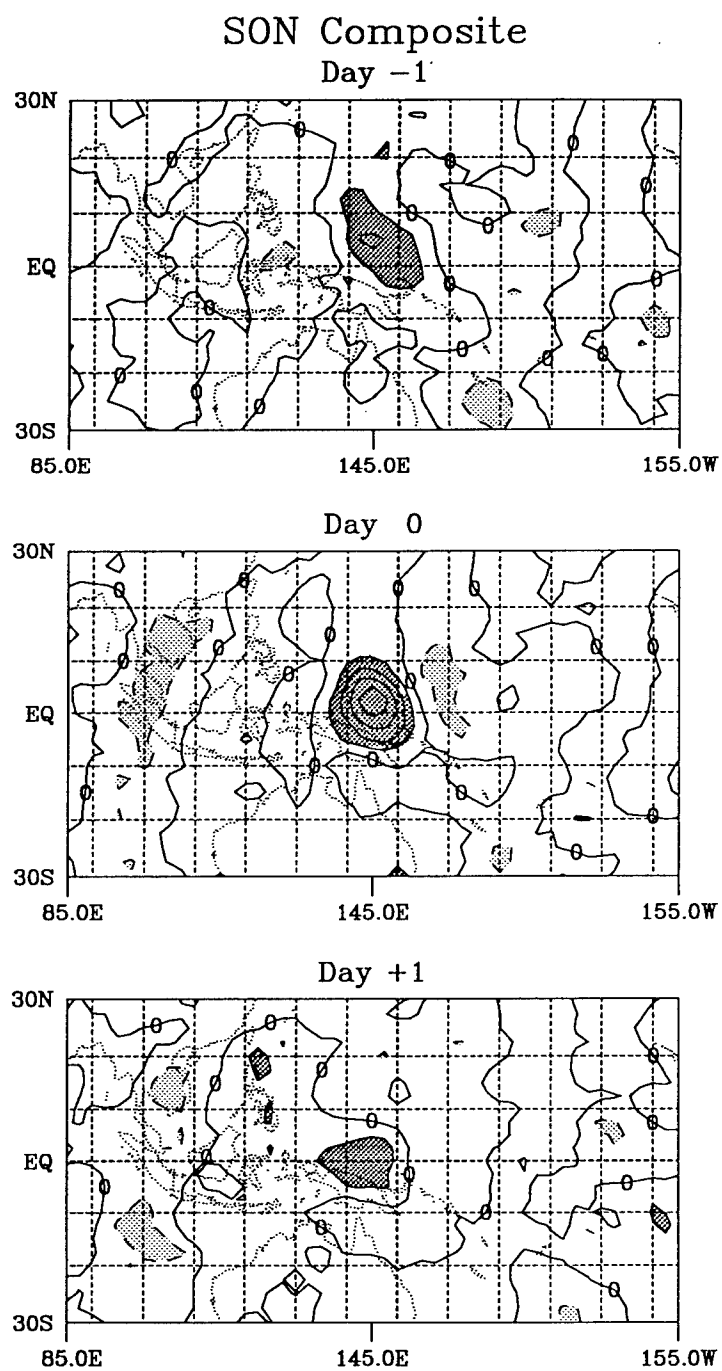
FIG. B17. As in Fig. B1, except for 18 events at 2.5°N, 145°E.

DJF Composite

Day −1

Day 0

Day +1
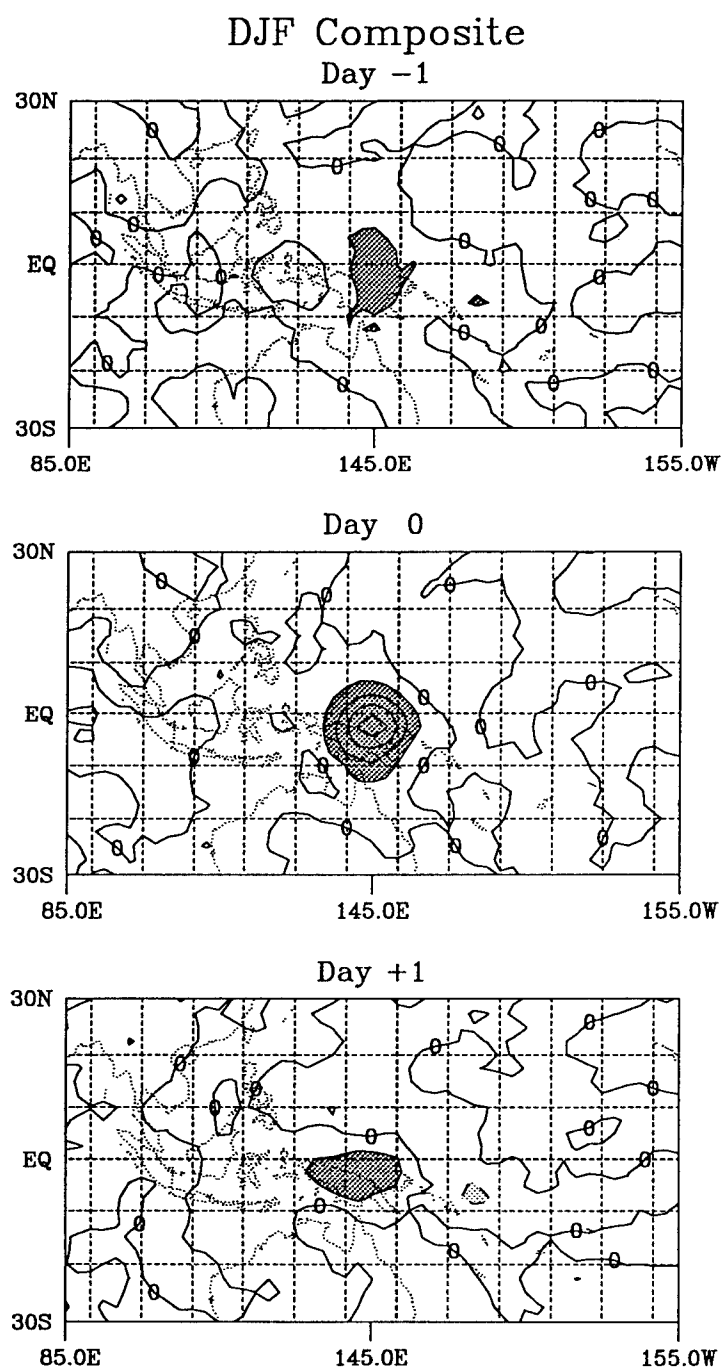
FIG. B18. As in Fig. B2, except for 33 events at 2.5°S, 145°E.

MAM Composite

Day −1

Day 0

Day +1
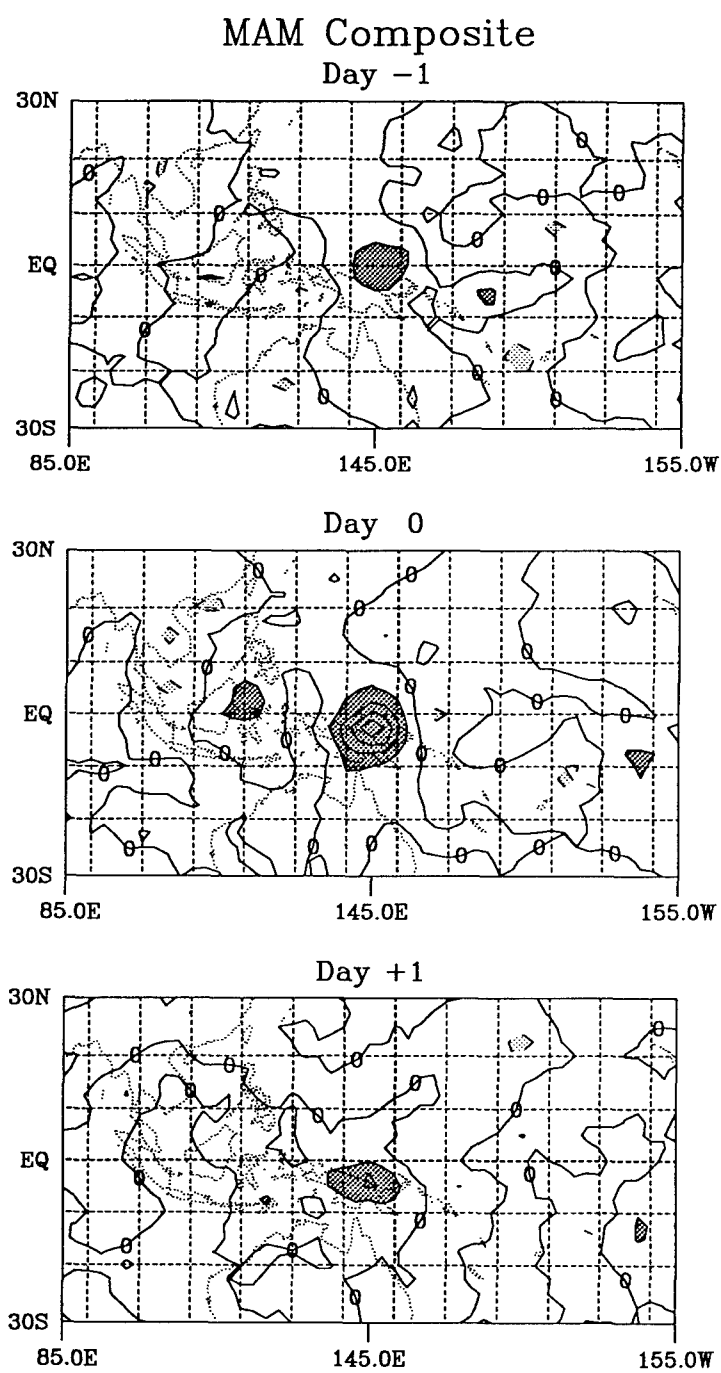
FIG. B19. As in Fig. B3, except for 18 events at 2.5°S, 145°E.

JJA Composite
Day −1

Day 0

Day +1
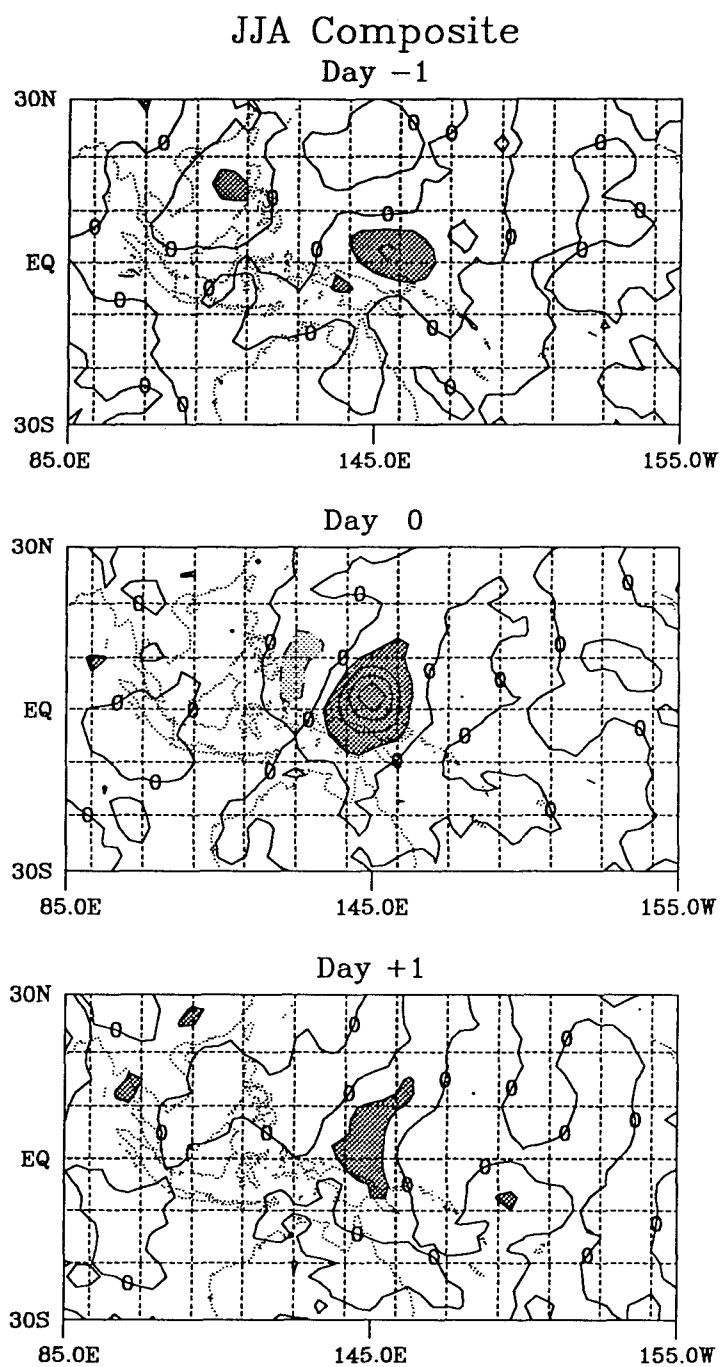
FIG. B20. As in Fig. B4, except for 22 events at 2.5°N, 145°E.

SON Composite
Day −1

Day 0

Day +1
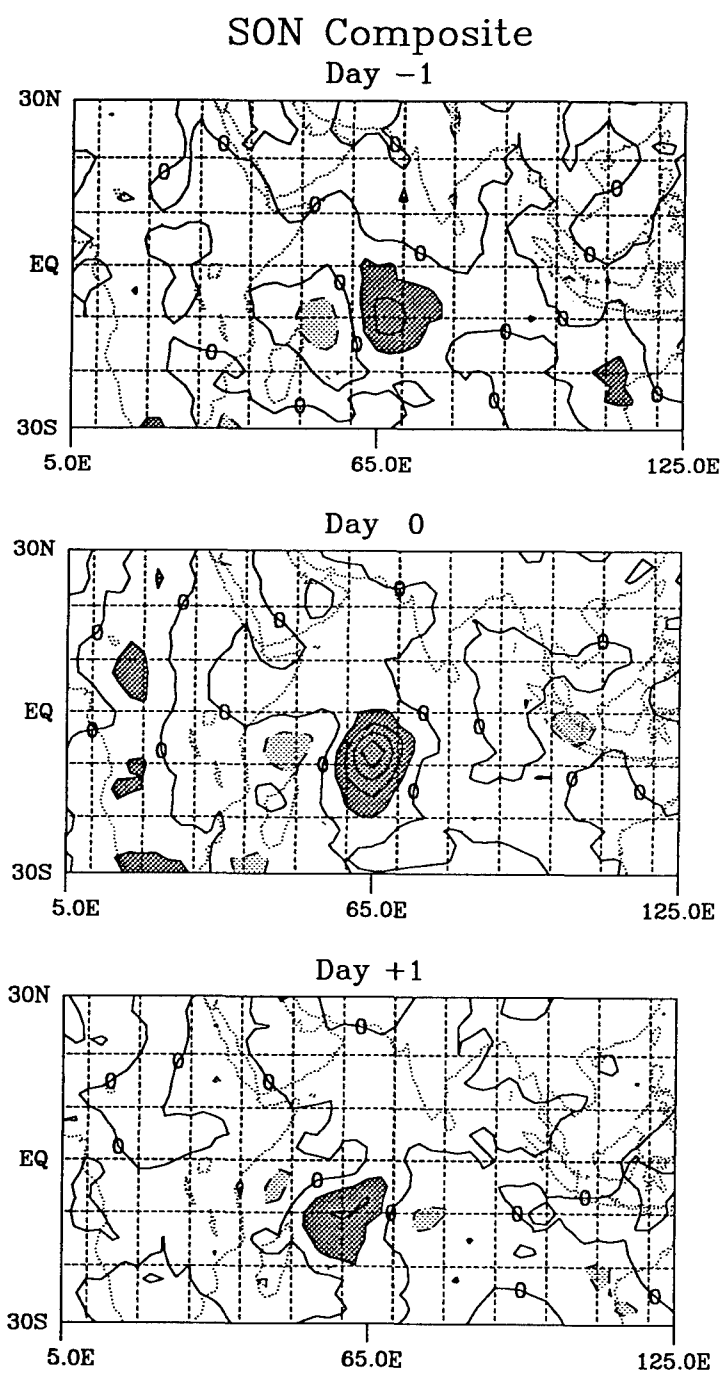
FIG. B21. As in Fig. B1, except for 29 events at 7.5°S, 65°E.

DJF Composite

Day −1

Day 0

Day +1
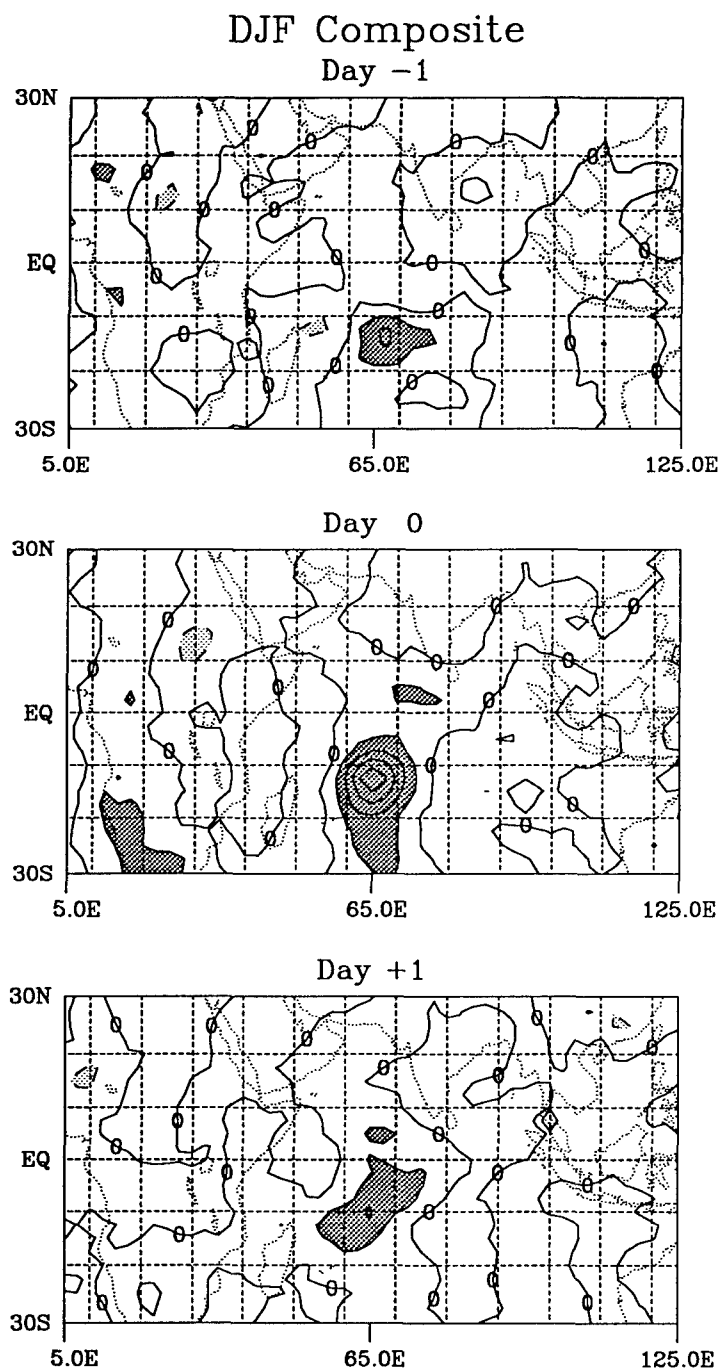
FIG. B22. As in Fig. B2, except for 33 events at 12.5°S, 65°E.

MAM Composite
Day −1

Day 0

Day +1
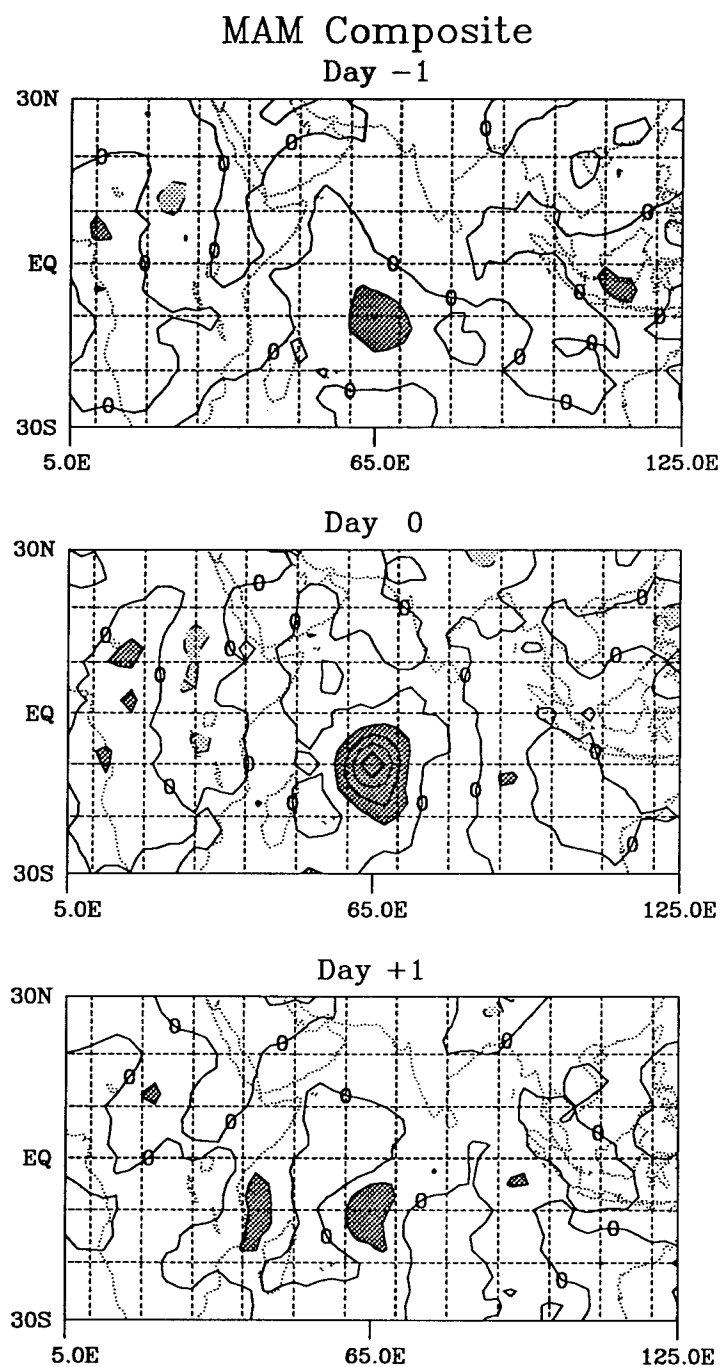
FIG. B23. As in Fig. B3, except for 26 events at 10°S, 65°E.

JJA Composite
Day −1

Day 0

Day +1
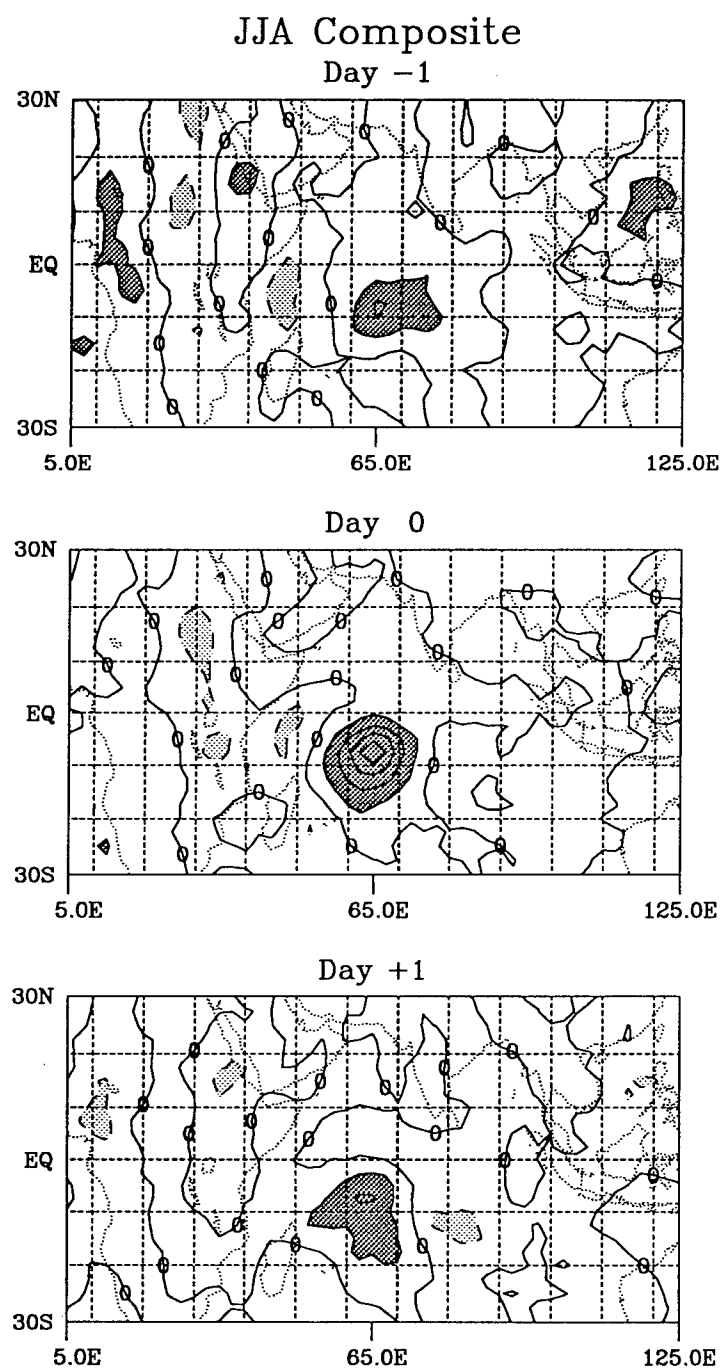
FIG. B24. As in Fig. B4, except for 21 events at 7.5°S, 65°E.

SON Composite
Day −1

Day 0

Day +1
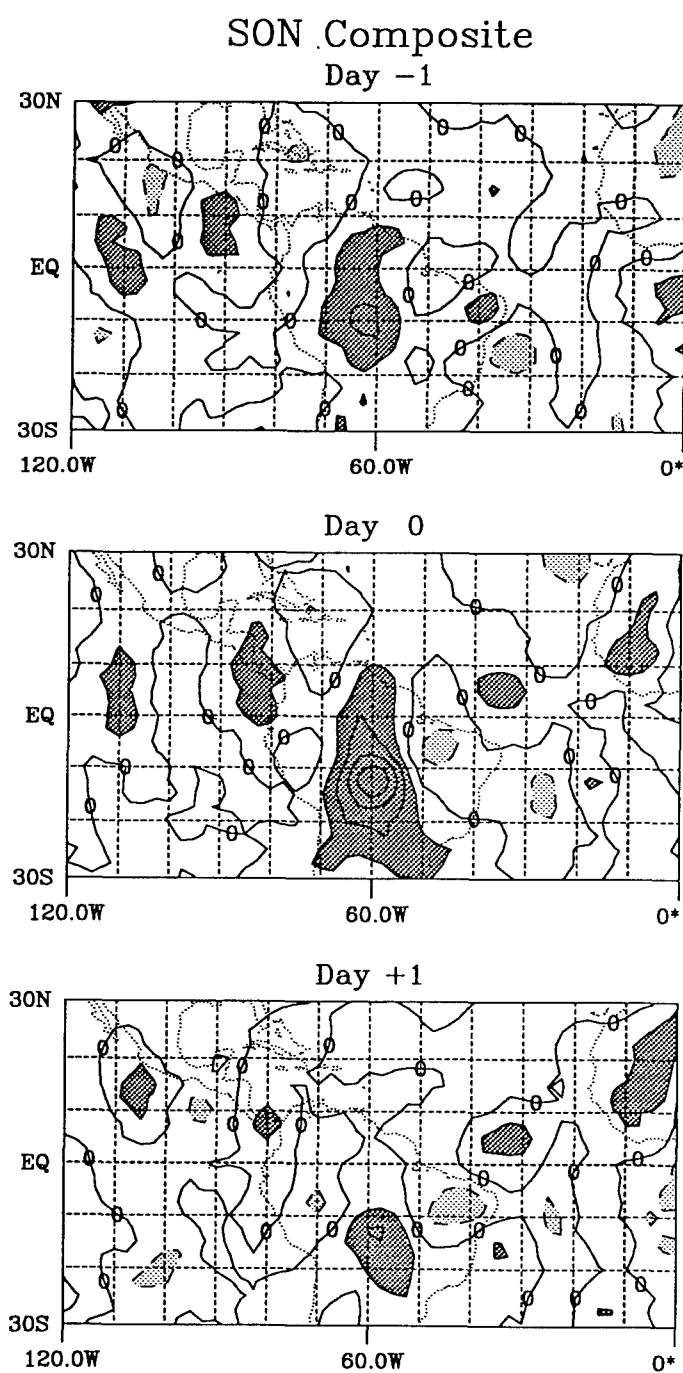
FIG. B25. As in Fig. B1, except for 40 events at 12.5°S, 60°W.
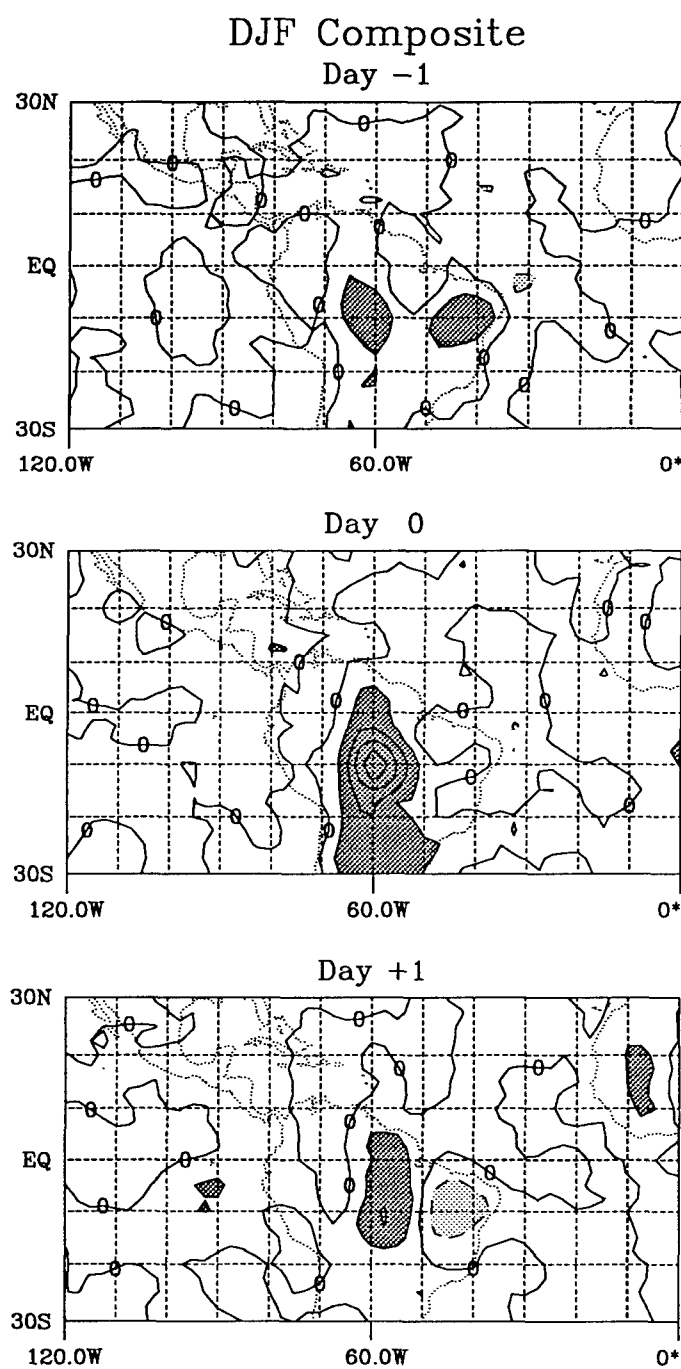
FIG. B26. As in Fig. B2, except for 39 events at 10°S, 60°W.
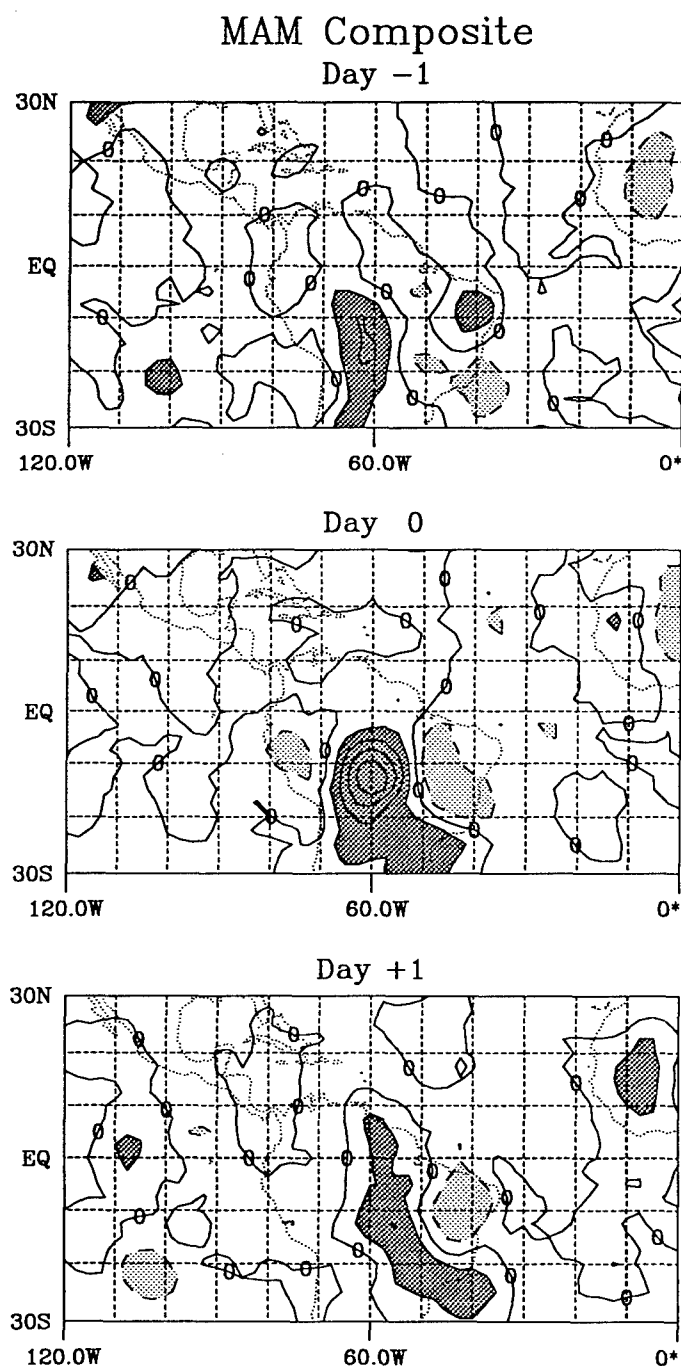
FIG. B27. As in Fig. B3, except for 52 events at 12.5°S, 60°W.

JJA Composite
Day −1

Day 0

Day +1
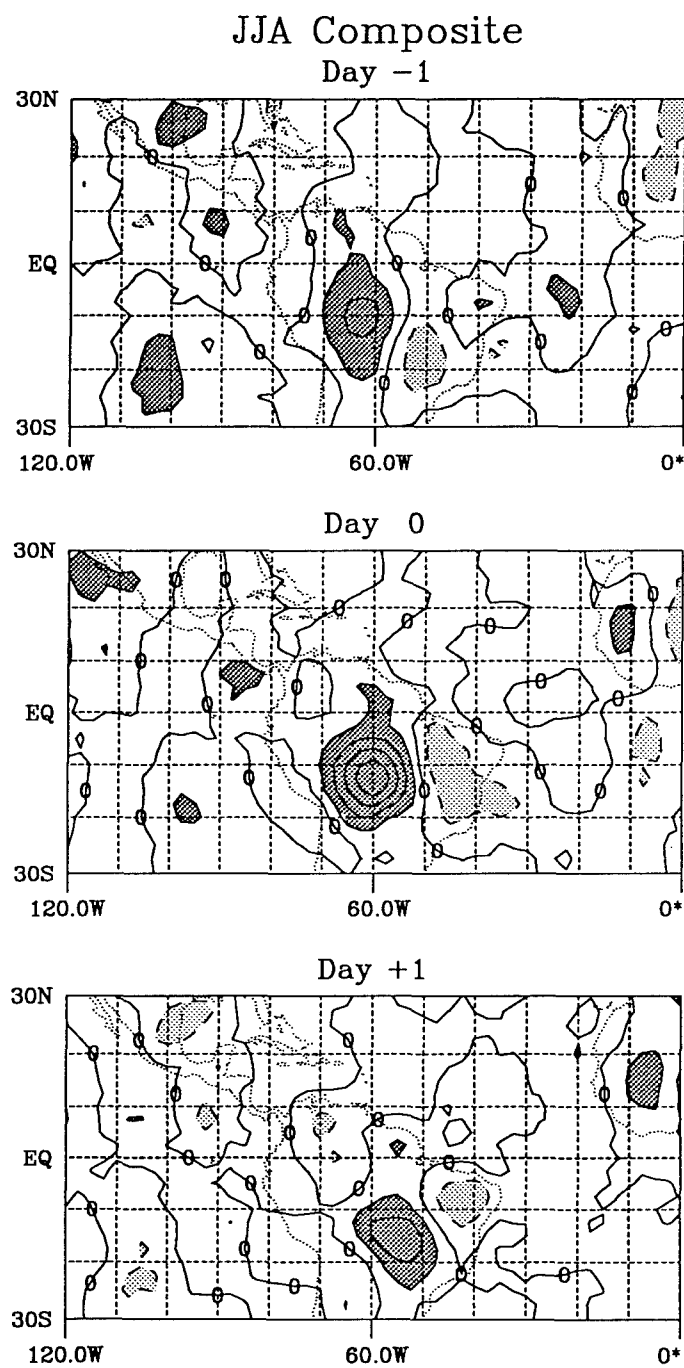
FIG. B28. As in Fig. B4, except for 41 events at 12.5°S, 60°W.

APPENDIX   C
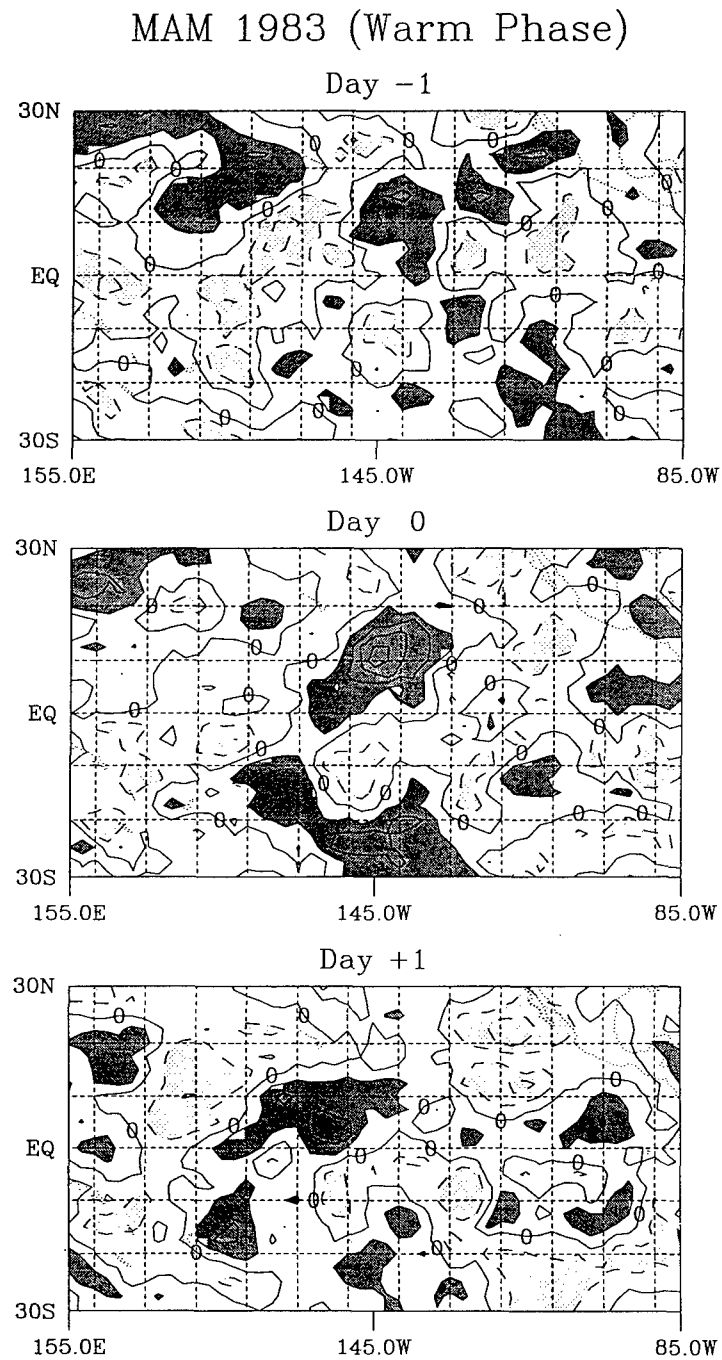
MAM 1983 (Warm Phase)

FIG. C1. As in Fig. B1, except for events exceeding +1.0 mm anomaly during MAM 1983 (El Niño warm phase).
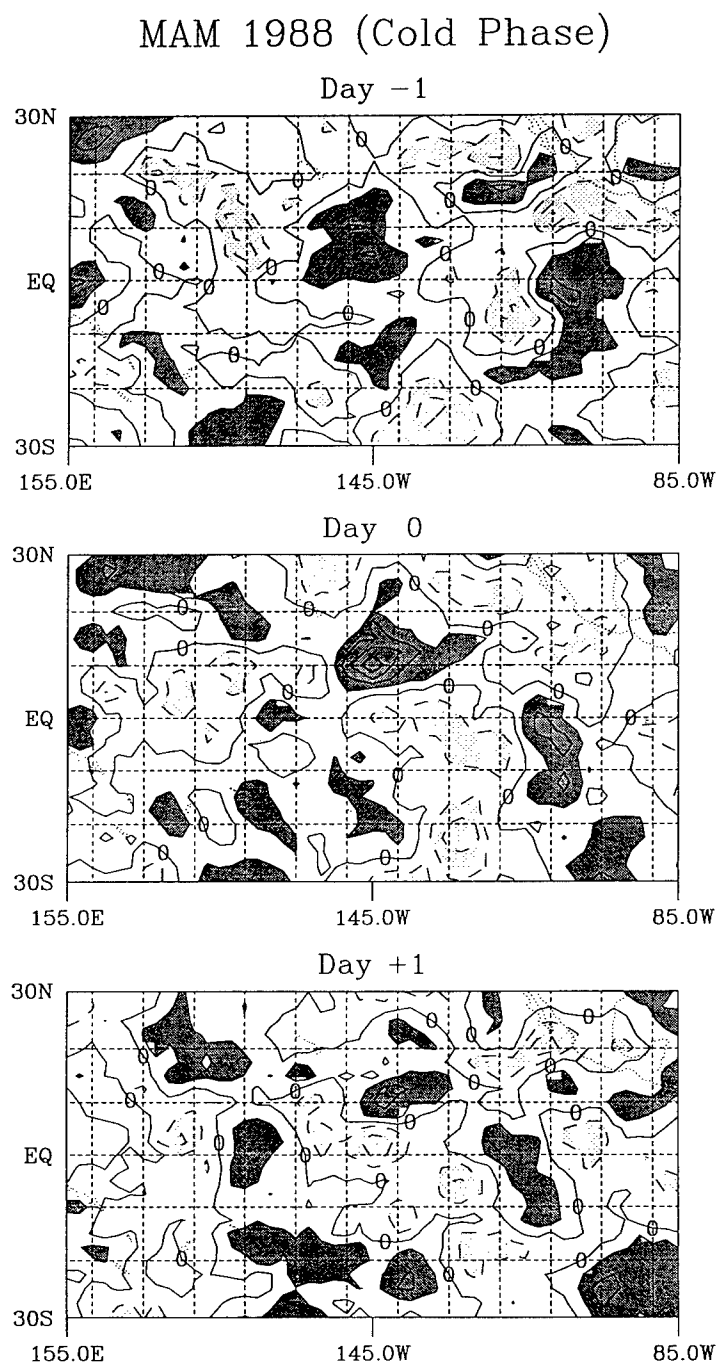
FIG. C2. As in Fig. C1, except during MAM 1988 (El Niño cold phase).

SON 1987 (Warm Phase)

Day −1

Day 0

Day +1
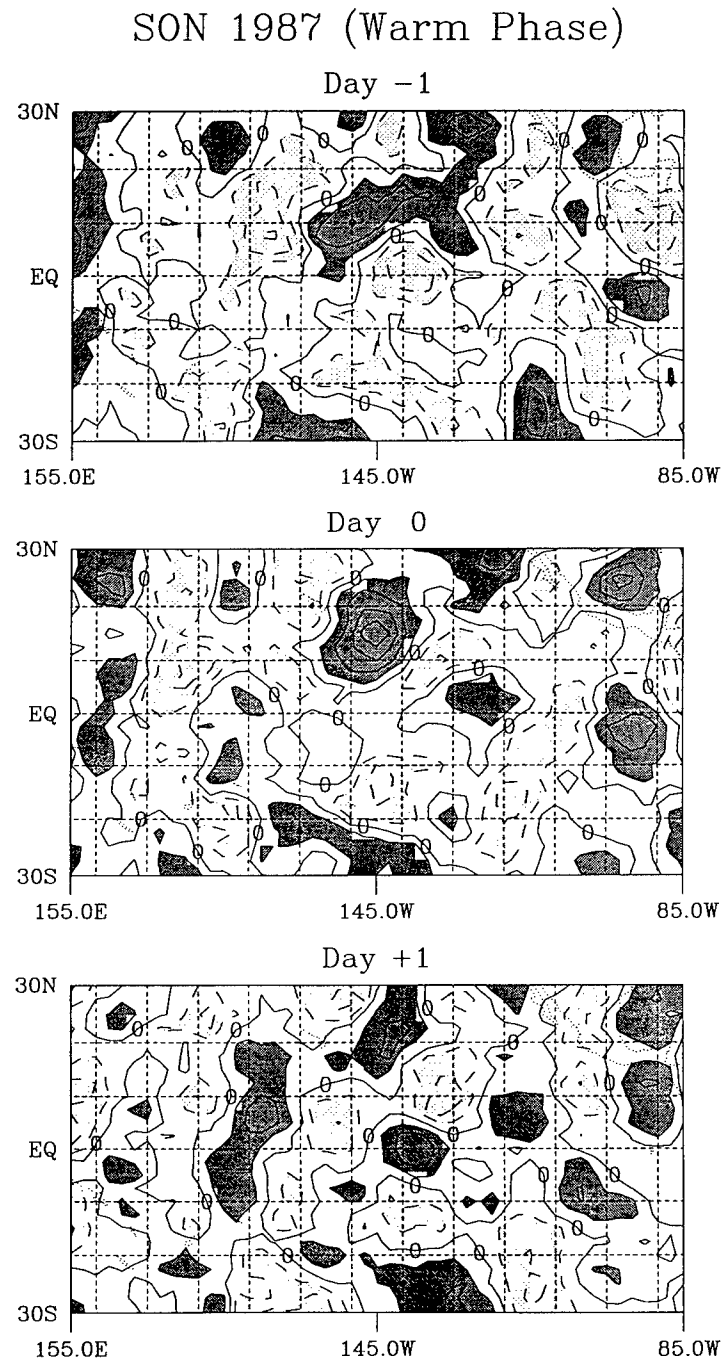
FIG. C3. As in Fig. C1, except at 15°N, 145°W during SON 1987 (El Niño warm phase).

SON 1988 (Cold Phase)

Day −1

Day 0

Day +1
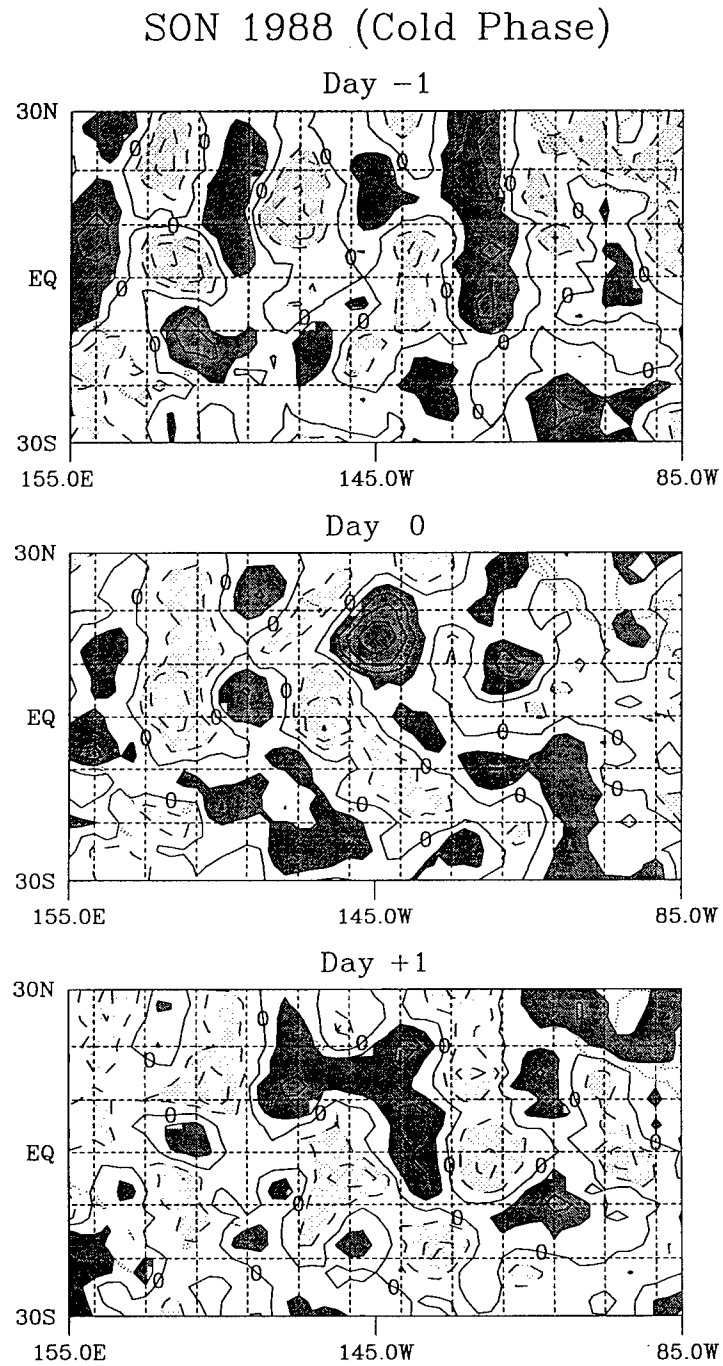
FIG. C4. As in Fig. C3, except during SON 1988 (El Niño cold phase).

MAM 1983 (Warm Phase)

Day −1

Day 0

Day +1
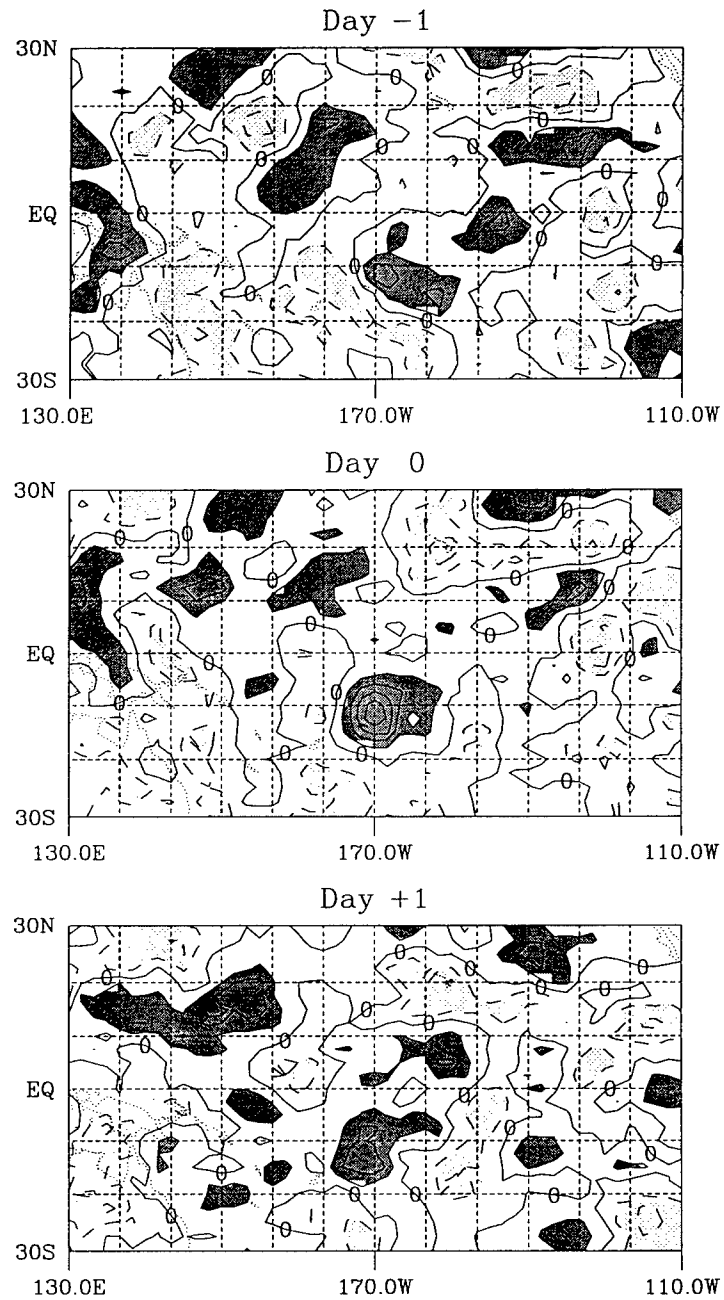
FIG. C5. As in Fig. C1, except at 12.5°S, 170°W.

MAM 1988 (Cold Phase)

Day −1

Day 0

Day +1
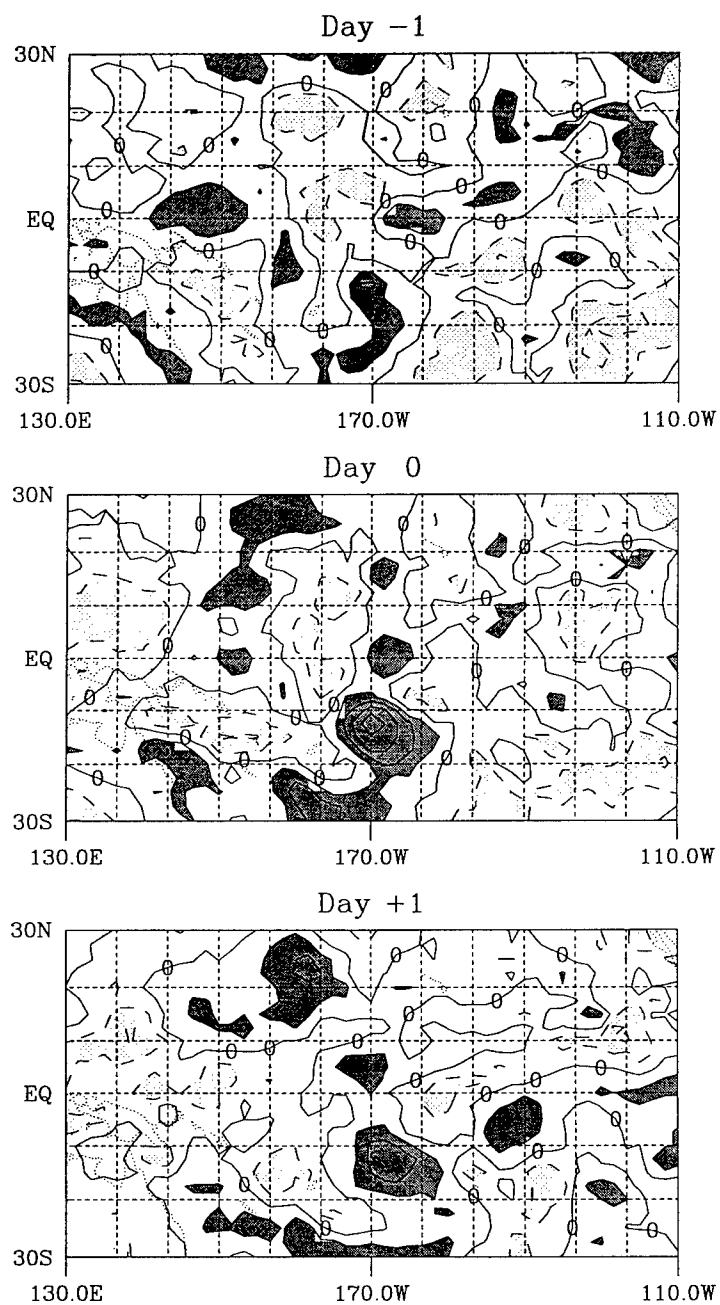
FIG. C6. As in Fig. C2, except at 12.5°S, 170°W.

SON 1987 (Warm Phase)

Day −1

Day 0

Day +1
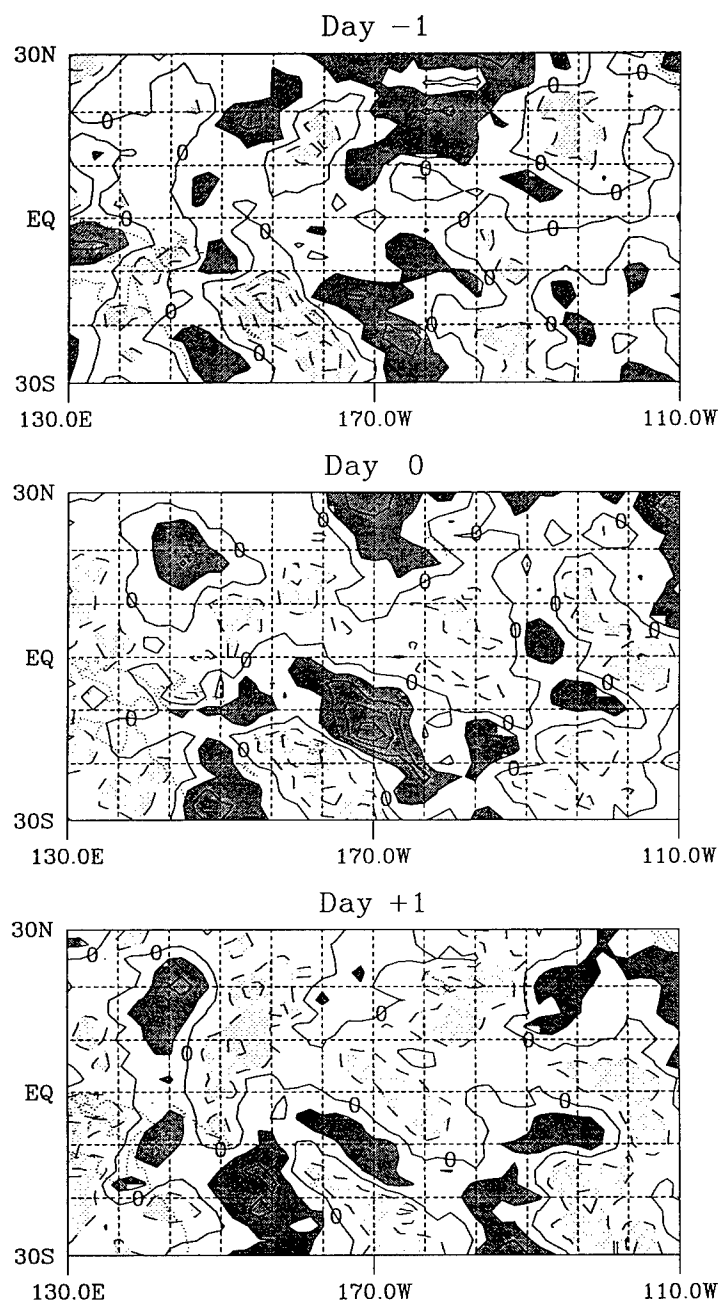
FIG. C7. As in Fig. C3, except at 15°S, 170°W.

SON 1988 (Cold Phase)

Day −1

Day 0

Day +1
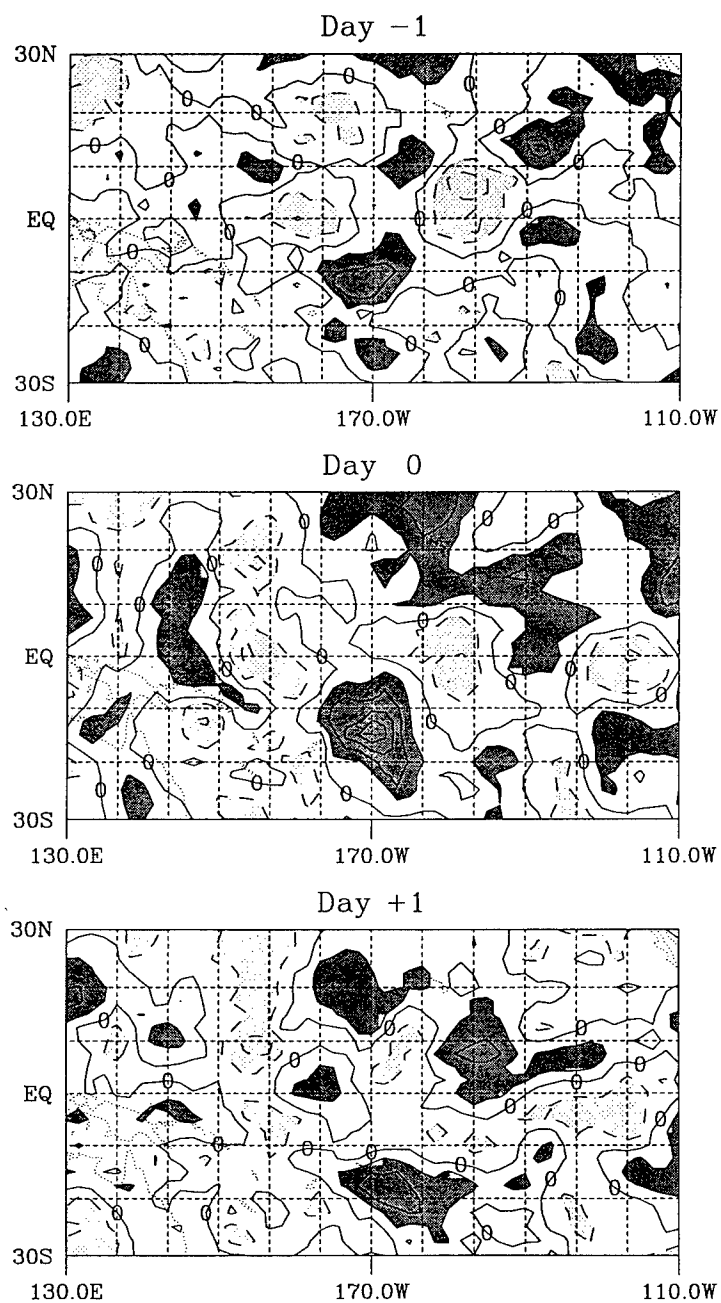
FIG. C8. As in Fig. C4, except at 15°S, 170°W.

MAM 1983 (Warm Phase)

Day −1

Day 0

Day +1
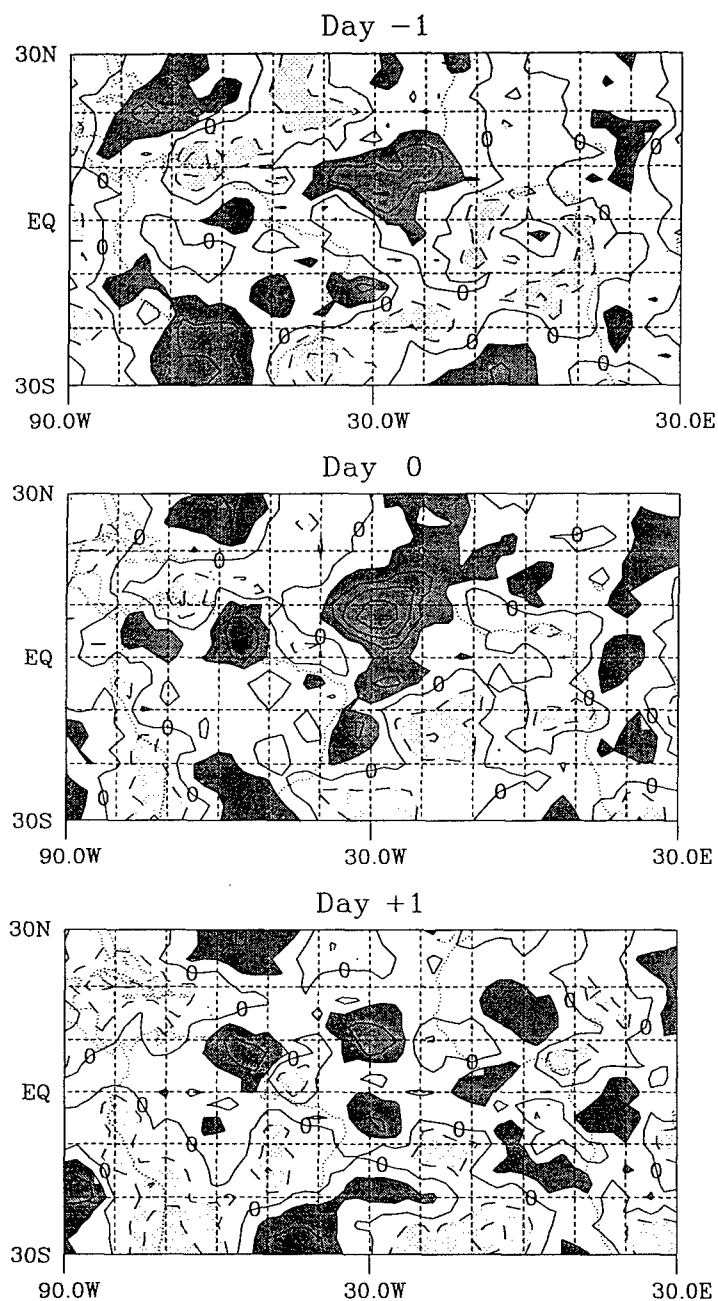
FIG. C9. As in Fig. C1, except at 7.5°N, 30°W.

MAM 1988 (Cold Phase)

Day −1

Day 0

Day +1
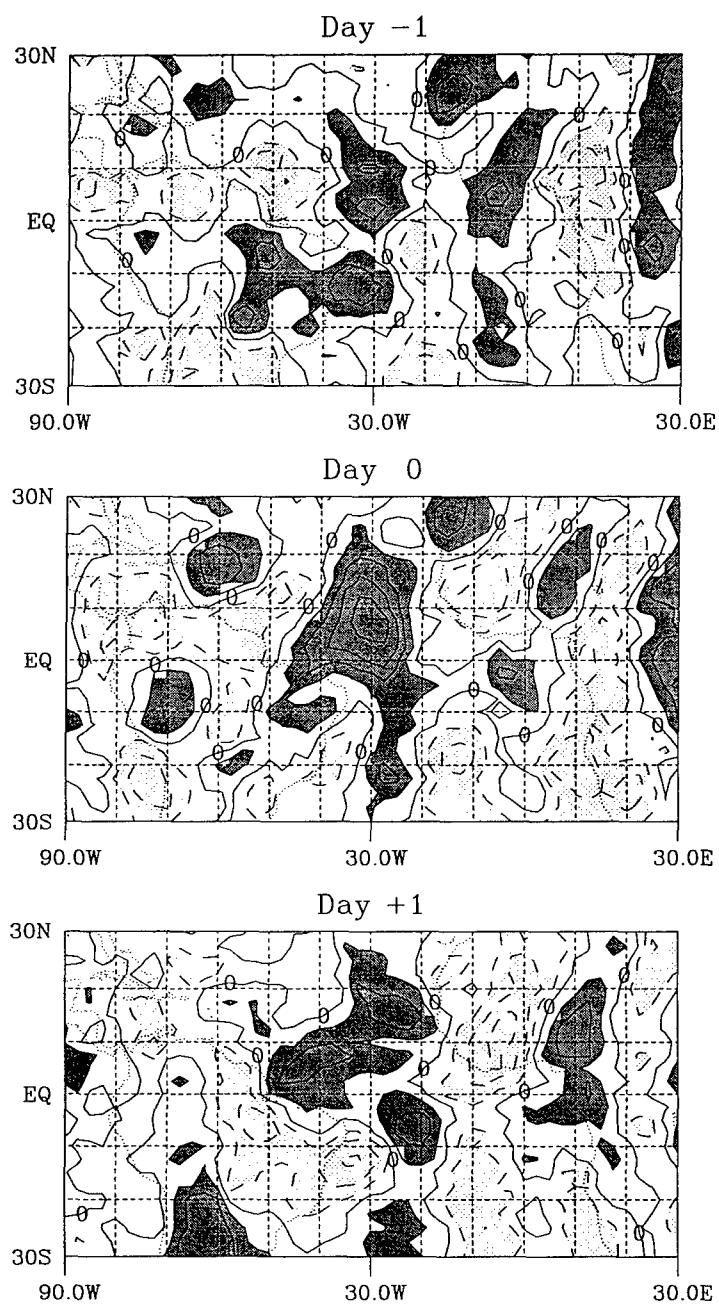
FIG. C10. As in Fig. C2, except at 7.5°N, 30°W.

SON 1987 (Warm Phase)

Day −1

Day 0

Day +1
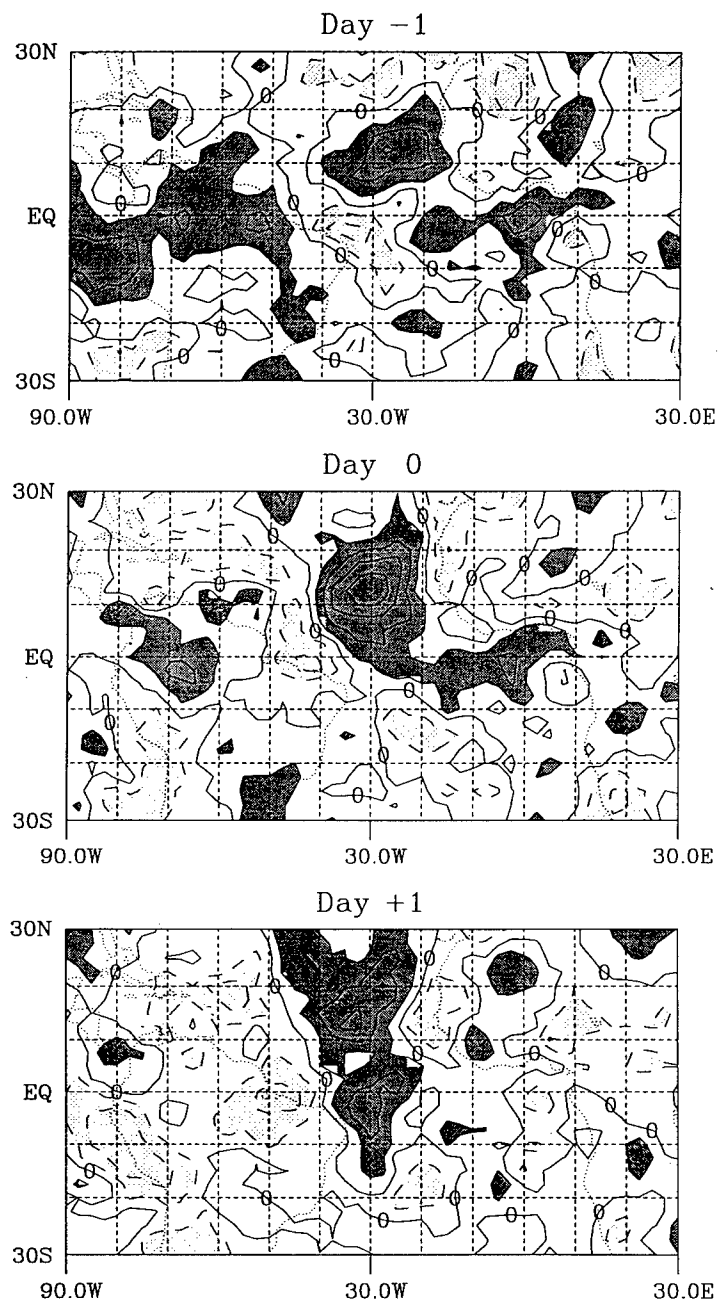
FIG. C11. As in Fig. C3, except at 12.5°N, 30°W.

SON 1988 (Cold Phase)

Day −1

Day 0

Day +1
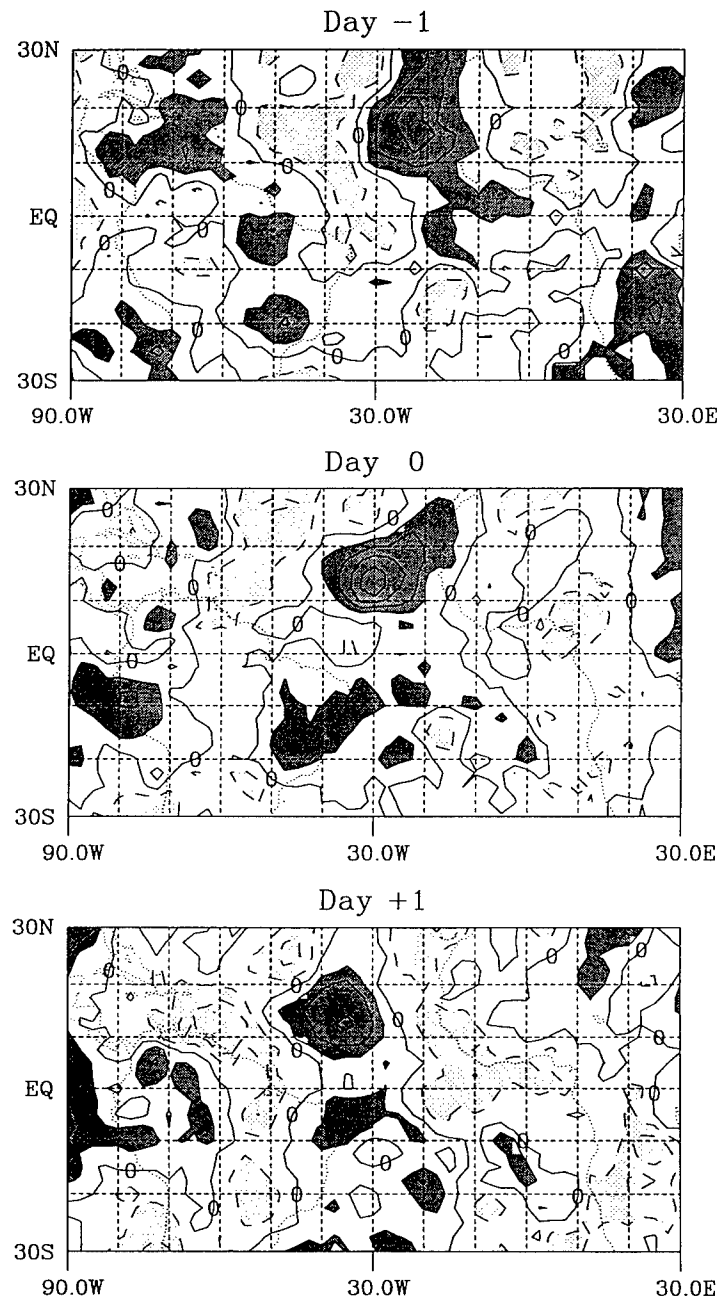
FIG. C12. As in Fig. C4, except at 12.5°N, 30°W.

MAM 1983 (Warm Phase)

Day −1

Day 0

Day +1
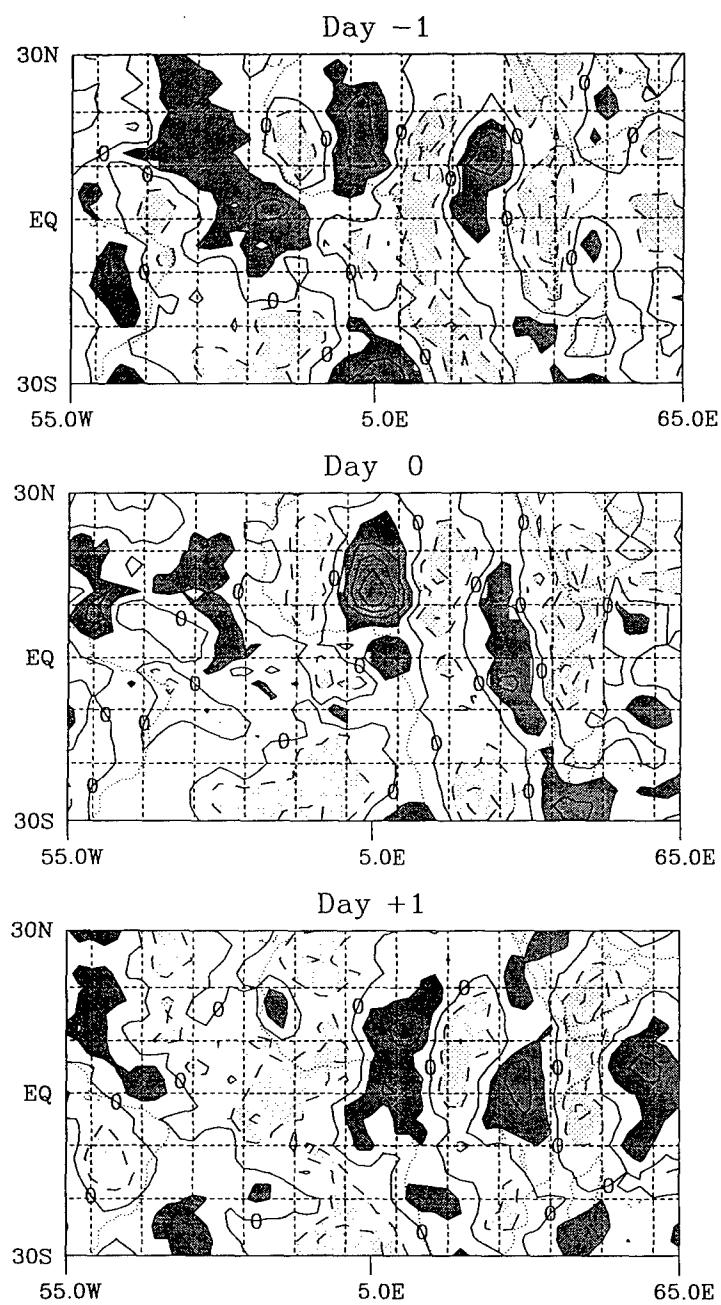
FIG. C13. As in Fig. C1, except at 12.5°N, 5°E.

MAM 1988 (Cold Phase)

Day −1

Day 0

Day +1
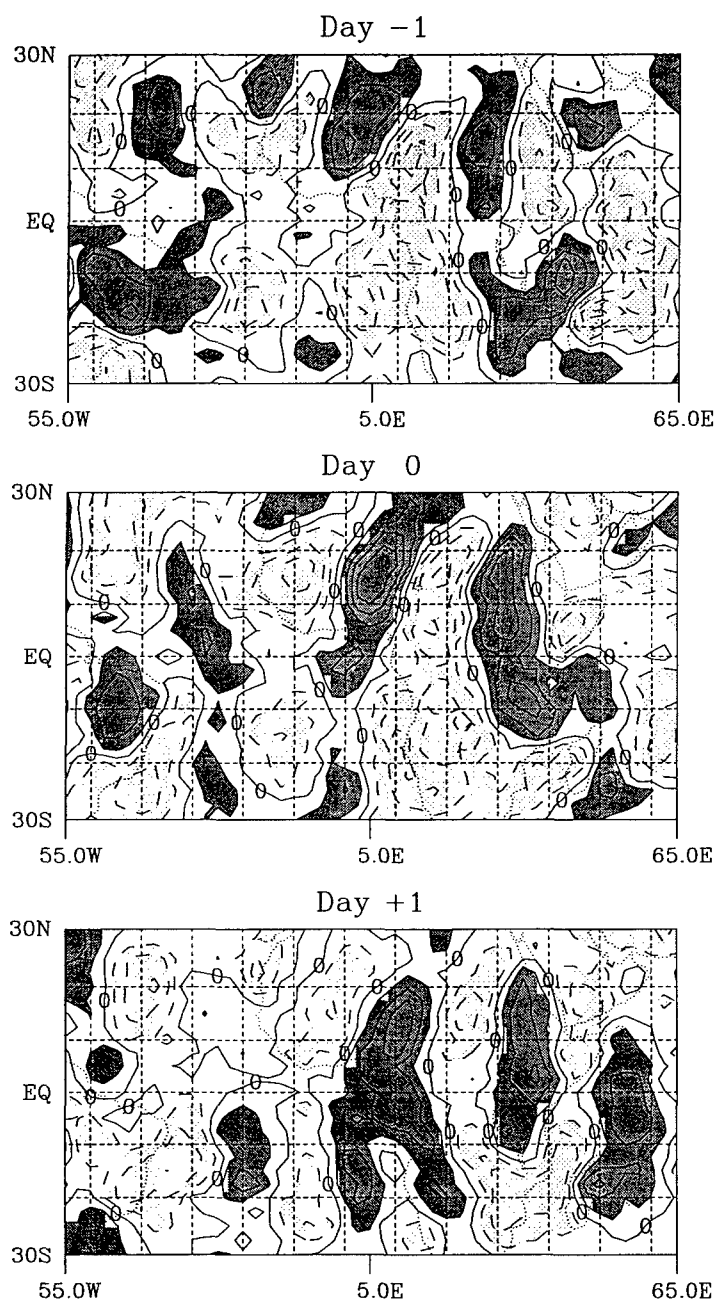
FIG. C14. As in Fig. C2, except at 12.5°N, 5°E.

SON 1987 (Warm Phase)

Day −1

Day 0

Day +1
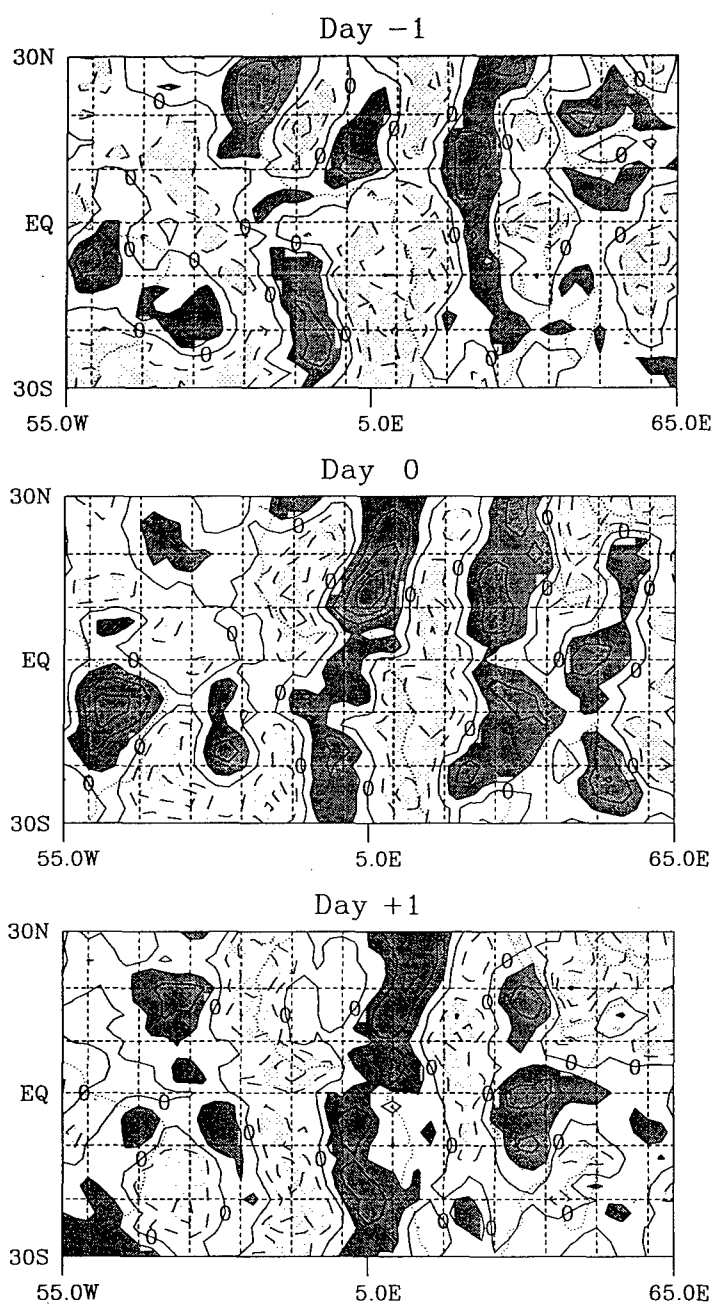
FIG. C15. As in Fig. C3, except at 12.5°N, 5°E.

SON 1988 (Cold Phase)

Day −1

Day 0

Day +1
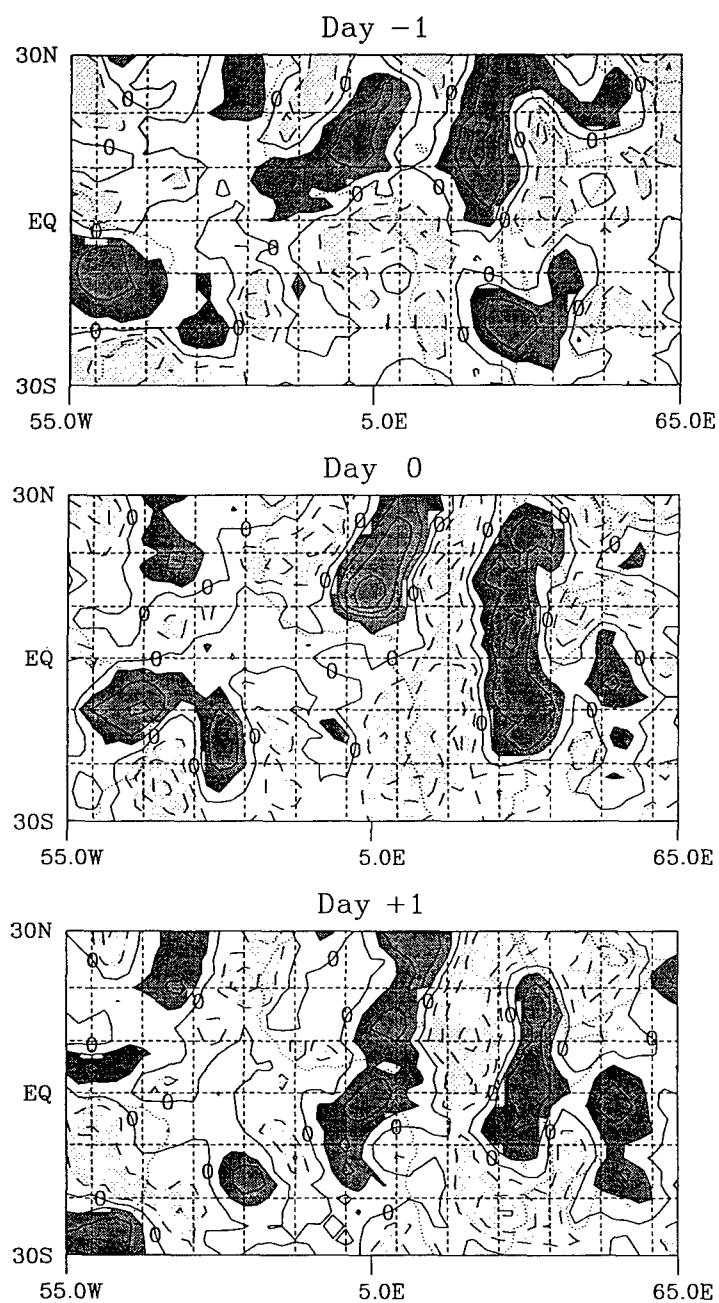
FIG. C16. As in Fig. C4, except at 12.5°N, 5°E.
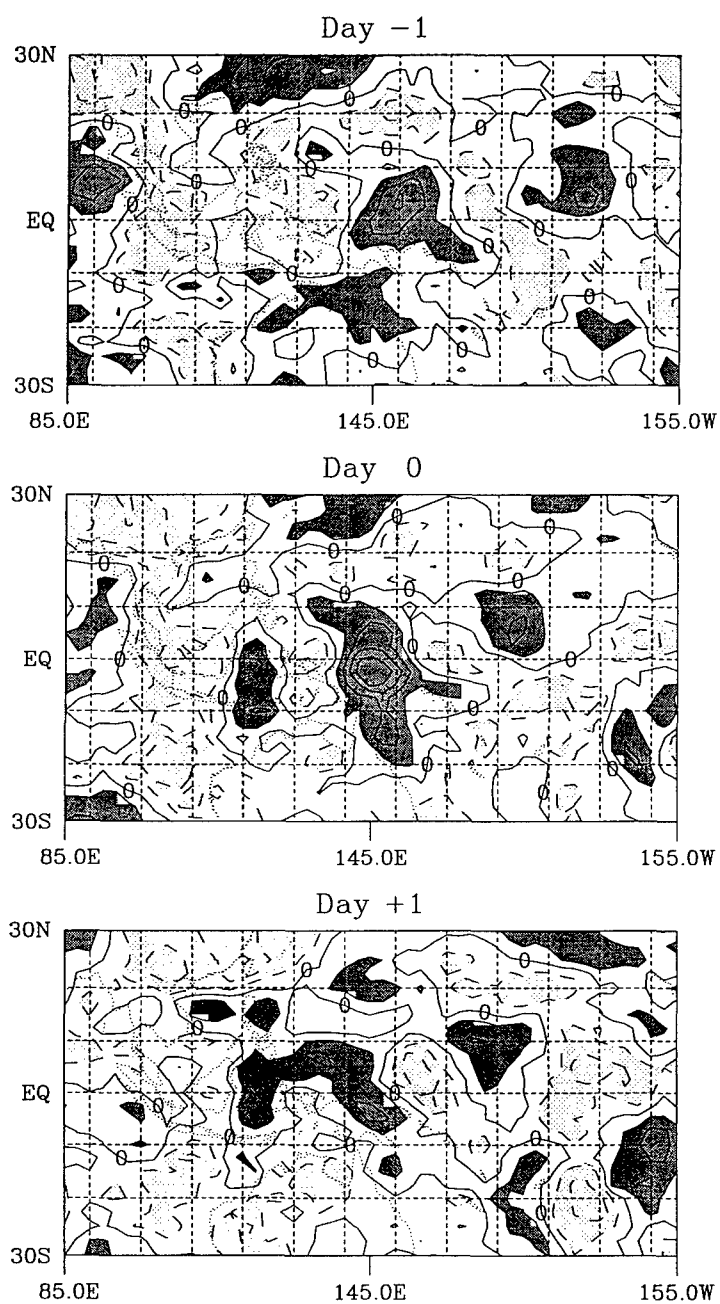
FIG. C17. As in Fig. C1, except at 2.5°S, 145°E.
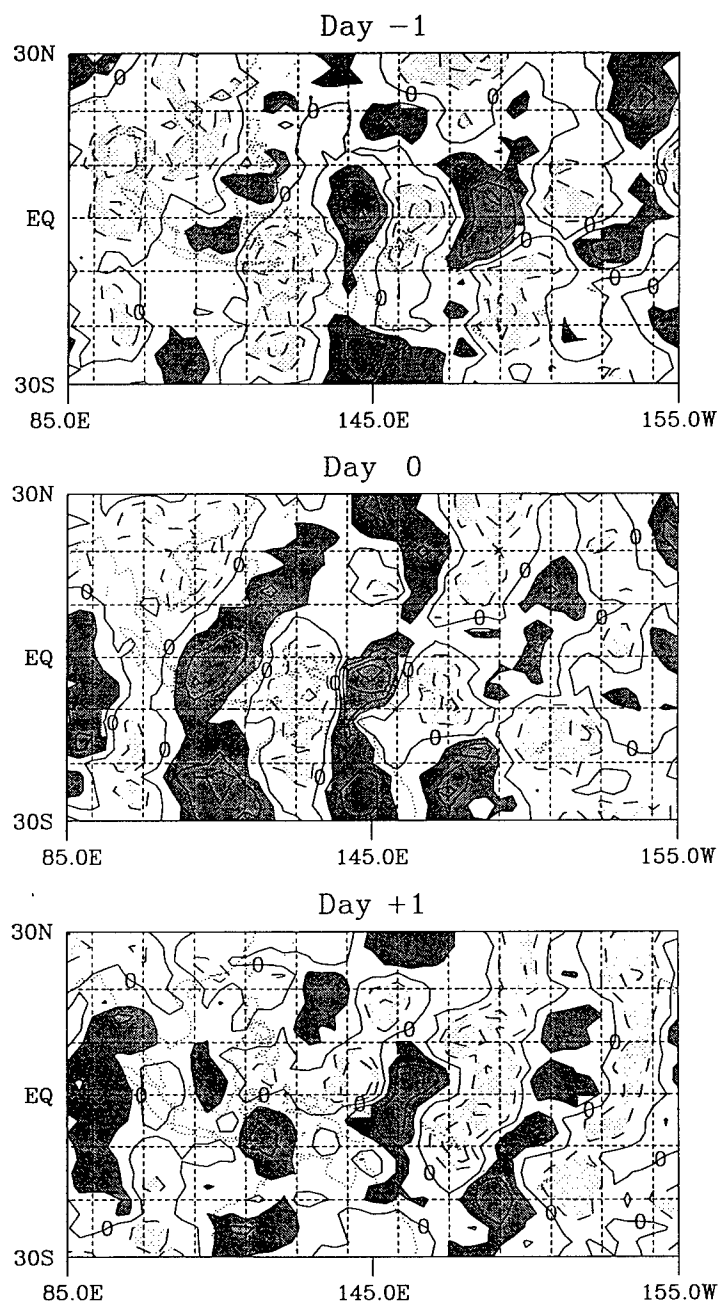
FIG. C18. As in Fig. C2, except at 2.5°S, 145°E.

SON 1987 (Warm Phase)

Day −1

Day 0

Day +1
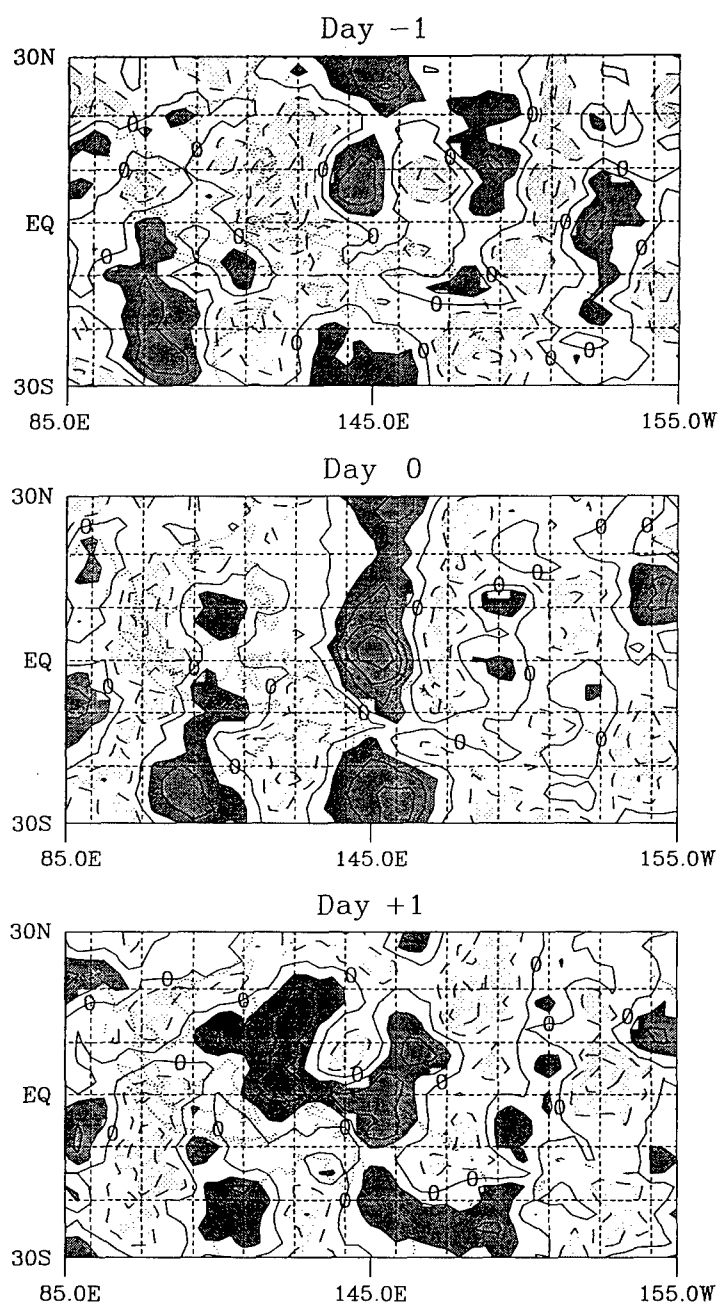
FIG. C19. As in Fig. C3, except at 2.5°N, 145°E.

SON 1988 (Cold Phase)

Day −1

Day 0

Day +1
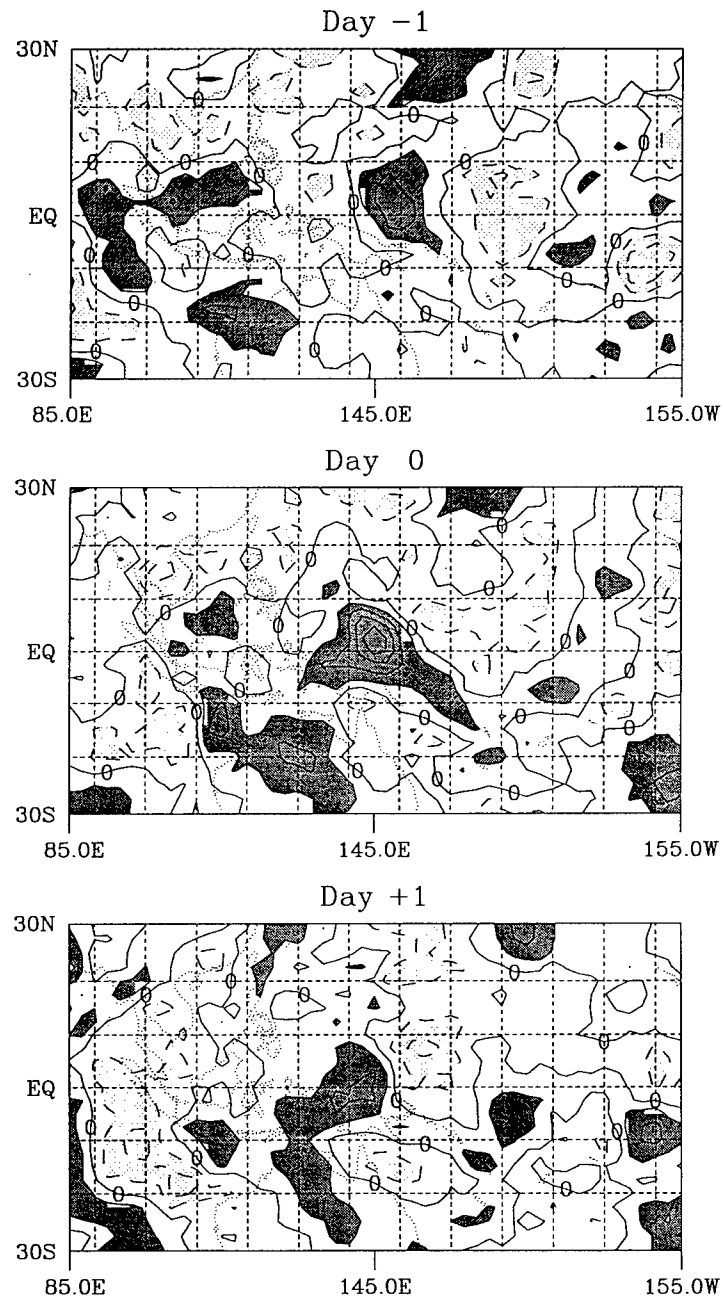
FIG. C20. As in Fig. C4, except at 2.5°N, 145°E.

MAM 1983 (Warm Phase)

Day −1

Day 0

Day +1
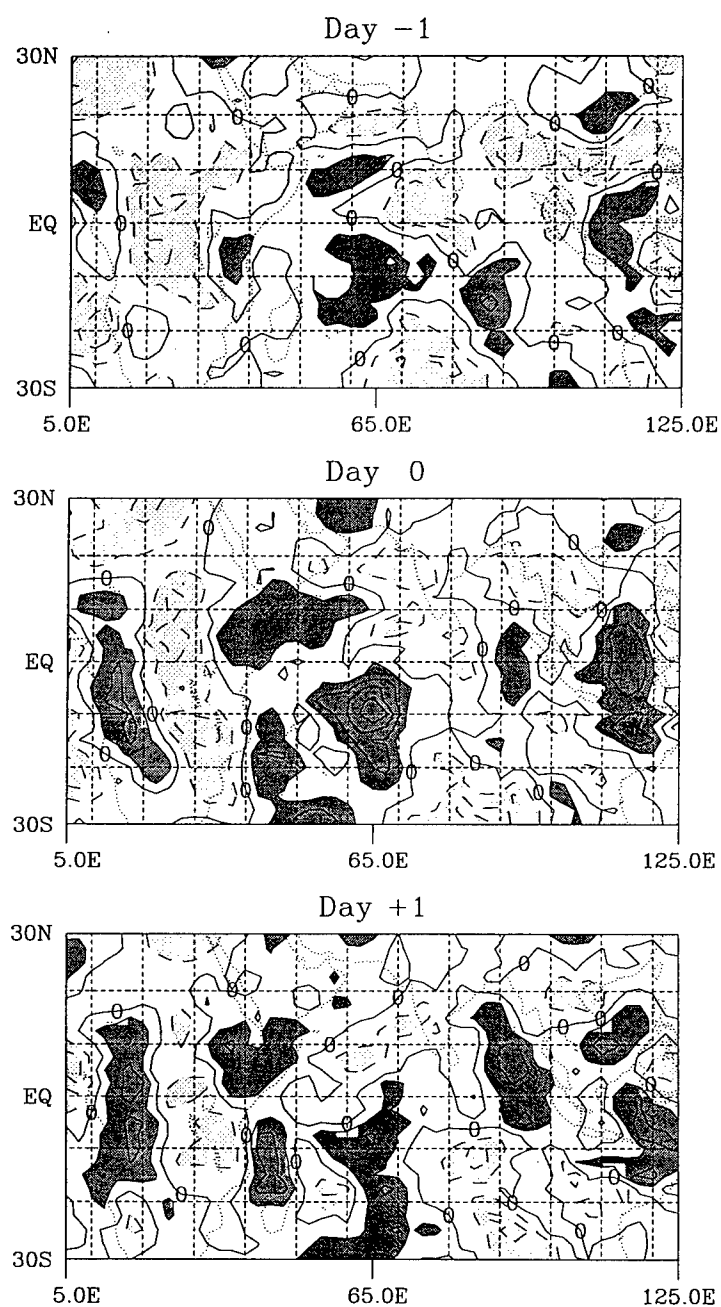
FIG. C21. As in Fig. C1, except at 10°S, 65°E.

MAM 1988 (Cold Phase)

Day −1

Day 0

Day +1
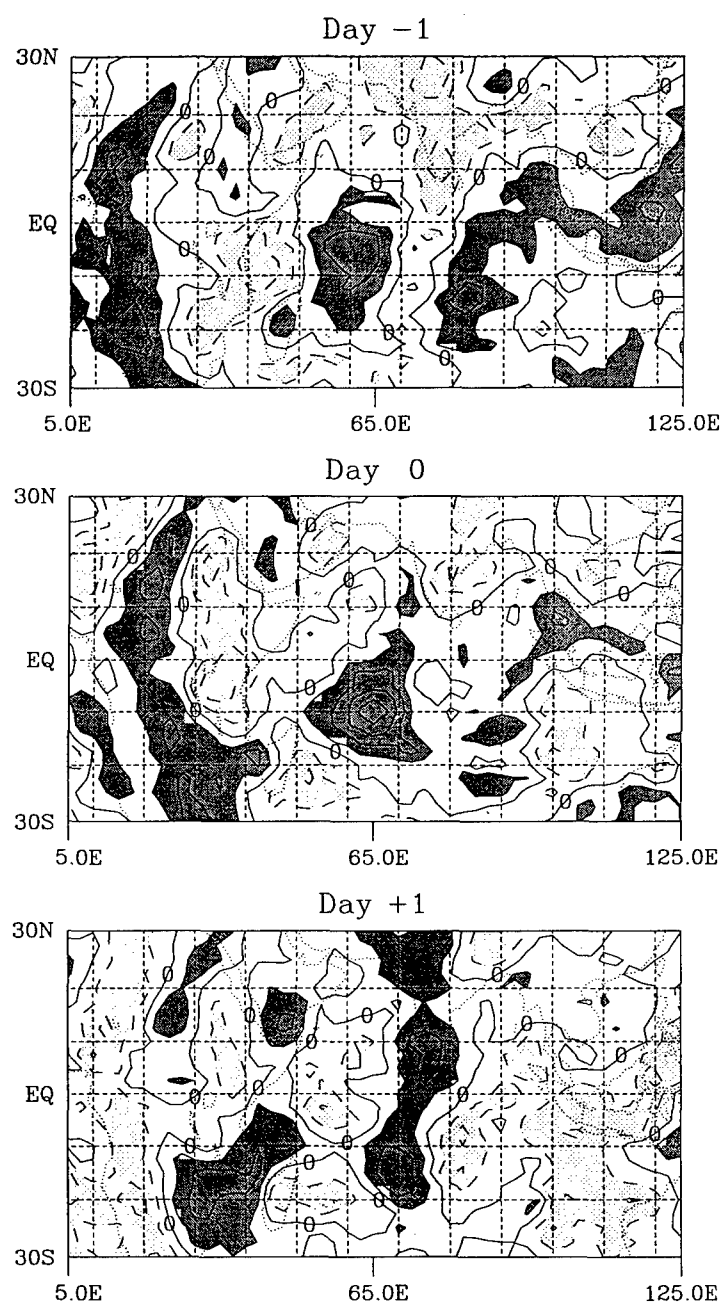
FIG. C22. As in Fig. C2, except at 10°S, 65°E.

SON 1987 (Warm Phase)

Day −1

Day 0

Day +1
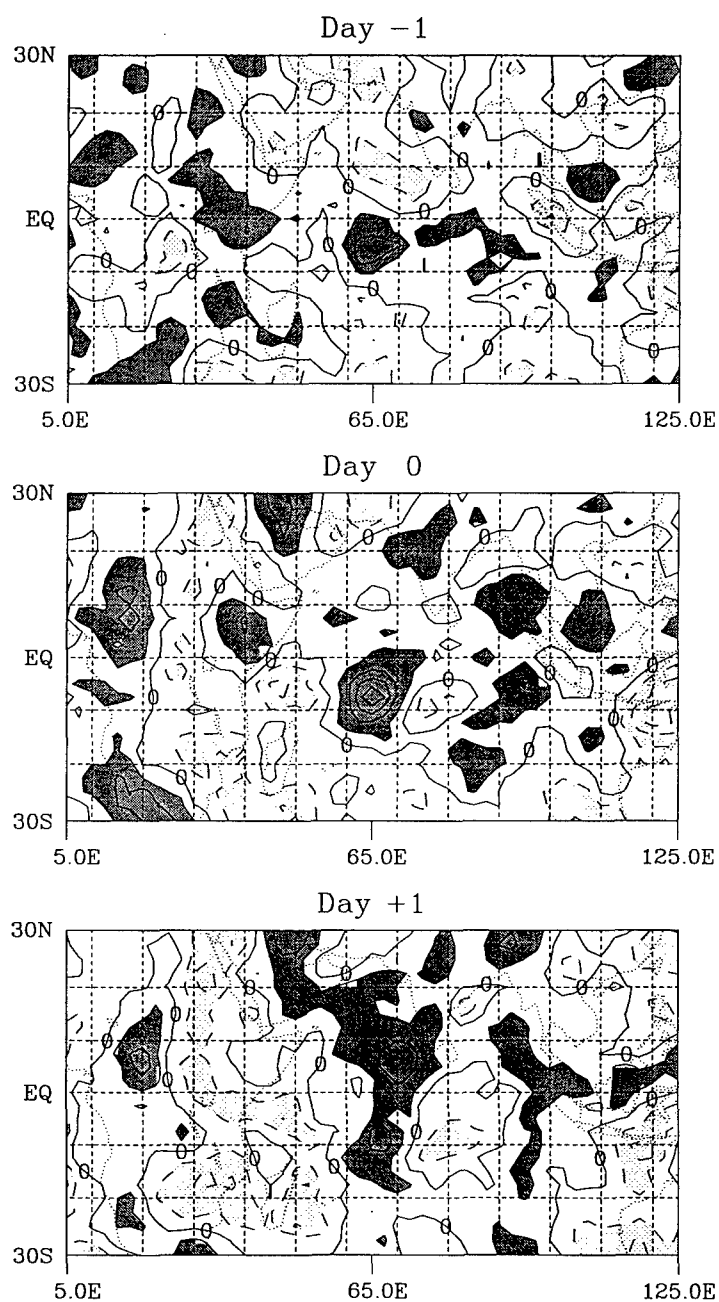
FIG. C23. As in Fig. C3, except at 7.5°S, 65°E.

SON 1988 (Cold Phase)

Day −1

Day 0

Day +1
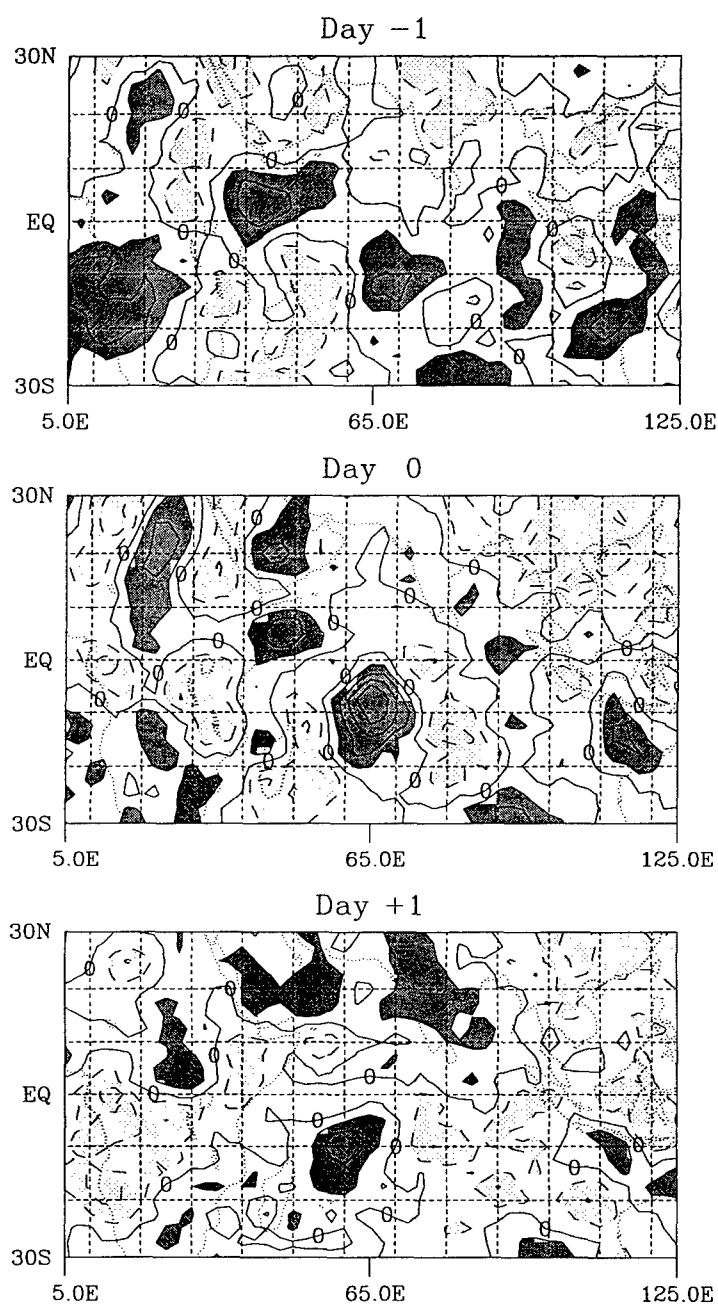
FIG. C24. As in Fig. C4, except at 7.5°S, 65°E.

MAM 1983 (Warm Phase)

Day −1

Day 0

Day +1
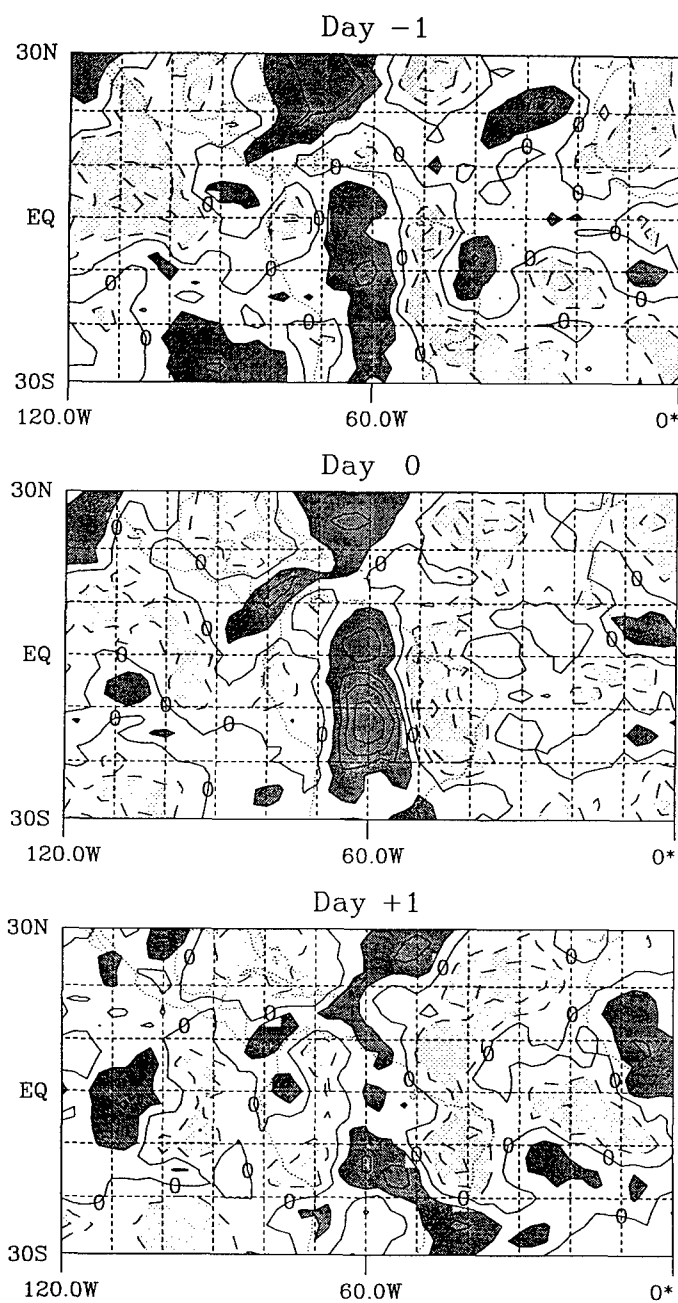
FIG. C25. As in Fig. C1, except at 12.5°S, 60°W.

MAM 1988 (Cold Phase)

Day −1

Day 0

Day +1
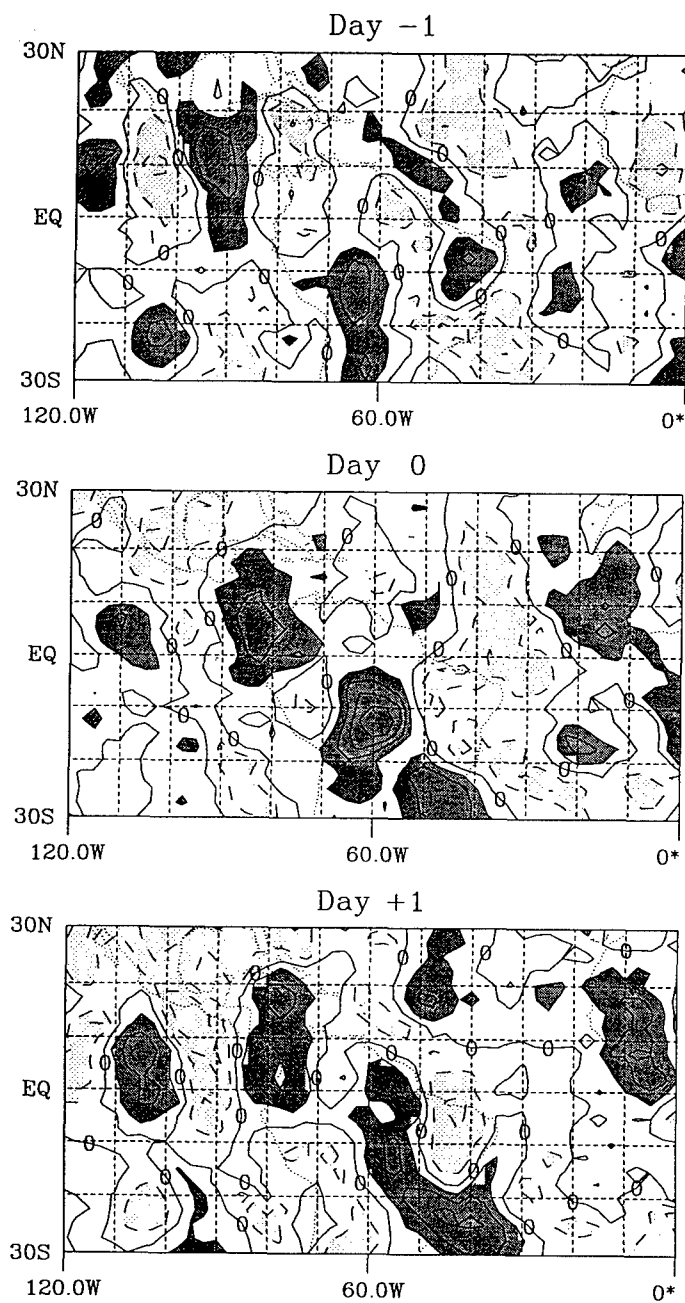
FIG. C26. As in Fig. C2, except at 12.5°S, 60°W.

SON 1987 (Warm Phase)

Day −1

Day 0

Day +1
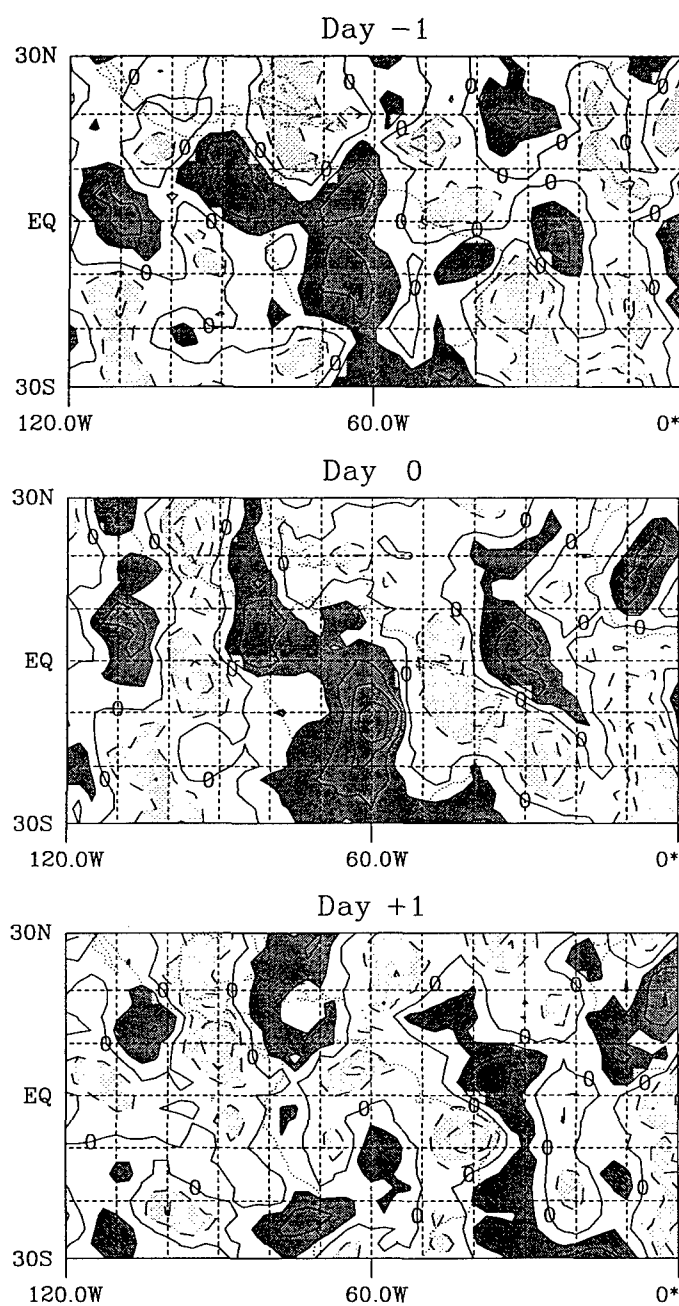
FIG. C27. As in Fig. C3, except at 12.5°S, 60°W.

SON 1988 (Cold Phase)

Day −1

Day 0

Day +1
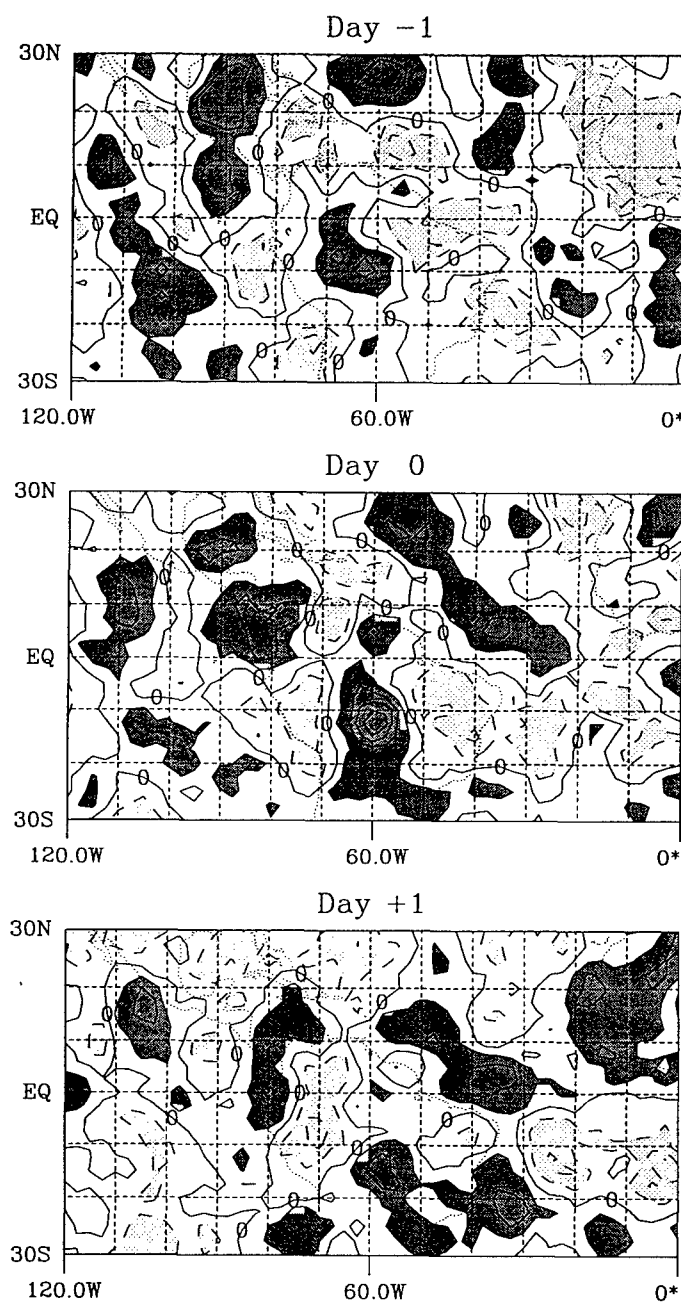
FIG. C28. As in Fig. C4, except at 12.5°S, 60°W.

APPENDIX   D

Synoptic Filtered Time—Longitude Plots at 30.0 N

SON 1989   (PW)
Missing Oct 9

(a)

SON 1989   (OLR)
No Missing Days

(b)

DJF 1989/1990   (PW)
Missing Dec 14

(c)

DJF 1989/1990   (OLR)
No Missing Days

(d)
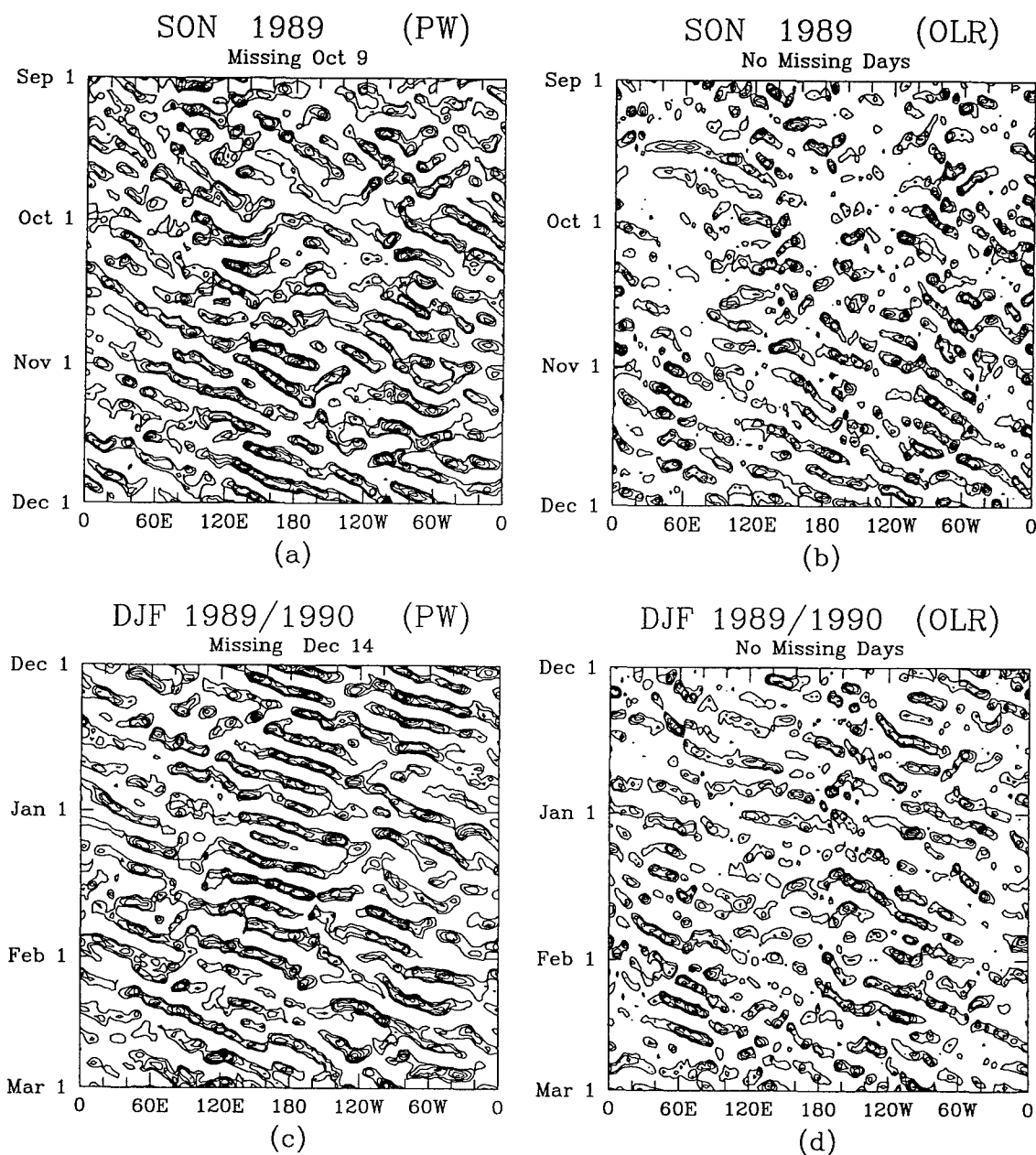
FIG. D1. Synoptic filtered time-longitude plots at 30°N during SON 1989 for (a) PW and (b) OLR anomalies and during DJF 1989/1990 for (c) PW and (d) OLR anomalies. Lowest (highest) contour for PW (OLR) anomalies is +0.5 mm (-5 Wm^{-2}) with an interval of 1.0 mm (10 Wm^{-2}). Days missing from each period are listed on plots.

Synoptic Filtered Time—Longitude Plots at 30.0 N

MAM 1989 (PW)
No Missing Days

(a)

MAM 1989 (OLR)
Missing May 31

(b)

JJA 1989 (PW)
No Missing Days

(c)

JJA 1989 (OLR)
No Missing Days

(d)
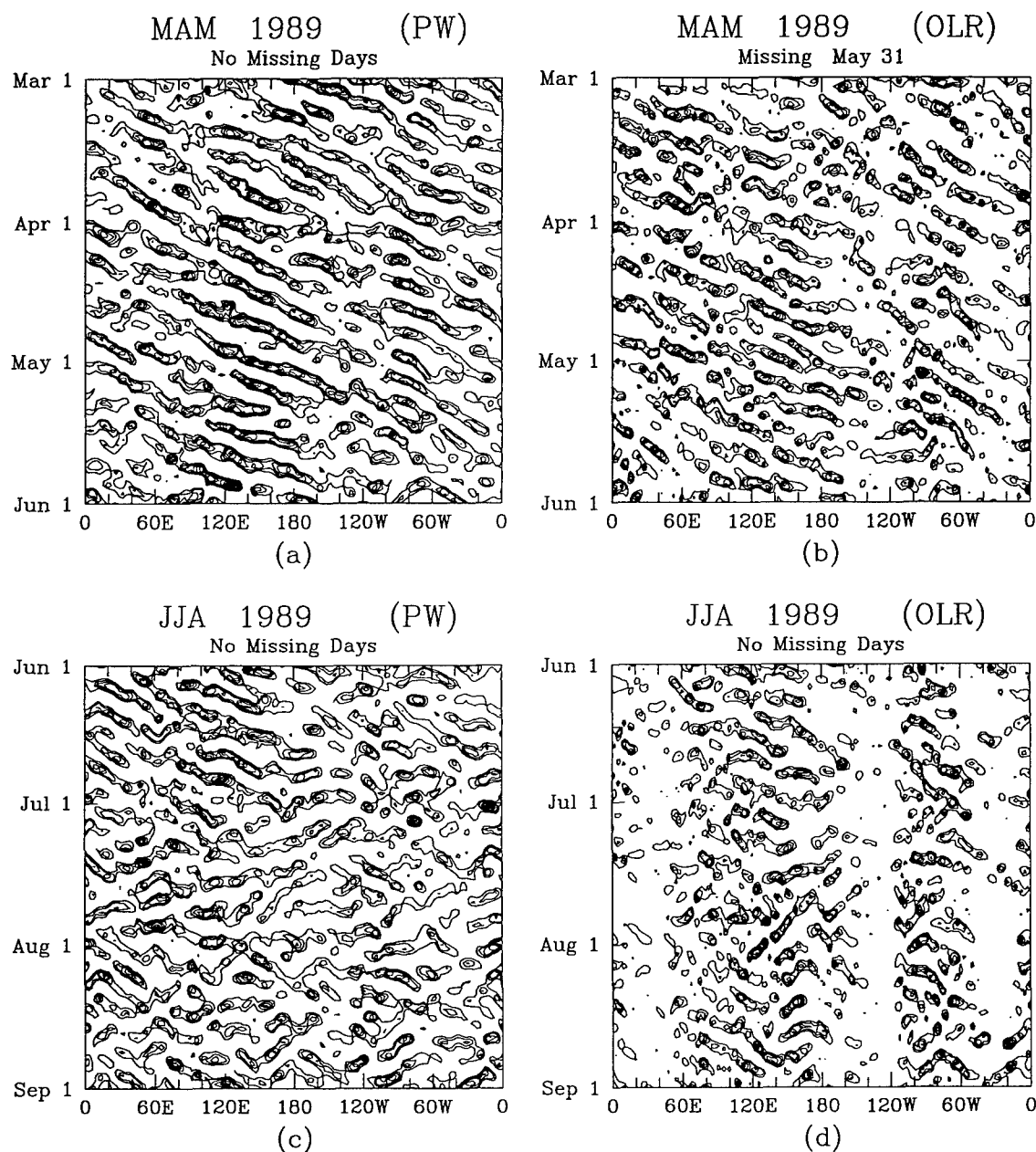
FIG. D2. As in Fig. D1, except during MAM 1989 for (a) PW and (b) OLR anomalies and during JJA 1989 for (c) PW and (d) OLR anomalies.

Synoptic Filtered Time–Longitude Plots at 20.0 N

SON 1989 (PW)
Missing Oct 9

(a)

SON 1989 (OLR)
No Missing Days

(b)

DJF 1989/1990 (PW)
Missing Dec 14

(c)

DJF 1989/1990 (OLR)
No Missing Days

(d)
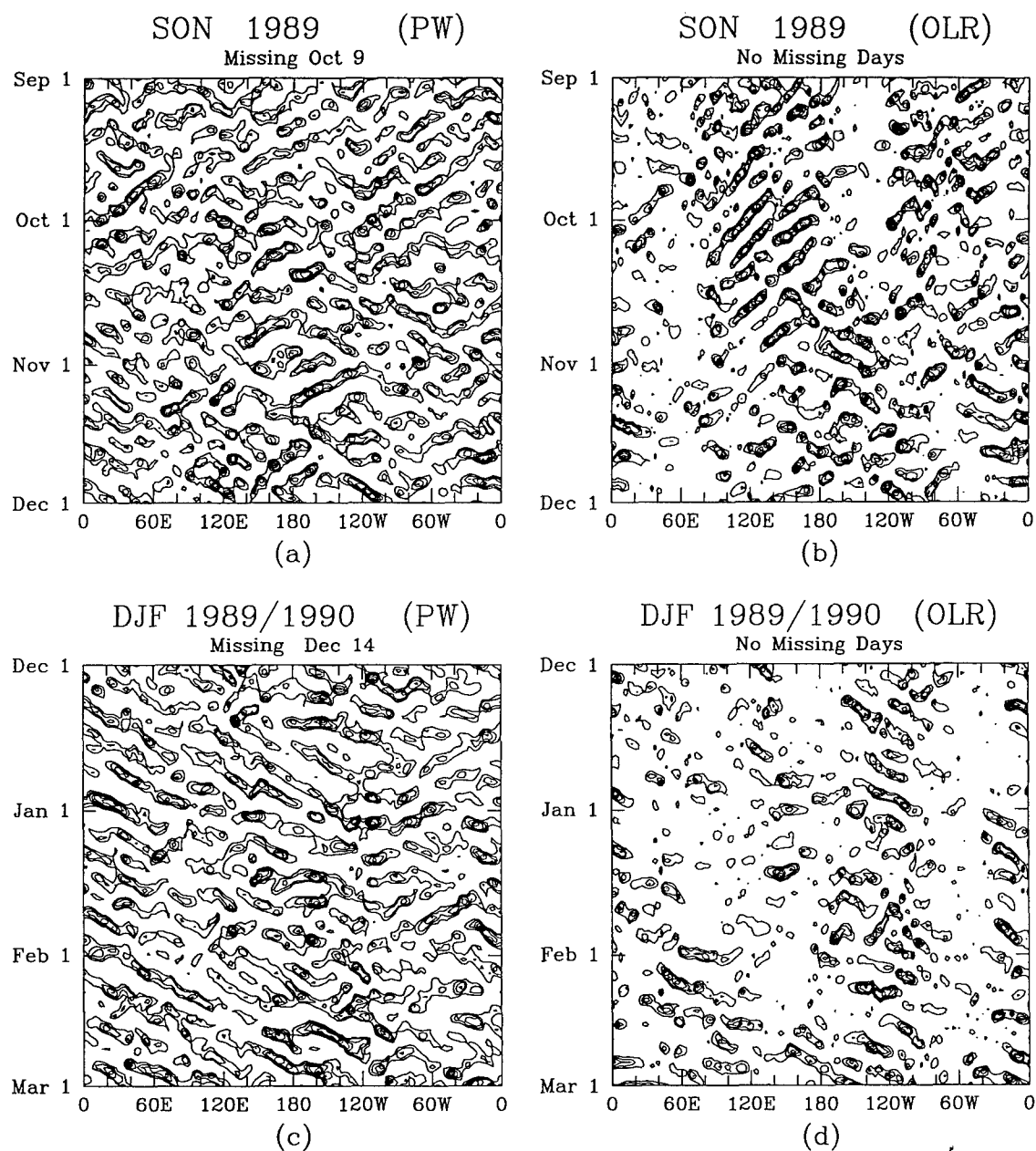
FIG. D3. As in Fig. D1, except at 20°N.

Synoptic Filtered Time–Longitude Plots at 20.0 N

MAM   1989   (PW)
No Missing Days

(a)

MAM   1989   (OLR)
Missing   May 31

(b)

JJA   1989   (PW)
No Missing Days

(c)

JJA   1989   (OLR)
No Missing Days

(d)
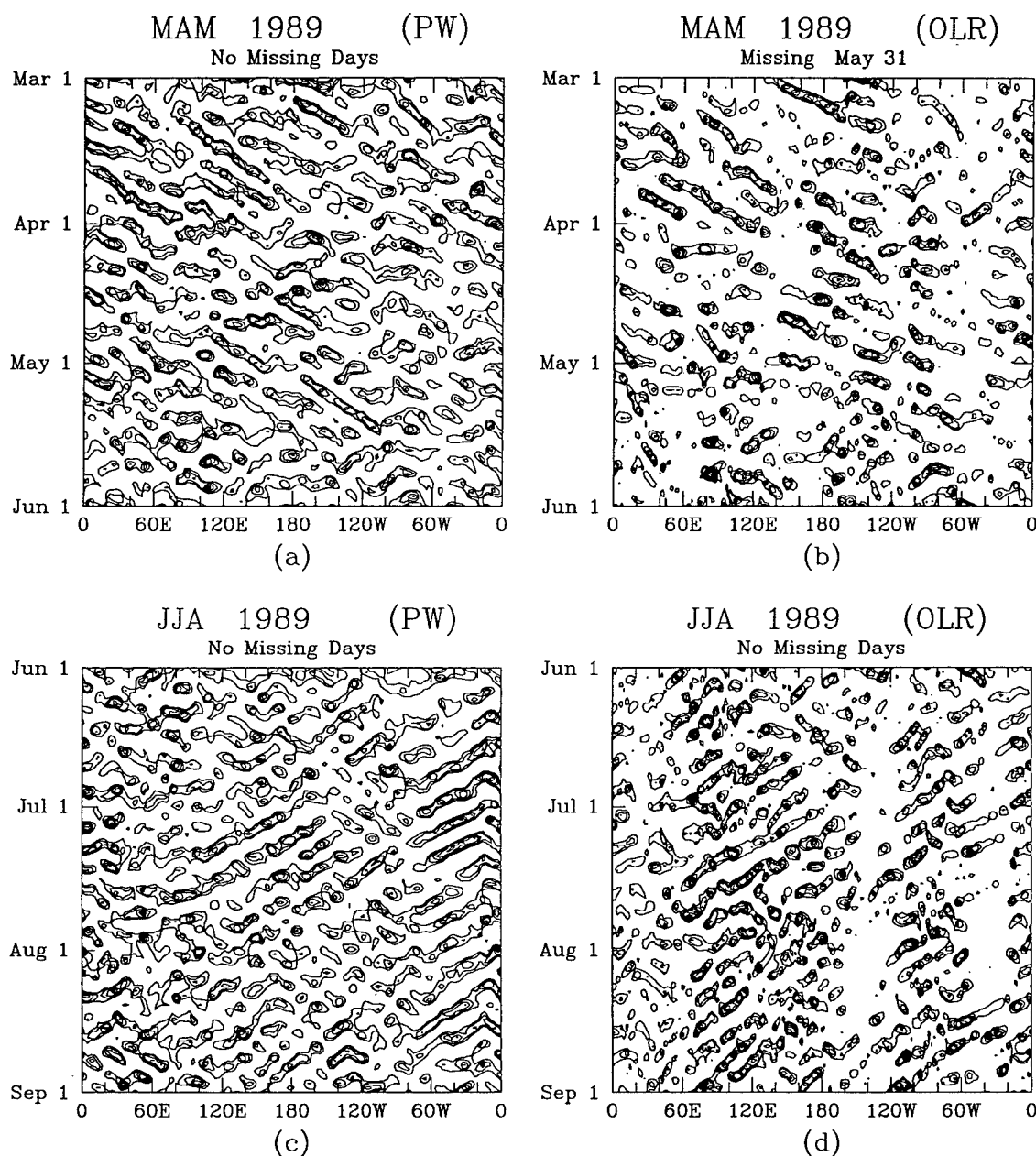
FIG. D4. As in Fig. D2, except at 20°N.

Synoptic Filtered Time–Longitude Plots at 10.0 N

SON 1989 (PW)
Missing Oct 9

SON 1989 (OLR)
No Missing Days

(a)

(b)

DJF 1989/1990 (PW)
Missing Dec 14

DJF 1989/1990 (OLR)
No Missing Days

(c)

(d)
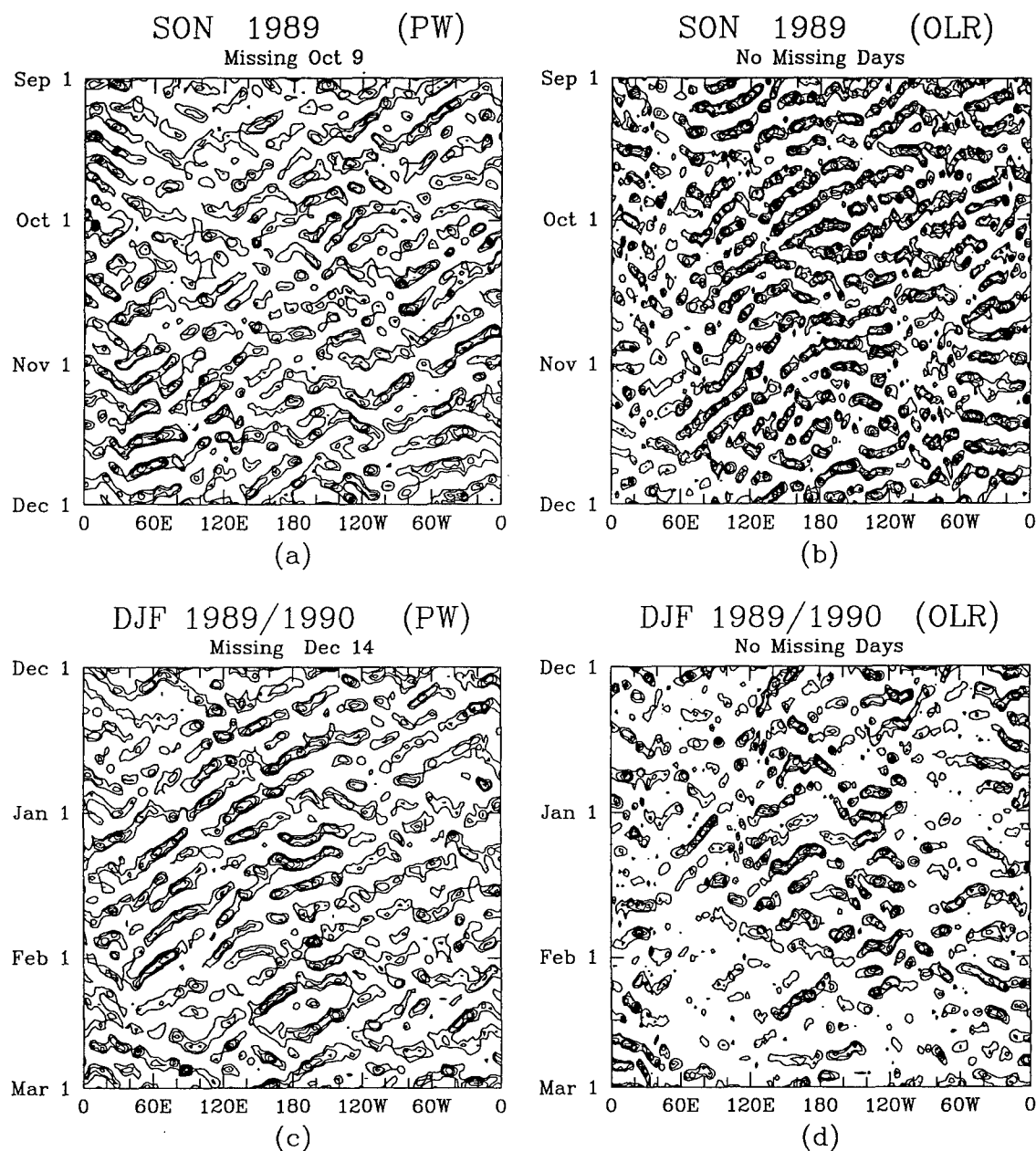
FIG. D5. As in Fig. D1, except at 10°N.

Synoptic Filtered Time–Longitude Plots at 10.0 N

MAM 1989 (PW)
No Missing Days

MAM 1989 (OLR)
Missing May 31

(a)

(b)

JJA 1989 (PW)
No Missing Days

JJA 1989 (OLR)
No Missing Days

(c)

(d)
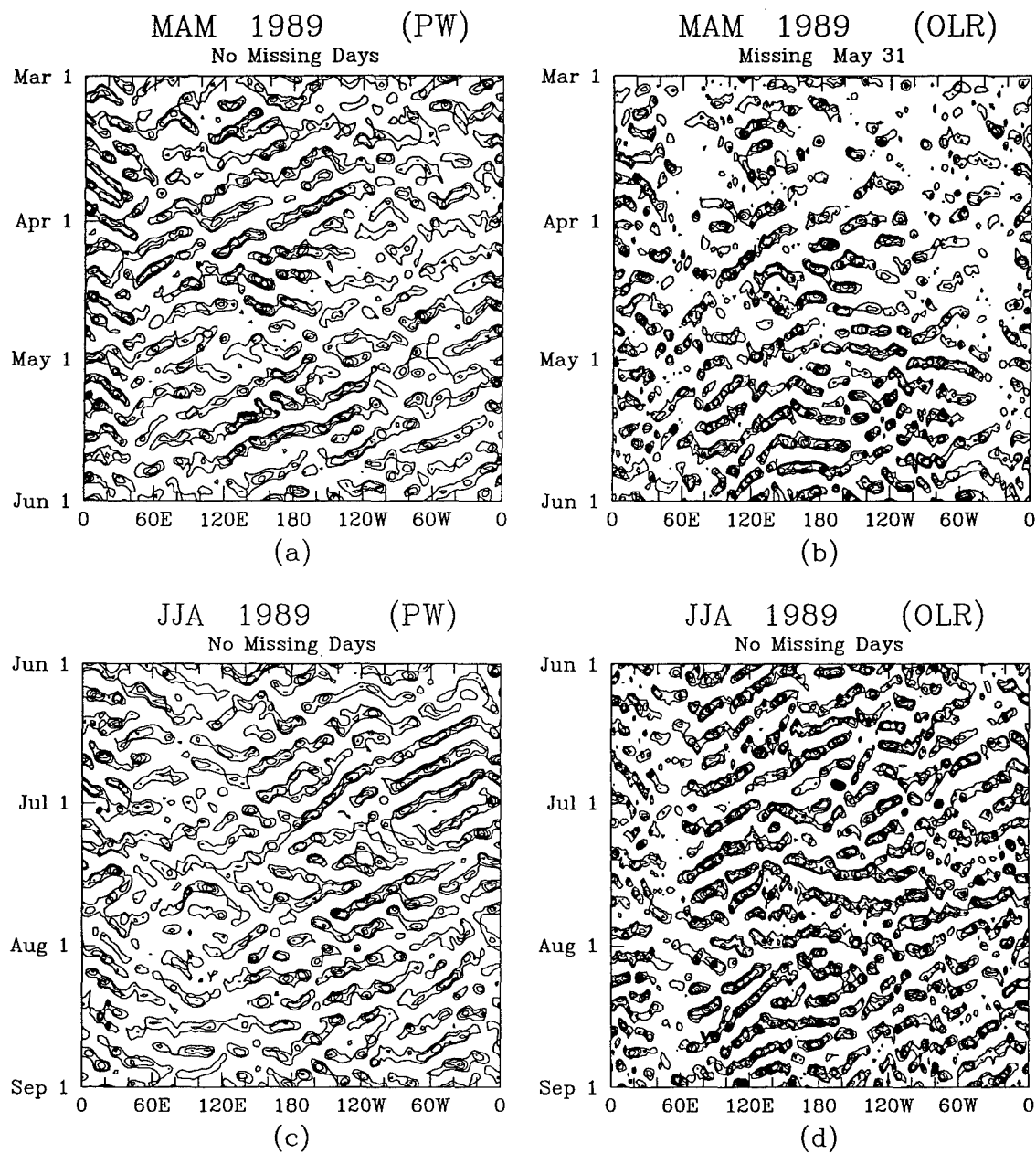
FIG. D6. As in Fig. D2, except at 10°N.

239

Synoptic Filtered Time−Longitude Plots at the EQ

SON 1989 (PW)
Missing Oct 9

(a)

SON 1989 (OLR)
No Missing Days

(b)

DJF 1989/1990 (PW)
Missing Dec 14

(c)

DJF 1989/1990 (OLR)
No Missing Days

(d)
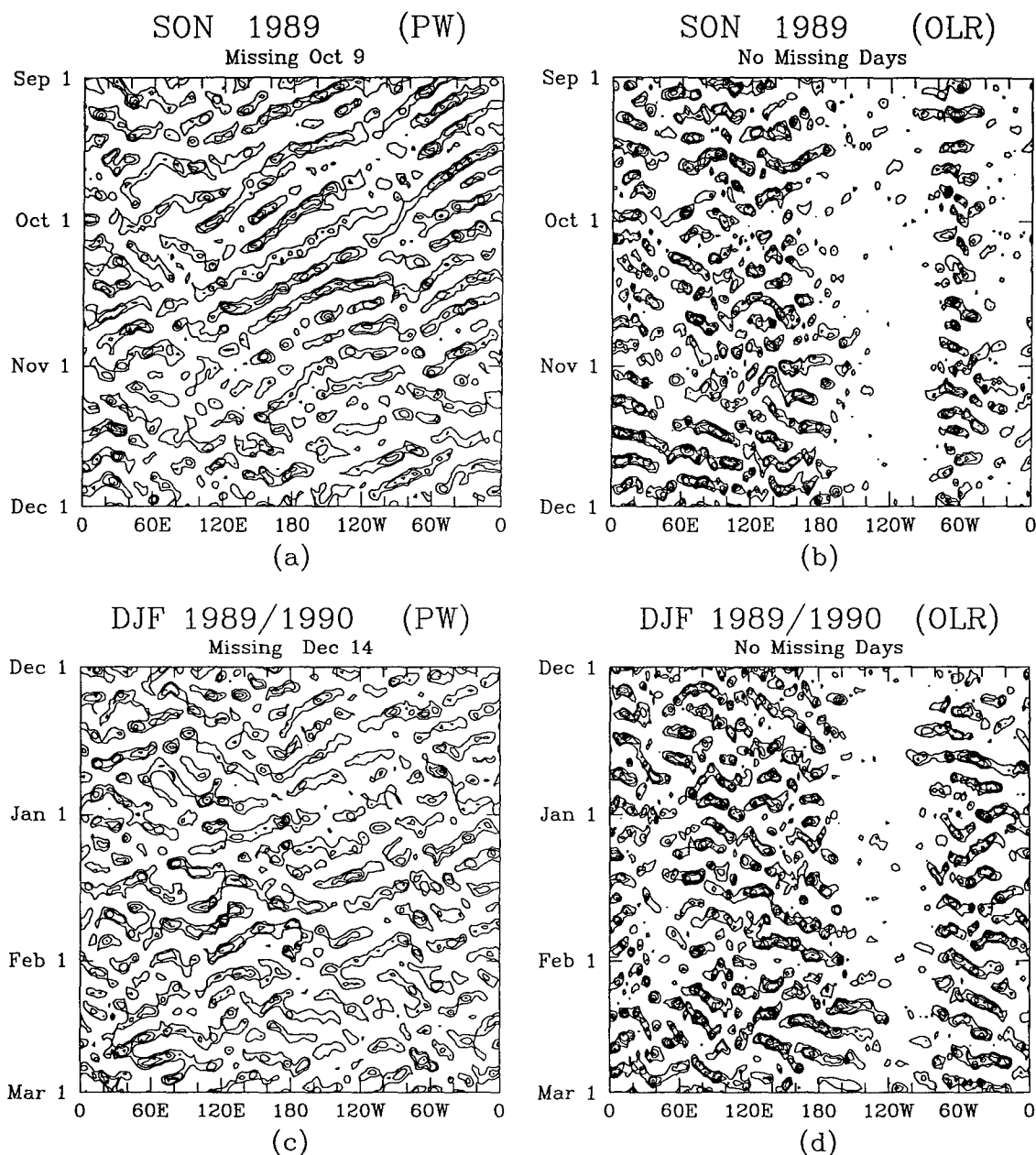
FIG. D7. As in Fig. D1, except at the equator.

Synoptic Filtered Time–Longitude Plots at the EQ

MAM 1989 (PW)
No Missing Days

MAM 1989 (OLR)
Missing May 31

(a)

(b)

JJA 1989 (PW)
No Missing Days

JJA 1989 (OLR)
No Missing Days

(c)

(d)
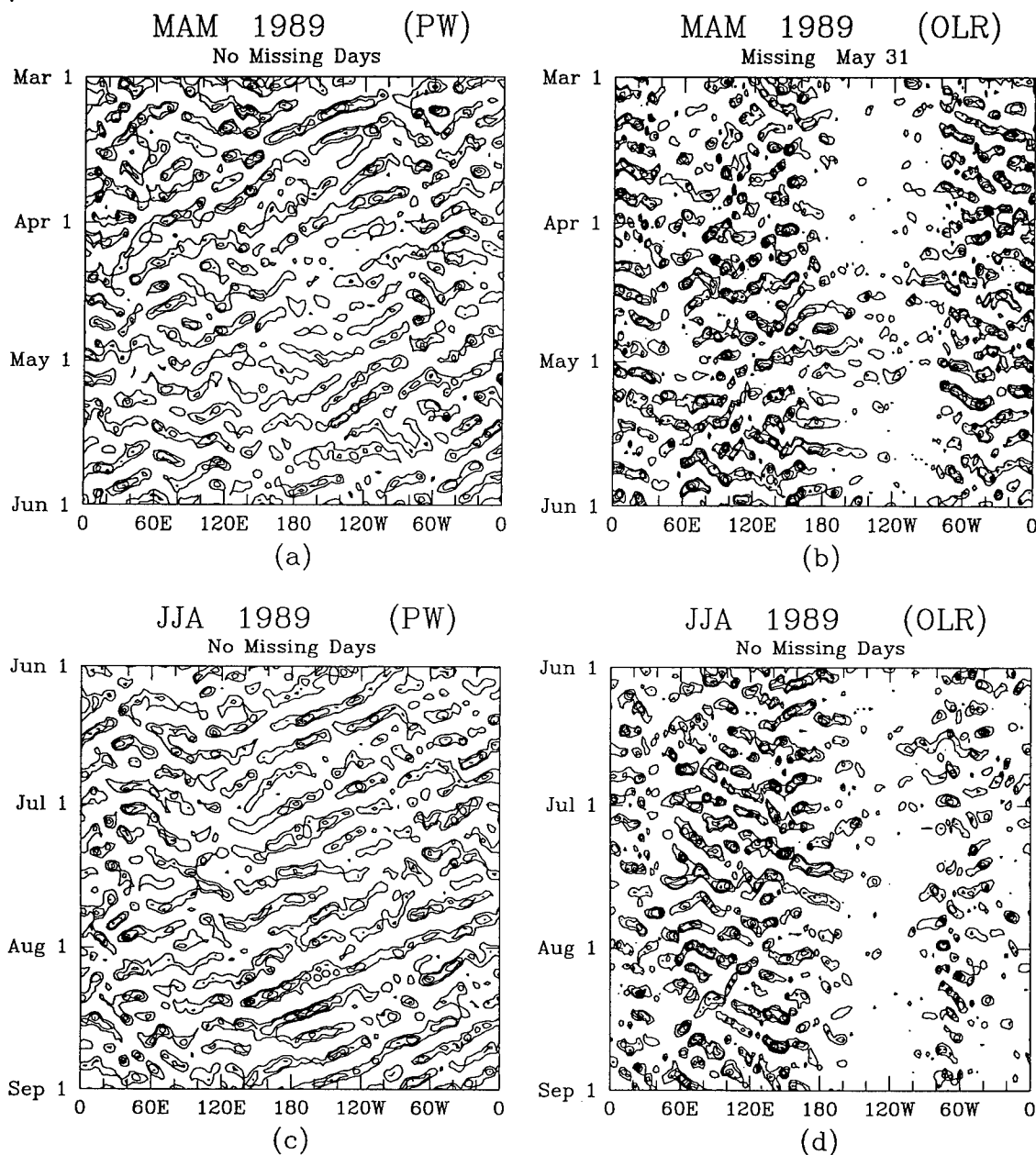
FIG. D8. As in Fig. D2, except at the equator.

Synoptic Filtered Time–Longitude Plots at 10.0 S

SON   1989   (PW)
Missing Oct 9

SON   1989   (OLR)
No Missing Days

(a)

(b)

DJF 1989/1990   (PW)
Missing Dec 14

DJF 1989/1990   (OLR)
No Missing Days

(c)

(d)
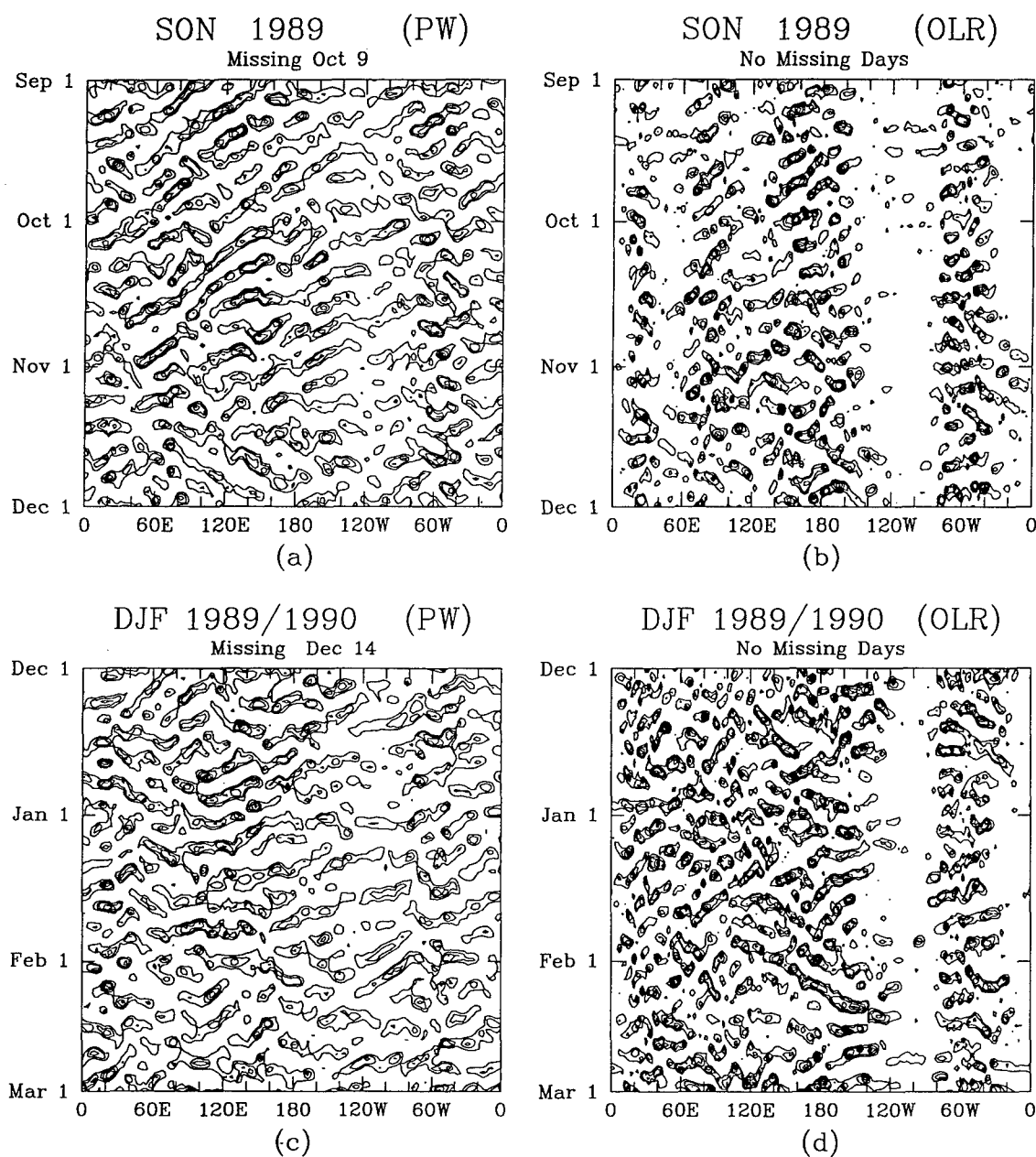
FIG. D9. As in Fig. D1, except at 10°S.

Synoptic Filtered Time–Longitude Plots at 10.0 S
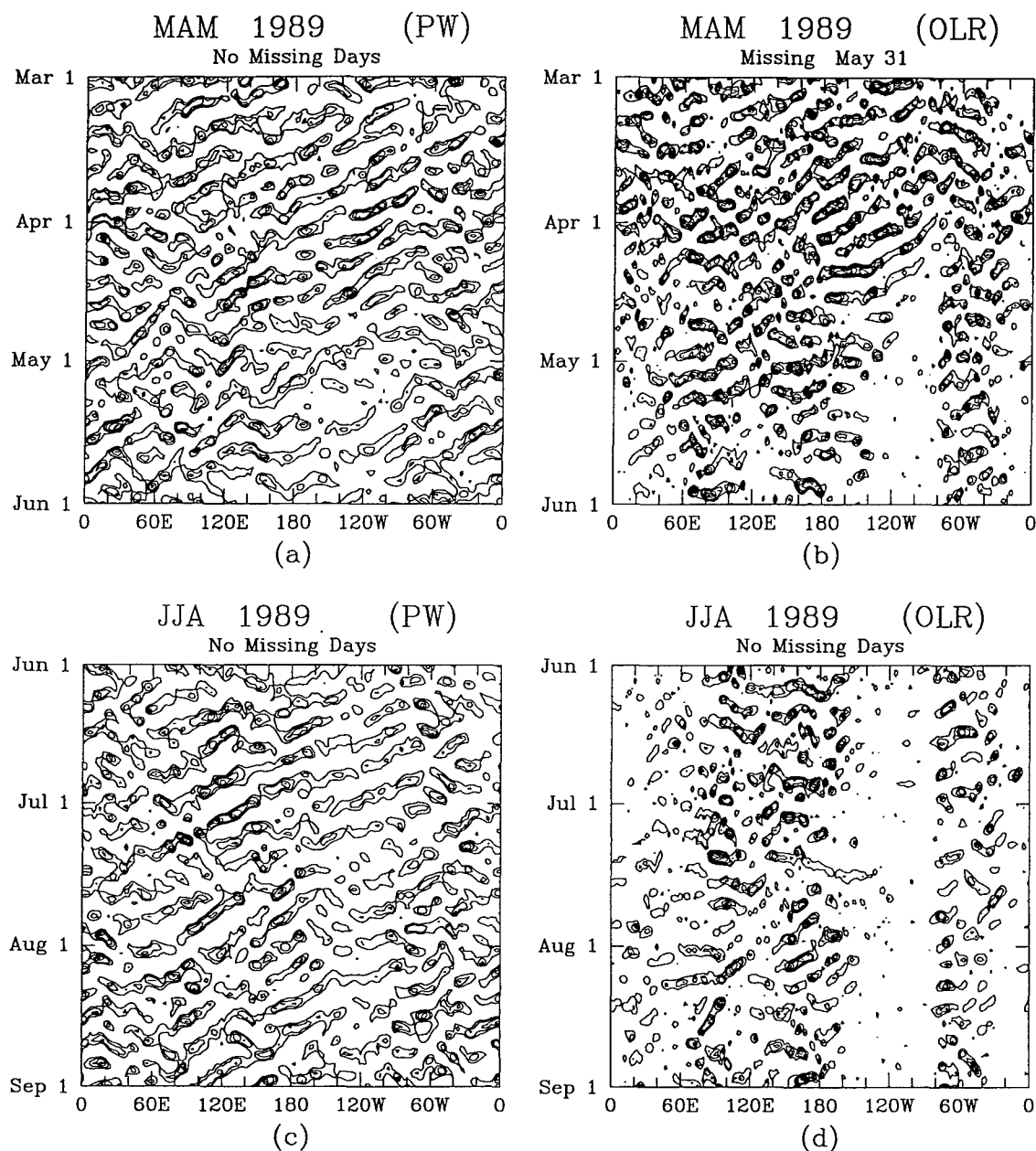
FIG. D10. As in Fig. D2, except at 10°S.

Synoptic Filtered Time–Longitude Plots at 20.0 S

SON 1989 (PW)
Missing Oct 9

SON 1989 (OLR)
No Missing Days

(a)

(b)

DJF 1989/1990 (PW)
Missing Dec 14

DJF 1989/1990 (OLR)
No Missing Days

(c)

(d)
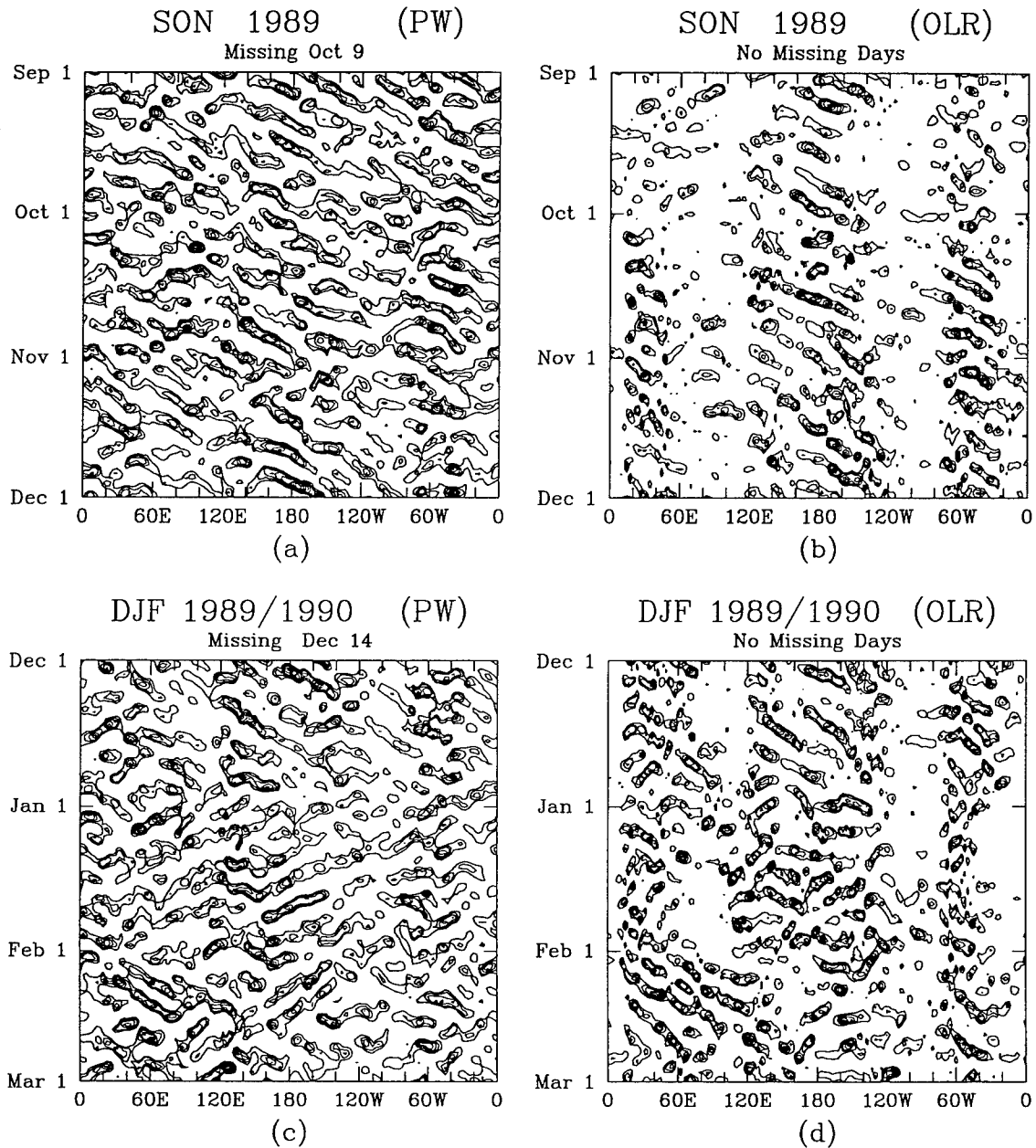
FIG. D11. As in Fig. D1, except at 20°S.

Synoptic Filtered Time–Longitude Plots at 20.0 S

MAM 1989 (PW)
No Missing Days

MAM 1989 (OLR)
Missing May 31

(a)

(b)

JJA 1989 (PW)
No Missing Days

JJA 1989 (OLR)
No Missing Days

(c)

(d)
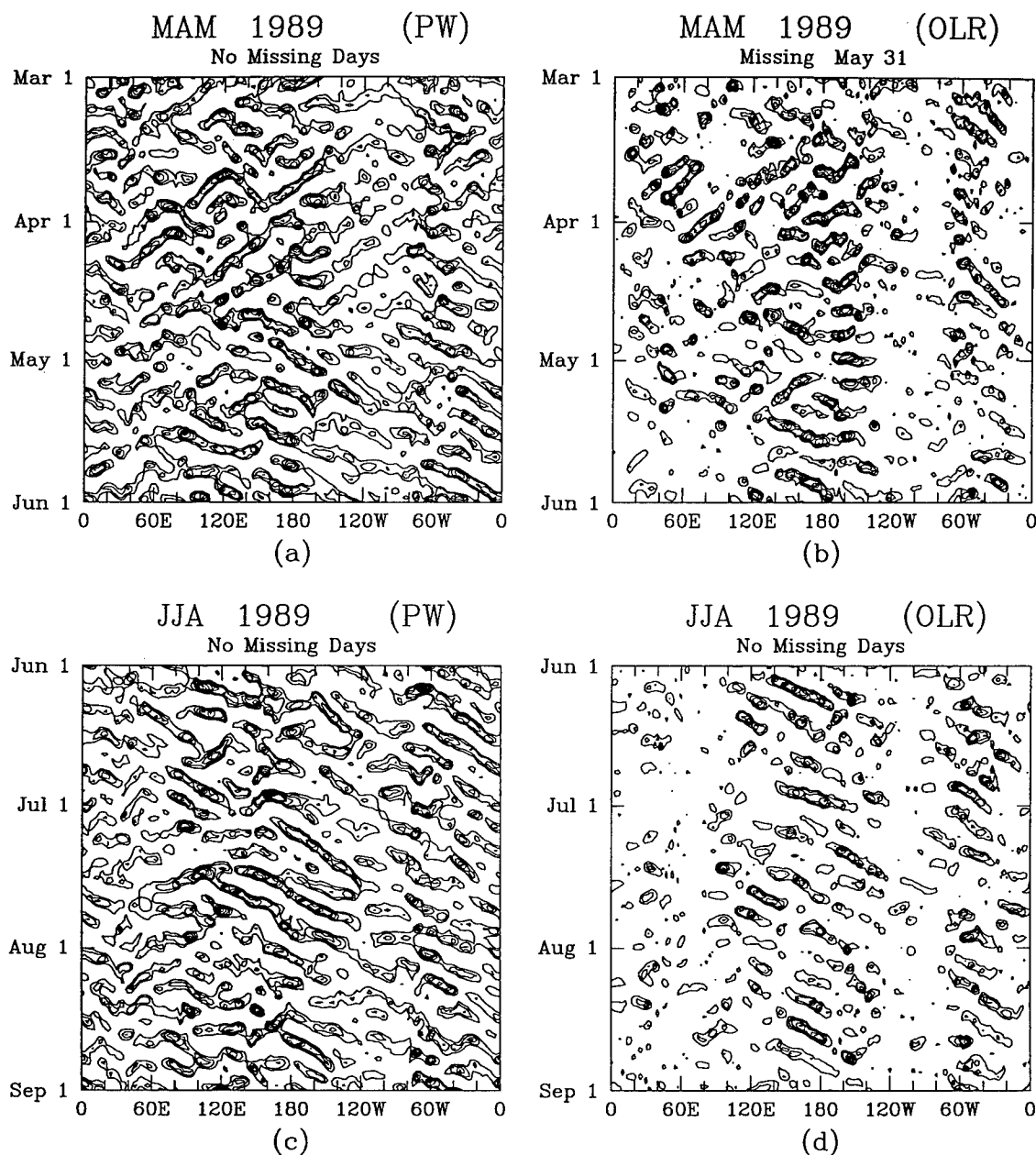
FIG. D12. As in Fig. D2, except at 20°S.

Synoptic Filtered Time–Longitude Plots at 30.0 S

SON 1989 (PW)
Missing Oct 9

SON 1989 (OLR)
No Missing Days

(a)

(b)

DJF 1989/1990 (PW)
Missing Dec 14

DJF 1989/1990 (OLR)
No Missing Days

(c)

(d)
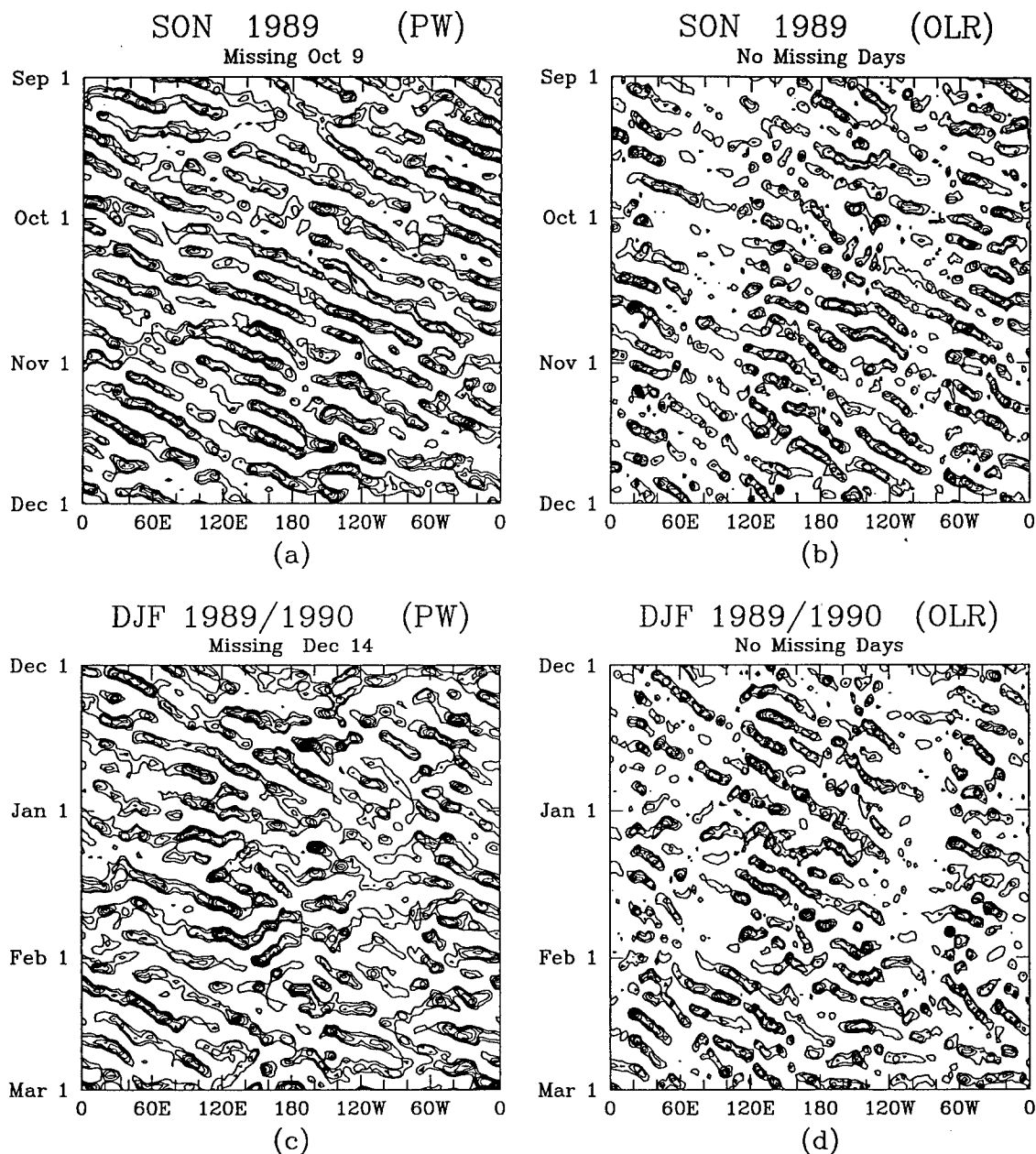
FIG. D13. As in Fig. D1, except at 30°S.

Synoptic Filtered Time–Longitude Plots at 30.0 S

MAM 1989 (PW)
No Missing Days

MAM 1989 (OLR)
Missing May 31

(a)

(b)

JJA 1989 (PW)
No Missing Days

JJA 1989 (OLR)
No Missing Days

(c)

(d)
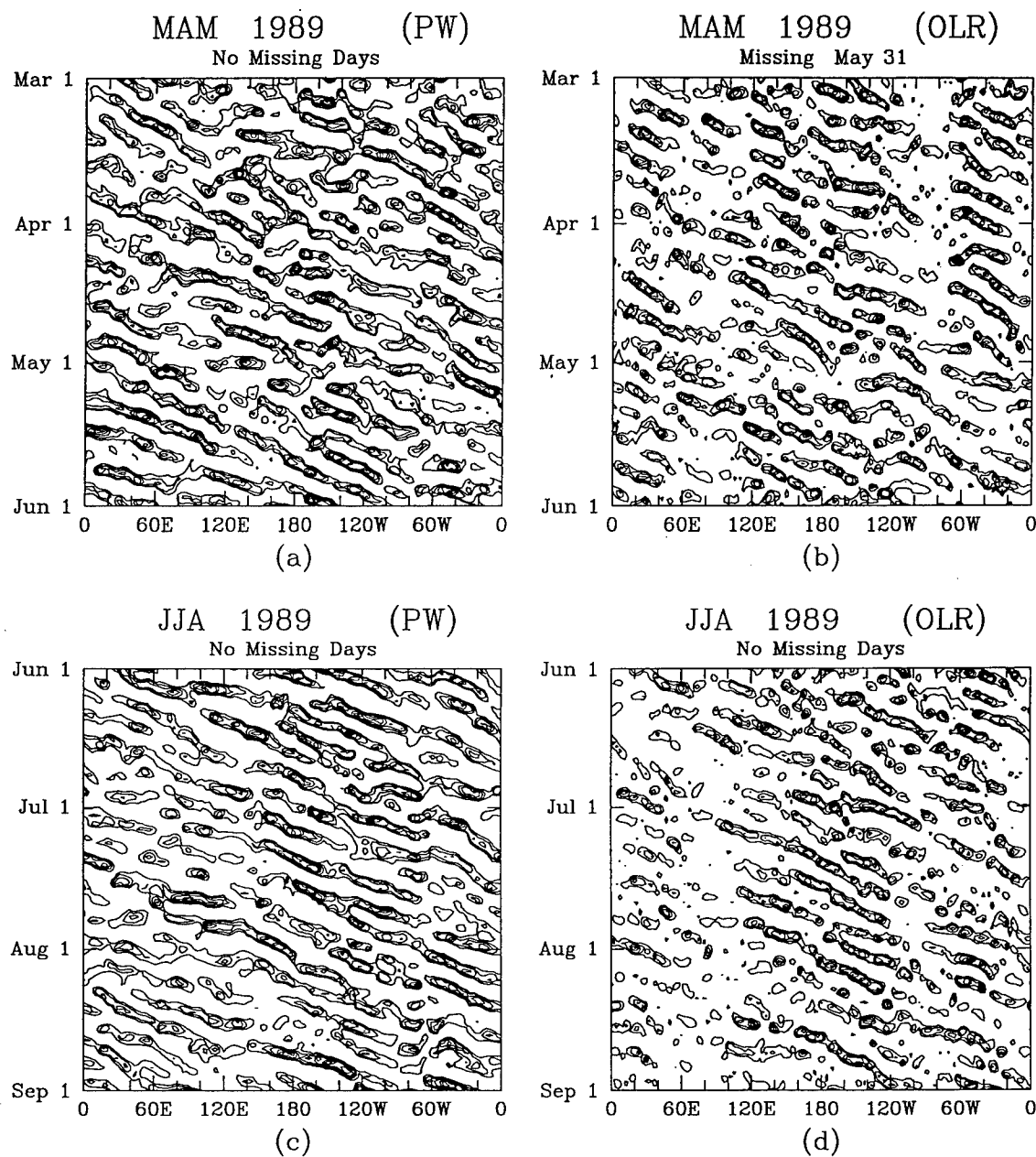
FIG. D14. As in Fig. D2, except at 30°S.

APPENDIX   E

SON 1989
15.0N, 145.0W — 14 Events
PW

(a)

OLR

(b)
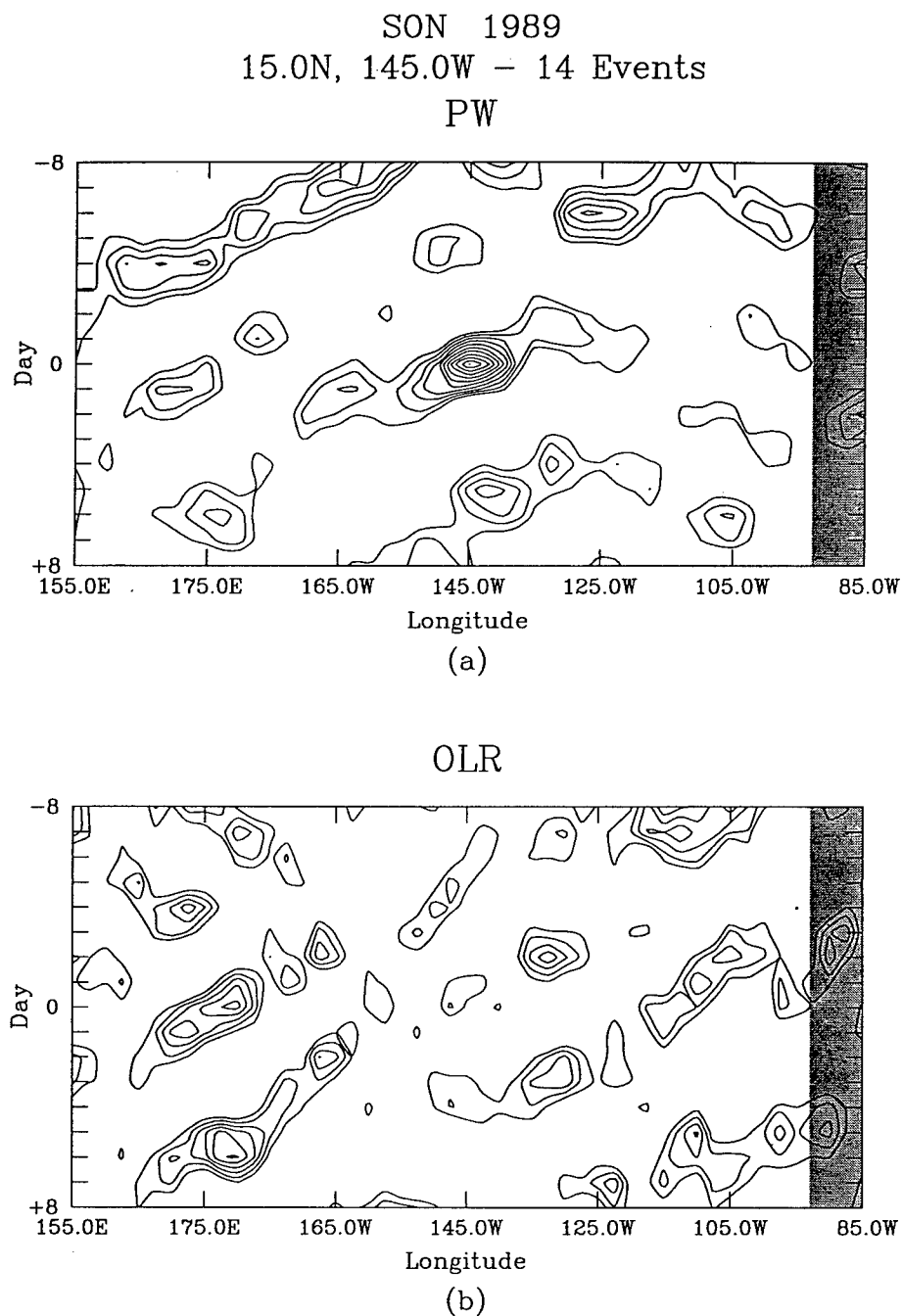
FIG. E1. Seasonal Hovmöller composite of (a) synoptic scale PW anomalies exceeding +1.0 mm and (b) synoptically filtered OLR data for the same event dates at 15°N, 145°W during SON 1989. Lowest (highest) contour for PW (OLR) is +0.25 mm (-2.5 Wm^{-2}) with an interval of 0.25 mm (2.5 Wm^{-2}). Shading denotes land. The total number of events is listed at the top of the figure.

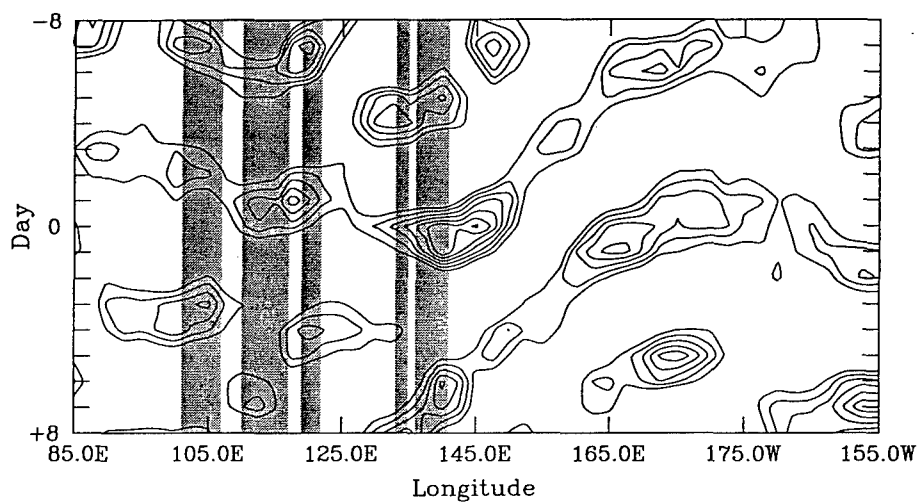DJF 1989/1990
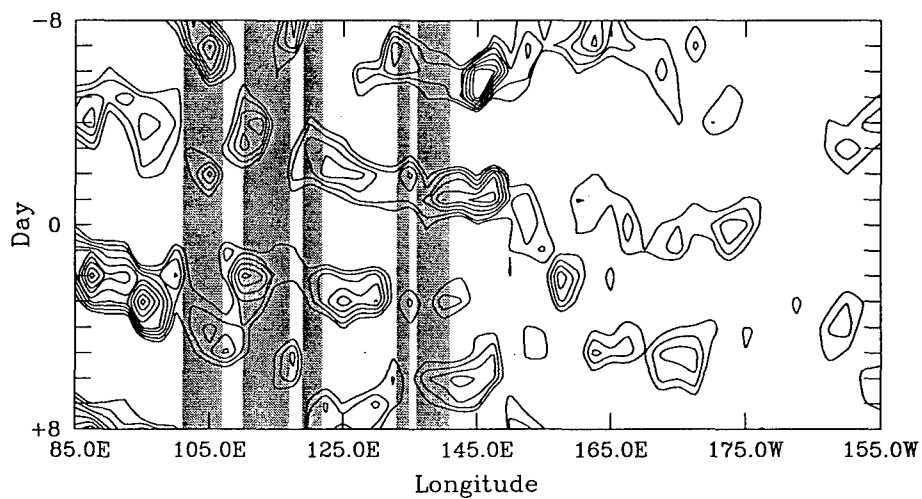10.0N, 145.0W − 10 Events
PW
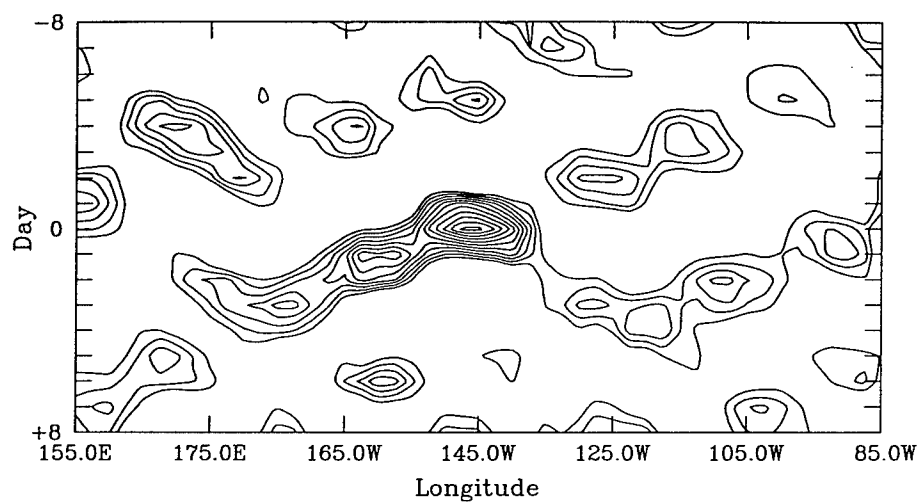
(a)

OLR
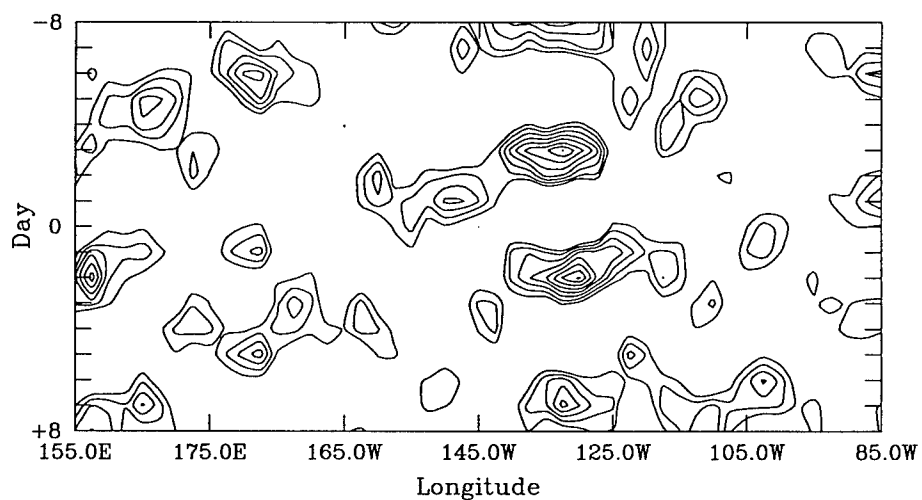
(b)

FIG. E2. As in Fig. E1, except at 10°N, 145°W during DJF 1989/1990.
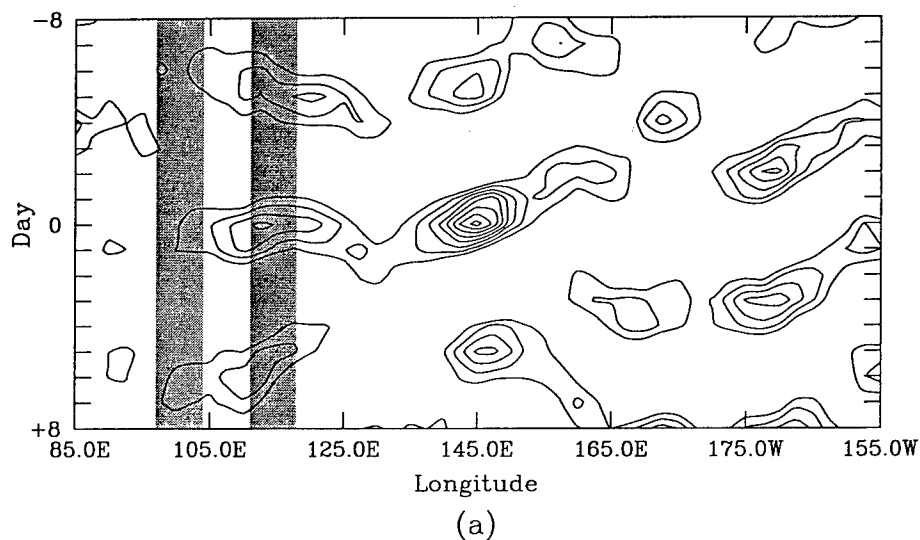
MAM 1989
10.0N, 145.0W − 12 Events
PW
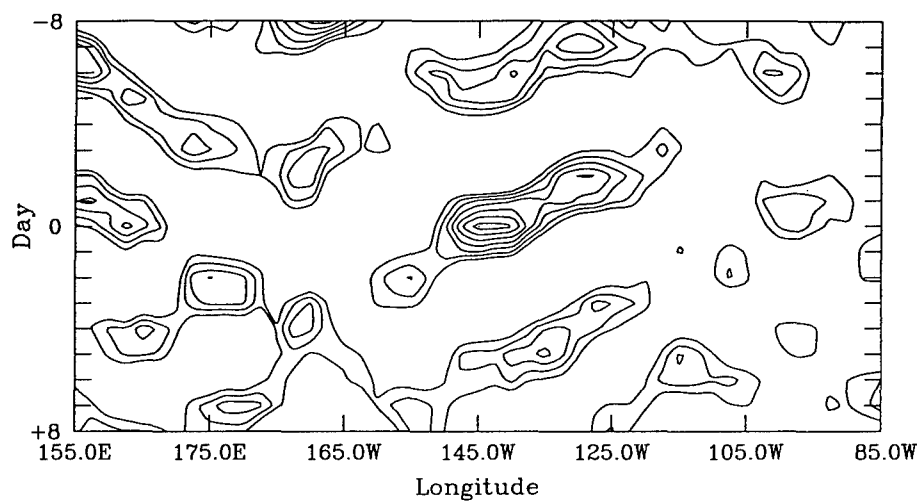
(a)

OLR
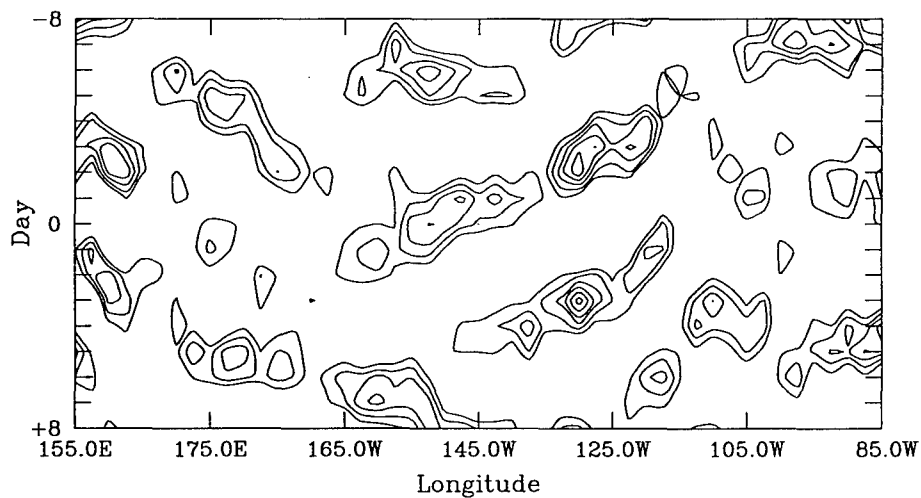
(b)

FIG. E3. As in Fig. E1, except at 10°N, 145°W during MAM 1989.
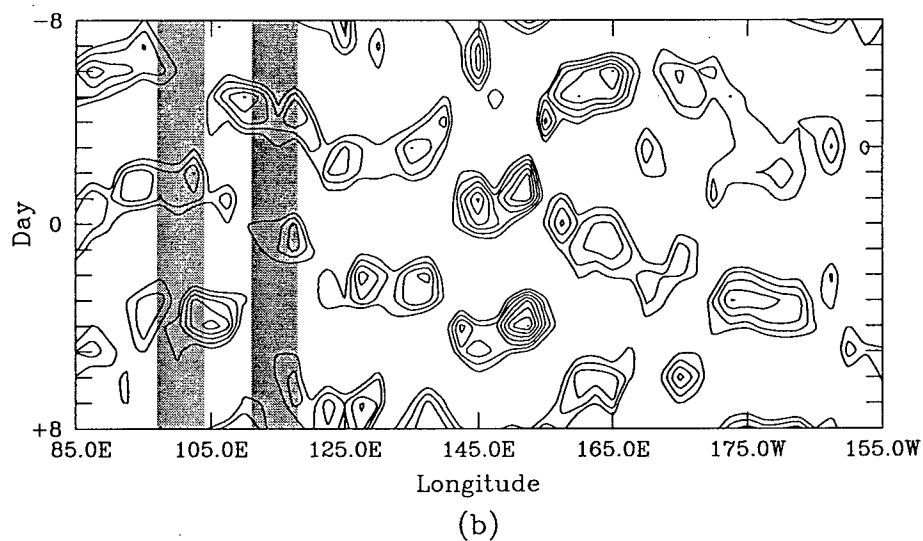
JJA   1989
12.5N, 145.0W − 13 Events
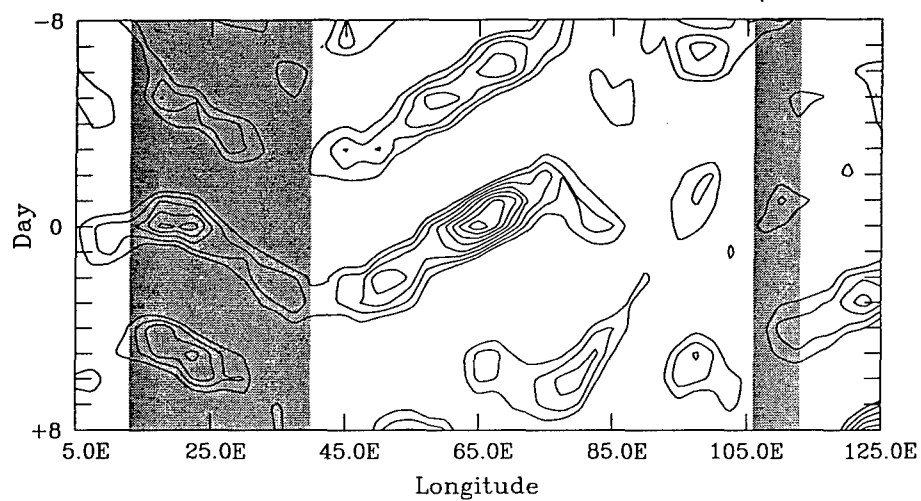PW

(a)

OLR

(b)
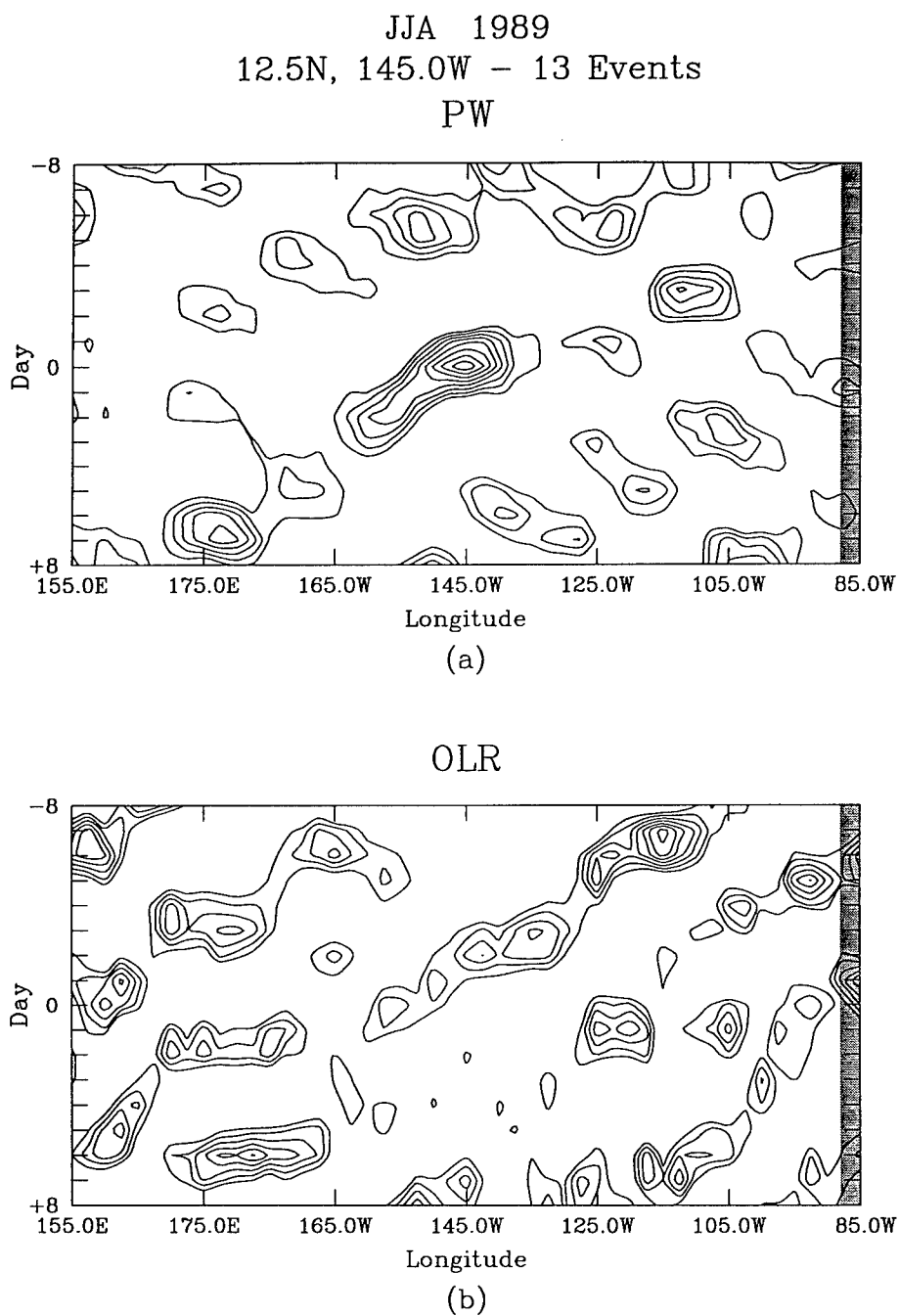
FIG. E4. As in Fig. E1, except at 12.5°N, 145°W during JJA 1989.

SON 1989
15.0S, 170.0W − 14 Events
PW

(a)

OLR
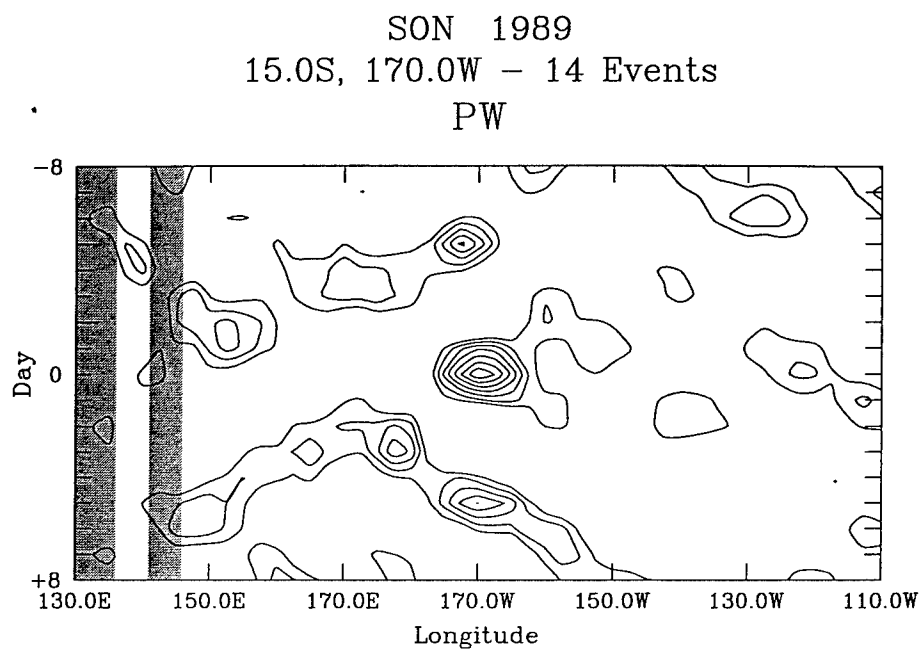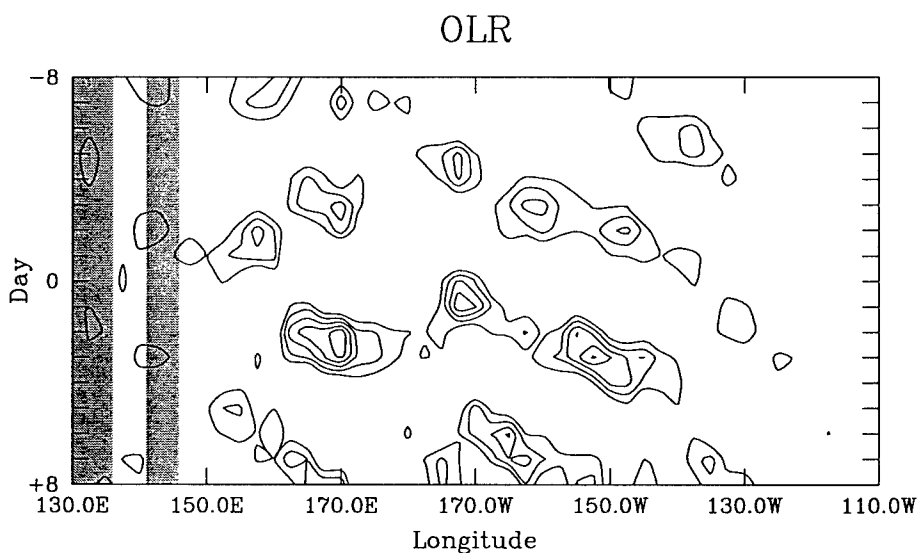
(b)

FIG. E5. As in Fig. E1, except at 15°S, 170°W during SON 1989.

DJF 1989/1990
17.5S, 170.0W — 11 Events
PW
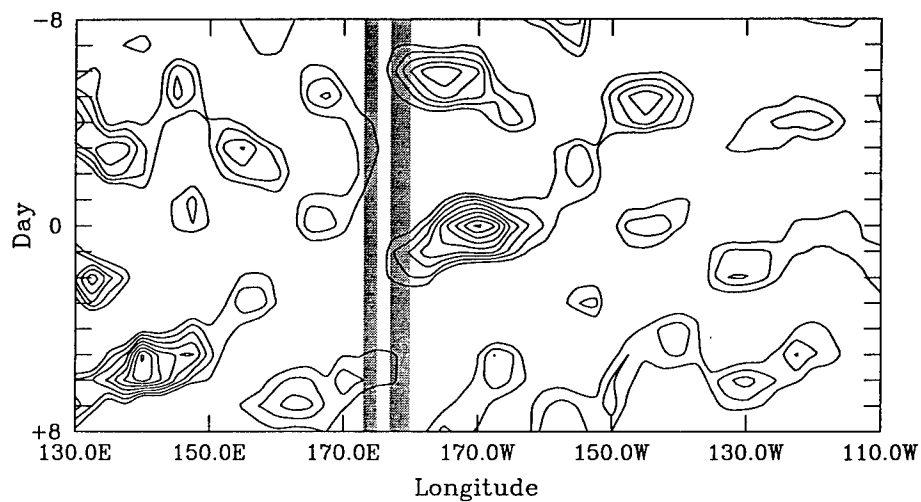
(a)

OLR
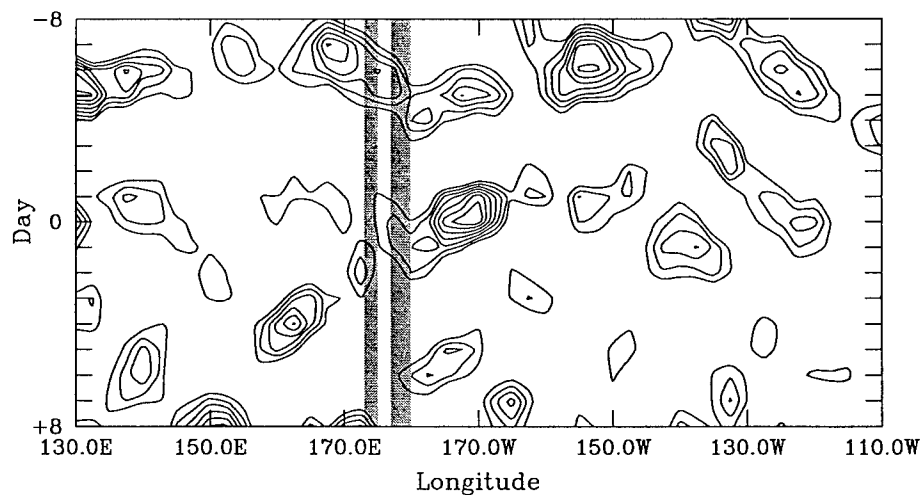
(b)

FIG. E6. As in Fig. E1, except at 17.5°S, 170°W during DJF 1989/1990.

MAM 1989
12.5S, 170.0W − 10 Events
PW
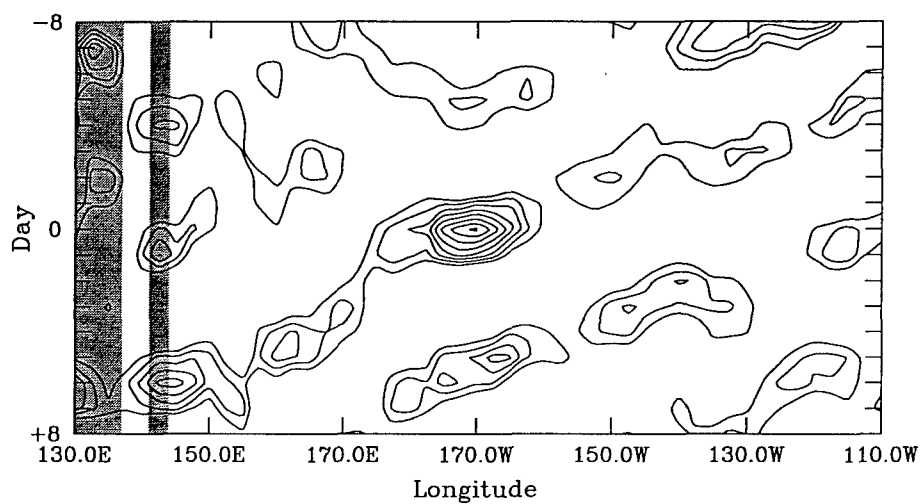
(a)

OLR
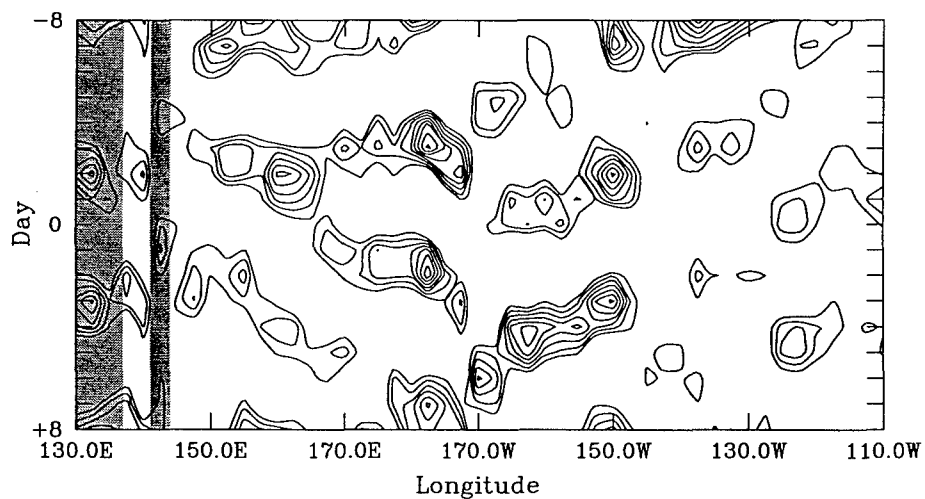
(b)

FIG. E7. As in Fig. E1, except at 12.5°S, 170°W during MAM 1989.

JJA 1989
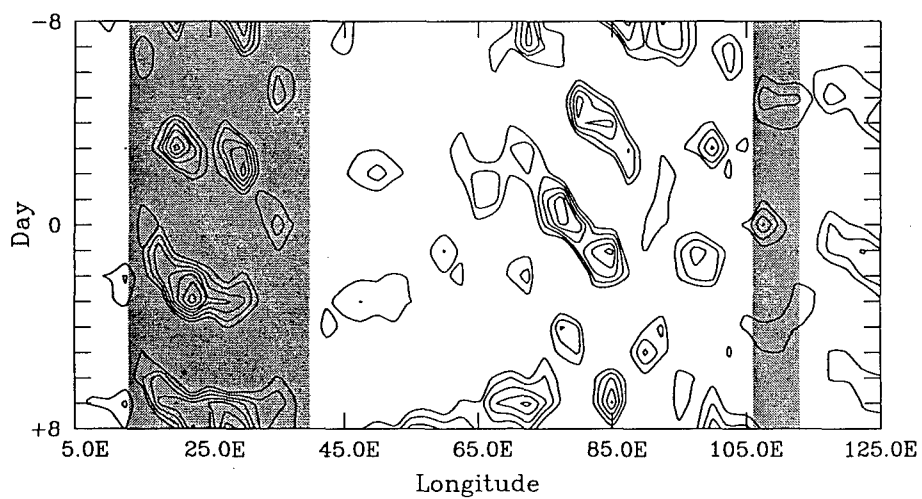15.0S, 170.0W – 12 Events
PW

(a)

OLR
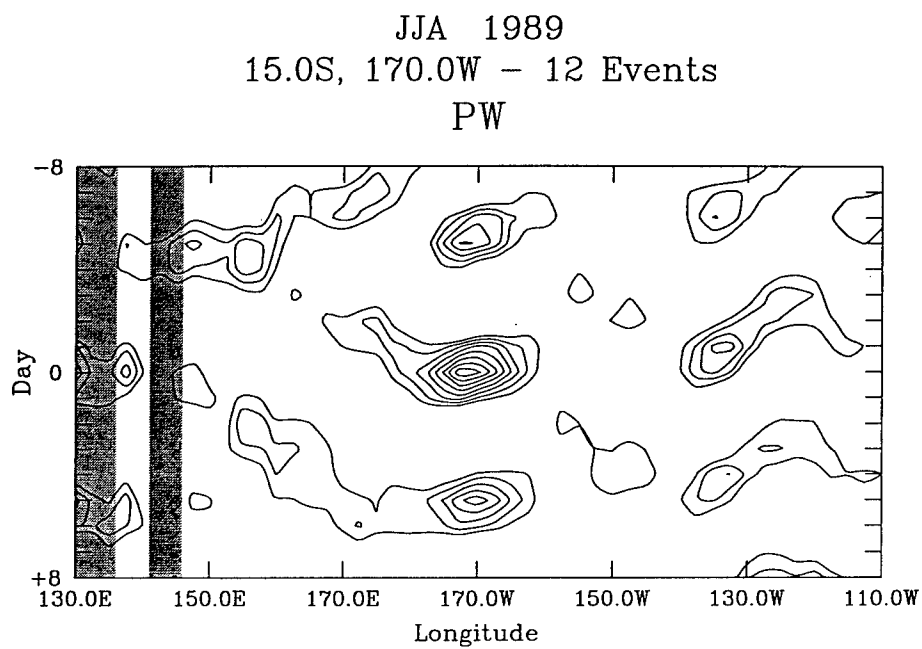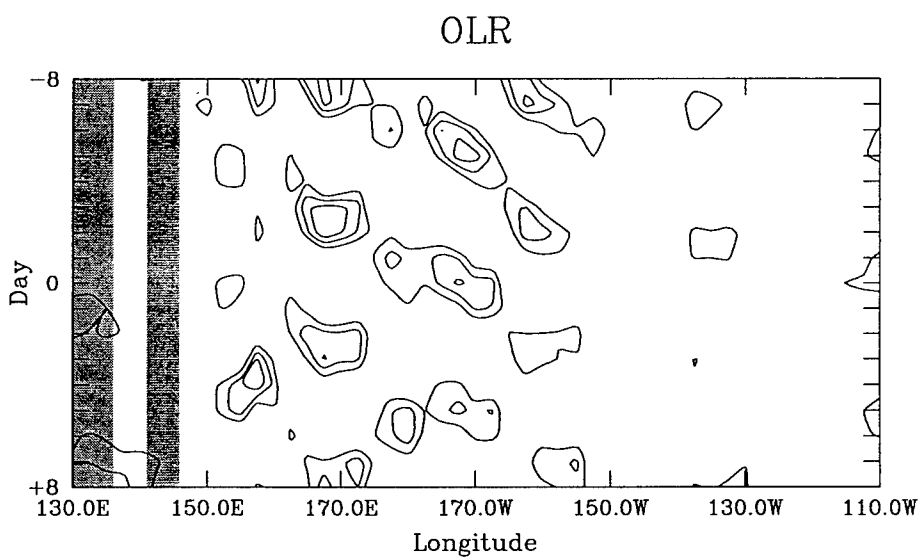
(b)

FIG. E8. As in Fig. E1, except at 15°S, 170°W during JJA 1989.
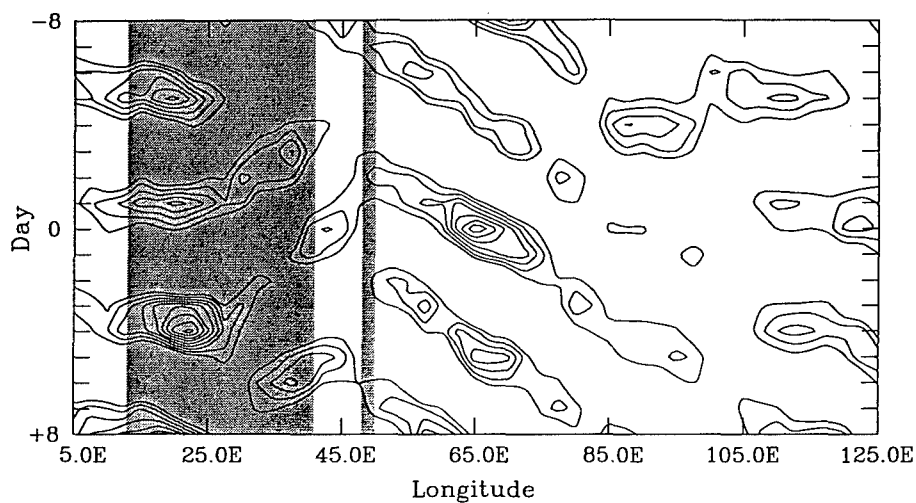
SON 1989
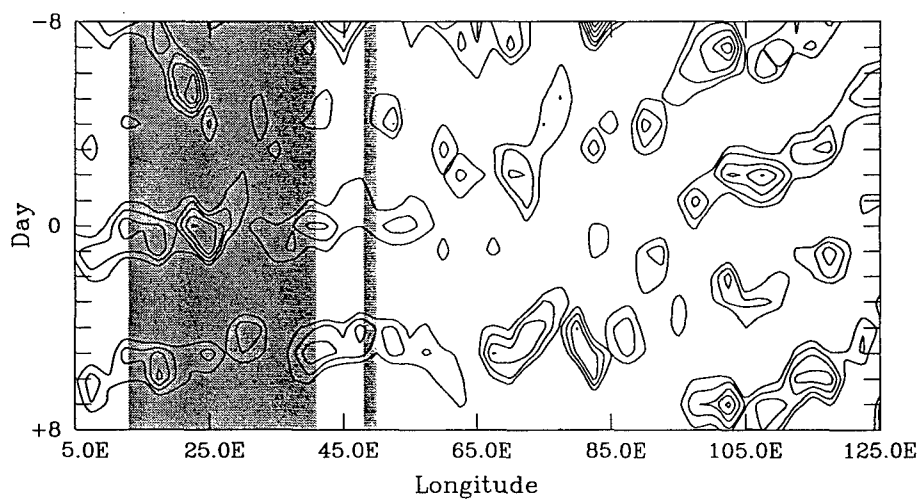12.5N, 30.0W − 12 Events
PW
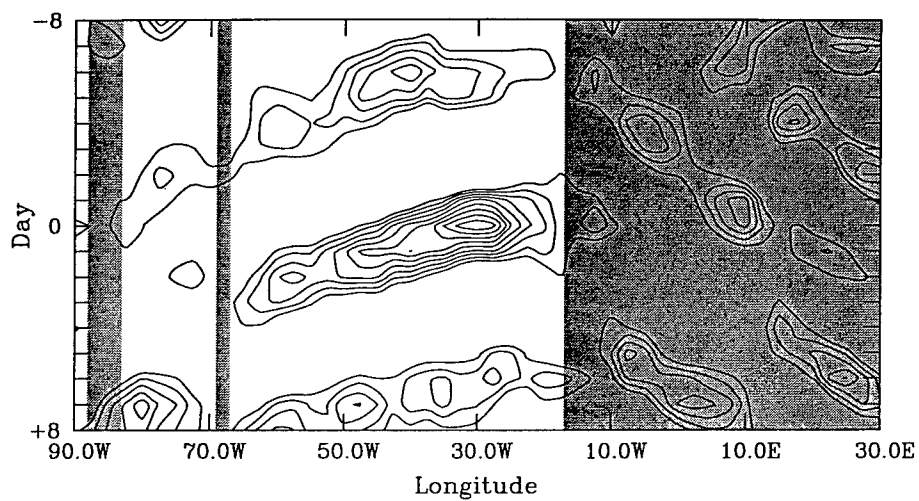
(a)

OLR
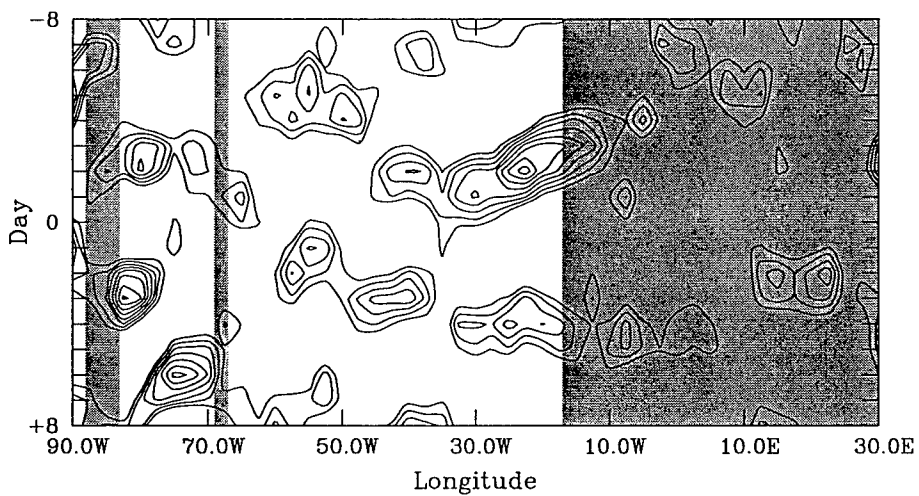
(b)

FIG. E9. As in Fig. E1, except at 12.5°N, 30°W during SON 1989.

DJF 1989/1990
7.5N, 30.0W — 9 Events

PW
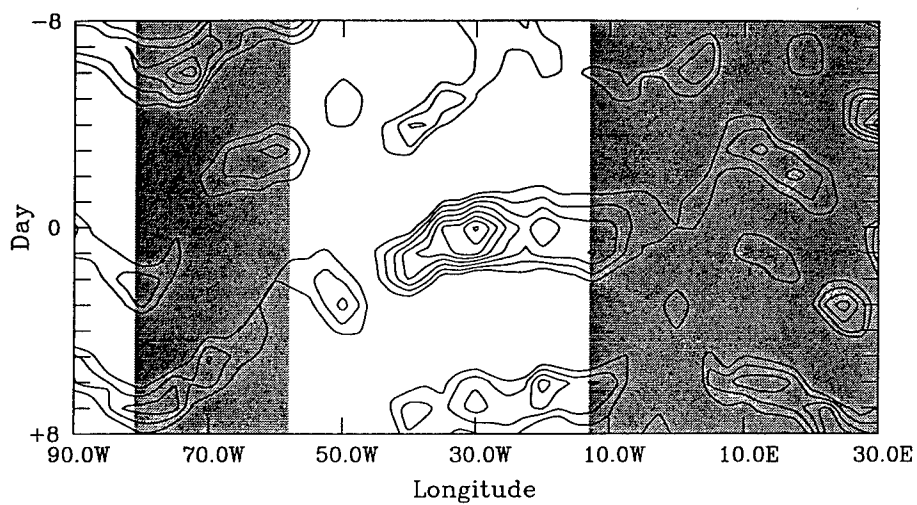
(a)

OLR
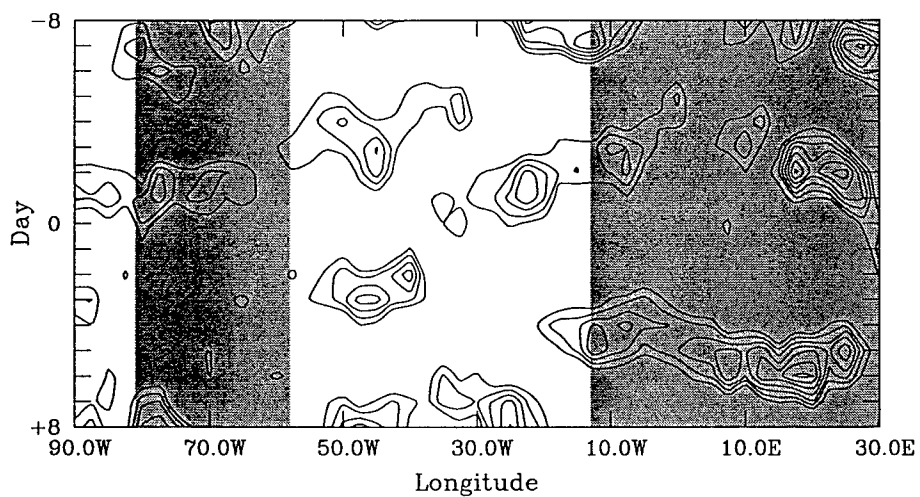
(b)

FIG. E10. As in Fig. E1, except at 7.5°N, 30°W during DJF 1989/1990.

MAM   1989
7.5N,   30.0W − 10 Events
PW
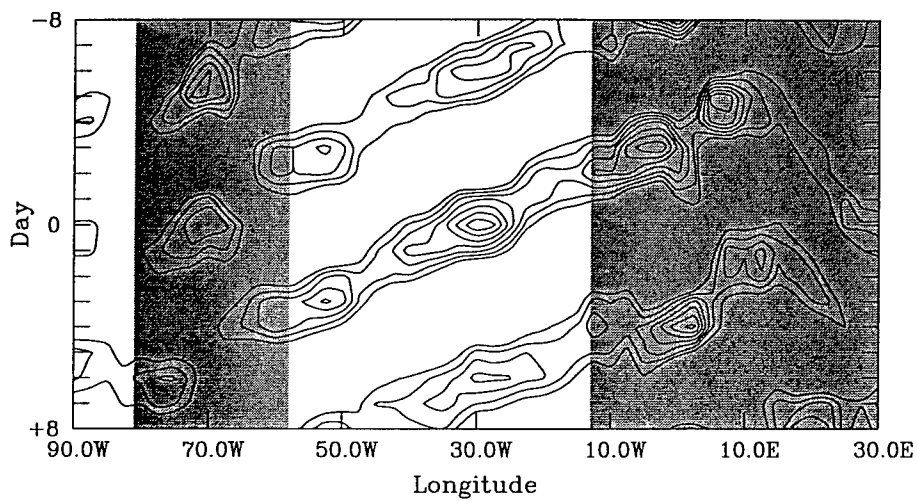
(a)

OLR
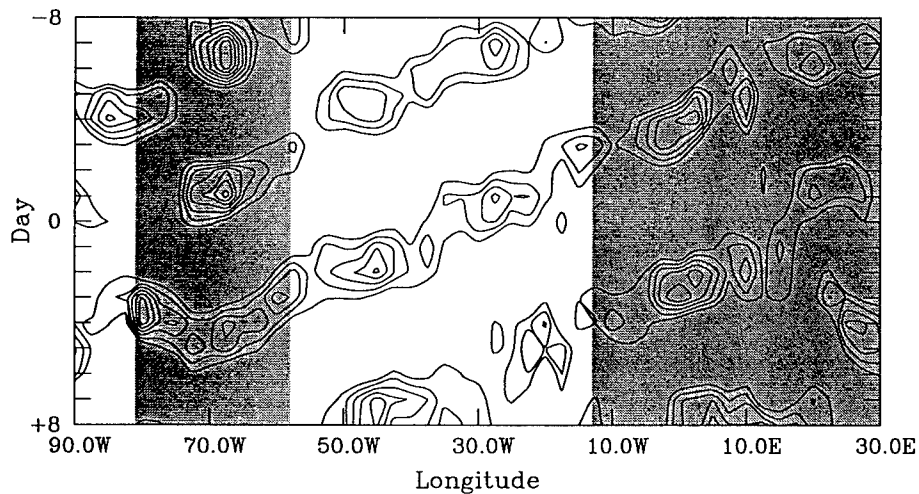
(b)

FIG. E11. As in Fig. E1, except at 7.5°N, 30°W during MAM 1989.

JJA 1989
12.5N, 30.0W – 11 Events
PW
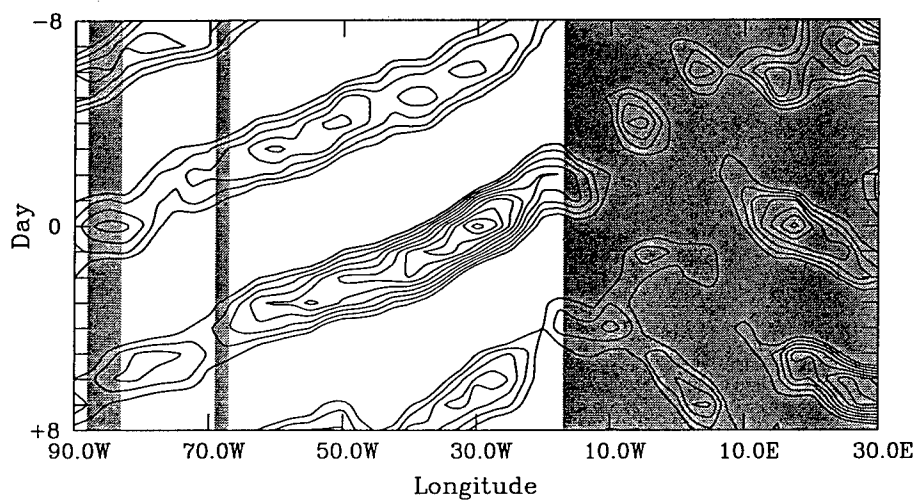
(a)

OLR
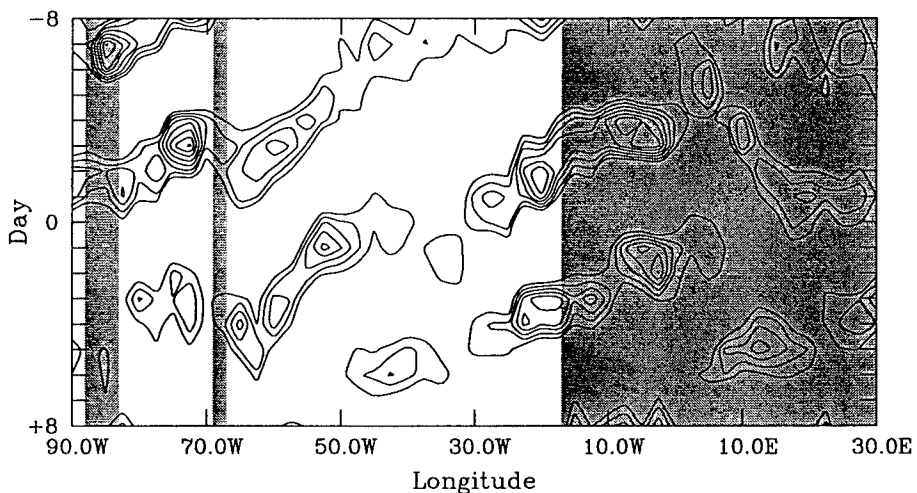
(b)

FIG. E12. As in Fig. E1, except at 12.5°N, 30°W during JJA 1989.

SON 1989
12.5N, 5.0E − 14 Events
PW
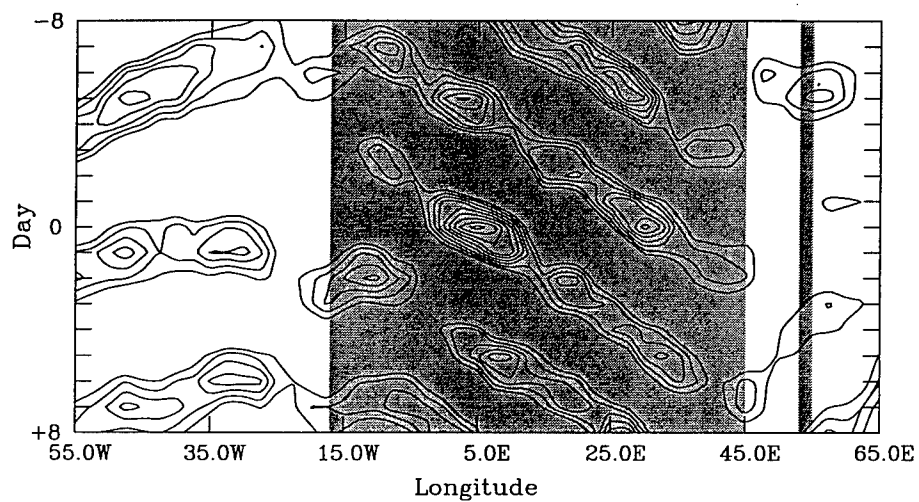
(a)

OLR
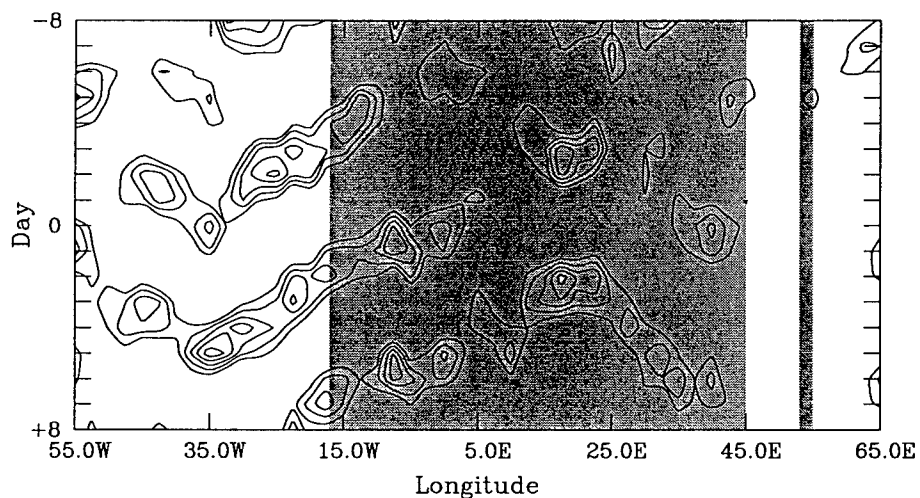
(b)

FIG. E13. As in Fig. E1, except at 12.5°N, 5°E during SON 1989.

DJF 1989/1990
7.5N,   5.0E − 11 Events
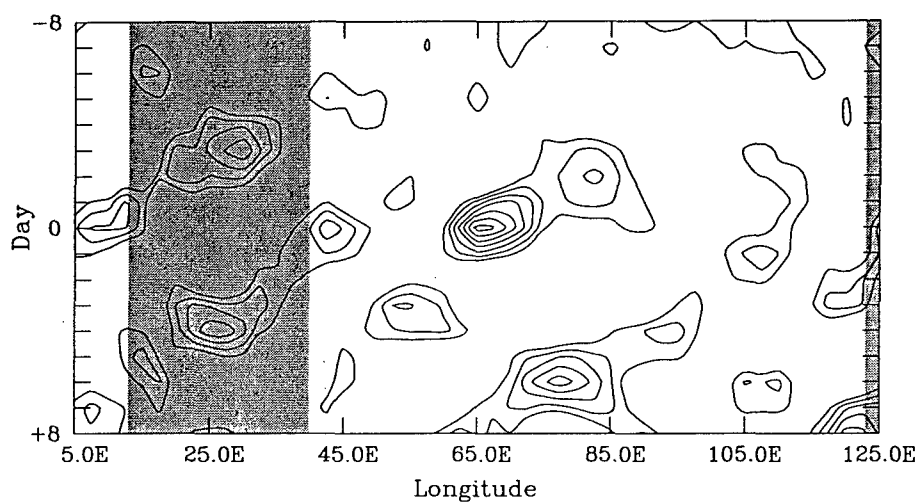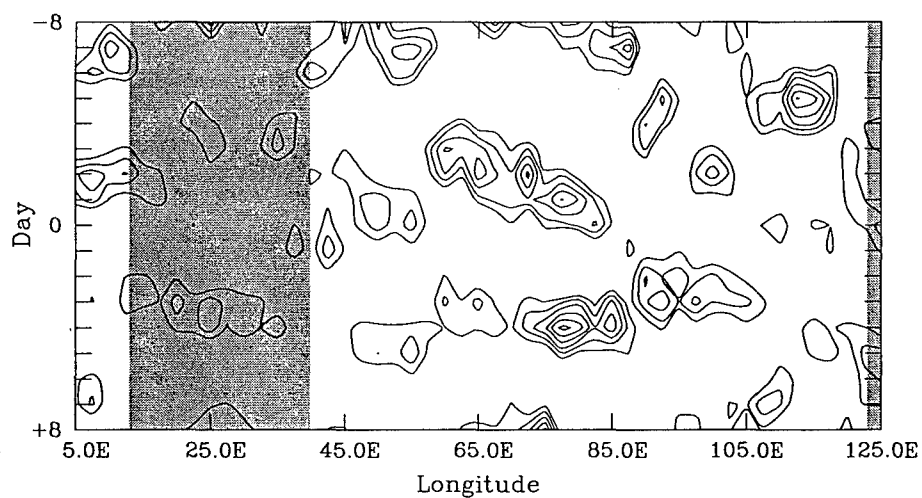PW
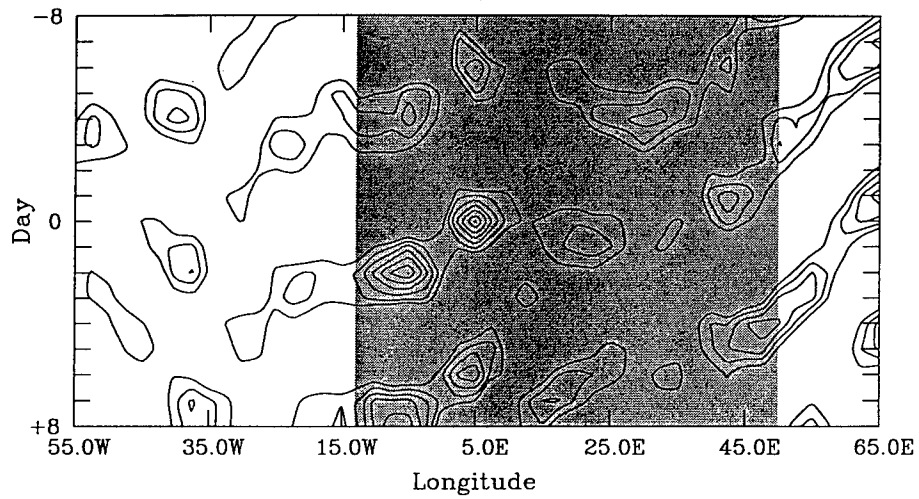
(a)

OLR
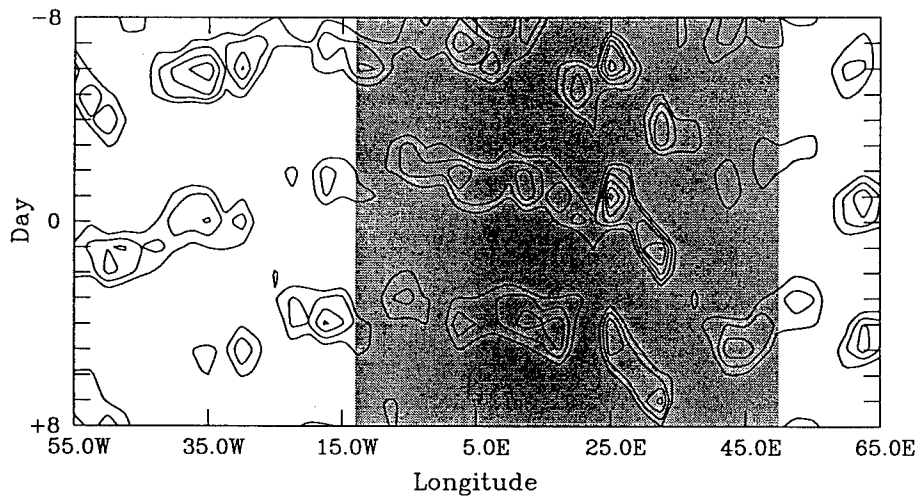
(b)

FIG. E14. As in Fig. E1, except at 7.5°N, 5°E during DJF 1989/1990.

MAM 1989
12.5N, 5.0E − 18 Events
PW
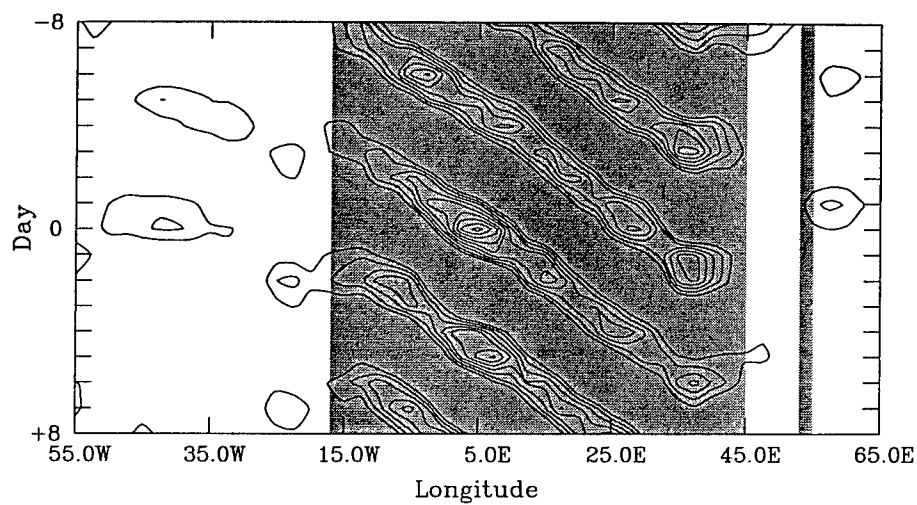
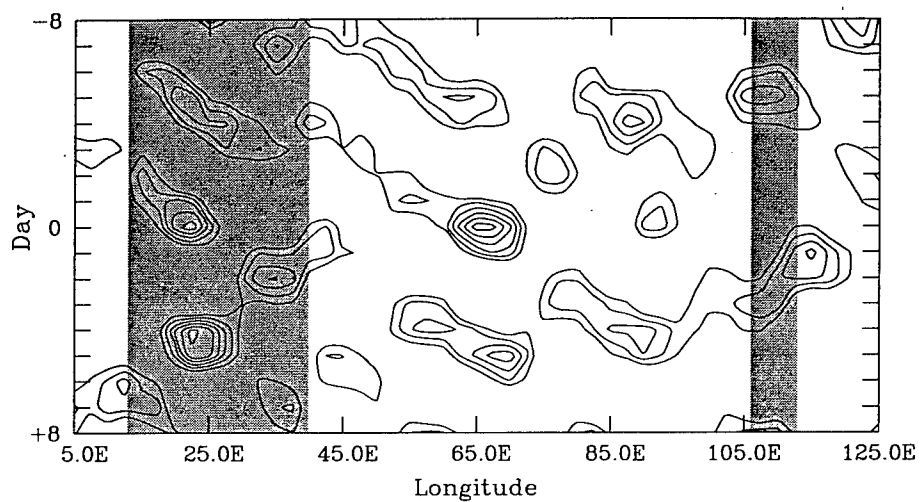
(a)

OLR
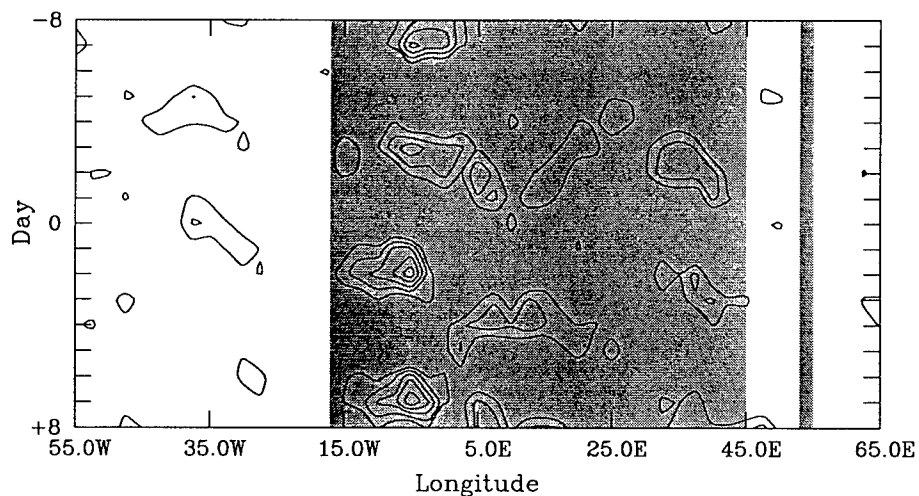
(b)

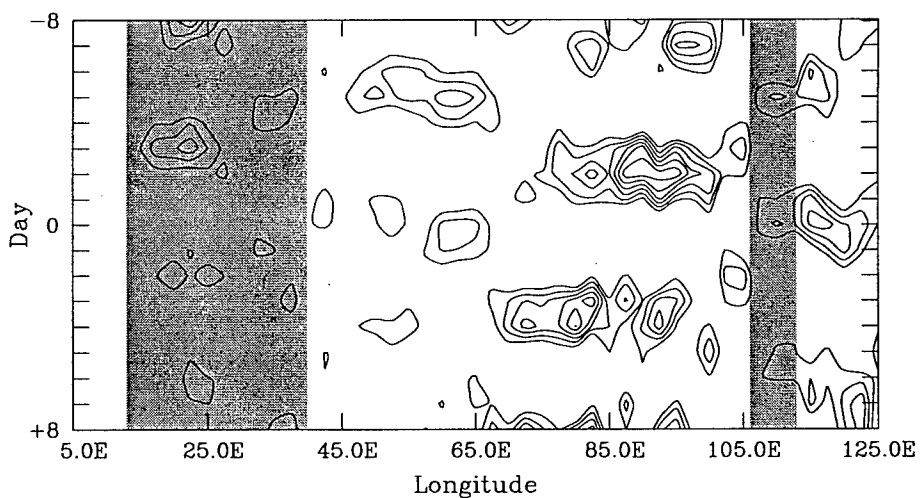FIG. E15. As in Fig. E1, except at 12.5°N, 5°E during MAM 1989.

JJA   1989
15.0N,   5.0E − 17 Events
PW
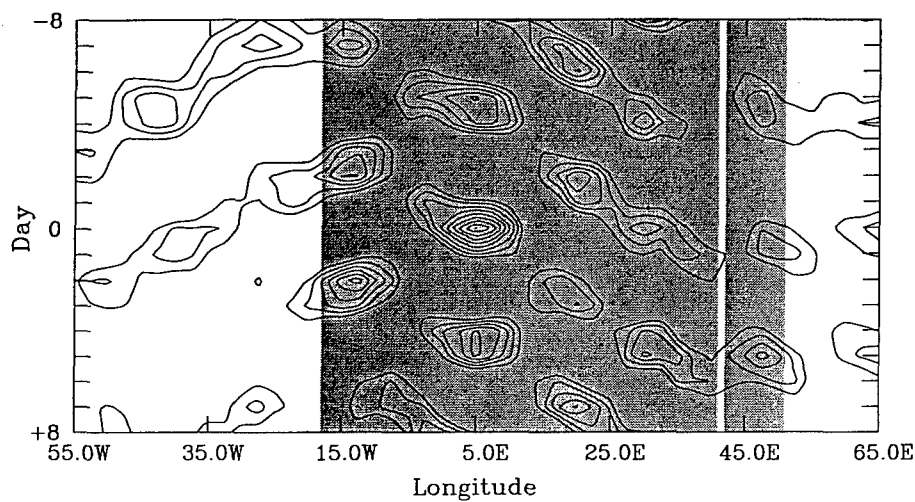
(a)

OLR
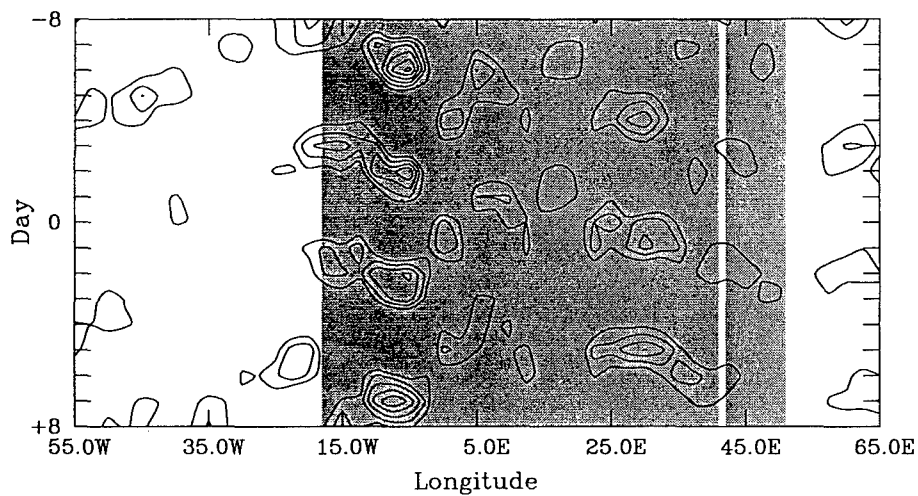
(b)

FIG. E16. As in Fig. E1, except at 15°N, 5°E during JJA 1989.

SON 1989
2.5N, 145.0E – 9 Events
PW
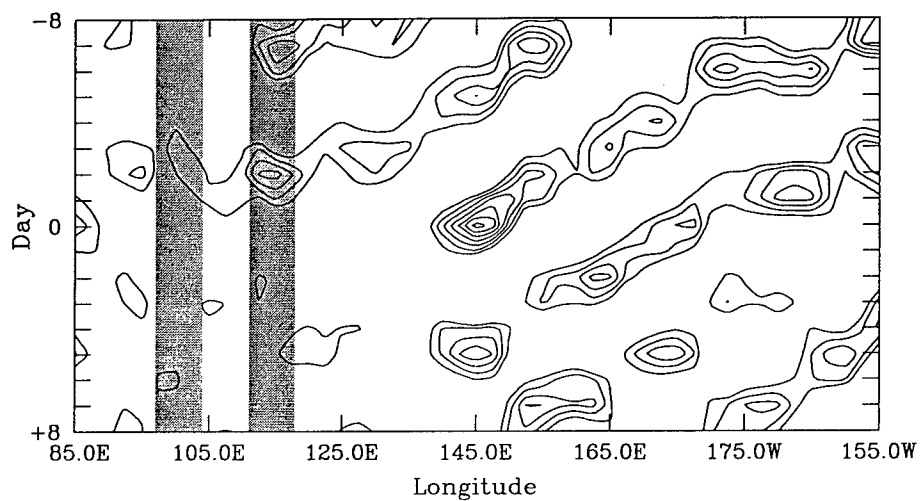
(a)

OLR
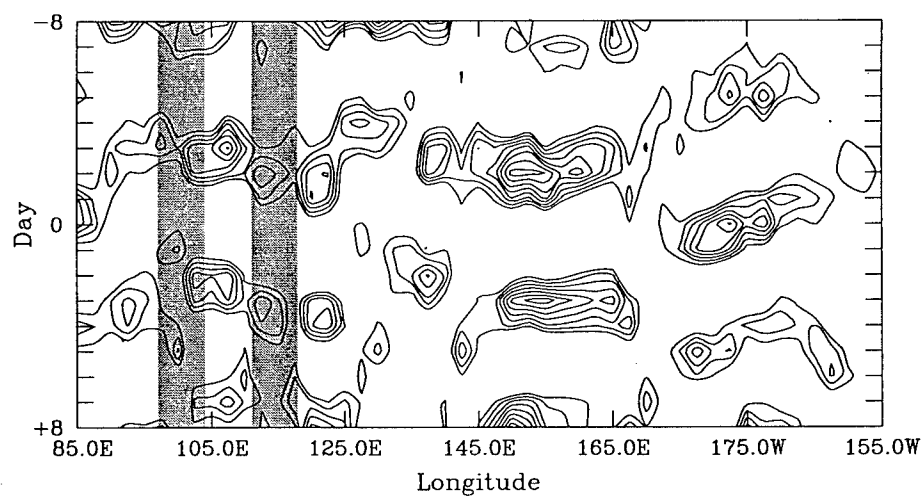
(b)

FIG. E17. As in Fig. E1, except at 2.5°N, 145°E during SON 1989.

DJF 1989/1990
2.5S, 145.0E — 9 Events
PW
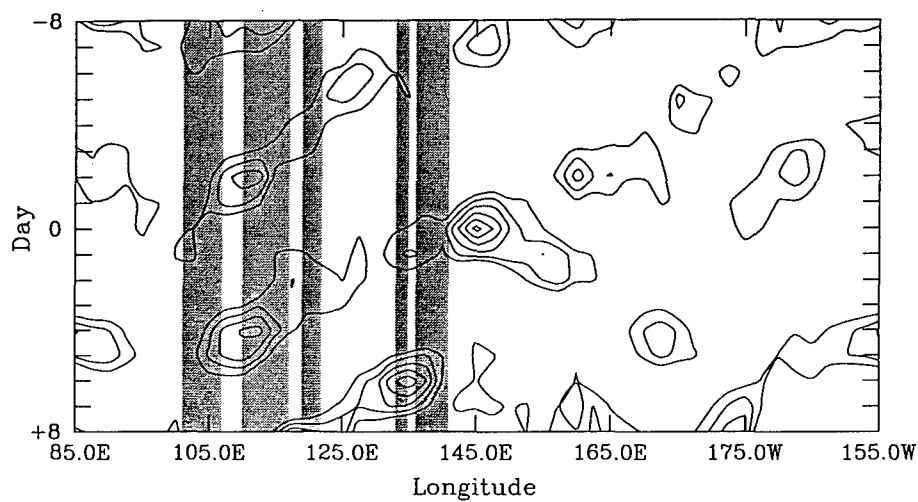
(a)

OLR
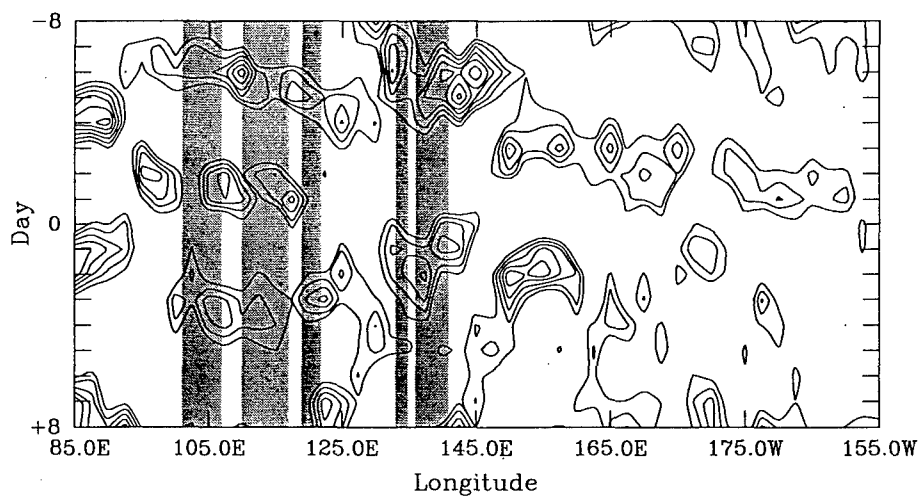
(b)

FIG. E18. As in Fig. E1, except at 2.5°S, 145°E during DJF 1989/1990.

MAM 1989
2.5S, 145.0E −   6 Events
PW

(a)

OLR

(b)

FIG. E19. As in Fig. E1, except at 2.5°S, 145°E during MAM 1989.

JJA 1989
2.5N, 145.0E − 13 Events
PW

(a)

OLR

(b)

FIG. E20. As in Fig. E1, except at 2.5°N, 145°E during JJA 1989.

SON 1989
7.5S, 65.0E − 12 Events
PW

(a)

OLR

(b)

FIG. E21. As in Fig. E1, except at 7.5°S, 65°E during SON 1989.

DJF 1989/1990
12.5S, 65.0E − 12 Events
PW

(a)

OLR

(b)

FIG. E22. As in Fig. E1, except at 12.5°S, 65°E during DJF 1989/1990.

MAM 1989
10.0S, 65.0E − 12 Events
PW

(a)

OLR

(b)

FIG. E23. As in Fig. E1, except at 10°S, 65°E during MAM 1989.

JJA   1989
7.5S,   65.0E −   9 Events
PW

(a)

OLR

(b)

FIG. E24. As in Fig. E1, except at 7.5°S, 65°E during JJA 1989.

SON 1989
12.5S, 60.0W − 12 Events
PW
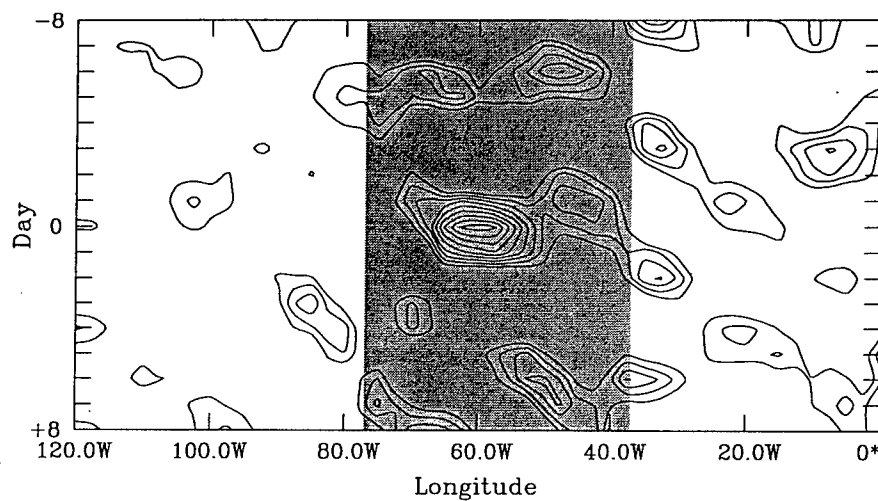
(a)

OLR
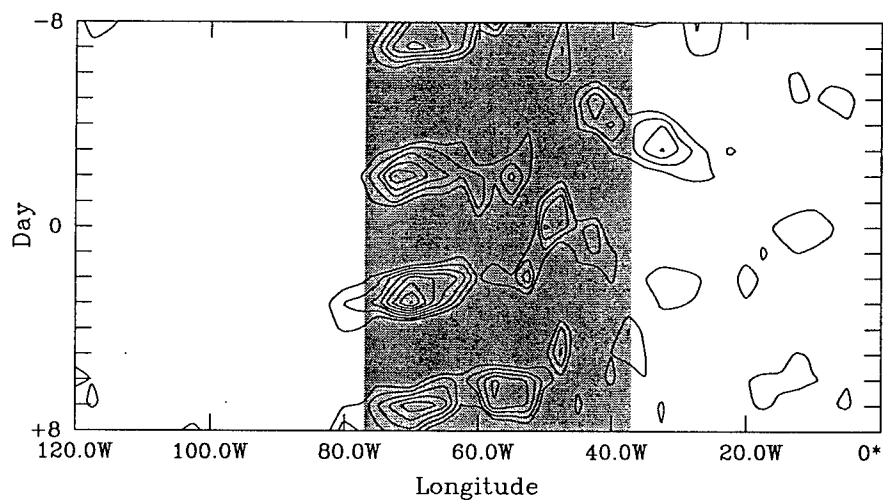
(b)

FIG. E25. As in Fig. E1, except at 12.5°S, 60°W during SON 1989.

DJF 1989/1990
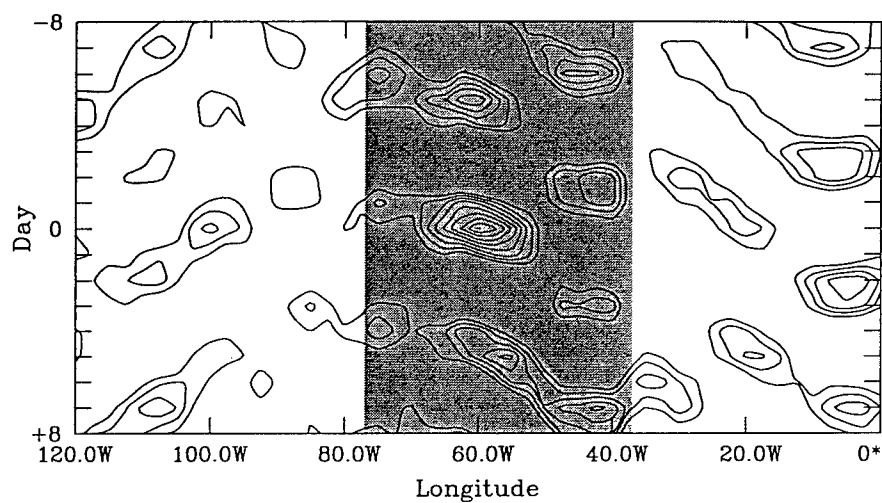10.0S, 60.0W − 12 Events
PW
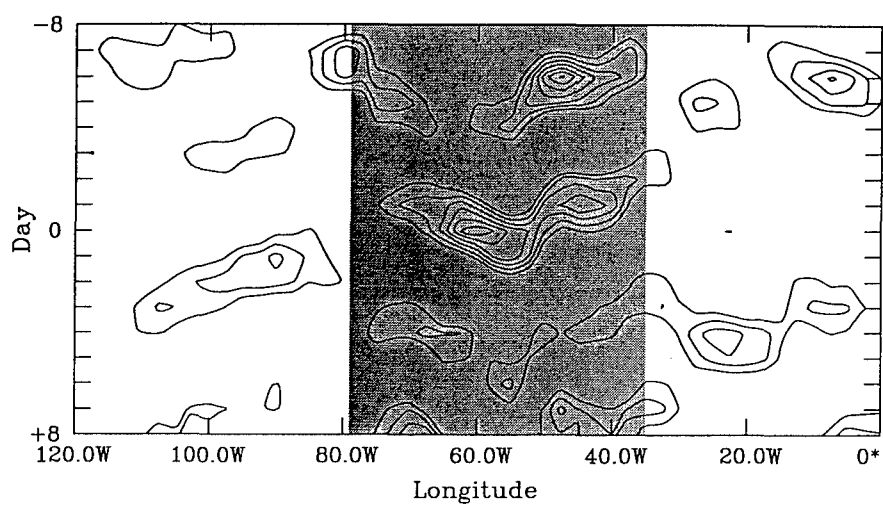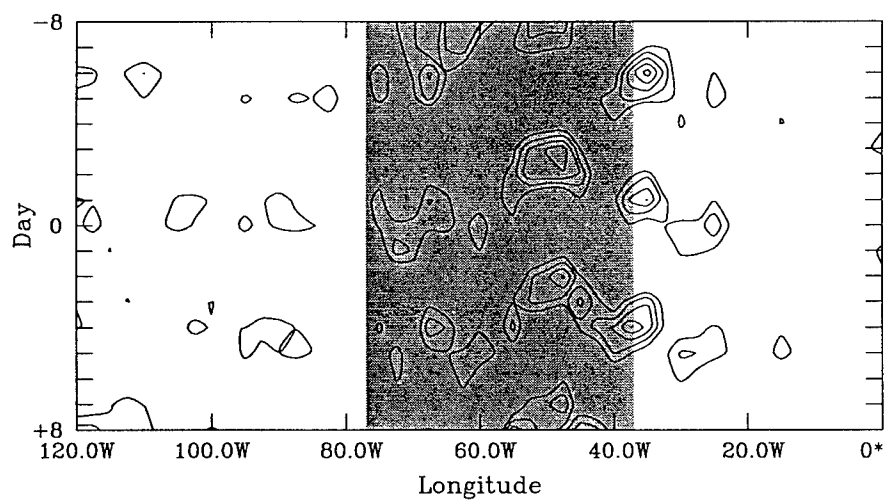

(a)

OLR
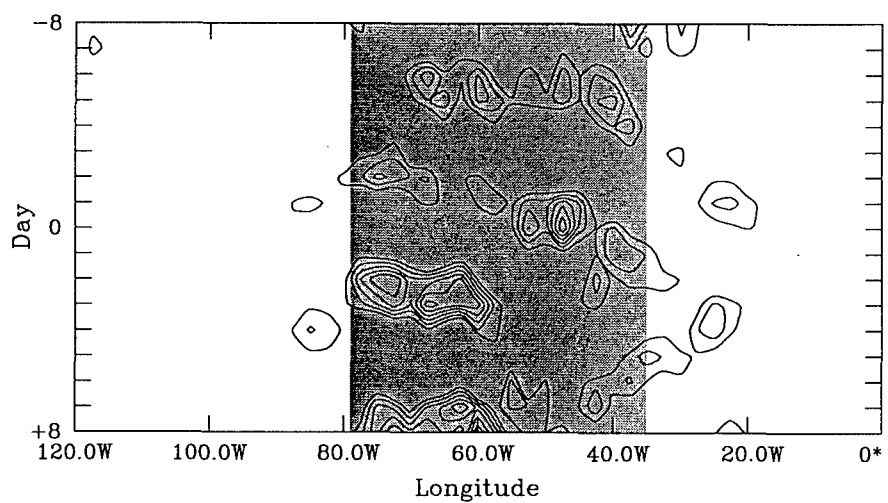
(b)

FIG. E26. As in Fig. E1, except at 10°S, 60°W during DJF 1989/1990.

MAM 1989
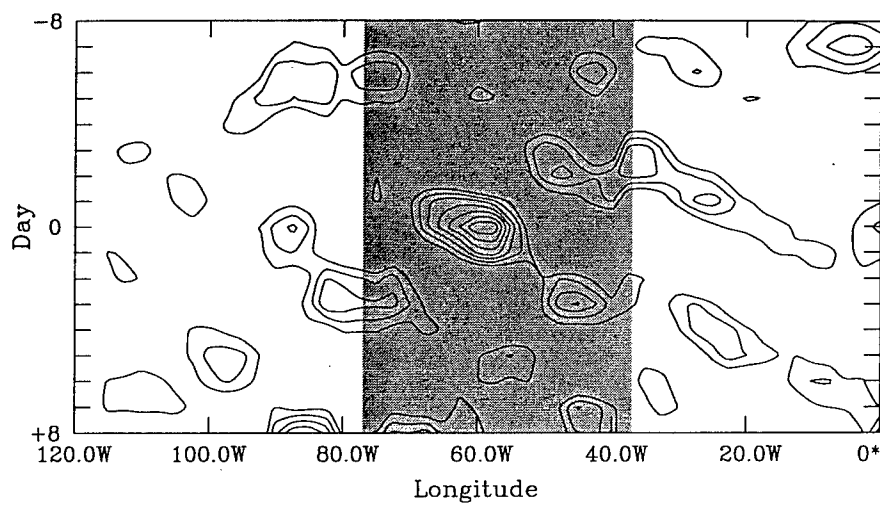12.5S, 60.0W — 15 Events
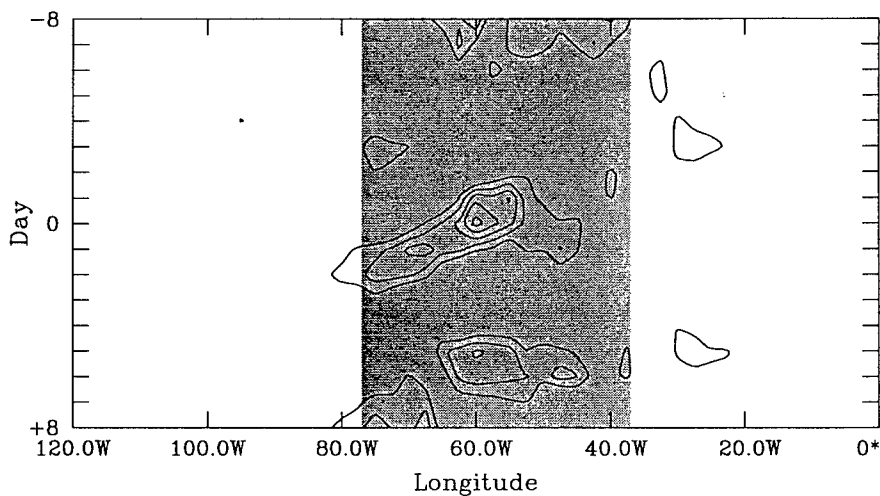PW

(a)

OLR

(b)

FIG. E27. As in Fig. E1, except at 12.5°S, 60°W during MAM 1989.

JJA 1989
12.5S, 60.0W − 13 Events
PW

(a)

OLR

(b)

FIG. E28. As in Fig. E1, except at 12.5°S, 60°W during JJA 1989.

VITA

Morgan Douglas Mackey ~~was born~~ ~~June 1, 1969 in~~ ~~to~~ Douglas and Ada Ruth Mackey. He grew up in Corona, California where he completed his secondary education at Corona Senior High School in June 1987. He attended the United States Air Force Academy his freshman and sophomore years before serving a two-year full-time mission for his church. Afterward, he returned to the Academy, where on June 1, 1994, he earned his Bachelor of Science degree in Geography and was commissioned an officer in the United States Air Force. His first assignment was to Texas A&M University in August 1994 under the sponsorship of the Air Force Institute of Technology.

Shortly after his assignment to Texas A&M University, he married Chandra Suman Prasad, formerly of Lautoka, Fiji Islands. They have two sons: Vikash and Jayant.

The author may be contacted at his permanent mailing address:

~~1200 Valley Ave.~~
~~Corona, CA 91720-1200~~